

# **Multifaceted Design Approaches for Eutectic Multi-Principal Element Alloys**

**Ph.D. Thesis**

By

**GOPI TALLURI**



**Department of Metallurgical Engineering and Materials Science**

**INDIAN INSTITUTE OF TECHNOLOGY INDORE**

**MAY 2024**



# **Multifaceted Design Approaches for Eutectic Multi-Principal Element Alloys**

**A THESIS**

*Submitted in partial fulfilment of the  
requirements for the award of the degree*

*of*

**DOCTOR OF PHILOSOPHY**

*by*

**GOPI TALLURI**



**Department of Metallurgical Engineering and Materials Science**

**INDIAN INSTITUTE OF TECHNOLOGY INDORE**

**MAY 2024**







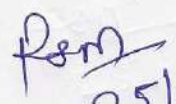
## INDIAN INSTITUTE OF TECHNOLOGY INDORE

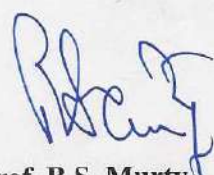
I hereby certify that the work which is being presented in the thesis entitled **Multifaceted Design Approaches for Eutectic Multi-Principal Element Alloys** in the partial fulfilment of the requirements for the award of the degree of **Doctor of Philosophy** and submitted in the **Department of Metallurgical Engineering and Materials Science, Indian Institute of Technology Indore**, is an authentic record of my own work carried out during the time period from 20.08.2020 to 30.05.2024 under the supervision of Dr. Ram Sajeewan Maurya, Assistant Professor at IIT Indore and Prof. B.S. Murty, Director at IIT Hyderabad.

The matter presented in this thesis has not been submitted by me for the award of any other degree of this or any other institute.

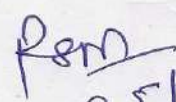
  
Gopi Talluri


-----  
This is to certify that the above statement made by the candidate is correct to the best of our knowledge.

  
25/09/2024  
Dr. Ram Sajeewan Maurya

  
Prof. B.S. Murty

-----  
Gopi Talluri has successfully given his Ph.D. Oral Examination held on 23.09.2024.

  
25/09/2024  
Dr. Ram Sajeewan Maurya

  
Prof. B.S. Murty



## ACKNOWLEDGEMENTS

I have greatly benefited from the support of many during this journey and I am immensely thankful to them all.

First, I acknowledge my debt to Dr. Ram, the thesis supervisor at IIT Indore, for allowing me to work on eutectic multi-principal element alloys (EMPEAs). He consistently provided directions on what to work on and what not to work on and I am thankful to him for tolerating me throughout this journey. Also, thanks to him, this thesis redefined its limits and made accelerated progress, taking its current shape. Thanks are also due to the opportunity given to mentor friends Vasanth and Shantanu for their BTP and MTP, respectively.

I extend gratitude to Dr. Indrasen and Dr. Eswar, thesis PSPC members at IIT Indore, for their time and valuable suggestions during CERPs and their kind support offline. Although I didn't have frequent interactions with Dr. Indrasen, his positivity and encouragement were always evident whenever I met him. Dr. Eswar's email signature quote, 'You don't use science to show you're right, you use science to become right - XKCD,' encapsulates his approach to research and has been truly inspiring for me to be an academician of his nature.

I am grateful to Dr. Vinod Kumar (who was also HOD when I joined the PhD program) for his helpful counselling and encouragement in multiple ways. Conversations with him feel like going through a review paper. His support greatly comforted my stay at IIT Indore, and he will be remembered and cherished throughout my life. I also thank Dr. Sumanta Samal (DPGC) and Dr. Ajay Kumar Kushwaha (HOD) for the opportunity to initiate the in-house symposiums of research scholars at the MEMS dept.

My friend Naveen's constant support, engaging technical discussions, jocular chats, tolerance of my occasional self-mocking diatribes and general advice on all matters under the sun have made a significant impact on me. He has always been the first to proofread my manuscripts or any presentations at IIT Indore. I am also thankful to Gokul, who always brings joy to his company. I will undoubtedly miss our morning chai sessions at the village cafe. Both Gokul and Naveen have consistently provided the right solutions whenever I've encountered problems, both personally and professionally. I also owe my gratitude to Naresh, Venkatesh, Venky Anna and Kishan for making me realize the value of friendship through their example.

I extend my gratitude to Dr. Arvindha Babu (DMRL) for his generous support in providing access to the vacuum arc melting equipment. I also owe my gratitude to Prof. G. Phanikumar from IIT Madras for granting access to Thermo-Calc. Also, I would like to thank Dr. Palguna and Dr. Rajesh Korla from IIT Hyderabad for their help with the micro-tensile study.

Further, I am grateful to several individuals who supported me throughout this journey. These include my B.Tech teacher and well-wisher Venky Sir and Veera Sreenu Sir from RGUKT; Lalith, Vignesh, Venu, Sheetal, Kavitha, Ramesh, Anlin, Meghana, Shubhi, Madhu, Ramamoorthy, Bhanu and Vasu from IIT Indore; Dr. Rahul John, Dr. Mayur and Neha Madam from IIT Hyderabad; Buchhi, Phani Sir and Sudeep from DMRL; Dr. Guruvadyathri (UOH); Dr. Karthick, Dr. Priyesh, Dr. Soumya, Dr. Nischay, Uma Shankar, Tejaswi, Ajith and Arpita from IIT Madras; Dr. Mohan (University of Münster); Dr. Lavanya Raman (Pennsylvania State University); Dr. Sufyan (Micron Technology, Inc.); Dr. Vikrant (NIMS); Dr. Ameey (IIT Ropar); Dr. Joydev (NISE); Dr. Khushbu (Amrita Vishwa Vidyapeetham); Dr. Raghavendra (CVRCE, Hyderabad); Adil (Queen's University); Dr. Rahul Bhattacharya (Lunds Tekniska Högskola); Dr. Monika Gupta (IIT Indore); Dr. N.S. Reddy (Gyeongsang National University); Dr. A.K. Prasada Rao (BMU); and Dr. Bhaskar Majumdar (DIAT, Pune). I also extend my thanks to all the members of the AML group at IIT Indore, the AMG group at DMRL Hyderabad and the AMR group of Prof. B.S. Murty, including Dr. Harish, Sujatha, Dr. Nagini, Gourav, Veda, Sudeepta, Sivateja, Prasad Sir, Sunil Sir and Dr. Hariharan, to whom I am particularly grateful for introducing me to Thermo-Calc. Also, grateful to Dr. Anirudha Karati for his helpful counselling and to Dr. Tripta Parida from AMES.

Many thanks to the department staff, namely, Brajesh Sir, Shubham Sir, Mayur Sir, Mahesh Sir, Pranjal Sir and Thapa Sir, for their consistent and timely help in organizing various conferences and workshops. Fellow PhD students, including Dr. Mahesh, Dr. Nilima, Dr. Sameena, Dr. Sandeep, Dr. Sarath, Dr. Sheetal, Dr. Subash and Dr. Yeeshu, as well as Abhishek D, Abhishek S, Akshay, Akshita, Ankush, Archana, Asish, Deepak, Girish, Hari, Hitesh, Lokanath, Manish B, Manish T, Manopriya, Mayank, Mukesh, Moupia, Nilesh, Piyush, Pratiksha, Samriddhi, Santosh, Shrish, Sheetal, Sourav, Sudhir, Sujit and Vikesh, must be thanked for nurturing positive vibes in the department. Grateful to all faculty of the department for ensuring this.

I hold Professors B. Cantor (Oxford University), Jien-Wei Yeh (NTHU) and S. Ranganathan (IISc) in high regard for their contributions to multi-principal element alloys and Prof. Yiping Lu for his pioneering work on EMPEAs. Also, Professors J. Willard Gibbs (Yale College), Ian Baker (Dartmouth College), Z.P. Lu (Oak Ridge National Laboratory), Jürgen Eckert (IFW Dresden), Sheng GUO (Chalmers University of Technology) and E. J. Mittemeijer (Max Planck Institute for Metals Research), whose work has given me much food for thought. I also take this opportunity to express my respect for Shri Ramakrishna Paramahansa, Srinivasa Ramanujan and Shri Bhagavad Ramanujacharya, whose lives have inspired me since childhood in the pursuit of education and egalitarianism.

Happy to express my gratitude to Sujatha Madam and Suseela Amma for their warm hospitality whenever I visit Prof. B.S. Murty at his home. Their genuine care for all his students is truly admirable. I am fortunate to have started experiencing this from B-28 (Pandya)-6B.

I owe my thankfulness to my sister, Sravani, her husband, Ravi, and their children, Persis Evangel and Asher Paul, as well as the family of Talluri, for keeping me smiling.

My wife, Suneetha, has made this whole enterprise feasible, not only by her confidence in her eccentric husband's pursuits but by always providing an affectionate domestic environment. I cannot possibly ever thank her enough, particularly for her understanding during my sporadic presence after her delivery and for her gracious management of our son Ujjwal Ramanujan's Annaprashana ceremony while I was engrossed in meeting manuscript deadlines (10.1016/j.scriptamat.2024.116178).

My parents, Sreenu and Manga, despite being an auto driver and a daily wage earner, respectively, understand the value of education. I hope my future generations will value their bold step in prioritizing my education over immediate small-scale financial stability, allowing me the freedom to pursue a PhD. They steadfastly encouraged me to seek higher education and I respect them for their foresight and support. It is to them that this thesis is dedicated as it should be.

Prof. B.S. Murty, whom I deeply admire and respect, holds a place in my heart akin to that of a father's. Our first meeting made it clear to me that he is a personality who would greatly influence me. His sacrosanct wisdom, belief in big dreams and unwavering commitment to perfection have been guiding me through the complexities of academia and self-discovery over the past half-decade. Despite his busy schedule as Director of IIT Hyderabad, he generously carves out time for our weekly meetings. It is this consistent support that has been the driving force behind this thesis. In essence, the philosophy I gained from this PhD journey, echoing his words, is that every person we meet in life, every experiment, indeed everything, tries to teach us a lesson, whether it be on how to be or how not to be. Whatever the lesson, the key is to continue to dream big and never give up.

To err is human, but to forgive is divine; I apologize for any inadvertent omissions from this list of acknowledgements.

---

gopi talluri

May 2024



# DEDICATION

## To My Parents

Sreenu (శ్రీను) – Manga (మంగ) (for their belief in education)

## To My Master

Prof. B.S. Murty

All that I am,  
and all that my world shall be,  
I owe to my Master, Prof. B.S. Murty

He urged us  
to dream big,  
to never give up,  
and to embrace the sacred truth that  
work is worship—  
to dedicate ourselves fully,  
eschewing half-hearted efforts.  
Illuminating that our path to true freedom,  
found only in the hearts of those  
who willingly sacrifice.

He taught us that  
every soul we meet imparts a lesson,  
guiding us in how to be or how not to be.

For in giving,  
we are truly living.

In doing so,  
he became a light to many—  
more than just a teacher.

His heart, ablaze with fire and passion,  
became a magnet, drawing us all.

Happy to be his 56<sup>th</sup>,  
a legacy that flourishes with warm regards.

---

gopi talluri

---

Inspired by  
*The Complete Works of Swami Vivekananda,*  
Volume 5, *Sayings and Utterances.*





# SYNOPSIS

## S1.1: Scope of the Present Thesis

The present thesis aims to develop multifaceted design approaches for predicting eutectic compositions prior to experimental realization in multi-principal element alloys (MPEAs). It first proposes a theoretical methodology for predicting eutectic compositions using just a pen and paper with the aid of binary phase diagrams. Acknowledging the inherent limitations of such an approach, the thesis will adopt the CALPHAD (CALculation of PHase Diagrams) methodology to efficiently design novel eutectic MPEAs (EMPEAs), aiming to develop an alloy that can surpass the longstanding AlCoCrFeNi<sub>2.1</sub> in terms of both design understanding and strength-ductility synergy. Moving further, the thesis will seek to identify the pseudo-eutectic compositional space and explore the quest for an invariant eutectic in MPEAs via *Thermo-Calc (TC)-Python*. In essence, the research presented in this thesis is anticipated to effectively establish a new frontier in the design and application of novel EMPEAs by addressing the existing research gaps in comprehending their physical metallurgy in alloy design.

## S1.2: Background

A careful overview of the field of EMPEAs as of April 18, 2024, reveals that approximately 353 studies have investigated various dual-phase fully eutectic compositions. Among these studies, 155 have specifically addressed AlCoCrFeNi<sub>2.1</sub> (further to note, 190 are of Al-Co-Cr-Fe-Ni alloy system only), the first reported alloy to apply the eutectic concept in MPEAs, representing approximately 43.9% of the literature. This extensive research interest in AlCoCrFeNi<sub>2.1</sub> highlights its exceptional mechanical properties at both cryogenic and elevated temperatures, as well as its excellent functional properties.

However, this concentrated focus on just one alloy also underscores a critical, persistent challenge in the field: the difficulty in designing new alloys that surpass the capabilities of AlCoCrFeNi<sub>2.1</sub> since its introduction in 2014 [R1]. For example, to date, no other alloy has ‘effectively’ surpassed the strength-ductility synergy exhibited by this alloy at room temperature [R2]. A primary reason for this stagnation is the incomplete understanding of the alloy design physical metallurgy of AlCoCrFeNi<sub>2.1</sub>, compounded by the lack of comprehensive higher-order phase diagrams. The seminal article by Lu *et al.* [R1] in 2014, which first reported AlCoCrFeNi<sub>2.1</sub>, suggested that a combination of FCC (Face-Centered Cubic) and BCC (Body-

Centered Cubic) eutectic structures would result in a synergy between strength and ductility in the as-cast state itself. However, this report does not provide a detailed rationale for selecting this specific alloy system or explain how the composition of AlCoCrFeNi<sub>2.1</sub> was identified as eutectic prior to experimental characterization. Over time, numerous EMPEAs have been reported, employing different design strategies such as the grouping strategy, pseudo-binary phase diagrams, empirical formulas based on binary eutectic clusters and VEC (Valence Electron Concentration), the simple mixing method, the mixing enthalpy method, eutectic lines approach and machine learning methods [R3,R4]. However, none of these design strategies is universal to design all types of binary eutectics (such as FCC+BCC, FCC+Laves phase, etc.) and none adequately addresses the quest for an invariant eutectic in MPEAs. It is also perplexing to observe that most design strategies have conceptually not diverged from the Co-Cr-Fe-Ni-M (M = Al, Zr, Ta, Nb, Hf) and also to cross-verify the proposed design method that applies to previously reported alloys. This clearly implies the challenges in identifying a design approach to determine eutectic compositions in MPEAs.

In conclusion, based on the hitherto reported literature, there is a need for new design approaches in at least the following areas: (1) effectively designing binary eutectics in MPEAs without relying solely on computational methods; (2) even when employing computational methods, there should be a way to quickly locate eutectic points without the need for extensive calculations; (3) irrespective of whether using the empirical or computational approach, it is essential to identify all binary eutectics present and to search for an invariant eutectic in MPEAs.

### **S1.3: Research Questions Addressed in the Present Thesis**

The present thesis addresses the following key research questions derived from the research gaps identified after a meticulous literature review, thereby guiding the exploration of new, multifaceted alloy design approaches:

1. How can binary eutectics in MPEA systems be designed effectively without relying on computational tools?
2. Even when employing computational tools, how can eutectic points in MPEAs be quickly located without extensive calculations?
3. How can all potential binary eutectics be identified in an MPEA system and what strategy can guide the discovery of higher-order eutectics, including invariant reactions?

## S1.4: Design Approaches Proposed in the Present Thesis

### S1.4.1: The Empirical Approach via Binary Eutectic Clusters

As mentioned in section S1.1, the thesis initially proposed an empirical approach via binary eutectic clusters, intended as a practical alternative to commercial software such as *Thermo-Calc*. The effectiveness of the proposed approach is validated through the design and development of a lightweight eutectic multi-principal element alloy (EMPEA) in the Al-Ti-V-Cr-Zr system, as illustrated in **(Figure S1.1(a))**. Additionally, the versatility of the approach is demonstrated through its extension to other alloy systems, such as Co-Fe-Ni-M (M = Nb, Zr and Ta) **(Figure S1.1(b))**.

Determining eutectic compositions in MPEAs requires first identifying such alloy systems exhibiting eutectic reactions. This preliminary step is necessary and efficient as it takes into account that not all MPEA systems may exhibit eutectic reactions, reflecting the variability seen in binary alloy systems. The observations from the compilation of reported eutectic alloys by Lu *et al.* [R5] have resulted in the formulation of a generalized method for the identification of EMPEA systems of the A-B-C-D-E type, as follows:

- Criteria 1 – Initial Binary Pair Selection (A-B): The enthalpy of mixing between elements A and B should be close to zero, ideally ranging between  $-2$  to  $0$  kJ/mol, essential for forming a stable single-phase disordered solid solution.
- Criteria 2 – Solid Solution Splitter (C): Element 'C' must display a significant enthalpy of mixing and an atomic size difference with elements A and B, sufficient to destabilize the A-B solid solution. Therefore, it should fulfil the criteria of  $-8.8$  kJ/mol.  $\leq \Delta H_{mix}^{A-B-C} \geq 4$  kJ/mol and  $\delta \geq 2.77\%$ .
- Criteria 3 – Additional Elements (D/E/F): Additional elements like D, E, or F can be incorporated if they are soluble with A and/or B. These elements should meet specific parameters:  $-2$  kJ/mol  $\geq \Delta H_{mix}^{A-D} \leq 0$  kJ/mol and  $\delta \leq 2.77\%$ .

Based on the above selection criteria, the Al-Ti-V-Cr-Zr system has been chosen, with the anticipation of designing a lightweight EMPEA, which is also outside the Co-Cr-Fe-Ni-M (M = Al, Ta, Zr, Nb and Hf) system. Based on the proportional mixing of binary eutectics, the eutectic composition in Al-Ti-V-Cr-Zr was identified as follows and the successful experimental realization of the same can be seen in **Figure S1.1(a)**:

- Step 1 entails pinpointing the eutectic compositions in the three binary systems involving Zr (Zr-Al, Zr-V, Zr-Cr). The determined eutectic compositions are  $Zr_{69}Al_{31}$ ,  $Zr_{57}V_{43}$  and  $Zr_{76}Cr_{24}$ .

- Step 2 involves calculating the mixing enthalpies for the Zr-Al, Zr-V and Zr-Cr binary equiatomic alloys, which are  $-43.7$ ,  $-3.7$  and  $-12$  kJ/mol, respectively.
- Step 3 involves calculating the eutectic composition ( $C_e$ ) of Zr-(Al-Ti-V-Cr) as follows:

$$C_e = x(\text{Zr}_{69}\text{Al}_{31}) + y(\text{Zr}_{57}\text{V}_{43}) + z(\text{Zr}_{76}\text{Cr}_{24})$$

$$x(\Delta H_{\text{mix}} \text{ of Zr - Al}) = y(\Delta H_{\text{mix}} \text{ of Zr - V}) = z(\Delta H_{\text{mix}} \text{ of Zr - Cr})$$

$$x(43.7) = y(3.7) \text{ and } y(3.7) = z(12), \text{ where } x + y + z = 1$$

$$y = \frac{x \times 43.7}{3.7}$$

$$x + \frac{x \times 43.7}{3.7} + \frac{\left(\frac{x \times 43.7}{3.7}\right) \times 3.7}{12} = 1$$

$$x + 11.81x + \frac{43.7x}{12} = 1$$

$$x + 11.81x + 3.64x = 1$$

$$x = \frac{1}{16.45} = 0.061$$

$$y = \frac{x \times 43.7}{3.7} = \frac{0.061 \times 43.7}{3.7} = 0.720$$

$$z = 1 - x - y = 1 - 0.061 - 0.720 = 0.219$$

$$C_e = 0.061(\text{Zr}_{69}\text{Al}_{31}) + 0.720(\text{Zr}_{57}\text{V}_{43}) + 0.219(\text{Zr}_{76}\text{Cr}_{24})$$

$$C_e = \text{Zr}_{4.21}\text{Al}_{1.89} + \text{Zr}_{41.04}\text{V}_{30.96} + \text{Zr}_{16.64}\text{Cr}_{5.26}$$

$$C_e = \text{Zr}_{61.89}\text{Al}_{1.89}\text{V}_{30.96}\text{Cr}_{5.26}$$

$$C_e = \text{Zr}_{61.9}(\text{AlTiVCr})_{38.1}$$

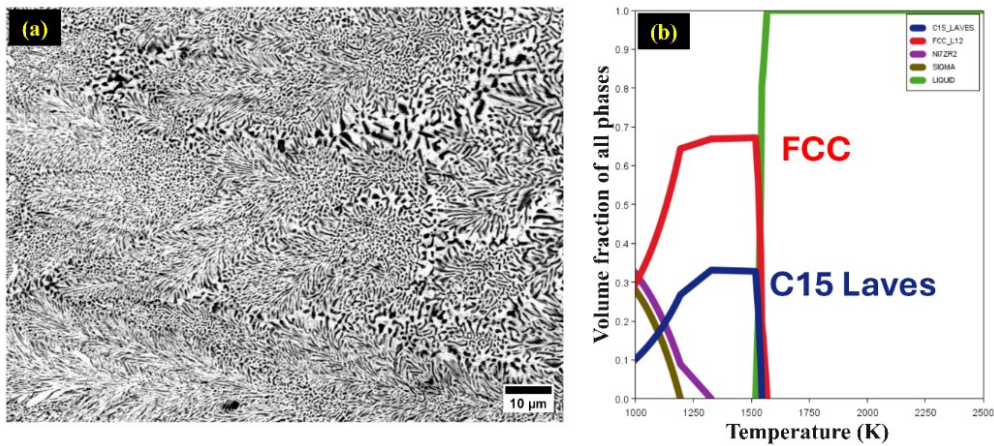


**Figure S1.1:** (a) SEM (scanning electron microscopy) image of the as-cast  $(\text{Zr})_{61.9}(\text{AlTiVCr})_{38.1}$  dual-phase eutectic alloy, (b)  $\text{Zr}_{9.5}(\text{CoCrFeNi})_{90.5}$ , predicted via the empirical approach proposed and experimentally reported by An *et al.* [R6].

### S1.4.2: The Single Phase Plus EFE (Eutectic Forming Element) Design Strategy via CALPHAD

Building upon the empirical approach presented in the previous section and considering the limitations of such an empirical approach, a new design strategy significantly advancing existing design strategies is proposed in this section. Termed 'Single Phase Plus EFE,' the proposed methodology employs pseudo-binary phase diagrams and Scheil solidification simulations through CALPHAD, enabling swift identification of EMPEAs. The accuracy of this approach has been validated by comparing its predictions with those of reported EMPEAs. Its practical applicability was demonstrated by designing and developing the first eutectic composition in the Al-Fe-Ti-V-Zr system. The efficacy of this proposed methodology was further substantiated by developing a novel EMPEA in the Al-Co-Fe-Ni system, which exhibited an exceptional synergy of strength and ductility at room temperature, surpassing most as-cast EMPEAs.

The simplistic and accelerated "Single Phase Plus EFE" design methodology for identifying EMPEAs unfolds in three key steps, as follows:

- (Step-1): Identify a multi-component single phase as a starting point, either a solid solution or an ordered/disordered phase.
- (Step-2): Identify a suitable EFE capable of forming an intermetallic compound and a binary eutectic with one of the elements (preferably with an enthalpy of mixing  $< -15 \text{ kJ/mol}$ ) present in the single phase considered in the first step.
- (Step-3): A pseudo-binary phase diagram, obtained through the single phase-EFE in the console mode of *Thermo-Calc* or through Scheil solidification or phase evolution simulations in the graphical interface, will disclose the eutectic in the alloy system.

After validating the single phase plus EFE design philosophy by developing the first eutectic in the Al-Fe-Ti-V-Zr system with a BCC+Laves combination, a new lightweight EMPEA with a B2+FCC combination was designed. The objective was to achieve a comparable strength-ductility synergy to that of AlCoCrFeNi<sub>2.1</sub>, which had a density of 7.38 g/cc, remarkable castability, significant elongation (17%) and high fracture strength (1009 MPa) [R7]. In this regard, four considerations guided the single phase plus EFE design approach to determine the optimal composition:

1. Considering elements from the *TCHEA5.1* database of the *Thermo-Calc* program.
2. Metallic elements with densities below 10 g/cc are to be considered to ensure that the designed alloy density is low.

3. Requiring the FCC phase fraction in the designed alloy to be more than 50% to get decent ductility, as implied from the literature.
4. Avoiding combinations involving both Fe and Cr to prevent the potential formation of the sigma phase.

The four criteria mentioned above were initially addressed by considering the Al-Co-Fe-Ni system. To address the first step of the "single phase plus EFE" design approach, the Al-Co-Fe system was chosen as the B2 phase former, guided by the binary phase diagrams of Al-Co and Al-Fe. The CALPHAD analysis, depicted in **Figure S1.2(a)**, swiftly determined the characteristic B2 phase of AlCoFe. X-ray diffraction (XRD) results obtained from the as-cast vacuum arc-melted button further substantiated the B2 nature of AlCoFe, as evidenced by a superlattice peak at  $31^\circ$  corresponding to the (100) plane.

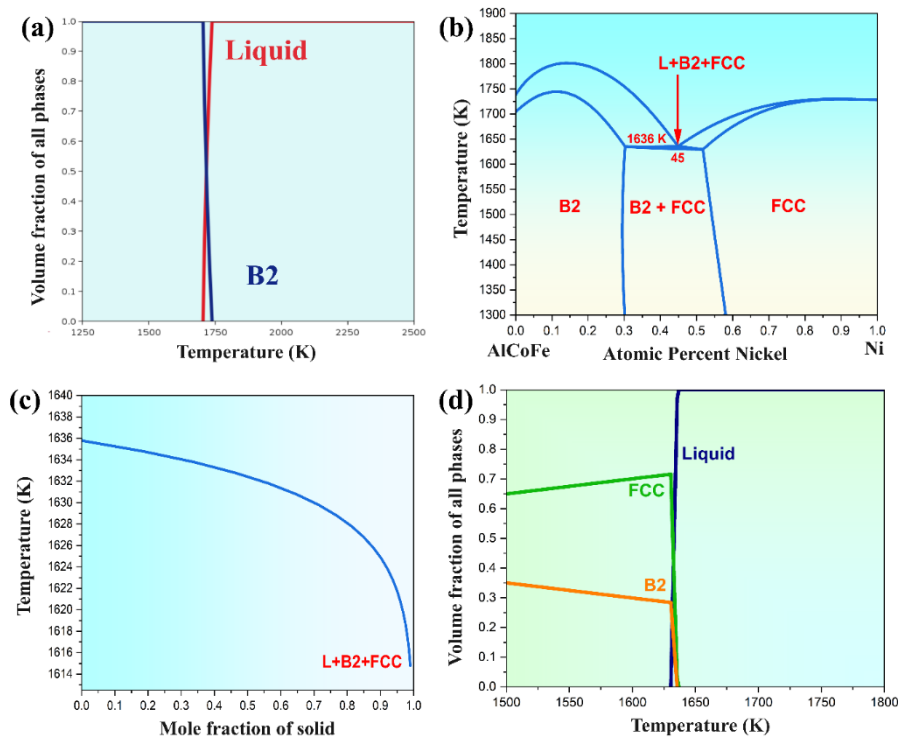


**Figure S1.2:** (a) Phase evolution plot for AlCoFe, (b) Pseudo-binary phase diagram for AlCoFe-Ni, (c) Scheil solidification simulation for (AlCoFe)<sub>55</sub>(Ni)<sub>45</sub> and (d) Phase evolution plot for (AlCoFe)<sub>55</sub>(Ni)<sub>45</sub>.

The second step of the "single phase plus EFE" design approach involves selecting the EFE, for which 'Ni' was the exclusive remaining option. Nickel, fitting perfectly into the role of EFE, indeed forms a strong intermetallic compound with Al (with an enthalpy of mixing of  $-22.30$  kJ/mol and a long-range order parameter 'L' of 0.92) and exhibits a binary eutectic at 75 at.% with Al. In addressing the third and final step, a pseudo-binary diagram analysis of AlCoFe-Ni revealed the eutectic reaction approximately at 45 at.% of Ni, as depicted in **Figure**



**S1.2(b).** Scheil solidification simulations and phase evolution plots were performed for  $(\text{AlCoFe})_{55}(\text{Ni})_{45}$  to comprehensively validate the formation of eutectic phases, as depicted in **Figure S1.2(c)** and **Figure S1.2(d)**, respectively. These findings indicate the eutectic formation of FCC+B2 phases at 1636 K with approximately 70% FCC phase fraction, which is necessary to achieve an elongation comparable to that of  $\text{AlCoCrFeNi}_{2.1}$ , which has a 65% FCC fraction. Guided by CALPHAD predictions, three compositions of  $(\text{AlCoFe})_{100-x}(\text{Ni})_x$  (where  $x = 40, 45$  and 50) were synthesized to substantiate the proposed design philosophy further. Of particular significance is the eutectic composition  $(\text{AlCoFe})_{55}(\text{Ni})_{45}$ , which exhibited an exquisite dual-phase eutectic microstructure of FCC+B2 confirmed via XRD and DSC (differential scanning calorimetry), which is shown in **Figure S1.3**. Further, as anticipated, the  $(\text{AlCoFe})_{55}(\text{Ni})_{45}$  surpassed the most as-cast EMPEAs, including the  $\text{AlCoCrFeNi}_{2.1}$ , in terms of both the design understanding and strength-ductility synergy.

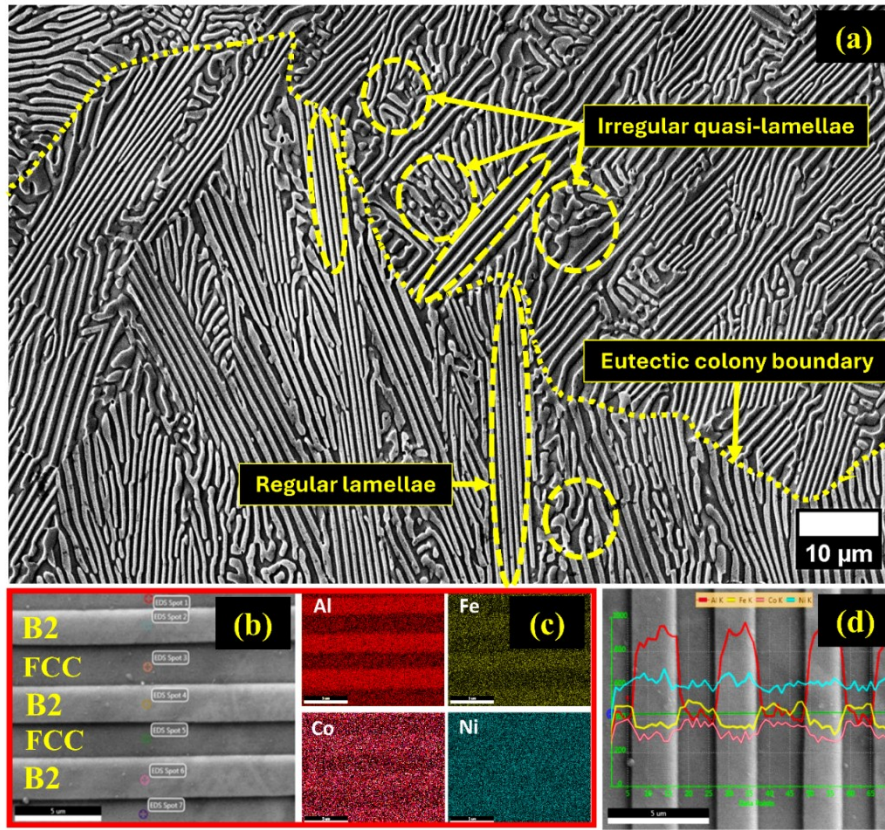


**Figure S1.3:** (a) SEM image of the exquisite dual-phase eutectic microstructure of the as-cast  $(\text{AlCoFe})_{55}(\text{Ni})_{45}$ , (b-c) EDS (energy-dispersive spectroscopy) elemental mapping and (d) EDS line analysis showing Al, Fe, Co and Ni.

#### S1.4.3: The High-Throughput CALPHAD Approach

Although the design approaches presented above, one empirically and the other via CALPHAD, offer several advantages over existing design strategies, the search for higher-

order eutectics, essentially an invariant eutectic, remains unexplored. Also, adhering to the Gibbs phase rule, the two-phase eutectic is essentially a pseudo-eutectic in MPEAs; therefore, there may be hundreds of thousands of eutectics of such kind. However, the approaches presented previously, much like the existing design strategies, focused only on identifying a single dual-phase eutectic.

The approach proposed in this section, "the high-throughput CALPHAD approach," addresses these exact research gaps by developing an in-house *Python* script capable of mapping all the binary eutectics present in MPEAs and searching for higher-order eutectics, including the invariant eutectic. The Al-Cr-Fe-Ni system is considered a case study to demonstrate the effectiveness of the proposed approach due to its cost-effectiveness and potential for lightweight alloy development.

The in-house *Python* script developed for the proposed high-throughput CALPHAD approach relied not just on liquidus-solidus but also on the phase formation temperature of each stable solid phase, enabling the identification of all possible pseudo-eutectics present in MPEAs. Executed in the *Spyder* platform, out of the 100,000 compositions generated via *Latin hyper-cube sampling (LHS)*, the in-house *TC-Python* script predicted 15,660 dual-phase eutectics featuring BCC+B2 (at.%,  $18.23 \leq \text{Al} \leq 36.99$ ,  $17.04 \leq \text{Cr} \leq 29.49$ ,  $16 \leq \text{Fe} \leq 33$  and  $21 \leq \text{Ni} \leq 36.35$ ), 5,699 eutectics featuring FCC+B2, (at.%,  $16 \leq \text{Al} \leq 19.38$ ,  $8 \leq \text{Cr} \leq 21.95$ ,  $16 \leq \text{Fe} \leq 33$  and  $34.40 \leq \text{Ni} \leq 50$ ) and 1,260 triple-phase eutectics featuring FCC, B2, BCC, (at.%,  $16 \leq \text{Al} \leq 17.85$ ,  $15.77 \leq \text{Cr} \leq 27.39$ ,  $16.00 \leq \text{Fe} \leq 32.98$  and  $31.36 \leq \text{Ni} \leq 42.73$ ), but no four phase invariant eutectic. The absence of an invariant eutectic in quaternary Al-Cr-Fe-Ni, even in high-throughput calculations, aligns with the trend observed in MPEAs, where no invariant eutectic has been reported. Achieving an invariant eutectic in MPEAs would necessitate suppressing configurational entropy, possibly through high negative enthalpy of mixing among all elements, thus forming distinct compounds rather than a single disordered solid solution. Additional CALPHAD calculations on the Al-Cr-Fe-Ni system across a broad compositional range (~100,000 compositions in the range of 5 to 85 at.% for each element) also did not reveal any invariant eutectic formations, reinforcing this hypothesis. Further, it has been observed that the formation of dual-phase and triple-phase eutectics in the Al-Cr-Fe-Ni system is significantly correlated with thermodynamic empirical design parameters, as can be seen in **Figure S1.4(a)**.

To substantiate the proposed hypothesis further, the *TC-Python* predictions, compared with literature-reported eutectic alloys in the Al-Cr-Fe-Ni system, validate the HT calculations



efficacy having the Euclidian distance of zero. Further, it should be noted that the elemental range for these predictions was derived from a limited number of alloys reported to exhibit fully eutectic dual-phase microstructures in the Al-Cr-Fe-Ni system, underscoring the vast compositional space yet to be explored and the capability of *TC-Python* approach in doing so. To justify the hypothesis further, a successful experimental verification has been carried out by casting  $\text{Al}_{17.6}\text{Cr}_{17.6}\text{Fe}_{17.6}\text{Ni}_{47.2}$  alloy composed of FCC+B2 phases. It is noteworthy that the yield strength of the developed alloy, relative to density, surpasses that of most as-cast reported alloys in the Al-Co-Cr-Fe-Ni system at a strain rate of  $1 \times 10^{-3} \text{ s}^{-1}$  and at room temperature. in **Figure S1.4(b)**.

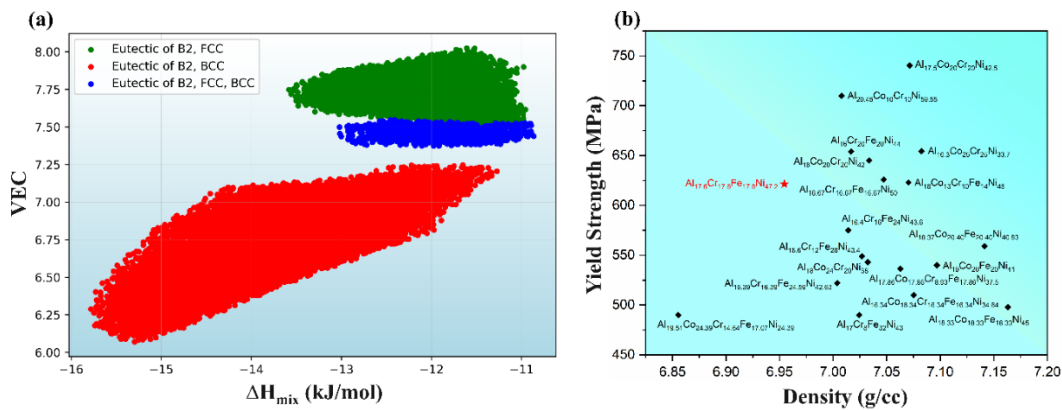


**Figure S1.4:** (a) Scatter plots of Valence Electron Concentration (VEC) vs enthalpy of mixing ( $\Delta H_{\text{mix}}$ ), (b) Comparison between yield strength and density of EMPEAs in Al-Co-Cr-Fe-Ni system (at a strain rate of  $1 \times 10^{-3} \text{ s}^{-1}$  and at room temperature in the as-cast condition).

## S1.5: Conclusions and Impact of the Present Thesis Findings

1. Firstly, it improved the established binary eutectic clusters approach by incorporating the concept of mixing enthalpy and refining the definition of EFE.
2. Building upon the empirical approach via binary eutectic clusters, where a single phase can serve as a starting point, the thesis significantly enhances existing pseudo-binary approaches by proposing the "single phase plus EFE" approach. CALPHAD results predicted via this approach are also experimentally validated, as evidenced by the discovery of the first eutectic in Al-Fe-Ti-V-Zr and the design and development of an EMPEA in Al-Co-Fe-Ni, surpassing the longstanding  $\text{AlCoCrFeNi}_{2.1}$  in both design understanding and strength-ductility synergy at room temperature.
3. Recognizing the limitations of the two proposed approaches (empirical approach via binary eutectic clusters and single phase plus EFE approach), the thesis introduces the "high-throughput CALPHAD approach." This approach successfully identifies all pseudo-

eutectics present in an alloy system and explores the presence of an invariant eutectic. The developed alloy, via this approach, also adhering with the single phase plus EFE approach,  $\text{Al}_{17.6}\text{Cr}_{17.6}\text{Fe}_{17.6}\text{Ni}_{47.2}$ , features FCC+B2 lamellar eutectic structure, reported to be the lightest EMPEA with excellent mechanical properties.

4. The potential outcomes of the thesis are clearly illustrated in the schematic representation of **Figure S1.5**, showcasing improvements to existing binary eutectic clusters and pseudo-binary diagram approaches, alongside the introduction of a new school of thought, the "high-throughput CALPHAD approach," facilitated by an in-house *Python* script.

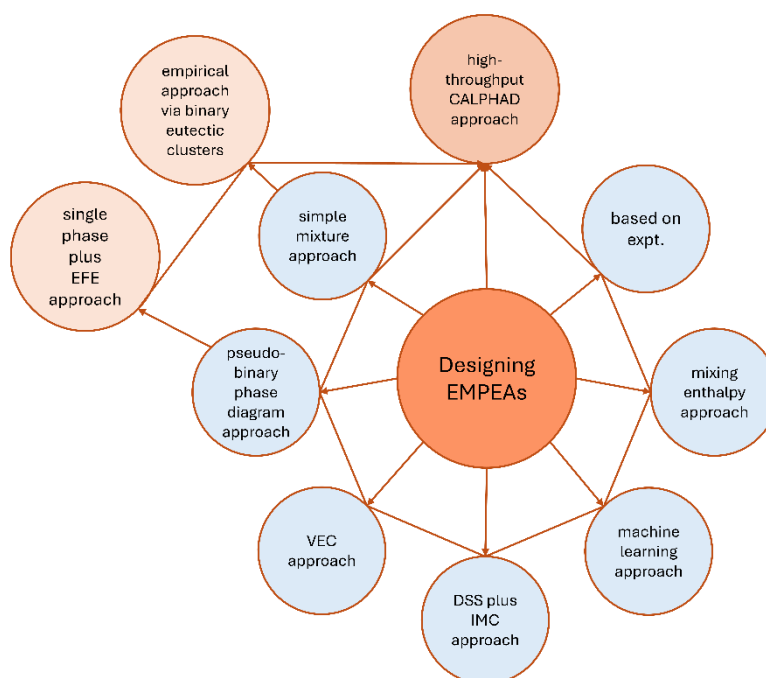


**Figure S1.5:** Schematic representation of existing design strategies for EMPEAs and the three design strategies proposed in the present thesis.

## S1.6: References

- [R1] Y. Lu, Y. Dong, S. Guo, L. Jiang, H. Kang, T. Wang, B. Wen, Z. Wang, J. Jie, Z. Cao, H. Ruan, T. Li, A promising new class of high-temperature alloys: Eutectic high-entropy alloys, *Sci Rep* 4 (2014). <https://doi.org/10.1038/srep06200>.
- [R2] Y. Lu, X. Gao, L. Jiang, Z. Chen, T. Wang, J. Jie, H. Kang, Y. Zhang, S. Guo, H. Ruan, Y. Zhao, Z. Cao, T. Li, Directly cast bulk eutectic and near-eutectic high entropy alloys with balanced strength and ductility in a wide temperature range, *Acta Mater* 124 (2017) 143–150. <https://doi.org/10.1016/j.actamat.2016.11.016>.
- [R3] J. Liu, Z. Li, D. Lin, Z. Tang, X. Song, P. He, S. Zhang, H. Bian, W. Fu, Y. Song, Eutectic high-entropy alloys and their applications in materials processing engineering: A review, *J Mater Sci Technol* 189 (2024) 211–246. <https://doi.org/10.1016/j.jmst.2023.10.057>.
- [R4] S. Wan, P. Ma, H. Yang, N. Zhang, Y. Fang, Y. Jia, K.G. Prashanth, Research Progress on Composition Design of Multicomponent Eutectic High Entropy Alloys, *Transactions of the Indian Institute of Metals* (2024). <https://doi.org/10.1007/s12666-023-03247-y>.

- [R5] Y. Lu, Y. Dong, H. Jiang, Z. Wang, Z. Cao, S. Guo, T. Wang, T. Li, P.K. Liaw, Promising properties and future trend of eutectic high entropy alloys, *Scr Mater* 187 (2020) 202–209. <https://doi.org/10.1016/j.scriptamat.2020.06.022>.
- [R6] X. An, C. Chu, H. Zhao, B. Shen, L. Zhou, P.K. Chu, CoNiFeNb0.45 eutectic multi-principal element alloy with excellent mechanical properties and corrosion resistance, *Materials Science and Engineering: A* 777 (2020). <https://doi.org/10.1016/j.msea.2020.139026>.
- [R7] S.R. Reddy, S. Yoshida, U. Sunkari, A. Lozinko, J. Joseph, R. Saha, D. Fabijanic, S. Guo, P.P. Bhattacharjee, N. Tsuji, Engineering heterogeneous microstructure by severe warm-rolling for enhancing strength-ductility synergy in eutectic high entropy alloys, *Materials Science and Engineering: A* 764 (2019). <https://doi.org/10.1016/j.msea.2019.138226>.



## LIST OF PUBLICATIONS FROM THE THESIS

1. G. Talluri, B.S. Murty, R.S. Maurya, The eutectic compositional space in Al-Cr-Fe-Ni system utilizing the high-throughput Calphad approach, *Scr Mater* 249 (2024) 116178. <https://doi.org/10.1016/j.scriptamat.2024.116178>.
2. G. Talluri, M. Nagini, D.A. Babu, Y. Palguna, K. Rajesh, B.S. Murty, R.S. Maurya, Designing a eutectic multi-principal element alloy for strength-ductility synergy, *J Alloys Compd* 976 (2024). <https://doi.org/10.1016/j.jallcom.2023.173278>.
3. G. Talluri, D.A. Babu, V.S. Hariharan, B.S. Murty, R.S. Maurya, A simplistic accelerated design methodology for eutectic multi-principal element alloys, *J Alloys Compd* 960 (2023). <https://doi.org/10.1016/j.jallcom.2023.170834>.
4. G. Talluri, M. Nagini, D. Arvindha Babu, B.S. Murty, R.S. Maurya, Microstructural verification of the theoretically designed novel eutectic multi-principal element alloy, *Mater Lett* 344 (2023). <https://doi.org/10.1016/j.matlet.2023.134420>.
5. G. Talluri, R.S. Maurya, B.S. Murty, Composition design of eutectic high-entropy alloys: a review, *J Mater Sci* (Accepted: *JMSC-D-24-04087R1*).



# TABLE OF CONTENTS

Acknowledgements	i
Synopsis	vii
List of Publications from the Thesis	xix
List of Figures	xxv
List of Tables	xxix
Nomenclature	xxx

## CHAPTER 1

### Introduction

1.1: Background	1
1.2: The Coming of EMPEAs (Eutectic Multi-Principal Element Alloys)	2
1.3: Objectives and Scope of the Present Thesis	4

## CHAPTER 2

### Literature Review and Key Research Questions

2.1: Introduction	5
2.2: Literature Collection and Organization	7
2.3: Microstructures and Mechanical Properties of EMPEAs	9
2.4: Existing Design Strategies of EMPEAs	13
2.4.1: The Pseudo-Binary Phase Diagram Approach	13
2.4.2: The Mixing Enthalpy Method	15
2.4.3: The Simple Mixture Method	16
2.4.4: The Machine Learning Approach	18
2.4.5: The VEC Criterion	19
2.4.6: DSS Plus IMC Approach	20
2.5: The Overlapping Research Gaps in Existing Design Strategies	23
2.6: Research Questions Addressed in the Present Thesis	26

## **CHAPTER 3**

### **Materials and Methods**

3.1: Introduction	27
3.2: Thermodynamic Calculations via CALPHAD	27
3.3: Alloy Synthesis via Vacuum Arc Melting	28
3.4: Phase Identification via XRD	29
3.5: Microstructural Characterization via SEM	29
3.6: Thermal Analysis via DSC	30
3.7: Assessing the Strength-Ductility Synergy via Tensile Testing	30

## **CHAPTER 4**

### **The Empirical Approach via Binary Eutectic Clusters**

4.1: Introduction	33
4.2: Exploring Eutectic Forming MPEA Systems	34
4.3: Identifying Eutectic Compositions in MPEAs	37
4.3.1: Designing a Lightweight EMPEA	39
4.3.2: Experimental Verification of the Designed Composition	41
4.4: Empirical Approach Extended to Other Systems	44
4.4.1: Co-Fe-Ni-Ta System	44
4.4.2: Co-Fe-Ni-Zr System	46
4.4.3: Co-Fe-Ni-Nb System	47
4.5: Limitations of the Empirical Approach	48
4.6: Summary	49

## **CHAPTER 5**

### **The Single Phase Plus EFE Design Strategy via CALPHAD**

5.1: Introduction	51
5.2: A Brief Note on the CALPHAD Aid	51
5.3: The "Single Phase Plus EFE" Design Strategy	52
5.3.1: The Three-Step Design Criteria	52
5.3.2: Reported Alloys Complying with the Single Phase Plus EFE Strategy	52
5.3.3: Advantages over Existing Design Strategies	54
5.4: Identifying the First EMPEA in Al-Fe-Ti-V-Zr	57



5.5: Experimental Verification of the EMPEAs of AlTiVZr-Fe	60
5.6: Designing an EMPEA for Strength-Ductility Synergy	66
5.7: Experimental Verification of the (AlCoFe) <sub>55</sub> (Ni) <sub>45</sub> alloy	71
5.8: Mechanical Properties of the (AlCoFe) <sub>55</sub> (Ni) <sub>45</sub> alloy	75
5.9: Inherent Limitations of the Single Phase Plus EFE Design Strategy	79
5.10: Summary	79

## CHAPTER 6

### The High-Throughput CALPHAD Approach

6.1: Introduction	81
6.2: Latin Hypercube Sampling in the Al-Cr-Fe-Ni System	82
6.2.1: Importing Essential Libraries	83
6.2.2: Ensuring Reproducible Results	83
6.2.3: Setting Parameters for Dataset Generation	83
6.2.4: Preparing Data Structures for Composition Generation	84
6.2.5: Generating Unique Alloy Compositions	84
6.2.6: Saving the Generated Dataset	84
6.2.7: Confirmation of Effective LHS Execution	85
6.3: In-House <i>Python</i> Script for Eutectic Identification	86
6.3.1: Imports and Initialization	87
6.3.2: Function Definitions	87
6.3.3: Configuration and Input Data	88
6.3.4: <i>Thermo-Calc</i> Setup and Calculations	88
6.3.5: Error Handling and Logging	88
6.3.6: Output	88
6.4: No Invariant Eutectic in Al-Cr-Fe-Ni	90
6.5: Comparison of <i>TC-Python</i> Predictions with Reported Alloys	92
6.6: The Compositional Space of B2 Plus FCC Eutectics in Al-Cr-Fe-Ni	95
6.6.1: Initialization and Data Preparation	96
6.6.2: Element Data and Enthalpy of Mixing Definitions	96
6.6.3: Composition Adjustments	96
6.6.4: Sum of Elements Check	96
6.6.5: Property Calculations	96

6.6.6: Processing the DataFrame	97
6.6.7: Output	97
6.7: Designing a Triple-Phase EMPEA from a Two-Phase EMPEA	104
6.8: Limitations	108
6.9: Summary	109

## **CHAPTER 7**

### **Conclusions and Future Research Directions**

7.1: Conclusions	111
7.2: Future Research Directions	117
References	121

# LIST OF FIGURES

Figure No.	Figure Caption	Page No.
2.1	Number of publications over time on EMPEAs (up to April 18, 2024).	6
2.2	Schematic representation of existing design strategies for EMPEAs.	7
2.3	Engineering tensile stress-strain curves of AlCoCrFeNi <sub>x</sub> (x = 2.0, 2.1, 2.2) alloys tested at room temperature.	11
2.4	High-magnification backscattered SEM images of CoFeNi <sub>2</sub> V <sub>0.5</sub> Nb <sub>0.75</sub> EHEAs in (a) as-cast condition and after heating at (b) 500 °C, (c) 600 °C, (d) 700 °C, (e) 800 °C and (f) 1000 °C.	11
2.5	Engineering stress-strain curves of the as-cast AlCoCrFeNi <sub>2.1</sub> EHEA under tensile testing at various temperatures.	12
2.6	(a) Pseudo-binary phase diagram of CoCrFeNi-Nb and (b) SEM-SE image of the CoCrFeNiNb <sub>0.65</sub> eutectic alloy.	14
2.7	Modified pseudo-binary phase diagram of CoCrFeNi-Ta.	15
2.8	Statistics on 400 near-eutectic compositions: (a) Content distributions of individual elements, (b) Maps showing Co, Cr, Fe and Ni contents corresponding to each Al content.	19
2.9	Schematic diagram illustrating the design concept of FCC + B2 EHEAs.	20
2.10	Solidification paths of NiAl-Mo <sub>x</sub> Cr <sub>x</sub> V <sub>x</sub> alloys simulated using <i>JMatPro</i> : (a) x = 3.33, (b) x = 6.67, (c) x = 8.7, (d) x = 10.0, (e) x = 13.3, (f) x = 16.67 at.%.	22
2.11	The dependent variable is represented in the graphical mode of the <i>Thermo-Calc</i> (FEDEMO database, <a href="https://thermocalc.com/support/getting-started-guides/Thermo-Calc-guide/">https://thermocalc.com/support/getting-started-guides/Thermo-Calc-guide/</a> ).	24
3.1	Vacuum arc-melted hemispherical button of the alloy.	29
3.2	Tensile test specimen (all dimensions are in mm).	30
4.1	Composition diagram of the EFE-E1-E2-E3 alloy system.	38
4.2	Comparative analysis of eutectic forming ability against the enthalpy of mixing for Fe, Co, Ni, Zr, Hf and Nb.	38
4.3	SEM image (BSE mode) of the as-cast alloy.	42
4.4	Elemental mapping of the as-cast alloy depicting the distribution of elements.	43
4.5	XRD diffractogram of the as-cast alloy.	43
4.6	DSC curve of the as-cast alloy.	44
4.7	Phase evolution plots of (a) Ta <sub>43.09</sub> Co <sub>25.78</sub> Fe <sub>16.25</sub> Ni <sub>14.88</sub> , (b) Ta <sub>43.09</sub> (CoFeNi) <sub>56.91</sub> and (c) Ta <sub>43.09</sub> (CoCrFeNi) <sub>56.91</sub> .	45
4.8	Phase evolution plots of (a) Zr <sub>9.5</sub> Co <sub>26.04</sub> Fe <sub>42.57</sub> Ni <sub>21.89</sub> , (b) Zr <sub>9.5</sub> (CoFeNi) <sub>90.5</sub> and (c) Zr <sub>9.5</sub> (CoCrFeNi) <sub>90.5</sub> .	47

4.9	Phase evolution plots of (a) $\text{Nb}_{11.25}\text{Co}_{25.75}\text{Fe}_{42.41}\text{Ni}_{20.59}$ , (b) $\text{Nb}_{11.25}(\text{CoFeNi})_{88.75}$ and (c) $\text{Nb}_{11.25}(\text{CoCrFeNi})_{88.75}$ .	48
5.1	(a) Classic Scheil solidification simulation for $\text{Al}_{16.39}\text{Co}_{16.39}\text{Cr}_{16.39}\text{Fe}_{16.39}\text{Ni}_{34.44}$ , (b) Pseudo-binary phase diagram of AlCoCrFe-Ni system.	54
5.2	Phase evolution plots for AlTi- $\text{Fe}_x\text{Cr}_x$ alloys: (a) $x = 45$ , (b) $x = 40$ , (c) $x = 35$ , (d) $x = 30$ , (e) $x = 25$ , (f) $x = 20$ , (g) $x = 15$ , (h) $x = 10$ , (i) $x = 5$ .	56
5.3	Phase evolution plots for (a) CrFeTi and (b) $\text{Al}_{12.01}(\text{CrFeTi})_{87.99}$ alloys.	57
5.4	Scheil solidification simulations for $\text{Fe}_x(\text{AlTiVZr})_{100-x}$ alloys: (a) $x = 20$ , (b) $x = 40$ , (c) $x = 60$ , (d) $x = 80$ .	58
5.5	(a) Scheil solidification simulation for $\text{Fe}_x(\text{AlTiVZr})_{100-x}$ ( $x = 73$ ), (b) Pseudo-binary phase diagram of AlTiVZr-Fe and (c) Phase evolution plot for $\text{Fe}_x(\text{AlTiVZr})_{100-x}$ ( $x = 73$ ).	59
5.6	SEM-BSE micrographs of (a) Fe70, (b) Fe73, (c) Fe75 and (d-e) Fe73 alloy at higher magnifications.	61
5.7	SEM-BSE micrograph of Fe73 alloy at lower magnification (180x).	62
5.8	EDS elemental mapping of (a) Fe70, (b) Fe73 and (c) Fe75 alloys.	63
5.9	XRD patterns of Fe70, Fe73 and Fe75 alloys.	64
5.10	DSC curve of Fe73 alloy.	64
5.11	Chemical mixing enthalpies for atomic pairs among the alloying elements; the dashed line indicates a binary eutectic reaction.	68
5.12	(a) Phase evolution plot for AlCoFe, (b) Pseudo-binary phase diagram for AlCoFe-Ni, (c) Scheil solidification simulation for $(\text{AlCoFe})_{55}(\text{Ni})_{45}$ and (d) Phase evolution plot for $(\text{AlCoFe})_{55}(\text{Ni})_{45}$ .	69
5.13	XRD patterns of the as-cast AlCoFe and $(\text{AlCoFe})_{55}(\text{Ni})_{45}$ alloys.	70
5.14	(a-c) Phase evolution plots of CoFeNi, AlFeNi and AlCoNi, respectively; (d-f) Pseudo-binary phase diagrams of CoFeNi-Al, AlFeNi-Co and AlCoNi-Fe, respectively; and (g-h) Phase evolution plots of $(\text{CoFeNi})_{84.8}(\text{Al})_{15.2}$ and $(\text{AlFeNi})_{47.4}(\text{Co})_{52.6}$ , respectively.	71
5.15	SEM secondary electron (SE) micrographs of (a) $(\text{AlCoFe})_{60}(\text{Ni})_{40}$ , (b) $(\text{AlCoFe})_{55}(\text{Ni})_{45}$ and (c) $(\text{AlCoFe})_{50}(\text{Ni})_{50}$ .	72
5.16	(a) SEM image of the dual-phase eutectic microstructure of the as-cast $(\text{AlCoFe})_{55}(\text{Ni})_{45}$ , (b-c) EDS elemental mapping and (d) EDS line analysis showing distributions of Al, Fe, Co and Ni.	73
5.17	DSC trace of $(\text{AlCoFe})_{55}(\text{Ni})_{45}$ alloy.	74
5.18	Compression stress-strain curve of $(\text{AlCoFe})_{55}(\text{Ni})_{45}$ alloy.	76
5.19	(a) Tensile stress-strain curve and (b) tensile fracture surface morphology of $(\text{AlCoFe})_{55}(\text{Ni})_{45}$ alloy.	78
5.20	Comparison of ultimate tensile strength versus uniform elongation for $(\text{AlCoFe})_{55}(\text{Ni})_{45}$ and literature-reported FCC+B2 EMPEAs at a strain rate of $1 \times 10^{-3} \text{ s}^{-1}$ and room temperature in the as-cast condition.	78
6.1	Representation of two-phase eutectics in different alloy systems: (a) binary, (b) ternary, (c) quaternary and (d) quinary.	82
6.2	Histograms showing the LHS distributions of Al, Cr, Fe and Ni.	85

6.3	Heatmap of correlation coefficients among the elements Al, Cr, Fe and Ni.	86
6.4	Schematic illustrations of (a) binary and (b) quaternary systems with the invariant eutectic at a single melting temperature and (c) quaternary system displaying the pseudo-eutectic behaviour over a temperature range.	89
6.5	Proportion of eutectic types in the Al-Cr-Fe-Ni alloy system.	91
6.6	Elemental composition ranges for eutectics in the Al-Cr-Fe-Ni alloy system.	92
6.7	Scatter plot of temperature differences between solid phase formation and liquidus-solidus temperatures for eutectics in the Al-Cr-Fe-Ni alloy system.	93
6.8	Heatmap displaying the correlations between thermodynamic descriptors for B2 and FCC eutectics.	98
6.9	Scatter plots of (a) Valence Electron Concentration (VEC) vs atomic size difference ( $\delta\%$ ) and (b) VEC vs enthalpy of mixing ( $\Delta H_{\text{mix}}$ ).	99
6.10	(a) Phase evolution plot for AlCrFe and (b) pseudo-binary phase diagram of AlCrFe-Ni.	100
6.11	SEM-BSE micrograph and elemental distribution map of the as-cast (AlCrFe) <sub>52.8</sub> (Ni) <sub>47.2</sub> alloy.	101
6.12	XRD pattern of the as-cast (AlCrFe) <sub>52.8</sub> (Ni) <sub>47.2</sub> alloy.	102
6.13	DSC trace of the as-cast (AlCrFe) <sub>52.8</sub> (Ni) <sub>47.2</sub> alloy.	102
6.14	Tensile engineering stress-strain curve of (AlCrFe) <sub>52.8</sub> (Ni) <sub>47.2</sub> alloy.	103
6.15	Mapping of yield strength versus density for EMPEAs in the Al-Co-Cr-Fe-Ni alloy system.	104
6.16	Scatter plots of (a) Valence Electron Concentration (VEC) vs atomic size difference ( $\delta\%$ ) and (b) enthalpy of mixing ( $\Delta H_{\text{mix}}$ ) vs $\delta\%$ .	105
6.17	Scatter plots of (a) Valence Electron Concentration (VEC) vs enthalpy of mixing ( $\Delta H_{\text{mix}}$ ) and (b) density ( $\rho$ ) vs VEC.	106
6.18	Parallel coordinate plot of Al, Cr, Fe and Ni relative to eutectic types with FCC as a phase.	107
6.19	Phase evolution plots for Al <sub>17.6</sub> Cr <sub>17.6</sub> Fe <sub>(17.6+x)</sub> Ni <sub>(47.2-x)</sub> : (a) x = 0, (b) x = 2, (c) x = 4, (d) x = 6, (e) x = 8, (f) x = 10, (g) x = 12, (h) x = 14, (i) x = 16.	108



# LIST OF TABLES

Table No.	Table Caption	Page No.
1.1	Characteristics of the two generations of HEAs.	2
4.1	Reported MPEAs with fully eutectic microstructure.	5
4.2	Enthalpy of mixing for selected binary alloy pairs (kJ/mol).	36
4.3	Reported EMPEA systems complying with proposed criteria.	37
4.4	Densities of selected elements.	39
4.5	EDS of the full area at 100x from ten different locations.	42
4.6	Point EDS at 8 different locations showing phase compositions.	42
5.1	Validation of the reported EMPEAs of different alloy systems of fully eutectic structure with the proposed "single phase plus EFE" design philosophy.	53
5.2	Binary eutectics among selected elements (✓ = eutectic present)	55
5.3	EDS of the full area at 100x at 5 different locations of the Fe70, Fe73 and Fe75.	60
5.4	The atomic radius (r), melting point ( $T_m$ ), valence electron concentration (VEC) and density ( $\rho$ )	65
5.5	$\Delta H_{mix}$ (kJ/mol) values of the constituent elements.	66
5.6	Calculated thermodynamic parameters of the developed EMPEAs.	66
5.7	Ultimate tensile strength (MPa) and uniform elongation for literature-reported EMPEAs of FCC+B2 at a strain rate of $1 \times 10^{-3} \text{ s}^{-1}$ done at room temperature in the as-cast condition (DIC = digital image correlation, E = extensometer, MD = machine data).	67
5.8	Elemental composition analysis of $(\text{AlCoFe})_{100-x}(\text{Ni})_x$ ( $x = 40, 45$ and $50$ ) at 10 different locations at 100x	73
5.9	Calculated thermodynamic parameters for $(\text{AlCoFe})_{55}(\text{Ni})_{45}$	75
5.10	Phase compositions for $(\text{AlCoFe})_{55}(\text{Ni})_{45}$	75
5.11	Compression fracture strength vs. elongation for literature-reported EMPEAs containing FCC phase at room temperature and a strain rate of $1 \times 10^{-3} \text{ s}^{-1}$ .	76
5.12	Chemical composition of phases on the tensile fracture surface of $(\text{AlCoFe})_{55}(\text{Ni})_{45}$	77
6.1	Comparison of <i>TC-Python</i> calculated and experimentally reported EHEA compositions of Al-Cr-Fe-Ni (E = Experimental, C = Calculated).	94

6.2	Comparison between overall B2 plus FCC compositional space and the designed alloy (AlCrFe) <sub>52.8</sub> (Ni) <sub>47.2</sub>	101
6.3	EDS of the full area at 100x from three locations.	102
7.1	Reported compositions across alloy systems comply with the high-throughput CALPHAD approach proposed in Chapter 6 ( $\Delta T$ = solidification range).	112



# NOMENCLATURE

ASM: American Society for Metals	SE: Secondary electron
B2: Ordered body-centred cubic.	SFEs: Stacking fault energies
BCC: Body-centered cubic	SOFCs: Solid oxide fuel cells
BMGs: Bulk metallic glasses	<i>TCHEA</i> : <i>Thermo-Calc</i> High-Entropy Alloys Database
BSE: Backscattered electron	<i>TCNI</i> : <i>Thermo-Calc</i> Ni-based superalloys database
CALPHAD: CALculation of PHase Diagrams	<i>TC-Python</i> API: <i>Thermo-Calc</i> 's <i>Python</i> Application Programming Interface
DIC: Digital image correlation	$T_e$ : Eutectic temperature
DSC: Differential scanning calorimetry	$T_{m_i}$ : Melting temperature of component i
EDS: Energy-dispersive spectroscopy	TWIP: Twinning-induced plasticity
EFE: Eutectic forming element	UTM: Universal testing machine
EMPEAs: Eutectic multi-principal element alloys	VEC: Valence electron concentration
FCC: Face-centered cubic	$x_i$ : Mole fraction of component i
FE-SEM: Field emission scanning electron microscopy	XRD: X-ray diffraction
HEAs: High-Entropy alloys	YS: Yield strength
HT: High-Throughput	$\delta$ : Atomic size difference
IMC: Intermetallic compound	$\Delta H_{mix}$ : Mixing enthalpy
KDE: Kernel density estimate	$\Delta S_{mix}$ : Mixing entropy
ML: Machine learning	$\Delta T(L-S)$ : Liquidus-solidus temperature difference
MPEAs: Multi-Principal element alloys	$\Delta\chi$ : Standard deviation of electronegativity
$n$ : Number of constituent elements	$\theta$ : Bragg diffraction angle
$R$ : Gas constant (8.314 J/K·mol)	$\rho$ : Density
$r_i$ : Atomic radius of element i	
FAB: fraction of assessed binaries	



# CHAPTER 1

## Introduction

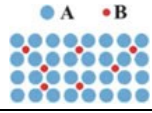
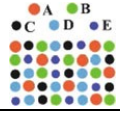
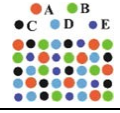
### 1.1: Background

Throughout history, the discovery, development and application of metals have been crucial in shaping human civilization. This influence is reflected in the naming of historical periods, such as the Bronze and Iron Ages, after the predominant metals used during those periods, underscoring their role in social and technological advancements. The earliest metallurgists, perhaps unwittingly, added small amounts of tin to copper, thus developing bronze, the first alloy. This breakthrough revolutionized prehistoric human life, notably in hunting and warfare and started the practice of incorporating secondary metals into primaries—a tradition aimed at enhancing properties and enabling diverse applications. However, this traditional approach to alloy design has historically been cautious, driven by the notion that adding secondary metals in larger quantities or introducing more metals into primary ones might result in undesirable compounds not suitable for structural applications, as can be seen in the ancient use of copper-tin intermetallic mirrors from the Indian subcontinent. These prevailing notions have historically limited the incorporation of substantial quantities of various metals into primary ones due to concerns about forming compounds less suited for structural applications. These restrictive ideas only began to substantially dissipate from 1995 onwards, when Professor Yeh (NTHU) proposed that high mixing entropy might decrease the formation of multiple phases in multi-principal element alloys (MPEAs), also referred to as High-Entropy Alloys (HEAs) [1]. In this regard, however, it's essential not to overlook the contributions of Karl Frank Achard's work "*Recherches sur les propriétés des alliages métalliques*" from the 18<sup>th</sup> century [2], Brian Cantor's (Oxford University) 2004 report that unveiled the first five-component MPEA with FCC (face-centred cubic) (CoCrFeMnNi) [3] and Prof. S. Ranganathan's (IISc) article on "*Alloyed Pleasures: Multimetallic Cocktails*" in 2003 [4].

HEAs were initially defined as metallic systems composed of five principal elements, each in proportions ranging from 5 to 35 atomic percent, characterized by a configurational entropy of  $1.5R$  or higher [5], offering a broad design space with diverse mechanical [6] and functional properties [7]. As such, HEAs represent a subset of MPEAs, distinguished by their high entropy of mixing. However, the evolution of HEAs has transitioned from an initial interest in equiatomic, single-phase structures to the current exploration of non-equiatomic,

multiphase solid solution alloys. This progression signifies the emergence of a second generation of HEAs, narrowing the definitional gap between HEAs and MPEAs, represented in **Table 1.1** [8].

**Table 1.1:** Characteristics of the two generations of HEAs [8].

Classification	Component	Feature	Atoms Arrangement	Typical Alloys
The traditional alloys	1-2 principal elements	Tougher than the elementary substance		Fe–Ni, Fe–C, Cu–Al, Al–Mg
The 1 <sup>st</sup> generation HEAs	At least five principal elements	Single phase, equimolar		CoCrFeMnNi AlCoCrFeNi
The 2 <sup>nd</sup> generation HEAs	At least four principal elements	Dual or complex phase, non-equimolar		AlCoCrFeNi <sub>2.1</sub> , Fe <sub>50</sub> Mn <sub>30</sub> Cr <sub>10</sub> Co <sub>10</sub>

## 1.2: The Coming of EMPEAs (Eutectic Multi-Principal Element Alloys)

Despite the promising potential of MPEAs, their industrial application is hampered by challenges such as the as-cast strength-ductility trade-off [6], poor casting fluidity and compositional segregation [9,10]. For instance, MPEAs with a body-centred cubic (BCC) structure, like NbMoTaW and VNbMoTaW, demonstrate exceptionally high yield strengths of 1058 MPa and 1246 MPa, respectively but exhibit minimal plasticity of just 2.0% and 1.5% [11]. Conversely, MPEAs with a face-centred cubic (FCC) structure offer higher plasticity but limited strength. The CoCrFeMnNi alloy, for example, with its FCC structure, shows a failure elongation of approximately 50% but a yield strength of only about 410 MPa [12]. Similarly, the (FeMn)<sub>80</sub>(CoCr)<sub>20</sub> alloy displays around 58% tensile ductility with a yield strength of only 240 MPa [13]. The Fe<sub>40</sub>Mn<sub>26</sub>Ni<sub>27</sub>Co<sub>5</sub>Cr<sub>2</sub> MPEA exhibits a total elongation to failure of approximately 58% but a yield strength of just about 95 MPa [14]. Furthermore, the poor castability and compositional segregation [9,15] of MPEAs cast reservations on their immediate engineering applications [10,16].

To address these challenges, a subset of MPEAs known as eutectic MPEAs (EMPEAs) was introduced in 2014, offering a promising solution [17,18]. EMPEAs, akin to traditional binary eutectic alloys, feature a dual-phase lamellar structure, which ensures excellent castability and macroscopic homogeneity. They typically possess a microstructure that comprises an FCC phase, associated with ductility, alongside a BCC (B2) or Laves phase, contributing to the strength, thus achieving an optimal balance of strength and plasticity

suitable for industrial applications [18]. Prominent examples include the AlCoCrFeNi<sub>2.1</sub> EMPEA, known for its low-temperature corrosion resistance and mechanical properties, presenting a viable alternative to copper alloys and stainless steels in icebreaker propellers [19]. Al-Co-Cr-Fe-Ni EMPEAs, with their exceptional damping properties, are considered suitable for shock absorbers [20]. The Co-Cr-Fe-Nb-Ni EMPEAs are recognized for their potential as a high-temperature sealant in Solid Oxide Fuel Cells (SOFCs) [21]. Recently, 'The Oerlikon Metco' company introduced an Al-Cr-Fe-Ni EMPEA for centrifugal pump impellers, targeting the replacement of duplex stainless steels [22]. Moreover, the distinctive features of eutectic alloys, such as low-phase boundary energy, stable defects and near-equilibrium microstructures, make EMPEAs promising candidates for high-temperature structural applications [18,23]. For instance, the AlCoCrFeNi<sub>2.1</sub> EMPEA maintains high strength and ductility up to 973 K, surpassing NiAl-based eutectic alloys [17]. The Al<sub>19</sub>Cr<sub>25</sub>Ti<sub>19</sub>Ni<sub>38</sub> EMPEA, with its BCC and L1<sub>2</sub> phases, exhibits enhanced hardness and specific yield strength at elevated temperatures compared to many refractory MPEAs and superalloys [24]. Furthermore, the Al-Co-Cr-Fe-Ni family of EMPEAs also demonstrated its resistance to seawater corrosion and high-temperature oxidation [25,26] due to the reasonable concentrations of Al and Cr [27,28].

Addressing the issue of castability and as-cast strength-ductility synergy in MPEAs by introducing the eutectic concept into MPEAs, however, has unveiled a significant challenge: the design of EMPEAs. Despite a decade gap following the first reported MPEA (CoCrFeMnNi), the first reported EMPEA with the eutectic concept (AlCoCrFeNi<sub>2.1</sub>) introduced in 2014 is without a comprehensive design methodology [3,17]. This omission has left a void in providing direction for the design of new alloys down the line. For example, the challenge of developing new EMPEAs is underscored by the inability to validate the first reported MPEA with the eutectic concept, AlCoCrFeNi<sub>2.1</sub>, applying the first design approach proposed for EMPEAs in 2015 [29]. It is also perplexing to observe that most design strategies have conceptually not diverged from the Co-Cr-Fe-Ni-M (M = Al, Zr, Ta, Nb, Hf) and also to cross-verify the proposed design method that applies to previously reported alloys. This clearly implies the challenges in identifying a design approach to determine eutectic compositions in MPEAs [18].

The bottleneck in identifying a universal design methodology for EMPEAs is primarily due to the lacuna of higher-order phase diagrams. Over the past nine years, various design methodologies for EMPEAs have been proposed, each with merits and limitations. These methodologies include the grouping strategy, simple mixture method, empirical formulas based

on valence electron concentration, the mixing enthalpy method, the eutectic lines approach, the machine learning approach and more [18]. However, all these approaches share a common limitation: they typically identify only a single dual-phase pseudo-eutectic composition. Furthermore, this identification does not validate the design strategy against previously reported alloys, nor does it possess the ability to investigate the invariant eutectic or pseudo-eutectic compositional space involving two or more phases in MPEAs.

### **1.3: Objectives and Scope of the Present Thesis**

The present thesis aims to develop multifaceted design approaches for predicting eutectic compositions prior to experimental realization in MPEAs. It first proposes a theoretical methodology for predicting eutectic compositions using just a pen and paper with the aid of binary phase diagrams. Acknowledging the inherent limitations of such an approach, the thesis will adopt the CALPHAD (CALculation of PHase Diagrams) methodology to efficiently design novel EMPEAs, aiming to develop an alloy that can surpass the longstanding AlCoCrFeNi<sub>2.1</sub> in terms of both design understanding and strength-ductility synergy. Moving further, the thesis will seek to identify the pseudo-eutectic compositional space and explore the quest for an invariant eutectic in MPEAs via *TC-Python*. In essence, the research presented in this thesis is anticipated to effectively establish a new frontier in the design and application of novel EMPEAs by addressing the existing research gaps in comprehending their physical metallurgy in alloy design.

## CHAPTER 2

# Literature Review and Key Research Questions

### 2.1: Introduction

If one enjoys 'dosa', the popular Indian breakfast dish, one might unknowingly be utilizing the concept of eutectics in daily life. These dosa pans are typically made of cast iron, an alloy of iron (Fe) and carbon (C). According to the Fe-C phase diagram, eutectic formations in these alloys can occur at carbon contents above 2%, with the invariant eutectic reaction, where the alloy has its lowest melting point, occurring at 4.3 wt.% C and 1147 °C [30]. This specific composition facilitates the simultaneous solidification of austenite and cementite, making these alloys ideal for casting, hence the name 'cast iron.' Similarly, sodium chloride (NaCl), commonly used for deicing roads in colder regions, demonstrates another practical application of eutectics. When spread on ice, NaCl forms a brine that reaches a eutectic composition of about 23.3% by weight, effectively lowering the freezing point of water to approximately 21.1 °C and preventing ice formation [17].

In essence, eutectic is an isothermal reversible reaction involving the transformation of a liquid solution into two or more intimately mixed solids upon cooling (austenite and cementite in the case of Fe-C), with the number of solids formed matching the number of components in the system. Similarly, in MPEAs, the transformation of the liquid phase into two solid phases, such as FCC (Co-Cr-Fe-Ni) and BCC (Al-Ni) in Al-Co-Cr-Fe-Ni, at approximately 1350 °C and at  $(\text{AlCoCrFe})_{65.57}(\text{Ni})_{34.43}$ , can be termed as a binary eutectic [17]. As can be noticed from **Figure 2.1**, the exploration of these binary eutectics in MPEAs became a new research hotspot in the metallic materials community as they are promising to offer strength-ductility synergy in the as-cast state, with their easily castable in-situ composite near-equilibrium microstructures [18].

However, a careful overview of the field of EMPEAs as of April 18, 2024, reveals that approximately 353 studies have investigated various dual-phase fully eutectic compositions. Among these studies, 155 have specifically addressed  $\text{AlCoCrFeNi}_{2.1}$  (further to note, 190 are of Al-Co-Cr-Fe-Ni), the first reported alloy to apply the eutectic concept in MPEAs, representing approximately 43.9% of the literature. This extensive research interest in  $\text{AlCoCrFeNi}_{2.1}$  highlights its exceptional mechanical properties at both low [31] and elevated temperatures, as well as its excellent functional properties [18,20].

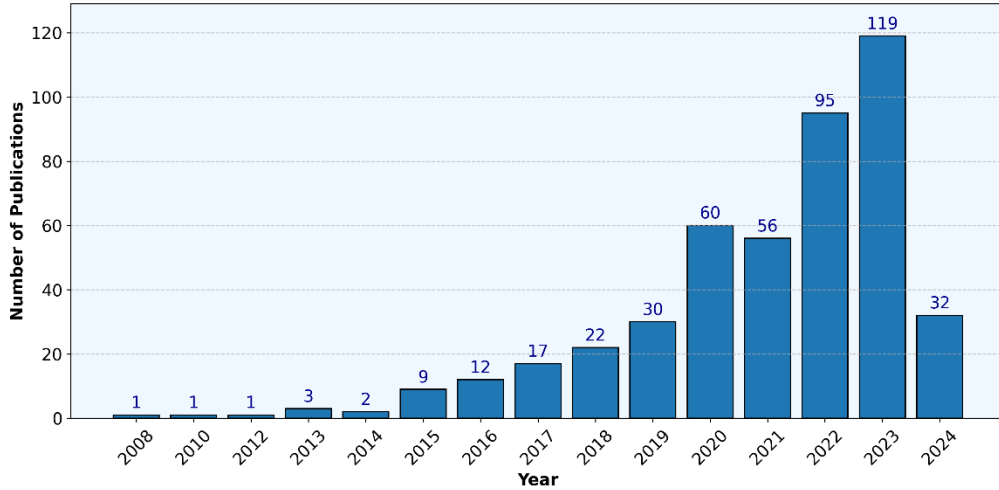


**Figure 2.1:** Number of publications over time on EMPEAs (up to April 18, 2024).

However, this concentrated focus on just one alloy also underscores a critical, persistent challenge in the field: the difficulty in designing new alloys that surpass the capabilities of AlCoCrFeNi<sub>2.1</sub> since its introduction in 2014 [17]. Just for example, to date, no other alloy has ‘effectively’ surpassed the synergy of strength and ductility exhibited by this alloy at room temperature. A primary reason for this stagnation is the incomplete understanding of the alloy design physical metallurgy of AlCoCrFeNi<sub>2.1</sub>, compounded by the lack of comprehensive higher-order phase diagrams. The seminal report by Lu *et al.* [17] in 2014, which first reported AlCoCrFeNi<sub>2.1</sub>, suggested that a combination of FCC and BCC eutectic structures would result in a synergy between strength and ductility in the as-cast condition itself. However, this report does not provide a detailed rationale for selecting this specific alloy system or explain how the composition of AlCoCrFeNi<sub>2.1</sub> was identified as eutectic prior to experimental characterization. Over time, numerous EMPEAs have been reported, employing different design strategies. Most of these reported design strategies can be categorized into seven different schools of thought (however, with some overlaps), as illustrated in **Figure 2.2**.

Also, none of these design strategies is universal to design all types of binary eutectics (such as FCC plus BCC, FCC plus Laves, etc.) and none adequately addresses the quest for an invariant eutectic in MPEAs. According to the Gibbs phase rule and the ASM materials engineering dictionary, the definition of eutectic should be forming the same number of solid phases as the number of components in an alloy system from a liquid phase while cooling. Thus, in a quinary system such as Al-Co-Cr-Fe-Ni, the two-phase binary eutectic is just a pseudo-eutectic and a true invariant eutectic should be of five solid phases. It is also perplexing to observe that most design strategies have conceptually not diverged from the Co-Cr-Fe-Ni-M (M = Al, Zr, Ta, Nb, Hf) and also to cross-verify the proposed design method that applies to



previously reported alloys. This clearly implies the challenges of identifying a design approach to determine eutectic compositions in MPEAs. This clearly implies the challenges in identifying a design approach to determine eutectic compositions in MPEAs. The present chapter will explore these challenges by critically assessing the significant design strategies proposed thus far and seeking to understand the universal research gap in the literature in designing new EMPEAs. Prior to this review, this chapter will also provide a brief overview of the as-cast mechanical properties and solidification microstructures of hitherto reported EMPEAs, along with the methodology followed for literature collection and analysis.

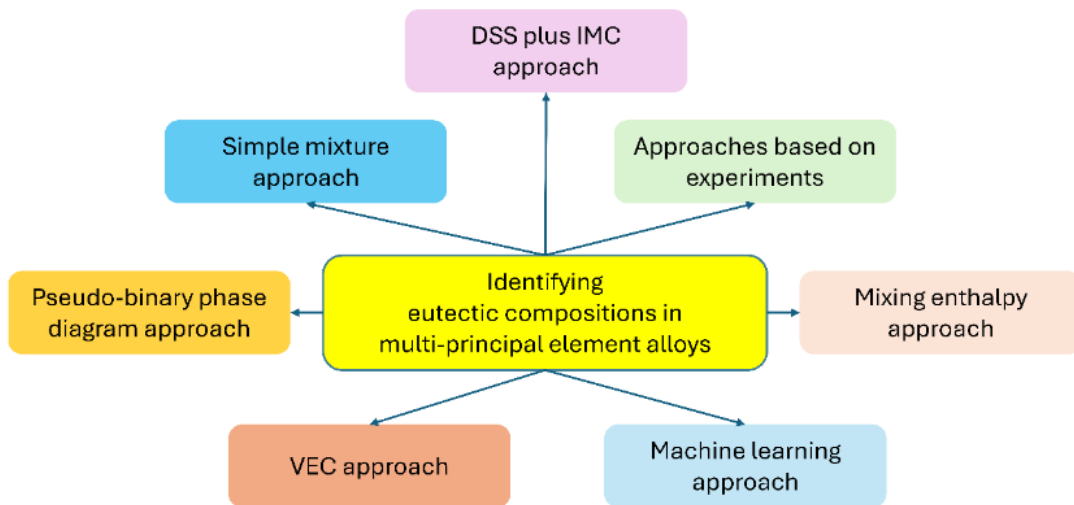


**Figure 2.2:** Schematic representation of existing design strategies for EMPEAs.

## 2.2: Literature Collection and Organization

Identifying eutectic compositions in MPEAs presents significant challenges, primarily due to the absence of comprehensive higher-order phase diagrams. Similarly, identifying the exact literature that addresses EMPEAs is also challenging to some extent because there is no universally accepted definition of what constitutes an EMPEA study. While 'multi' typically implies the inclusion of more than one or many elements, it remains debatable whether a ternary eutectic alloy qualifies as an EMPEA. Moreover, these alloys are often categorized under titles or keywords such as 'eutectic HEAs,' 'eutectic medium entropy alloys,' 'compositionally complex alloys, or 'eutectic multicomponent alloys. Consequently, one should "carefully" merge all these search terms so as not to miss any reports, though challenges persist because the term 'eutectic' might not appear in the title or keywords in most studies, as exemplified by the study '*Effects of Hf on the microstructure and mechanical properties of CoCrFeNi HEA*' reporting the CoCrFeNiHf<sub>0.4</sub> eutectic composition with 569 HV [32]. Furthermore, including 'eutectic' in search terms can result in studies unrelated to EMPEAs, such as those investigating

HEAs under conditions involving liquid-bismuth eutectic such as ‘*Degradation of tensile mechanical properties of two  $Al_xCoCrFeNi$  ( $x=0.3$  and  $0.4$ ) HEAs exposed to liquid lead-bismuth eutectic at 350 and 500 °C*’ [33]. Excluding 'liquid-bismuth' from search terms could result in missing reports that discuss eutectic HEAs in the liquid-bismuth eutectic medium, which might have reported the new eutectic composition with a new design strategy. Further to this, where one searches these reports also matters. For example, the report "*A Brief Perspective on the Status and Future Prospects of Eutectic High-Entropy Alloys*" by Bhattacharjee *et al.* [34] may not be identified in searching *Scopus documents*, but it can definitely give an overview on this topic, more towards thermomechanical processing.

Thus, considering the challenges mentioned above, among others (such as accessing those articles, etc.), a rigorous literature collection (with a custom Scopus code) has been conducted with the specific criterion that any report on a four-element combination describing a eutectic system is included. Once all the reports are collected, it is essential to analyze them carefully. For example, the concept of mixing a disordered solid solution with an intermetallic phase to identify a eutectic composition has been reported in various studies, with slight variations and without citing prior reports (indicating possible independent developments), as will be detailed in the subsequent sections. However, understanding the origin of the design idea and giving necessary credit is important, requiring meticulous organization of the literature collected. For this purpose, each collected report (PDF) has been carefully renamed with the concatenated info of the format 'Published date\_First Author\_Journal Name\_DOI (without the slash)', for example, '2014.08.27\_Yiping Lu\_Scientific Reports\_10.1038/srep06200'. This format includes the full name as it appears in the publication to facilitate precise identification since references such as 'Lu *et al.*' could refer to multiple authors like Z.P. Lu or Y.P. Lu. To further enhance the efficiency of literature exploration, particularly when searching for specific compositions without needing to open each PDF, all collected literature has been merged into a single PDF, organized chronologically by published date and thoroughly analyzed.

One notable outcome of this meticulous literature analysis is the clarification of the historical record concerning the first reported EMPEA. Contrary to the popular citation of " $AlCoCrFeNi_{2.1}$ " reported by Yiping Lu in 2014 as the pioneering example, the actual first reported EMPEA is ‘Fe-Ni-Mn-Al’ by Ian Baker in 2008 [17,35]. This fact highlights the frequent misconceptions in the literature post-2015. Interestingly, Baker *et al.* [35] also published a review in 2019 titled "*Eutectic/eutectoid multi-principle component alloys: A review*," further solidifying their contributions to this field. However, it is the  $AlCoCrFeNi_{2.1}$  alloy that was first associated with the eutectic concept, offering a detailed pre-experimental

characterization of how the eutectic concept could be beneficially applied to MPEAs. Therefore, it is more appropriate to state that the first reported EMPEA is  $\text{Fe}_{30}\text{Ni}_{20}\text{Mn}_{35}\text{Al}_{15}$  [35,36], while the first MPEA reported with a clear application of the eutectic concept is  $\text{AlCoCrFeNi}_{2.1}$  [17].

### 2.3: Microstructures and Mechanical Properties of EMPEAs

The term 'eutectic' means 'easily melting' and is derived from the ancient Greek εὐτηκτος (eútēktos, "easily melted"), which comes from εὖ (eû, "well") and τέκω (tēkō, "to melt"), suggesting that an alloy should only be termed eutectic if it forms through a liquid route. However, numerous studies have reported the formation of 'eutectics' via various methods, such as powder metallurgy or mechanical alloying [37,38]. These might more appropriately be referred to as alloys with eutectic morphology, technically designated as pseudo-eutectics, even if these alloys comply with the Gibbs phase rule. Considering this distinction, this section will focus exclusively on EMPEAs synthesized by methods involving liquid as one of the phases, such as vacuum arc melting and induction melting.

Over the years, in EMPEAs, the eutectics identified thus far predominantly consist of dual phases and exhibit microstructures similar to those observed in conventional eutectic systems. These include lamellar, rod-like, broken lamellar, quasi-regular and complex regular morphologies. Additionally, novel eutectic morphologies such as sunflower-like [39], chrysanthemum-like and seaweed patterns have also been observed [40,41]. Despite this diversity in microstructural morphologies, the excellent mechanical properties of EMPEAs are often associated with lamellar-type eutectics akin to binary alloys. Consequently, microstructures in EMPEAs typically can be categorized as either lamellar or non-lamellar.

However, given the composition of multiple elements in varying proportions, the theory of eutectic solidification in these alloys is not yet fully understood. The preliminary conclusions based on alloys reported to date suggest that EMPEAs often exhibit finer lamellar structures compared to traditional eutectics. Also, eutectics containing FCC as one of the phases generally display lamellar structures, whereas eutectics with BCC plus B2 combinations, commonly reported in Al-Cr-Fe-Ni systems, typically have a maze-like morphology [17,42]. For example, the industrial-scale 2.5 kg  $\text{AlCoCrFeNi}_{2.1}$  EMPEAs have demonstrated an interlamellar spacing of approximately 2  $\mu\text{m}$  [17]. Other notable inter-lamellar spacings include about 0.25  $\mu\text{m}$  in  $\text{CoCrFeNiNb}_{0.65}$  and  $\text{CoFeNi}_2\text{V}_{0.5}\text{Nb}_{0.75}$  [43], 0.15–0.2  $\mu\text{m}$  in  $\text{CoCrFeNiTa}_{0.4}$  [44], 3  $\mu\text{m}$  in  $\text{Al}_{19.3}\text{Co}_{15}\text{Cr}_{15}\text{Ni}_{50.7}$  and around 0.20  $\mu\text{m}$  in bulk  $\text{CoCrFeNiNb}_{0.45}$  EMPEAs [44,45]. In

CrFeNi<sub>2.2</sub>Al<sub>0.8</sub> EMPEAs, the lamellae widths for FCC and B2 phases are approximately 1  $\mu\text{m}$  and 0.40  $\mu\text{m}$ , respectively [46]. Noting further, Nb<sub>25</sub>Sc<sub>25</sub>Ti<sub>25</sub>Zr<sub>25</sub> is reported to have an inter-lamellar spacing ranging from 5 to 40 nm, while the Co<sub>2</sub>Mo<sub>0.8</sub>Ni<sub>2</sub>VW<sub>0.8</sub> has spacings of about 0.4–0.6  $\mu\text{m}$  [47,48]. Also, as all these EMPEAs are primarily produced via vacuum arc melting or induction melting, processes that yield an ultrafine solidification structure are rarely seen in directly cast traditional eutectic alloys at industrial scales. This structural refinement, combined with significant solid solution hardening, is hypothesized to enhance the mechanical properties of as-cast EMPEAs [49].

Due to their in-situ composite structure and excellent castability, EMPEAs have demonstrated outstanding mechanical properties in the as-cast state, often eliminating the need for additional heat treatments or thermo-mechanical processing techniques [17,18]. For instance, as illustrated in **Figure 2.3**, the AlCoCrFeNi<sub>2.1</sub> EMPEA at room temperature exhibits a yield strength ( $\sigma_y$ ) of approximately 500 MPa and a ductility ( $\varepsilon$ ) of around 17% (measured with DIC) [50]. This combination of strength and ductility is markedly different from the properties typically observed in single-phase MPEAs, where the yield strength and ductility are generally around 200 MPa and 40%, respectively [51].

However, this enhanced performance is characteristic only of eutectics with FCC plus B2 phase combinations. In contrast, FCC plus Laves phase eutectics usually do not exhibit this synergistic balance between strength and ductility in the as-cast state, although they do possess good strength and high hardness. This discrepancy is primarily due to the incorporation of refractory elements such as Ta, Nb, Mo, Hf, Zr and W, which form Laves phases with Ni or Al in most cases. Probably, this could have led to reporting mechanical properties such as strength and plasticity via compression tests in the literature rather than strength and ductility via tensile tests as most EMPEAs outside the Al-Co-Cr-Fe-Ni system are of Co-Cr-Fe-Ni-M, where M denotes a refractory element. However, the thermal stability of these alloys is exceptional, as they are primarily near-equilibrium structures due to eutectic reactions, which means they may not form additional phases upon heating. The typical disorder-to-order transformation is also not generally observed in these types of alloys. For example, the EMPEA CoFeNi<sub>2</sub>V<sub>0.5</sub>Nb<sub>0.75</sub> exhibits only slow growth kinetics even when annealed at 1000 °C, maintaining hardness similar to that in the as-cast state, as shown in **Figure 2.4** [43]. Also, the bulk 2.5 kg CoCrFeNiNb<sub>0.45</sub> prepared via directional solidification with 200 nm ultrafine lamellar structure maintained its high strength up to 800 °C superior to some of the traditional nanostructured and ultrafine-microstructure materials [45].

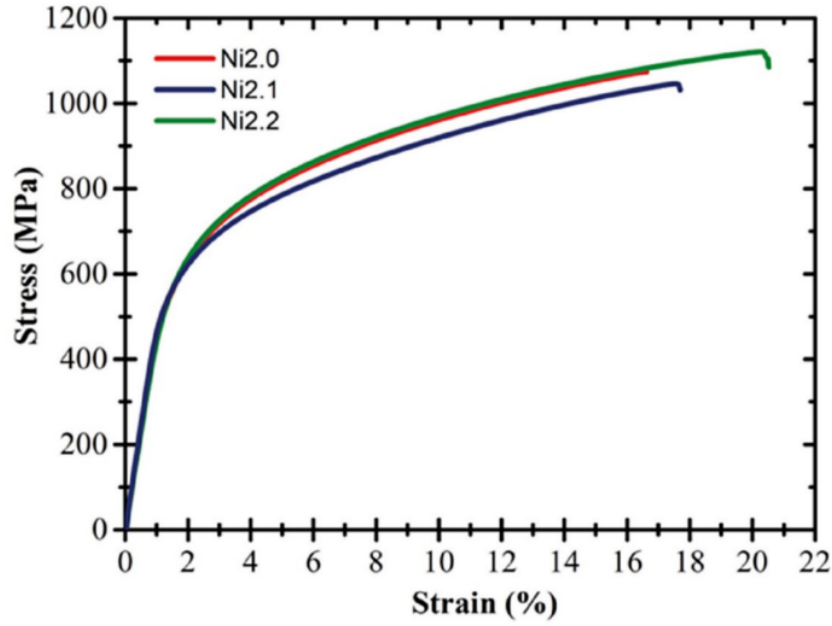


**Figure 2.3:** Engineering tensile stress-strain curves of  $\text{AlCoCrFeNi}_x$  ( $x = 2.0, 2.1, 2.2$ ) alloys tested at room temperature [19].

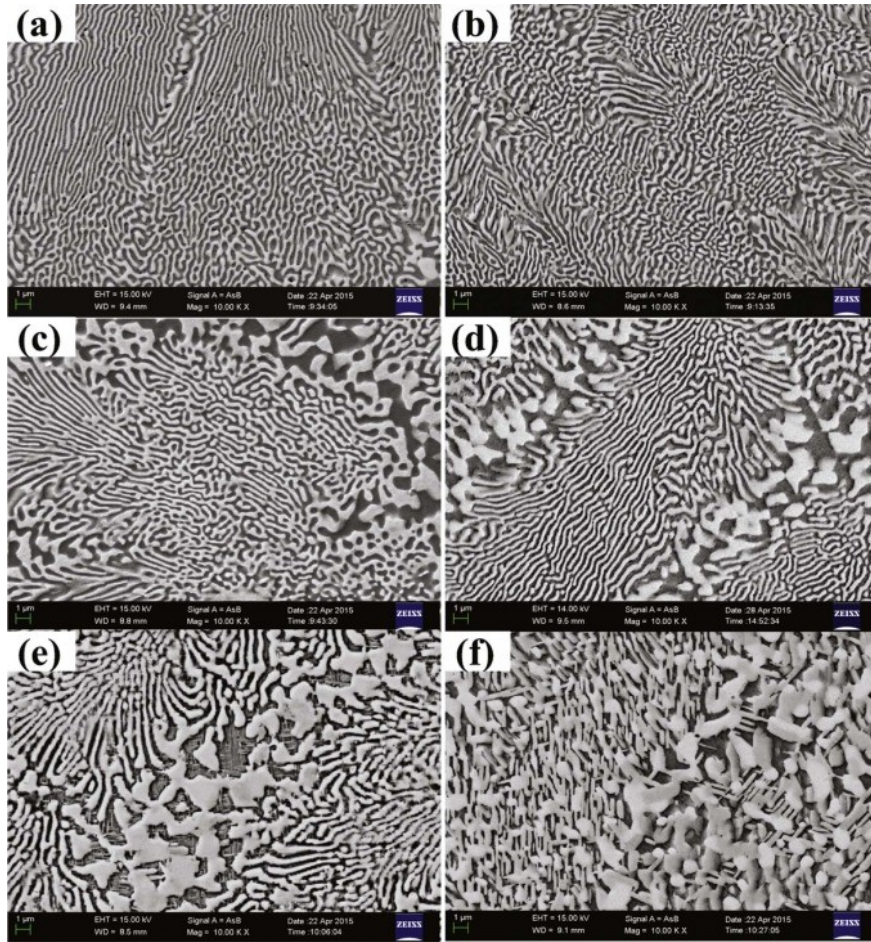


**Figure 2.4:** High-magnification backscattered SEM images of  $\text{CoFeNi}_2\text{V}_{0.5}\text{Nb}_{0.75}$  EHEAs in (a) as-cast condition and after heating at (b) 500 °C, (c) 600 °C, (d) 700 °C, (e) 800 °C and (f) 1000 °C [43].

Moreover, it is noteworthy that EMPEAs of FCC plus BCC combinations typically do not exhibit necking, as demonstrated in **Figure 2.3**. Unlike traditional metals such as pure nickel (Ni) and iron (Fe), which uniformly thin and eventually break at a specific area, EMPEAs display a strain distribution in a wavy pattern across the material. This behaviour arises because EMPEAs consist of alternating soft and hard regions. During tensile testing, the soft regions deform first and subsequently harden, while the initially hard regions begin to deform later. This alternation between soft and hard regions continues, developing a wave-like pattern in the material stretching behaviour. Also, many MPEAs, such as CoCrFeMnNi, CoCrNi [52] and Co<sub>10</sub>Cr<sub>10</sub>Fe<sub>50</sub>Mn<sub>30</sub>, exhibit stacking fault energies (SFEs) that range from -30 mJ/m<sup>2</sup> to 50 mJ/m<sup>2</sup> [53,54]. These values are significantly lower than the 100-150 mJ/m<sup>2</sup> observed in pure nickel (Ni). The reduced SFE in these alloys facilitates deformation mechanisms such as twinning, allowing the alloys to exhibit good mechanical properties at low temperatures [55,56]. This characteristic is also observed in dual-phase EMPEAs, which demonstrate twinning-induced plasticity (TWIP), maintaining both strength and ductility at cryogenic temperatures [57]. For example, as depicted in **Figure 2.5**, the AlCoCrFeNi<sub>x</sub> alloy retains significant strength and ductility at cryogenic temperatures up to -196 °C [19,31]. However, the exact microstructural origins of these excellent mechanical properties exhibited by EMPEAs remain to be thoroughly investigated.

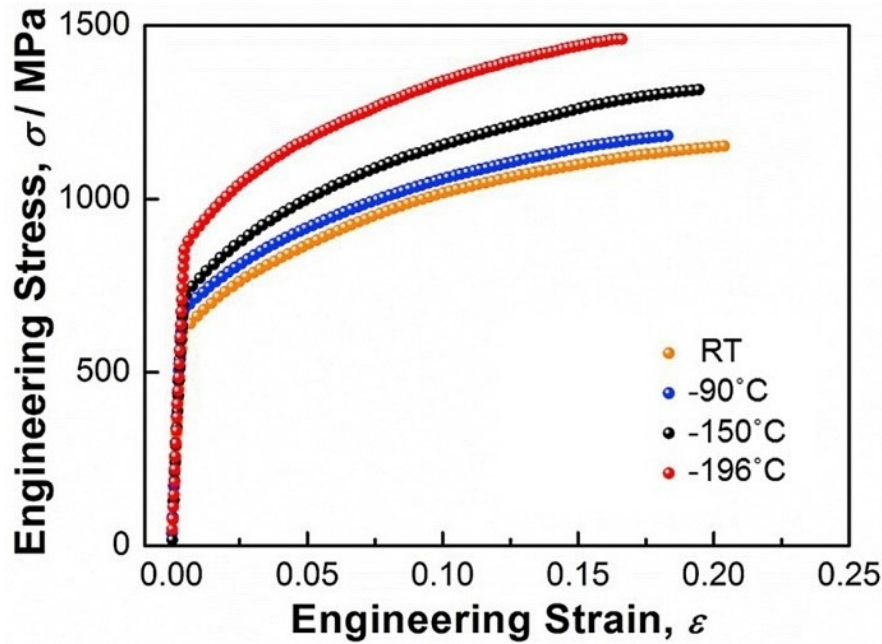


**Figure 2.5:** Engineering stress-strain curves of the as-cast AlCoCrFeNi<sub>2.1</sub> EHEA under tensile testing at various temperatures [31].

## 2.4: Existing Design Strategies of EMPEAs

Although, as detailed above, these EMPEAs demonstrate outstanding mechanical properties with ultrafine lamellar structures, the design of an optimum composition with tailored mechanical properties has remained a persistent question since 2014. Thus, as mentioned in the introduction section, the subsequent sections will discuss each of the most significant design strategies proposed to date. This discussion aims to aid in formulating a solution to the question of developing a 'universal design strategy' that can identify all types of eutectics present in MPEAs, thus discovering the optimum compositions for tailored applications.

### 2.4.1: The Pseudo-Binary Phase Diagram Approach

In 2015, He *et al.* [29] reported the first design strategy for identifying eutectic compositions in MPEAs, noticing that CoCrFeNi, forming a single-phase disordered solid solution with an FCC structure, could be considered a pseudo-element. Further, recognizing that each element in this pseudo-element, Co, Cr, Fe and Ni, exhibit binary eutectic reactions with Nb at around 14 at.%, He *et al.* [29] employed the CALPHAD methodology using *Thermo-Calc* software (*TCNI* database) to generate a pseudo-binary phase diagram for CoCrFeNi-Nb. This analysis in the Co-Cr-Fe-Ni-Nb system predicted a eutectic composition of CoCrFeNiNb<sub>0.45</sub>, as shown in **Figure 2.6(a)**, but subsequent experimental findings by He *et al.* [29] revealed that the actual eutectic composition was CoCrFeNiNb<sub>0.65</sub>, as depicted in **Figure 2.6(b)**.



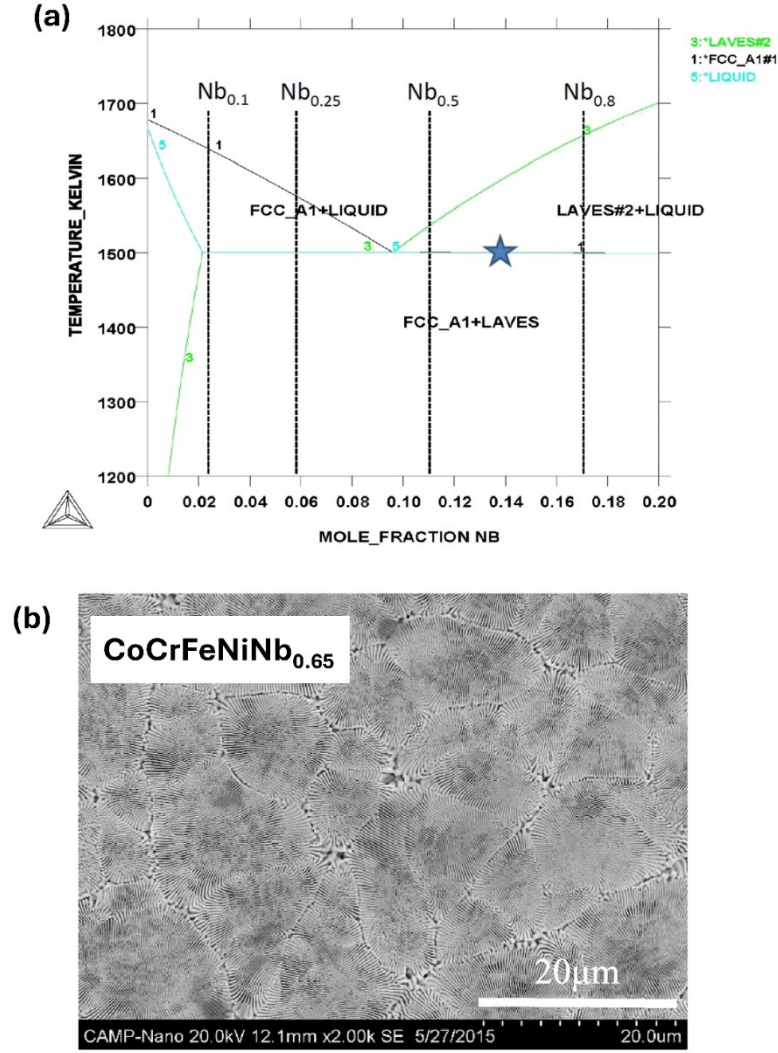


**Figure 2.6:** (a) Pseudo-binary phase diagram of CoCrFeNi-Nb and (b) SEM-SE image of the CoCrFeNiNb<sub>0.65</sub> eutectic alloy [29].

Following this approach, a number of alloys developed down the line; Huang *et al.* [58] calculated the eutectic composition of CoCrNiTa<sub>0.4</sub> using the *Thermo-Calc TTNI7* database, considering that Ta forms binary eutectics with Co, Cr and Ni. Incorporating Fe into the single-phase CoCrNi alloy, as Fe-Ta also exhibits a binary eutectic reaction, Mukarram *et al.* [59] calculated the pseudo-binary phase diagram of CoCrFeNi-Ta, revealing the eutectic point CoCrFeNiTa<sub>0.5</sub> via the *Thermo-Calc HEA5* database (*TCHEA5*) in graphical mode, as shown in **Figure 2.7**. However, subsequent experiments by Mukarram *et al.* [59] revealed the eutectic point to be CoCrFeNiTa<sub>0.75</sub> instead of CoCrFeNiTa<sub>0.5</sub>. Ai *et al.* [60] also utilized this concept via *JMatPro 7.0* with the *Ni-superalloy* database, predicting the CoCrFeNiTa<sub>0.5</sub> to be the fully eutectic composition; however, subsequent experimental findings revealed the eutectic composition to be CoCrFeNiTa<sub>0.43</sub>. In a related study, Xue *et al.* [61] examined the same alloy system by removing Cr, calculating the pseudo-binary phase diagram of CoFeNi-Ta and



reporting the eutectic composition as CoFeNiTa<sub>0.5</sub> using *JMatPro* with the *NiFe-based superalloys* database. Similarly, Wu *et al.* [62] investigated the VNbTi-Si system (where Si forms binary eutectics with V, Nb and Ti) and reported near-eutectic alloys using the *Pandat* software with a custom-made refractory *HEA* database.

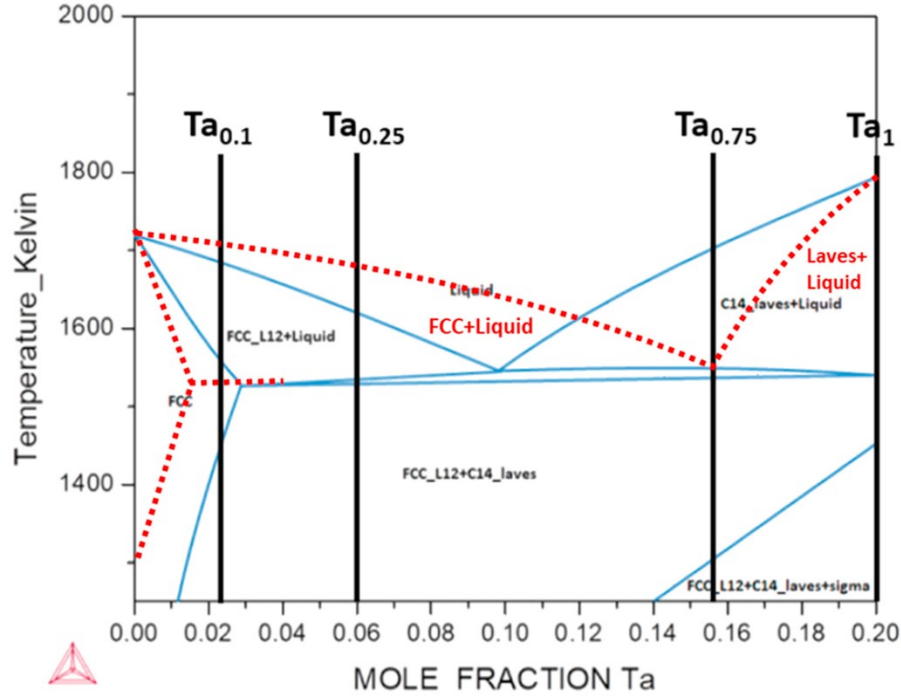


**Figure 2.7:** Modified pseudo-binary phase diagram of CoCrFeNi-Ta [59].

#### 2.4.2: The Mixing Enthalpy Method

Numerous experiments led to the discovery of AlCoCrFeNi<sub>2.1</sub> as a eutectic composition by Lu *et al.* [17] in 2014. Following this, in 2017, Lu *et al.* [63] proposed a method to develop new EMPEAs based on the enthalpy of mixing. Observing that Al and Ni have a very high negative enthalpy of mixing and the elements Co, Cr, Fe and Ni have close mixing enthalpies and similar atomic radius in the AlCoCrFeNi<sub>2.1</sub>, Lu *et al.* [17] grouped Al, Ni into one group and Co, Cr, Fe, Ni into another and hypothesized that elements with very negative enthalpy of mixing with Ni (Zr-Ni, Nb-Ni, Hf-Ni and Ta-Ni are -49, -30, -42 and -29 kJ/mol, respectively, all more negative than that of Al-Ni -22 kJ/mol) could replace Al as follows:

$$\frac{\text{Zr}}{\text{Al}} = \frac{x}{1} = \frac{-22}{-49}, \text{Zr} = 0.45$$

$$\frac{\text{Nb}}{\text{Al}} = \frac{x}{1} = \frac{-22}{-30}, \text{Nb} = 0.73$$

$$\frac{\text{Hf}}{\text{Al}} = \frac{x}{1} = \frac{-22}{-42}, \text{Hf} = 0.52$$

$$\frac{\text{Ta}}{\text{Al}} = \frac{x}{1} = \frac{-22}{-29}, \text{Ta} = 0.76$$

With this insight, Lu *et al.* [63] designed four new eutectic compositions:  $\text{Zr}_{0.45}\text{CoCrFeNi}_{2.1}$  ( $\text{Zr}_{8.11}\text{Co}_{18.02}\text{Cr}_{18.02}\text{Fe}_{18.02}\text{Ni}_{37.84}$ ),  $\text{Nb}_{0.73}\text{CoCrFeNi}_{2.1}$  ( $\text{Nb}_{12.52}\text{Co}_{17.15}\text{Cr}_{17.15}\text{Fe}_{17.15}\text{Ni}_{36.02}$ ),  $\text{Hf}_{0.52}\text{CoCrFeNi}_{2.1}$  ( $\text{Hf}_{9.25}\text{Co}_{17.79}\text{Cr}_{17.79}\text{Fe}_{17.79}\text{Ni}_{37.37}$ ) and  $\text{Ta}_{0.76}\text{CoCrFeNi}_{2.1}$  ( $\text{Ta}_{12.97}\text{Co}_{17.06}\text{Cr}_{17.06}\text{Fe}_{17.06}\text{Ni}_{35.84}$ ). However, these were experimentally found to be near-eutectic alloys. After adjusting the Ni concentration from  $\text{Ni}_{2.1}$  to  $\text{Ni}_{2.0}$  in calculations and fine-tuning the compositions through trial-and-error experiments, the fully eutectic microstructures were identified to be  $\text{Zr}_{0.6}\text{CoCrFeNi}_{2.0}$  ( $\text{Zr}_{10.71}\text{Co}_{17.86}\text{Cr}_{17.86}\text{Fe}_{17.86}\text{Ni}_{35.71}$ ),  $\text{Nb}_{0.74}\text{CoCrFeNi}_{2.0}$  ( $\text{Nb}_{12.89}\text{Co}_{17.42}\text{Cr}_{17.42}\text{Fe}_{17.42}\text{Ni}_{34.84}$ ),  $\text{Hf}_{0.55}\text{CoCrFeNi}_{2.0}$  ( $\text{Hf}_{9.91}\text{Co}_{18.02}\text{Cr}_{18.02}\text{Fe}_{18.02}\text{Ni}_{36.04}$ ) and  $\text{Ta}_{0.65}\text{CoCrFeNi}_{2.0}$  ( $\text{Ta}_{11.50}\text{Co}_{17.70}\text{Cr}_{17.70}\text{Fe}_{17.70}\text{Ni}_{35.40}$ ).

#### 2.4.3: The Simple Mixture Method

As the Lu *et al.* [63] method is based on the known eutectic composition of  $\text{AlCoCrFeNi}_{2.1}$ , further utilizing  $\text{AlCoCrFeNi}_{2.0}$  as the base alloy, still necessitating the experimental adjustments, it does not effectively guide the design of new eutectic compositions in other alloy systems. Addressing this research gap, Jiang *et al.* [64], in 2018 (some of the same group of researchers of Lu *et al.* [63]) predicted new eutectic compositions in the same alloy systems (Co-Cr-Fe-Ni-M (M = Al, Zr, Ta, Nb and Hf)) by summing up all individual binary eutectic compositions according to the equal molar ratio of 1:1 as follows:

$$\begin{aligned} &= \frac{1}{4}\text{Ni}_{84.5}\text{Nb}_{15.5} + \frac{1}{4}\text{Co}_{86.1}\text{Nb}_{13.9} + \frac{1}{4}\text{Cr}_{88}\text{Nb}_{12} + \frac{1}{4}\text{Fe}_{89.4}\text{Nb}_{10.6} \\ &= \text{Co}_{21.53}\text{Cr}_{22}\text{Fe}_{22.35}\text{Ni}_{21.13}\text{Nb}_{13} \\ &= \frac{1}{4}\text{Ni}_{86.3}\text{Ta}_{13.7} + \frac{1}{4}\text{Co}_{92}\text{Ta}_8 + \frac{1}{4}\text{Cr}_{87}\text{Ta}_{13} + \frac{1}{4}\text{Fe}_{92.5}\text{Ta}_{7.5} \\ &= \text{Co}_{23}\text{Cr}_{21.75}\text{Fe}_{23.13}\text{Ni}_{21.58}\text{Ta}_{10.55} \\ &= \frac{1}{4}\text{Ni}_{91.2}\text{Zr}_{8.8} + \frac{1}{4}\text{Co}_{90.5}\text{Zr}_{9.5} + \frac{1}{4}\text{Cr}_{82.8}\text{Zr}_{17.2} + \frac{1}{4}\text{Fe}_{90.2}\text{Zr}_{9.8} \\ &= \text{Co}_{22.63}\text{Cr}_{20.7}\text{Fe}_{22.55}\text{Ni}_{22.8}\text{Zr}_{11.33} \\ &= \frac{1}{4}\text{Ni}_{87.5}\text{Hf}_{12.5} + \frac{1}{4}\text{Co}_{89}\text{Hf}_{11} + \frac{1}{4}\text{Cr}_{87}\text{Hf}_{13} + \frac{1}{4}\text{Fe}_{92.1}\text{Hf}_{7.9} \end{aligned}$$

$$= \text{Co}_{22.25}\text{Cr}_{21.75}\text{Fe}_{23.03}\text{Ni}_{21.88}\text{Hf}_{11.10}$$

However, all these predicted compositions are identified to be near eutectics and the trial-and-error experiments revealed the fully eutectic compositions to be  $\text{CoCrFeNiNb}_{0.45}$  ( $\text{Co}_{22.47}\text{Cr}_{22.47}\text{Fe}_{22.47}\text{Ni}_{22.47}\text{Nb}_{10.11}$ ),  $\text{CoCrFeNiTa}_{0.4}$  ( $\text{Co}_{22.73}\text{Cr}_{22.73}\text{Fe}_{22.73}\text{Ni}_{22.73}\text{Ta}_{9.09}$ ),  $\text{CoCrFeNiZr}_{0.55}$  ( $\text{Co}_{21.98}\text{Cr}_{21.98}\text{Fe}_{21.98}\text{Ni}_{21.98}\text{Zr}_{12.09}$ ) and  $\text{CoCrFeNiHf}_{0.4}$  ( $\text{Co}_{22.73}\text{Cr}_{22.73}\text{Fe}_{22.73}\text{Ni}_{22.73}\text{Hf}_{9.09}$ ). Further, Jiang *et al.* [65] utilized this approach sequentially, predicting eutectic compositions as  $\text{FeNiNb}_{0.30}$  ( $\text{Fe}_{43.48}\text{Ni}_{43.48}\text{Nb}_{13.04}$ ),  $\text{CoFeNiNb}_{0.46}$  ( $\text{Co}_{28.90}\text{Fe}_{28.90}\text{Ni}_{28.90}\text{Nb}_{13.29}$ ) and  $\text{CoCrFeNiNb}_{0.6}$  ( $\text{Co}_{21.74}\text{Cr}_{21.74}\text{Fe}_{21.74}\text{Ni}_{21.74}\text{Nb}_{13.04}$ ).

$$\begin{aligned} &= \frac{1}{2}\text{Ni}_{84.5}\text{Nb}_{15.5} + \frac{1}{2}\text{Fe}_{89.4}\text{Nb}_{10.6} = \text{Fe}_{44.7}\text{Ni}_{42.25}\text{Nb}_{13.05} \\ &= \frac{1}{3}\text{Ni}_{84.5}\text{Nb}_{15.5} + \frac{1}{3}\text{Co}_{86.1}\text{Nb}_{13.9} + \frac{1}{3}\text{Fe}_{89.4}\text{Nb}_{10.6} = \text{Co}_{28.7}\text{Fe}_{29.8}\text{Ni}_{28.17}\text{Nb}_{13.33} \end{aligned}$$

However, subsequent experimental findings by Jiang *et al.* [65] revealed the actual eutectic compositions to be  $\text{FeNiNb}_{0.35}$  ( $\text{Fe}_{42.55}\text{Ni}_{42.55}\text{Nb}_{14.89}$ ),  $\text{CoFeNiNb}_{0.50}$  ( $\text{Co}_{28.57}\text{Fe}_{28.57}\text{Ni}_{28.57}\text{Nb}_{14.29}$ ) and  $\text{CoCrFeNiNb}_{0.45}$  ( $\text{Co}_{22.47}\text{Cr}_{22.47}\text{Fe}_{22.47}\text{Ni}_{22.47}\text{Nb}_{10.11}$ ). Wen *et al.* [66] also utilized this concept, reporting the near-eutectic composition  $\text{Ni}_{1.5}\text{CrCoFe}_{0.5}\text{Mo}_{0.1}\text{Nb}_{0.7}$  ( $\text{Ni}_{31.25}\text{Cr}_{20.83}\text{Co}_{20.83}\text{Fe}_{10.42}\text{Mo}_{2.08}\text{Nb}_{14.58}$ ). In 2023, Jiao *et al.* [67] also applied this concept to predict the eutectic composition in a senary HEA system. They combined the calculations for Nb and Ta previously proposed by Jiang *et al.* [64], introducing a coefficient of 0.5 to merge these calculations effectively as follows:

$$\begin{aligned} &= \frac{1}{2} \left( \frac{1}{4}\text{Ni}_{84.5}\text{Nb}_{15.5} + \frac{1}{4}\text{Co}_{86.1}\text{Nb}_{13.9} + \frac{1}{4}\text{Cr}_{88}\text{Nb}_{12} + \frac{1}{4}\text{Fe}_{89.4}\text{Nb}_{10.6} \right) + \frac{1}{2} \left( \frac{1}{4}\text{Ni}_{86.3}\text{Ta}_{13.7} + \right. \\ &\quad \left. \frac{1}{4}\text{Co}_{92}\text{Ta}_8 + \frac{1}{4}\text{Cr}_{87}\text{Ta}_{13} + \frac{1}{4}\text{Fe}_{92.5}\text{Ta}_{7.5} \right) \\ &= \text{Co}_{22.26}\text{Cr}_{21.88}\text{Fe}_{22.74}\text{Ni}_{21.35}\text{Nb}_{6.5}\text{Ta}_{5.28} \end{aligned}$$

Following this strategy, Jiao *et al.* [67] predicted three other compositions,  $\text{CoCrFeNiTa}_{0.24}\text{Hf}_{0.25}$  ( $\text{Co}_{22.27}\text{Cr}_{22.27}\text{Fe}_{22.27}\text{Ni}_{22.27}\text{Ta}_{5.35}\text{Hf}_{5.57}$ ),  $\text{CoCrFeNiNb}_{0.20}\text{Zr}_{0.17}\text{Hf}_{0.17}$  ( $\text{Co}_{22.03}\text{Cr}_{22.03}\text{Fe}_{22.03}\text{Ni}_{22.03}\text{Nb}_{4.41}\text{Zr}_{3.74}\text{Hf}_{3.74}$ ) and  $\text{CoCrFeNiZr}_{0.17}\text{Hf}_{0.17}\text{Ta}_{0.16}$  ( $\text{Co}_{22.22}\text{Cr}_{22.22}\text{Fe}_{22.22}\text{Ni}_{22.22}\text{Zr}_{3.78}\text{Hf}_{3.78}\text{Ta}_{3.56}$ ). However, all these were found to be near eutectic compositions and experimental adjustments were still required to identify the fully eutectic compositions,  $\text{CoCrFeNiNb}_{0.25}\text{Ta}_{0.20}$  ( $\text{Co}_{22.47}\text{Cr}_{22.47}\text{Fe}_{22.47}\text{Ni}_{22.47}\text{Nb}_{5.62}\text{Ta}_{4.49}$ ),

CoCrFeNiTa<sub>0.25</sub>Hf<sub>0.25</sub> (Co<sub>22.22</sub>Cr<sub>22.22</sub>Fe<sub>22.22</sub>Ni<sub>22.22</sub>Ta<sub>5.56</sub>Hf<sub>5.56</sub>), CoCrFeNiNb<sub>0.15</sub>Zr<sub>0.15</sub>Hf<sub>0.15</sub>  
 (Co<sub>22.47</sub>Cr<sub>22.47</sub>Fe<sub>22.47</sub>Ni<sub>22.47</sub>Nb<sub>3.37</sub>Zr<sub>3.37</sub>Hf<sub>3.37</sub>) and CoCrFeNiZr<sub>0.17</sub>Hf<sub>0.16</sub>Ta<sub>0.16</sub>  
 (Co<sub>22.27</sub>Cr<sub>22.27</sub>Fe<sub>22.27</sub>Ni<sub>22.27</sub>Zr<sub>3.79</sub>Hf<sub>3.56</sub>Ta<sub>3.56</sub>).

#### 2.4.4: The Machine Learning Approach

The application of machine learning in predicting new EMPEAs is currently in its nascent stage. As the effectiveness of these techniques heavily depends on extensive datasets, the lack of comprehensive data specific to each eutectic EMPEA system significantly constrains their utility in predicting new compositions. Moreover, suppose the data pool indiscriminately includes all types of eutectic systems. In that case, it is likely to result in inaccurate predictions due to variations in alloy system descriptors such as VEC, atomic size differences and enthalpy of mixing across different alloy systems. Consequently, the primary application of machine learning in EMPEAs currently focuses more on analyzing elemental behaviour in previously reported alloys rather than actually predicting new eutectic compositions in different alloy systems.

For instance, Wu *et al.* [68] utilized a dataset comprising 321 alloys to explore the interrelationships among elements in the Al-Co-Cr-Fe-Ni system. This dataset included 11 experimentally reported entries, while the remaining 310 near-eutectic entries were generated using CALPHAD by randomly varying the content of each element. Employing an artificial neural network model with a testing correlation coefficient ( $R$ ) of 0.983, Wu *et al.* [68] identified 400 groups of near-eutectic compositions having a pro-eutectic phase of less than 5%. Based on statistical data represented in **Figure 2.8**, they categorized elements in the Al-Co-Cr-Fe-Ni system into three groups: (1) a critical element with narrow ranges, Al; (2) an element strongly associated with the critical element, Cr; and (3) miscible elements with each other, Co, Fe and Ni.

From these insights, Wu *et al.* [68] hypothesized that EMPEAs in this system could be effectively designed in three steps: firstly, by selecting a reasonable Al content, then determining the associated Cr content adjusting with Al and finally, confirming the contents of Ni, Co and Fe via VEC. In a similar study, Liu *et al.* [69] in the Al-Co-Cr-Ni system utilized four experimentally reported EMPEAs and 96 CALPHAD-guided near-eutectic compositions as datasets. Using a support vector machine algorithm, which achieved a correlation coefficient ( $R$ ) of 0.916, they successfully predicted 341 sets of near-eutectic compositions. These statistical results by Liu *et al.* [69] identified Al as a critical element, with Ni being strongly associated with Al. They further employed constraints based on previously reported

experimental observations in the identified 341 near-eutectic compositions, with specific compositional limits,  $15 \leq y$ ,  $z \leq 20$ ,  $16 \leq w \leq 22$ ,  $x = 100 - y - z - w$ , leading to reporting two new eutectics in  $\text{Ni}_x\text{Co}_y\text{Cr}_z\text{Al}_w$  namely,  $\text{Ni}_{49}\text{Co}_{16}\text{Cr}_{16}\text{Al}_{19}$  and  $\text{Ni}_{46.7}\text{Co}_{15}\text{Cr}_{20}\text{Al}_{18.3}$ .

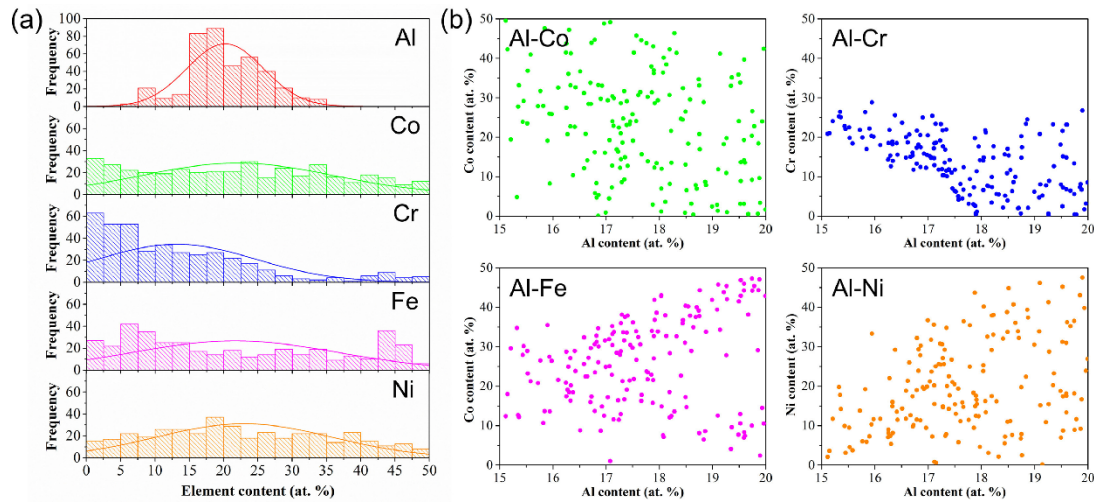


**Figure 2.8:** Statistics on 400 near-eutectic compositions: (a) Content distributions of individual elements, (b) Maps showing Co, Cr, Fe and Ni contents corresponding to each Al content [68].

## 2.4.5: The VEC Criterion

Following the grouping strategy proposed by Lu *et al.* [63] in 2017, Dong *et al.* [70] considered that  $\text{AlCoCrFeNi}_{2.1}$  could be divided into two groups,  $\text{AlNi}$  and  $\text{CoCrFeNi}_{1.1}$  and applied the VEC criterion to predict the eutectic composition between these groups. This decomposition extended to the general Al-Co-Cr-Fe-Ni system, where Dong *et al.* [70] deduced that the alloy formula  $\text{AlCo}_a\text{Cr}_b\text{Fe}_c\text{Ni}_d$  would lead to the formation of an  $\text{AlNi}$  B2 structure and a  $\text{Co}_a\text{Cr}_b\text{Fe}_c\text{Ni}_{d-1}$  FCC phase, provided that the variables  $a$ ,  $b$ ,  $c$  and  $d-1$  ( $d > 1$ ) meet the condition  $\text{VEC} > 8$ , which promotes FCC phase formation. Further, to guarantee the eutectic structure in these dual-phase alloys, Dong *et al.* [70], based on  $\text{AlCoCrFeNi}_{2.1}$ , hypothesized that the volume fractions of B2 and FCC phases should maintain a ratio of  $V(\text{NiAl})/V(\text{Co}_a\text{Cr}_b\text{Fe}_c\text{Ni}_{d-1}) = 0.587$ . Based on these two conditions, Dong *et al.* [70] efficiently designed nine EMPEAs, seven of which were verified to be complete eutectics. These include  $\text{AlCo}_{0.8}\text{CrFeNi}_{2.3}$ ,  $\text{AlCo}_{1.2}\text{CrFeNi}_{1.9}$ ,  $\text{AlCoCr}_{1.2}\text{Fe}_{0.8}\text{Ni}_{2.1}$ ,  $\text{AlCoCr}_{0.8}\text{Fe}_{1.2}\text{Ni}_{2.1}$ ,  $\text{AlCo}_{0.6}\text{CrFe}_{1.43}\text{Ni}_{2.1}$ ,  $\text{AlCo}_{1.2}\text{CrFe}_{0.81}\text{Ni}_{2.1}$  and  $\text{AlCo}_{1.2}\text{Cr}_{0.81}\text{FeNi}_{2.1}$ . The schematic diagram of this design idea is shown in **Figure 2.9**. Applying this concept to Al-Cr-Fe-Ni based on reported  $\text{AlCrFeNi}_3$ , Yuan *et al.* [71] (some of the same group of researchers of Dong *et al.* [70]) reported two new eutectic compositions,  $\text{AlCr}_{1.18}\text{FeNi}_{2.8}$  and  $\text{AlCrFe}_{1.46}\text{Ni}_{2.5}$ . In a similar work by Wu *et al.* [72], the Co

in AlCoCrFeNi<sub>2.1</sub> was replaced with Fe and Ni in equal proportions, thus not changing the VEC of the overall alloy significantly (VEC values of Fe, Co, Ni are 8, 9, 10) and reported the eutectic composition AlCrFe<sub>1.5</sub>Ni<sub>2.6</sub>. Vikram *et al.* [73] also applied the VEC criterion in their report on the near-eutectic alloy AlCo<sub>1.9</sub>CrFeNi, which exhibits excellent mechanical properties with a VEC of 7.47, closely aligning with Ni-based EMPEAs. However, this report did not provide detailed information on the precise design strategy used to deduce this composition via the VEC criterion.

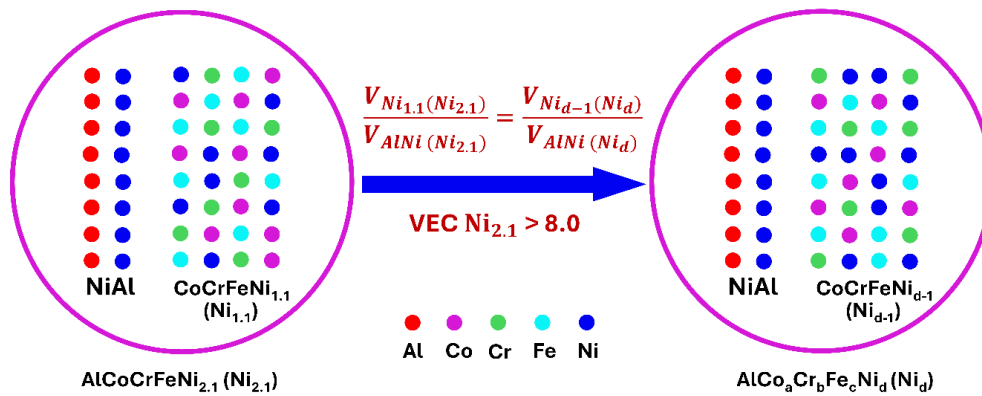


**Figure 2.9:** Schematic diagram illustrating the design concept of FCC + B2 EHEAs [70].

#### 2.4.6: DSS Plus IMC Approach

This school of thought, possibly the most efficient above all, effectively combines a disordered solid solution (DSS) and an intermetallic compound (IMC) in a pseudo-binary fashion, which was first applied in 2018 by Jin *et al.* [74]. They considered the reported single phases, CoCrFeNi<sub>2</sub>, Co<sub>2</sub>CrFeNi, CoCrFe<sub>2</sub>Ni and NiAl, as the intermetallic compound. By stoichiometrically mixing these two phases, such as AlNi with CoCrFeNi<sub>2</sub> resulting in AlCoCrFeNi<sub>3</sub>, AlNi with Co<sub>2</sub>CrFeNi leading to AlCo<sub>2</sub>CrFeNi<sub>2</sub> and AlNi with CoCrFe<sub>2</sub>Ni forming AlCoCrFe<sub>2</sub>Ni<sub>2</sub>, Jin *et al.* [74] initially hypothesized these resulting compositions to be of eutectics. However, subsequent experimental findings did not confirm this. Later, by increasing the Al content and decreasing the Ni content, Jin *et al.* [74] identified the fully eutectic compositions as Al<sub>17</sub>Co<sub>14.3</sub>Cr<sub>14.3</sub>Fe<sub>14.3</sub>Ni<sub>40.1</sub>, Al<sub>17</sub>Co<sub>28.6</sub>Cr<sub>14.3</sub>Fe<sub>14.3</sub>Ni<sub>25.8</sub> and Al<sub>17</sub>Co<sub>14.3</sub>Cr<sub>14.3</sub>Fe<sub>28.6</sub>Ni<sub>25.8</sub>. If one notices carefully, this is similar to He *et al.*'s [29] pseudo-binary approach, except the fact that here, the eutectic forming is not actually the element but a pseudo-element (NiAl).

Later, in 2021, Zhang *et al.* [75] applied this concept to the (FeCoNi)-(NiAl) system, preparing five quaternary alloys: Fe<sub>26</sub>Co<sub>26</sub>Ni<sub>37</sub>Al<sub>11</sub>, Fe<sub>23.3</sub>Co<sub>23.3</sub>Ni<sub>38.4</sub>Al<sub>15</sub>,

$\text{Fe}_{20.7}\text{Co}_{20.7}\text{Ni}_{39.6}\text{Al}_{19}$ ,  $\text{Fe}_{20}\text{Co}_{20}\text{Ni}_{40}\text{Al}_{20}$  and  $\text{Fe}_{14.7}\text{Co}_{14.7}\text{Ni}_{42.6}\text{Al}_{28}$ . Out of these five, the alloy  $\text{Fe}_{20.7}\text{Co}_{20.7}\text{Ni}_{39.6}\text{Al}_{19}$  was identified as a fully eutectic composition, confirmed both experimentally and through CALPHAD simulations. Further on this design framework, Ye *et al.* [76] reported new eutectic compositions in the (V-Cr-Mo)-(NiAl) systems based on the observation that (V)-(NiAl), (Cr)-(NiAl) and (Mo)-(NiAl) each exhibit eutectic formations. They proposed that any combination of V, Cr and Mo would form a BCC structure, which, when mixed with NiAl, leads to a BCC plus B2 eutectic structure. Ye *et al.* [76] termed this method the 'infinite solid solution approach,' highlighting that any combination of V-Cr, V-Cr-Mo, Cr-Mo, or V-Mo could replace the BCC phase in an M-NiAl system (where M = V, Cr, Mo), thus facilitating the formation of BCC plus B2 eutectic structures. The reported compositions by Ye *et al.* [77] are  $(\text{NiAl})_{63}\text{V}_{20}\text{Cr}_{17}$ ,  $(\text{NiAl})_{65}\text{V}_{30}\text{Mo}_5$ ,  $(\text{NiAl})_{65}\text{Cr}_{30}\text{Mo}_5$  and  $(\text{NiAl})_{65}\text{V}_{20}\text{Cr}_{10}\text{Mo}_5$ . One can notice that the intermetallic (NiAl) composition in all these alloys is maintained at approximately 65 at.%. Ye *et al.* [77] later applied this approach to the (CoCrFeNi)-(TaNbMoW) system with the hypothesis that any combination of Ta-Nb-Mo-W would form a BCC structure and all these elements have been reported to form eutectics with CoCrFeNi, such as CoCrFeNi-Ta, CoCrFeNi-Nb, CoCrFeNi-Mo and CoCrFeNi-W. With this insight, Ye *et al.* [77] reported four new eutectic compositions:  $(\text{CoCrFeNi})_{90}\text{Nb}_6\text{Ta}_4$ ,  $(\text{CoCrFeNi})_{87}\text{Nb}_8\text{Mo}_5$ ,  $(\text{CoCrFeNi})_{88}\text{Nb}_5\text{Ta}_4\text{Mo}_3$  and  $(\text{CoCrFeNi})_{88}\text{Nb}_5\text{Ta}_3\text{Mo}_2\text{W}_2$ . However, these two reports by Ye *et al.* [76,77] of BCC plus B2 and FCC plus Laves phase eutectics did not provide a detailed rationale for selecting those specific compositions prior to experimental characterization, limiting the ability to design new compositions based on this approach. Addressing this exact research gap, Wang *et al.* [78], in 2022, demonstrated that a careful simulation approach could aid in specific composition selection before experimental characterization. Wang *et al.* [78] considered the (NiAl)-(MoCrV) pseudo-binary approach and to pinpoint the exact eutectic, they employed the CALPHAD methodology via *JMatPro* software, as illustrated in **Figure 2.10**.

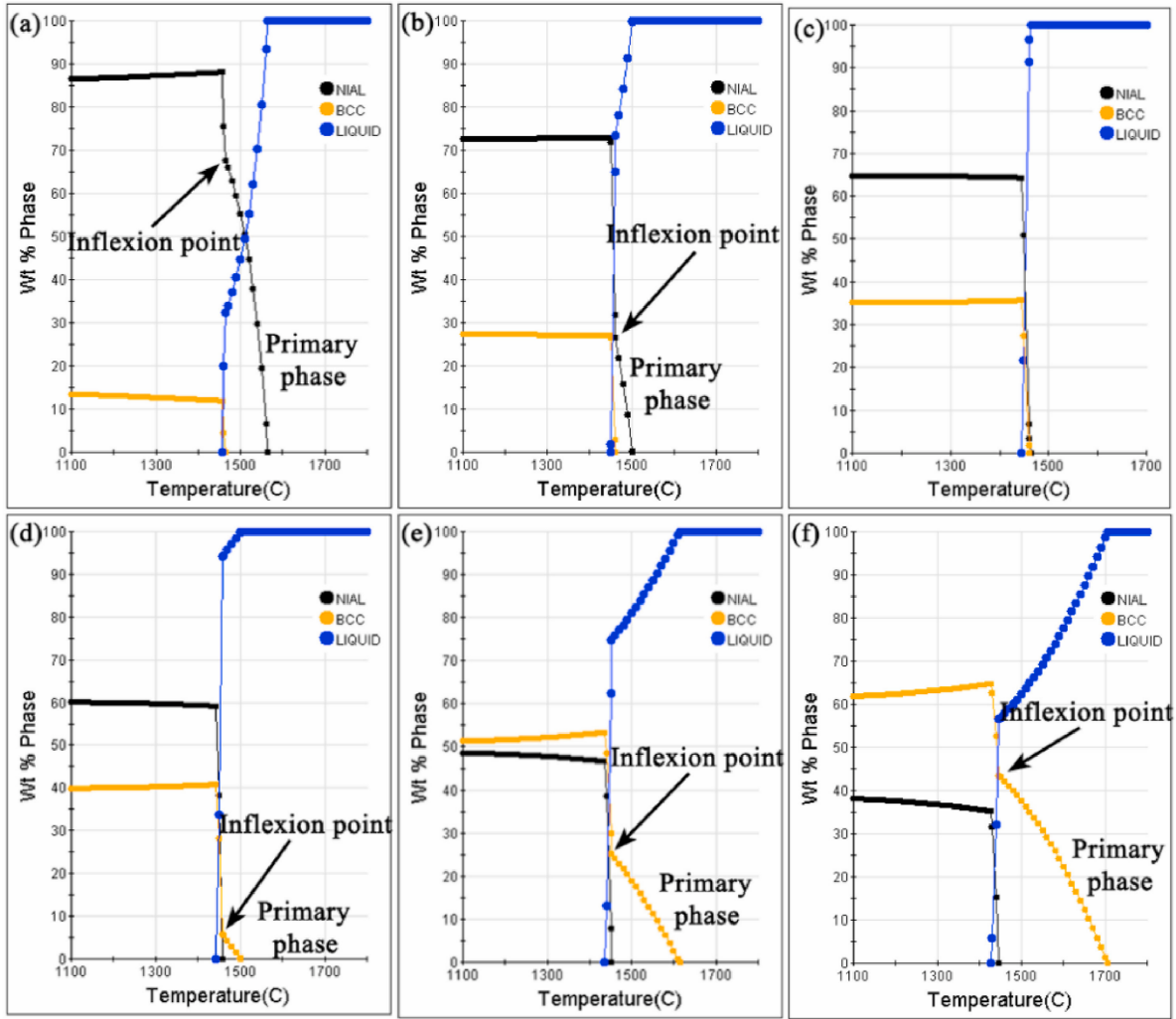


**Figure 2.10:** Solidification paths of NiAl-Mo<sub>x</sub>Cr<sub>x</sub>V<sub>x</sub> alloys simulated using *JMatPro*: (a)  $x = 3.33$ , (b)  $x = 6.67$ , (c)  $x = 8.7$ , (d)  $x = 10.0$ , (e)  $x = 13.3$ , (f)  $x = 16.67$  at.% [78].

It was observed that in the NiAl-Mo<sub>x</sub>Cr<sub>x</sub>V<sub>x</sub> system, when  $x$  is approximately 8.5, a eutectic composition with BCC plus B2 structures becomes apparent, leading to the identification of the eutectic composition (NiAl)-Mo<sub>8.7</sub>Cr<sub>8.7</sub>V<sub>8.7</sub>. Similarly, as Mo-V-Cr forms a stable BCC structure, Mo-Cr-Fe is also expected to form BCC. Following this, Wang *et al.* [78] conducted simulations for the NiAl-Mo<sub>x</sub>Cr<sub>x</sub>Fe<sub>x</sub> system, identifying the eutectic point at  $x = 14.3$  with a discernible solidification range. Extending this methodology further, Wang *et al.* [78] also explored the NiAl-Mo<sub>x</sub>Cr<sub>x</sub>V<sub>x</sub>Fe<sub>x</sub> system and determined the eutectic composition at  $x = 10$ . The three predicted compositions, (NiAl)<sub>73.9</sub>Mo<sub>8.7</sub>Cr<sub>8.7</sub>V<sub>8.7</sub>, (NiAl)<sub>56.5</sub>Mo<sub>14.5</sub>Cr<sub>14.5</sub>Fe<sub>14.5</sub> and (NiAl)<sub>60</sub>Mo<sub>10</sub>Cr<sub>10</sub>V<sub>10</sub>Fe<sub>10</sub>, were subsequently experimentally verified to be fully eutectic compositions. In 2023, Li *et al.* [79] employed the DSS plus IMC concept with a slight variation. Initially, they started with the reported eutectic composition Ni<sub>41</sub>Ti<sub>39</sub>Nb<sub>20</sub>, using the pseudo-binary approach of (Ni-Ti)<sub>80</sub>-Nb<sub>20</sub>. They then replaced 11 at.% of Ni with Fe and 9 at.%



of Hf with Ti, predicting the new eutectic composition as  $\text{Ni}_3\text{FeTi}_3\text{HfNb}_2$ . This composition was subsequently verified experimentally [80]. Essentially, while maintaining the original intermetallic forming element composition (which otherwise can be treated as a eutectic forming element (EFE)), Li *et al.* [79], in 2023, expanded the disordered solid solution phase by introducing new elements that can partially substitute the existing elements without altering the disordered (BCC) crystal structure, which is very similar to the infinite solid solution approach proposed by Ye *et al.* [77] in 2021.

## 2.5: The Overlapping Research Gaps in Existing Design Strategies

Besides the design strategies mentioned above, there are other notable approaches, such as the grouping strategy via d-orbital energy level proposed by Li *et al.* [81], the eutectic lines approach by Shafiei *et al.* [82,83], the high-temperature centrifugation by Löffler *et al.* [84] and electromagnetic directional crystallization by He *et al.* [85], among others. However, these strategies typically determine new compositions solely through experimentation or based on previously reported fully eutectic compositions with relatively not-easy calculations.

Thus, although various design methods have been proposed empirically via CALPHAD, experimentally, or based on binary eutectics, most of these strategies still rely on a trial-and-error approach. Additionally, there is considerable overlap among these design strategies. For example, the pseudo-binary phase diagram approach, which is very similar to the DSS plus IMC approach, although instrumental in advancing the development of several alloys down the line, exhibits some fundamental issues. The primary concern lies in the calculation of the pseudo-binary phase diagram itself. The *Thermo-Calc* symbol, displayed at the lower left corner in **Figure 2.6(a)**, indicates that this diagram was possibly generated using the graphical mode of *Thermo-Calc*, which is not intended for generating accurate pseudo-binary phase diagrams. In graphical mode, one variable must be set as dependent, as indicated in **Figure 2.11** (<https://thermocalc.com/support/getting-started-guides/Thermo-Calc-guide/>). This suggests that the diagram in **Figure 2.6(a)** might not accurately represent the pseudo-binary phase diagram of CoCrFeNi-Nb but rather that of CoCrFe-Nb, CoCrNi-Nb, or CrFeNi-Nb, potentially leading to an incorrect prediction of the eutectic composition.

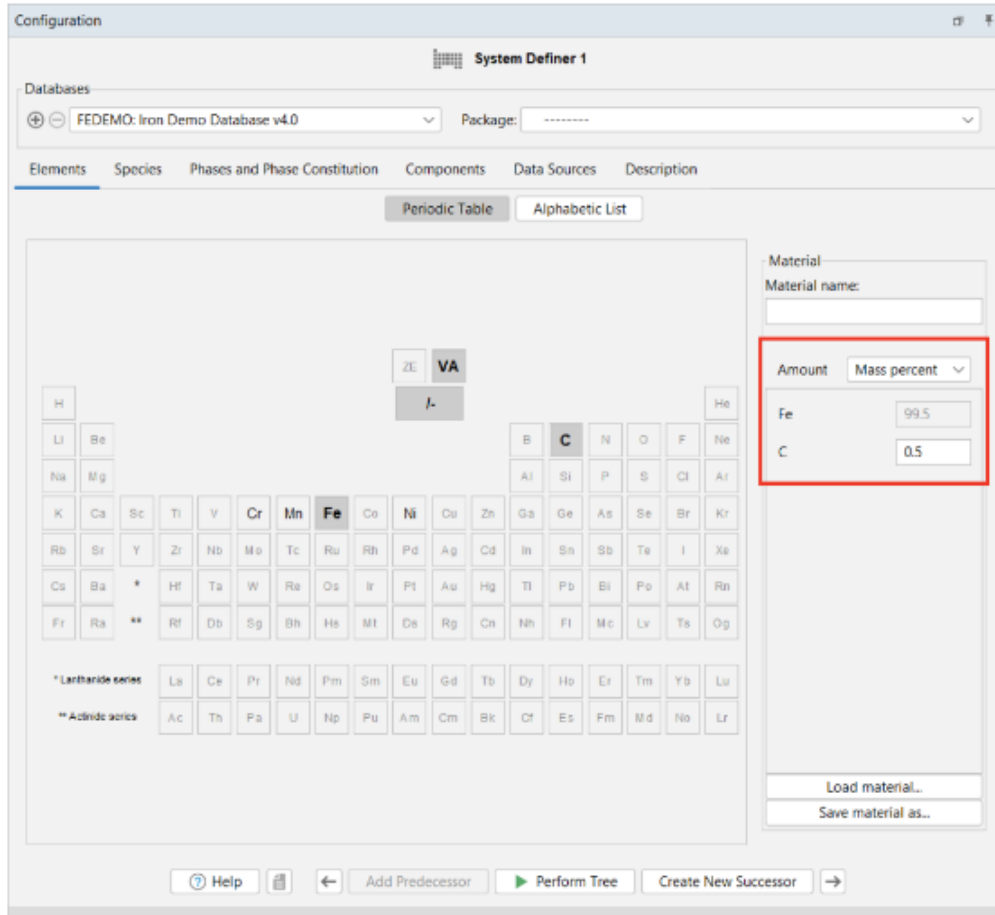


**Figure 2.11:** The dependent variable is represented in the graphical mode of the *Thermo-Calc* (FEDEMO database, <https://thermocalc.com/support/getting-started-guides/Thermo-Calc-guide/>).

Additionally, the choice of the *Ni*-database (the exact version, however, is not provided) instead of a more specialized database like *TCHEA*, which offers more precise predictions, may have compromised the results. Thus, while there is room to refine this approach in execution, it has provided valuable insights into the design of new alloys. Further, however, conceptually also, the necessity of restricting the eutectic forming element (Nb in this case of Co-Cr-Fe-Ni-Nb) to exhibit binary eutectic reactions with every other element in the alloy system considered may not be essential. For instance, the first reported MPEA incorporating the eutectic concept, AlCoCrFeNi<sub>2.1</sub>, introduced in 2014, lacked a single element capable of forming binary eutectics with all other elements, raising questions about the applicability of this methodology to new alloy systems. Moreover, this restriction could inadvertently limit designing new EMPEAs to mostly FCC plus Laves phase combinations, as only Zr, Nb, Hf and Ta form binary eutectics (of FCC plus Laves) with most of the FCC forming transition elements such as Co, Fe and Ni. This limitation could hinder the design of alloys optimized for structural applications that require a synergy of strength and ductility, such as the FCC plus BCC combination, which is

the very rationale behind introducing EMPEAs to address the challenges of casting HEAs and achieving strength-ductility synergy in the as-cast state. This same problem persists with the simple mixture approach. As outlined in Section 2.6, in all the approaches proposed by various researchers, the EFE must form binary eutectics with every other element in the considered alloy system. Also, starting with a single phase that includes elements such as Co, Fe and Ni, as in the DSS plus IMC approach, the pseudo-binary phase diagram approach, or the VEC approach, might limit the eutectic type to only a dual-phase.

Additionally, the mixing enthalpy method, primarily based on incorporating refractory elements, typically results in alloys with FCC as one of the phases and Laves as the other, but not BCC, thus may not effectively guide the eutectics with BCC as one of the phases. Also, notably, this strategy excludes the substitution of Ti for Ni despite Ti having a more negative mixing enthalpy with Ni than Al (-34.50 kJ/mol for Ni-Ti vs. -22.30 kJ/mol for Ni-Al) [86]. Additionally, Al, which also exhibits significant negative mixing enthalpy with refractory elements, could potentially form Laves phases, yet the rationale for only considering elements forming Laves phases with Ni is not elaborated. Furthermore, the strong negative mixing enthalpy of Al-Co (-18.80 kJ/mol) suggests that higher atomic fractions of Co might also form eutectics, such as in the  $\text{AlCo}_{1.9}\text{CrFeNi}$  system [73]. Thus, the grouping of only AlNi as one and CoCrFeNi as the other could overlook potential eutectics with higher fractions of other elements in all these methods utilizing the grouping approach. Additionally, the methods, such as the VEC criterion and DSS plus IMC approach, have only identified nearby eutectic compositions through trial and error or adjustments of one or two elements in reported alloys. Also, in the simple mixture method, apart from not being able to identify a eutectic with BCC as one of the phases, there is no logical metallurgical reason for assuming a linear combination of eutectic components results in near-eutectic compositions. The same goes for the stoichiometric approach of the DSS plus the IMC approach.

Most importantly, all the methods proposed so far, however, are able to achieve a near-eutectic composition but often fail to cross-verify whether that design strategy is applicable to previously reported alloys and capable of designing new alloys across systems. Also, given the vast number of potential eutectic compositions, achieving an exact eutectic or exploring the entire binary eutectic compositional space remains an untouched area in all these design strategies. In conclusion, the following can be deduced from existing design strategies:

- One can definitively identify eutectics in MPEAs by aggregating binary eutectic clusters, which is a valuable strategy as it is without any computational support. However, the

present strategies proposed still require a trial-and-error experimental approach, and there is no clear metallurgical logic in adding them to a linear combination.

- Based on approaches with computational aid, of all the software tools available, CALPHAD via *Thermo-Calc* has proven to be very efficient, provided the right database and interface mode are employed.
- The numerous eutectic compositions in the Co-Cr-Fe-Ni-M (M = Al, Zr, Ta, Nb, Hf and Mo) systems indicate that multiple, possibly hundreds of binary eutectics are present in MPEAs adhering to the Gibbs phase rule.
- There is no attempt in the currently existing design strategies to map the complete eutectic compositional space of these binary eutectics in any of the MPEA systems.
- There are no reports of invariant eutectic compositions, nor is there a search for such compositions in the existing design strategies.

## **2.6: Research Questions Addressed in the Present Thesis**

As outlined in Section 1.3 of the introduction, this thesis addresses the following key research questions derived from the identified research gaps (Section 2.5) to guide the exploration of new, multifaceted alloy design approaches:

1. How can binary eutectics in MPEA systems be designed effectively without relying on computational tools?
2. Even when employing computational tools, how can eutectic points in MPEAs be quickly located without extensive calculations?
3. How can all potential binary eutectics be identified in an MPEA system and what strategy can guide the discovery of higher-order eutectics, including invariant eutectic reactions?

## CHAPTER 3

### Materials and Methods

#### 3.1: Introduction

Chapter 3 briefly details the theoretical and experimental methodologies followed in the thesis to develop novel EMPEAs. It starts with the thermodynamic analysis using the CALPHAD methodology, followed by the synthesis of alloys through vacuum arc melting. Subsequent sections describe the characterization techniques employed on the developed alloys.

#### 3.2: Thermodynamic Calculations via CALPHAD

All thermodynamic calculations in this study were performed via the CALPHAD methodology, utilizing *Thermo-Calc* software (version 2022a) equipped with the *TCHEA5* database. Pseudo-binary phase diagrams via CALPHAD were computed using an in-house script run in *Thermo-Calc* console mode. The eutectic nature (temperature and elemental composition) of the alloys is deduced through phase evolution plots and Scheil solidification models in graphical mode. The classic Scheil model, employed in *Thermo-Calc* software for non-equilibrium calculations, posits complete solute mixing in the liquid phase and no diffusion in the solid phase—conditions typically associated with very high cooling rates. In this, the temperature is methodically lowered in specified increments, calculating the fraction and composition of liquid and solid phases at each stage. An equilibrium calculation is performed at every temperature step using the liquid composition from the preceding step, with the residual liquid concentration matched to that from equilibrium calculations. The increase in solid phase fraction is calculated and phase fractions are adjusted accordingly. This process continues until the solid fraction reaches 0.99, enabling the simulation of solidification paths under conditions that approximate the non-equilibrium cooling rates seen in experimental scenarios.

The *TCHEA5* database, tailored for HEAs or MPEAs, provides comprehensive thermodynamic and physical property data for 26 elements: Al, B, C, Co, Cr, Cu, Fe, Hf, Ir, Mn, Mo, N, Nb, Ni, Re, Rh, Ru, Si, Sn, Ta, Ti, V, W, Y, Zn and Zr. This includes assessments of 310 binary systems—covering nearly their entire composition and temperature ranges—and 501 ternary systems, with 192 fully evaluated. The database also models 518 solid solutions

and intermetallic phases, featuring key phases like the B2 and L1<sub>2</sub> and their disordered counterparts, BCC\_A2 and FCC\_A1, through a partitioning model essential for predicting second-order transformations. Utilizing the *Thermo-Calc* property module sublattice symmetry approach, the distinction between ordered and disordered structures is carried out. *TC-Python* (*Python*<sup>™</sup> language-based SDK available with *Thermo-Calc*) was utilized on the *TCHEA5* database for high-throughput calculations, with the in-house *Python* script being developed and executed on the *Spyder* platform.

### 3.3: Alloy Synthesis via Vacuum Arc Melting

All the designed alloys were synthesized in-house employing Edmund Bühler GmbH Mini Vacuum Arc Melter-1, equipped with a water-cooled oxygen-free high conductivity copper hearth, capable of simultaneously melting up to six alloy ingots. Its advanced pumping system features an oil-free scroll pump and a high vacuum turbo molecular pump, capable of reaching vacuum levels down to  $1 \times 10^{-5}$  mbar. A DC power supply facilitates the melting process via contactless ignition, capable of reaching up to 3500 °C. High-purity metals Al, Co, Cr, Fe, Ni, Ti, V, Cr and Zr were used as raw materials with a purity level of  $\geq 99.7\%$ . The charge weights for melting were precisely calculated using a *Python* script that converted *Thermo-Calc* calculated atomic percentages into weight percentages.

Preparing the raw materials involved cutting and filing to achieve the required weights. To ensure sample cleanliness, surface oxides and contaminants were removed with steel wool and tissue paper, followed by ultrasonication in an acetone solution. Elements contributing a total charge of 15 to 20 grams were placed inside the melting chamber, arranged by their melting points. To maintain a contamination-free environment, the furnace chamber—loaded with the alloy charges and a Zr/Ti getter—was evacuated to no more than  $2.5 \times 10^{-5}$  mbar and then backfilled with argon to 25 mbar to create an inert atmosphere. Before melting the charge, the titanium getter was melted to absorb any residual oxygen in the chamber. It was then maintained at a high temperature throughout the melting process to ensure maximum efficiency in removing impurities. Each alloy button was subjected to five cycles of melting and inversion to ensure complete melting and homogeneity. The melted ingot was weighed to confirm the synthesis efficiency compared to the pre-melted charge. The final product, a shiny hemispherical alloy button with a radius of  $\sim 24$  mm, is shown in **Figure 3.1**.



**Figure 3.1:** Vacuum arc-melted hemispherical button of the alloy.

### **3.4: Phase Identification via XRD**

Phase formation in the as-cast polished samples was analyzed using a Malvern Panalytical Empyrean X-ray diffraction (XRD) system, utilizing Cu-K $\alpha$  radiation with a wavelength of 1.54 Å. The diffraction patterns were obtained within a  $2\theta$  range of 20° to 90°, employing a step size of 0.0131°. The voltage and current settings were maintained at 30 kV and 45 mA, respectively. For peak analysis, X'Pert HighScore Plus software was utilized.

### **3.5: Microstructural Characterization via SEM**

The microstructural analysis of as-cast eutectic alloys started with polishing using SiC papers at grit sizes of 400, 800, 1500, 2000 and 2500, achieving a mirror finish with an alumina powder (M301) of up to 0.3  $\mu\text{m}$ . Subsequently, the samples underwent ultrasonic cleaning for 5 minutes in an acetone-filled beaker, which was repeated two to three times for each specimen to ensure thorough cleanliness.

After preparation, followed by etching using a 10% perchloric acid and 90% ethanol solution, the samples were examined with a JEOL JSM-7610F-Plus scanning electron microscopy (SEM) coupled with energy-dispersive x-ray spectra (EDS, Oxford Instruments, X-Max<sup>N</sup>) for elemental analysis. This facilitated the elemental mapping and spot and line analyses to detail the phase distribution and elemental compositions of the alloy. Compositional analysis was performed via SEM-EDS across 3 to 10 areas per sample at 100x magnification. The backscattered electron imaging was executed at a working distance of 15 mm and 15 and 20 kV. The average lamellar spacing in eutectic colonies was measured using *ImageJ* software, leveraging multiple SEM images to obtain accurate measurements.

### 3.6: Thermal Analysis via DSC

For thermal analysis, a precise section was cut from the edge of the as-cast button using an IsoMet™ low-speed precision cutter with a 4-inch diamond blade. The sample was then polished to remove residual oil, followed by ultrasonic cleaning in acetone. Afterwards, the samples underwent ultrasonic cleaning in acetone and were dried using hot air to ensure no moisture or contaminants could affect the thermal analysis.

The PerkinElmer simultaneous thermal analyzer 8000 was utilized to observe phase transformations during heating or prolonged exposure to high temperatures in the as-cast samples. To ensure the reliability and accuracy of the data, baseline scans were conducted before the actual measurements. The samples, weighing between 40 and 60 mg, were subjected to heating from room temperature up to 1430 °C at a controlled rate of 20 K/min. This process was carried out in an alumina crucible, with a nitrogen flow maintained at 20 mL/min.

### 3.7: Assessing the Strength-Ductility Synergy via Tensile Testing

All tensile and compression tests were carried out using an Instron-5967 universal testing machine (UTM), operating at a strain rate of  $1 \times 10^{-3} \text{ s}^{-1}$  at room temperature. For the compression tests, cylindrical samples with a 1.5 aspect ratio were sectioned from the as-cast button. Tensile testing samples, consisting of two specimens with a 10 mm gauge length (shown in **Figure 3.2**), were prepared from the as-cast buttons using wire electrical discharge machining and then polished with 2000 grit SiC sandpaper for a smooth finish.

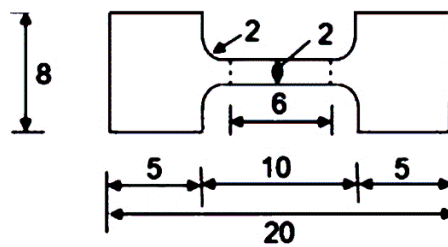


**Figure 3.2:** Tensile test specimen (all dimensions are in mm).

The tensile engineering strain was measured through the digital image correlation (DIC) method. This involved applying a speckle pattern of black dots against a white background on the sample surfaces, enabling precise strain tracking. Imaging during the tests was conducted using a high-speed camera system operated with VIC-Snap 9 software, ensuring high-quality capture of the deformation process. Subsequent post-image analysis was done with VIC-2D software from Correlated Solutions Inc., USA. This software analysis utilized a subset size of



31 and a step size of 7 pixels, optimizing strain measurement accuracy. The data on strain and displacement collected from this analysis facilitated the generation of detailed engineering stress-strain curves.



## CHAPTER 4

# The Empirical Approach via Binary Eutectic Clusters

### 4.1: Introduction

The challenge of identifying optimal eutectic compositions in multi-principal element alloys (EMPEAs) can be readily understood from the existing strategies limitations as discussed in Chapter 2. This challenge is underscored by the decade-long gap between the report of the first multi-principal element alloy (MPEA) and the emergence of the first eutectic MPEA, AlCoCrFeNi<sub>2.1</sub>, in 2014, which was developed without a comprehensive design strategy [3,17]. He *et al.* [29] later introduced the first systematic design approach for EMPEAs in 2015 using pseudo-binary phase diagrams via the CALPHAD (CALculation of PHase Diagrams) method in the Co-Cr-Fe-Ni-Nb system. However, this approach did not classify the AlCoCrFeNi<sub>2.1</sub> composition as eutectic since no single element forms binary eutectics with all other elements in this system [29]. Despite numerous strategies proposed over the years for the development of new EMPEAs, the focus has predominantly been on varying elements in the Al-Co-Cr-Fe-Ni-M alloy system, where M represents elements such as Zr, Ta, Nb and Hf, or on approaches that heavily rely on CALPHAD calculations. Although CALPHAD is a robust computational tool for predicting phase behaviour, its effectiveness is limited by the need for extensive databases and access to commercial software, such as *Thermo-Calc* or *JMatPro*, which restricts its availability. Furthermore, the databases commonly used in CALPHAD are predominantly developed for Ni-based superalloys, steels, Ti-alloys and Al-alloys, leading to potential inaccuracies in compositions rich in elements outside these systems. A promising alternative to CALPHAD-based design strategies is the binary eutectic clusters model, a well-established approach in the study of bulk metallic glasses (BMGs) [87]. In BMGs, a deep eutectic alloy is known to facilitate the formation of a glassy phase with ease [88]. The deep eutectic theory posits that binary alloys positioned at the deep eutectic point exhibit characteristics such as low liquidus temperature, relatively high glass transition temperature, difficult crystal nucleation and high glass forming ability (GFA). Numerous investigations have validated the empirical binary eutectic cluster model proposed by Lu *et al.* [87] for metallic glasses and this model has been successfully employed to predict novel bulk metallic glass compositions in systems such as Zr-Cu-Ni-Al [89–91]. The binary eutectic clusters model, originally formulated for BMGs, offers a viable alternative strategy for EMPEA design, focusing on identifying binary eutectic compositions, especially deep eutectics. This approach

provides a pathway for discovering new eutectic compositions without dependence on computational methods or restricted-access tools. As the development of EMPEAs progresses, expanding beyond CALPHAD methodologies will be crucial in exploring a broader range of compositions and developing novel alloys with tailored properties.

This chapter explores the potential of the binary eutectic clusters model, leveraging the enthalpy of mixing, to manually identify eutectic compositions in multi-principal element alloys (MPEAs). The approach begins by identifying potential eutectic forming MPEA systems and then narrows down to specific eutectic compositions. The proposed empirical approach is validated through the design and development of a lightweight eutectic MPEA in the Al-Ti-V-Cr-Zr system. Additionally, this chapter outlines the limitations of the presented empirical approach and suggests directions for future research.

## 4.2: Exploring Eutectic Forming MPEA Systems

Determining eutectic compositions in MPEAs requires first identifying such alloy systems that exhibit eutectic reactions. This preliminary step is necessary as it takes into account that not all MPEA systems may exhibit eutectic reactions, reflecting the variability seen in binary alloy systems. For instance, binary elemental pairs such as Cu-Ni, which are isomorphous and Co-Ni and Fe-Cr, known for their single-phase disordered solid solutions of face-centred cubic (FCC) and body-centred cubic (BCC) structures, typically do not show eutectic reactions. In contrast, systems like Ni-Nb and Al-Zr are known for their pronounced eutectic reactions. Similarly, in MPEAs, alloys such as Co-Cr-Fe-Ni, usually reported to form single-phase disordered solid solutions of FCC, do not exhibit eutectic compositions until refractory elements like Nb, Zr, Hf, or Ta are added, inducing eutectic reactions [64]. Therefore, accurately identifying which MPEA systems can exhibit eutectic reactions is crucial, saving significant time and energy in determining their eutectic compositions.

Upon analyzing the alloy compositions documented by Lu *et al.* [18], as shown in **Table 4.1**, three key observations emerge from the dataset comprising 47 alloys with 17 distinct elements (Al, Co, Cr, Cu, Fe, Hf, Mn, Mo, Nb, Ni, Pd, Sc, Ta, Ti, V, W and Zr). Nickel (Ni) stands out for its prevalence, appearing in 46 of these compositions. Furthermore, the most frequent occurrences of binary combinations, Ni-Fe and Ni-Co, in 44 and 36 alloy systems, respectively, are to be noted. The minimal enthalpy of mixing values between Co and Ni (-0.20 kJ/mol) and Fe and Ni (-1.60 kJ/mol) (**Table 4.2**) suggests a propensity for forming single-phase solid solutions with face-centred cubic (FCC) structures. This observation essentially

underscores that there is at least one binary pair in the reviewed eutectic systems represented in **Table 4.1** that has an enthalpy of mixing near zero.

**Table 4.1:** Reported MPEAs with fully eutectic microstructure.

SN	Alloy Composition	Alloy System	Year	Density (g/cc)	Ref.
01	Al <sub>23.81</sub> Cr <sub>23.81</sub> Fe <sub>23.81</sub> Mo <sub>4.76</sub> Ni <sub>23.81</sub>	Al-Cr-Fe-Mo-Ni	2013	6.48	[6]
02	Al <sub>25</sub> Cr <sub>25</sub> Fe <sub>25</sub> Ni <sub>25</sub>	Al-Cr-Fe-Ni	2013	6.25	[6]
03	Al <sub>19.35</sub> Cr <sub>16.13</sub> Cu <sub>16.13</sub> Fe <sub>16.13</sub> Ni <sub>32.26</sub>	Al-Cr-Cu-Fe-Ni	2013	6.89	[7]
04	Al <sub>16.39</sub> Co <sub>16.39</sub> Cr <sub>16.39</sub> Fe <sub>16.39</sub> Ni <sub>34.43</sub>	Al-Co-Cr-Fe-Ni	2014	7.07	[1]
05	Co <sub>19.05</sub> Fe <sub>19.05</sub> Nb <sub>14.29</sub> Ni <sub>38.1</sub> V <sub>9.52</sub>	Co-Fe-Nb-Ni-V	2015	8.33	[8]
06	Co <sub>18.52</sub> Fe <sub>18.52</sub> Mo <sub>18.52</sub> Ni <sub>25.93</sub> V <sub>18.52</sub>	Co-Fe-Mo-Ni-V	2015	8.41	[9]
07	Co <sub>21.74</sub> Fe <sub>21.74</sub> Mo <sub>13.04</sub> Ni <sub>21.74</sub> V <sub>21.74</sub>	Co-Fe-Mo-Ni-V	2015	8.18	[9]
08	Al <sub>15</sub> Fe <sub>30</sub> Mn <sub>35</sub> Ni <sub>20</sub>	Al-Fe-Mn-Ni	2015	6.83	[10]
09	Al <sub>23.53</sub> Cr <sub>23.53</sub> Fe <sub>23.53</sub> Ni <sub>23.53</sub> Ti <sub>5.88</sub>	Al-Cr-Fe-Ni-Ti	2015	6.12	[11]
10	Co <sub>21.51</sub> Cr <sub>21.51</sub> Fe <sub>21.51</sub> Nb <sub>13.98</sub> Ni <sub>21.51</sub>	Co-Cr-Fe-Nb-Ni	2016	8.25	[29]
11	Co <sub>30.3</sub> Mo <sub>12.12</sub> Ni <sub>30.3</sub> V <sub>15.15</sub> W <sub>12.2</sub>	Co-Mo-Ni-V-W	2016	10.19	[47]
12	Al <sub>14.1</sub> Cr <sub>6</sub> Fe <sub>28.2</sub> Mn <sub>32.9</sub> Ni <sub>18.8</sub>	Al-Cr-Fe-Mn-Ni	2016	6.85	[98]
13	Al <sub>13</sub> Fe <sub>36</sub> Mn <sub>33</sub> Ni <sub>18</sub>	Al-Fe-Mn-Ni	2016	6.95	[99]
14	Al <sub>30.23</sub> Cr <sub>23.26</sub> Fe <sub>23.26</sub> Ni <sub>23.26</sub>	Al-Cr-Fe-Ni	2017	5.94	[42]
15	Co <sub>17.42</sub> Cr <sub>17.42</sub> Fe <sub>17.42</sub> Nb <sub>12.89</sub> Ni <sub>34.84</sub>	Co-Cr-Fe-Nb-Ni	2017	8.36	[63]
16	Co <sub>17.7</sub> Cr <sub>17.7</sub> Fe <sub>17.7</sub> Ni <sub>35.4</sub> Ta <sub>11.5</sub>	Co-Cr-Fe-Ni-Ta	2017	9.71	[63]
17	Co <sub>17.86</sub> Cr <sub>17.86</sub> Fe <sub>17.86</sub> Ni <sub>35.71</sub> Zr <sub>10.71</sub>	Co-Cr-Fe-Ni-Zr	2017	7.96	[63]
18	Co <sub>18.02</sub> Cr <sub>18.02</sub> Fe <sub>18.02</sub> Hf <sub>9.91</sub> Ni <sub>36.04</sub>	Co-Cr-Fe-Hf-Ni	2017	9.20	[63]
19	Co <sub>22.73</sub> Cr <sub>22.73</sub> Fe <sub>22.73</sub> Ni <sub>22.73</sub> Ta <sub>9.09</sub>	Co-Cr-Fe-Ni-Ta	2017	9.30	[64,100]
20	Al <sub>19</sub> Co <sub>20</sub> Fe <sub>20</sub> Ni <sub>41</sub>	Al-Co-Fe-Ni	2018	7.10	[101]
21	Co <sub>22.22</sub> Cr <sub>22.22</sub> Fe <sub>22.22</sub> Ni <sub>22.22</sub> Zr <sub>11.11</sub>	Co-Cr-Fe-Ni-Zr	2018	7.84	[102]
22	Co <sub>22.75</sub> Cr <sub>22.75</sub> Fe <sub>22.75</sub> Ni <sub>22.75</sub> Ta <sub>8.99</sub>	Co-Cr-Fe-Ni-Ta	2018	9.29	[103]
23	Nb <sub>25</sub> Sc <sub>25</sub> Ti <sub>25</sub> Zr <sub>25</sub>	Nb-Sc-Ti-Zr	2016	-	[48]
24	Co <sub>25</sub> Fe <sub>25</sub> Mn <sub>5</sub> Ni <sub>25</sub> Ti <sub>20</sub>	Co-Fe-Mn-Ni-Ti	2018	7.34	[104]
25	Co <sub>28.57</sub> Fe <sub>28.57</sub> Nb <sub>14.29</sub> Ni <sub>28.57</sub>	Co-Fe-Nb-Ni	2018	8.54	[105]
26	Al <sub>19.3</sub> Co <sub>15</sub> Cr <sub>15</sub> Ni <sub>50.7</sub>	Al-Co-Cr-Ni	2018	7.01	[106]
27	Co <sub>20.83</sub> Cr <sub>20.83</sub> Fe <sub>20.83</sub> Mo <sub>16.67</sub> Ni <sub>20.83</sub>	Co-Cr-Fe-Mo-Ni	2018	8.60	[107]
28	Co <sub>14.71</sub> Cr <sub>14.71</sub> Fe <sub>14.71</sub> Mn <sub>14.71</sub> Ni <sub>14.71</sub> Pd <sub>26.47</sub>	Co-Cr-Fe-Mn-Ni-Pd	2018	-	[108]
29	Co <sub>15.62</sub> Cr <sub>15.62</sub> Fe <sub>15.62</sub> Mn <sub>15.62</sub> Ni <sub>15.62</sub> Pd <sub>21.87</sub>	Co-Cr-Fe-Mn-Ni-Pd	2018	-	[108]
30	Co <sub>16.67</sub> Cr <sub>16.67</sub> Fe <sub>16.67</sub> Mn <sub>16.67</sub> Ni <sub>16.67</sub> Pd <sub>16.67</sub>	Co-Cr-Fe-Mn-Ni-Pd	2018	-	[108]
31	Co <sub>17.86</sub> Cr <sub>17.86</sub> Fe <sub>17.86</sub> Mn <sub>17.86</sub> Ni <sub>17.86</sub> Pd <sub>10.71</sub>	Co-Cr-Fe-Mn-Ni-Pd	2018	-	[108]
32	Co <sub>22.47</sub> Cr <sub>22.47</sub> Fe <sub>22.47</sub> Nb <sub>10.11</sub> Ni <sub>22.47</sub>	Co-Cr-Fe-Nb-Ni	2018	8.23	[44,64]
33	Co <sub>21.98</sub> Cr <sub>21.98</sub> Fe <sub>21.98</sub> Ni <sub>21.98</sub> Zr <sub>12.09</sub>	Co-Cr-Fe-Ni-Zr	2018	7.81	[64]
34	Co <sub>22.73</sub> Cr <sub>22.73</sub> Fe <sub>22.73</sub> Hf <sub>9.09</sub> Ni <sub>22.73</sub>	Co-Cr-Fe-Hf-Ni	2018	9.00	[64]
35	Al <sub>17</sub> Co <sub>14.3</sub> Cr <sub>14.3</sub> Fe <sub>14.3</sub> Ni <sub>40.1</sub>	Al-Co-Cr-Fe-Ni	2018	7.08	[74]
36	Al <sub>17</sub> Co <sub>14.3</sub> Cr <sub>14.3</sub> Fe <sub>28.6</sub> Ni <sub>25.8</sub>	Al-Co-Cr-Fe-Ni	2018	6.95	[74]
37	Al <sub>17</sub> Co <sub>28.6</sub> Cr <sub>14.3</sub> Fe <sub>14.3</sub> Ni <sub>25.8</sub>	Al-Co-Cr-Fe-Ni	2018	7.07	[74]
38	Al <sub>16</sub> Cr <sub>20</sub> Fe <sub>20</sub> Ni <sub>44</sub>	Al-Cr-Fe-Ni	2019	7.02	[46]
39	Al <sub>18</sub> Co <sub>30</sub> Cr <sub>10</sub> Fe <sub>10</sub> Ni <sub>30</sub> W <sub>2</sub>	Al-Co-Cr-Fe-Ni-W	2019	7.38	[109]
40	Al <sub>18</sub> Co <sub>30</sub> Cr <sub>10</sub> Fe <sub>10</sub> Ni <sub>32</sub>	Al-Co-Cr-Fe-Ni	2019	7.10	[110]
41	Al <sub>16</sub> Co <sub>41</sub> Cr <sub>15</sub> Fe <sub>10</sub> Ni <sub>18</sub>	Al-Co-Cr-Fe-Ni	2019	7.17	[111]

42	Co <sub>10</sub> Cr <sub>15</sub> Fe <sub>25.3</sub> Mn <sub>5</sub> Nb <sub>9.7</sub> Ni <sub>25</sub> V <sub>10</sub>	Co-Cr-Fe-Mn-Nb-Ni-V	2019	7.94	[112]
43	Al <sub>16.67</sub> Co <sub>10</sub> Cr <sub>16.67</sub> Fe <sub>16.67</sub> Ni <sub>40</sub>	Al-Co-Cr-Fe-Ni	2020	7.04	[113]
44	Al <sub>16.67</sub> Co <sub>13.33</sub> Cr <sub>16.67</sub> Fe <sub>16.67</sub> Ni <sub>36.67</sub>	Al-Co-Cr-Fe-Ni	2020	7.04	[113]
45	Al <sub>16.67</sub> Co <sub>3.33</sub> Cr <sub>16.67</sub> Fe <sub>16.67</sub> Ni <sub>46.67</sub>	Al-Co-Cr-Fe-Ni	2020	7.05	[113]
46	Al <sub>16.67</sub> Co <sub>6.67</sub> Cr <sub>16.67</sub> Fe <sub>16.67</sub> Ni <sub>43.33</sub>	Al-Co-Cr-Fe-Ni	2020	7.05	[113]
47	Al <sub>16.67</sub> Cr <sub>16.67</sub> Fe <sub>16.67</sub> Ni <sub>50</sub>	Al-Cr-Fe-Ni	2020	7.05	[113]

**Table 4.2:** Enthalpy of mixing for selected binary alloy pairs (kJ/mol).

	Al	Ti	V	Cr	Fe	Co	Ni	Zr	Nb	Hf	Ta
Al	0										
Ti	-29.5	0									
V	-16.3	-1.7	0								
Cr	-9.9	-7.5	-2	0							
Fe	-11.1	-16.8	-7.1	-1.5	0						
Co	-18.8	-28.3	-14	-4.5	-0.6	0					
Ni	-22.3	-34.5	-18	-6.7	-1.6	-0.2	0				
Zr	-43.7	-0.2	-3.7	-12	-24.6	-40.3	-48.4	0			
Nb	-18.2	2	-1	-7.2	-15.7	-24.5	-29.9	3.9	0		
Hf	-38.5	0.2	-2.2	-9.3	-20.5	-34.7	-42.2	-0.2	3.9	0	
Ta	-19.2	1.4	-1	-6.7	-15	-23.9	-29.2	2.7	0	2.9	0

Also, it is important to note that at least one element among Al, Zr, Ta, Hf and Nb is present in most of these systems. These elements show a high negative enthalpy of mixing and significant atomic size difference with binary pairs like Ni-Co or Ni-Fe, which play a crucial role in inducing eutectic reactions. Thus, by drawing parallels with the eutectic reaction in Ni-Nb systems, it is hypothesized that the (Co-Ni)-Nb system might exhibit similar eutectic reactions. This hypothesis opens up the possibility of adding compatible elements to the initial binary pair single phase. For example, introducing Fe to this (Co-Ni)-Nb system could develop a (Co-Fe-Ni)-Nb system, while incorporating Cr could further lead to a (Co-Cr-Fe-Ni)-Nb system, underscoring the identification of new alloy systems with EMPEAs.

These fundamental observations have resulted in the formulation of a generalized method for the identification of EMPEA systems of the A-B-C-D-E type. The approach starts by selecting a binary elemental pair (A-B) characterized by a disordered single-phase solid solution, thus exhibiting an enthalpy of mixing close to zero. Following this, an element, C, can be introduced into the system, acting as a solid solution splitter for A-B due to its high negative mixing enthalpy and atomic size difference relative to A-B. Subsequently, additional elements like D or E can be added to the system as long as they can dissolve into the A-B solid solution. This hypothesis, aligned with the experimentally reported alloy systems in **Table 4.3**, is defined by the following three criteria:

- *Criteria 1 – Initial Binary Pair Selection (A-B):* The enthalpy of mixing between elements A and B should be close to zero, ideally ranging between -2 to 0 kJ/mol, essential for forming a stable single-phase disordered solid solution.
- *Criteria 2 – Solid Solution Splitter (C):* Element 'C' must display a significant enthalpy of mixing and an atomic size difference with elements A and B, sufficient to destabilize the A-B solid solution. Therefore, it should fulfil the criteria of  $-8.8 \text{ kJ/mol} \leq \Delta H_{mix}^{A-B-C} \leq 4 \text{ kJ/mol}$  and  $\delta \geq 2.77\%$ .
- *Criteria 3 – Additional Elements (D/E/F):* Additional elements like D, E, or F can be incorporated if they are soluble with A and/or B. These elements should meet specific parameters:  $-2 \text{ kJ/mol} \geq \Delta H_{mix}^{A-D} \geq 0 \text{ kJ/mol}$  and  $\delta \leq 2.77\%$ .

**Table 4.3:** Reported EMPEA systems complying with proposed criteria.

SN	A-B	C	D/E/F/G	Alloy System	Ref.
01	Co-Ni	Al	Cr	Al-Co-Cr-Ni	[106]
02	Co-Ni	Al	Fe	Al-Co-Fe-Ni	[101]
03	Fe-Ni	Al	Cr	Al-Cr-Fe-Ni	[42,46,92,113]
04	Fe-Ni	Al	Mn	Al-Fe-Mn-Ni	[96,99]
05	Co-Ni	Nb	Fe	Co-Fe-Nb-Ni	[105]
06	Co-Ni	Al	Cr, Fe	Al-Co-Cr-Fe-Ni	[17,74,110,111,113]
07	Fe-Ni	Al	Cr, Mn	Al-Cr-Fe-Mn-Ni	[98]
08	Co-Ni	Hf	Cr, Fe	Co-Cr-Fe-Hf-Ni	[63,64]
09	Co-Ni	Mo	Cr, Fe	Co-Cr-Fe-Mo-Ni	[107]
10	Co-Ni	Nb	Cr, Fe	Co-Cr-Fe-Nb-Ni	[29,63,64,100]
11	Co-Ni	Ta	Cr, Fe	Co-Cr-Fe-Ni-Ta	[44,63,64,103]
12	Co-Ni	Zr	Fe, Cr	Co-Cr-Fe-Ni-Zr	[63,64,102]
13	Co-Ni	Mo	Fe, V	Co-Fe-Mo-Ni-V	[95]
14	Co-Ni	Nb	Fe, V	Co-Fe-Nb-Ni-V	[94]
15	Co-Ni	Nb	Cr, Fe, Mn, V	Co-Cr-Fe-Mn-Nb-Ni-V	[112]

### 4.3: Identifying Eutectic Compositions in MPEAs

After confirming the presence of a eutectic reaction in an A-B-C-D-E type alloy system, the subsequent step is to determine its eutectic composition precisely. This process begins by identifying the element that forms the greatest number of binary eutectics with the other elements in the system, designating it as the EFE. While ideally, the EFE would form binary eutectics with all other elements, this is not a strict requirement. Illustrated in **Figure 4.1**, the system includes EFE-E1-E2-E3, where EFE is the eutectic forming element and ET1, ET2 and ET3 denote the eutectics formed between EFE and the remaining elements (E1, E2, E3, etc.). Consequently, as reported by Lu *et al.* [87], the most stable eutectic clusters are those formed

between the EFE and each of the other elements, resulting in a eutectic cluster formula of  $x(\text{EFE-E1}) + y(\text{EFE-E2}) + z(\text{EFE-E3})$ , where  $x$ ,  $y$  and  $z$  are constants that sum to 1.

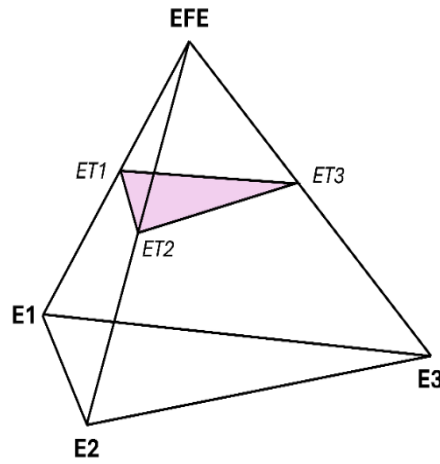


**Figure 4.1:** Composition diagram of the EFE-E1-E2-E3 alloy system.

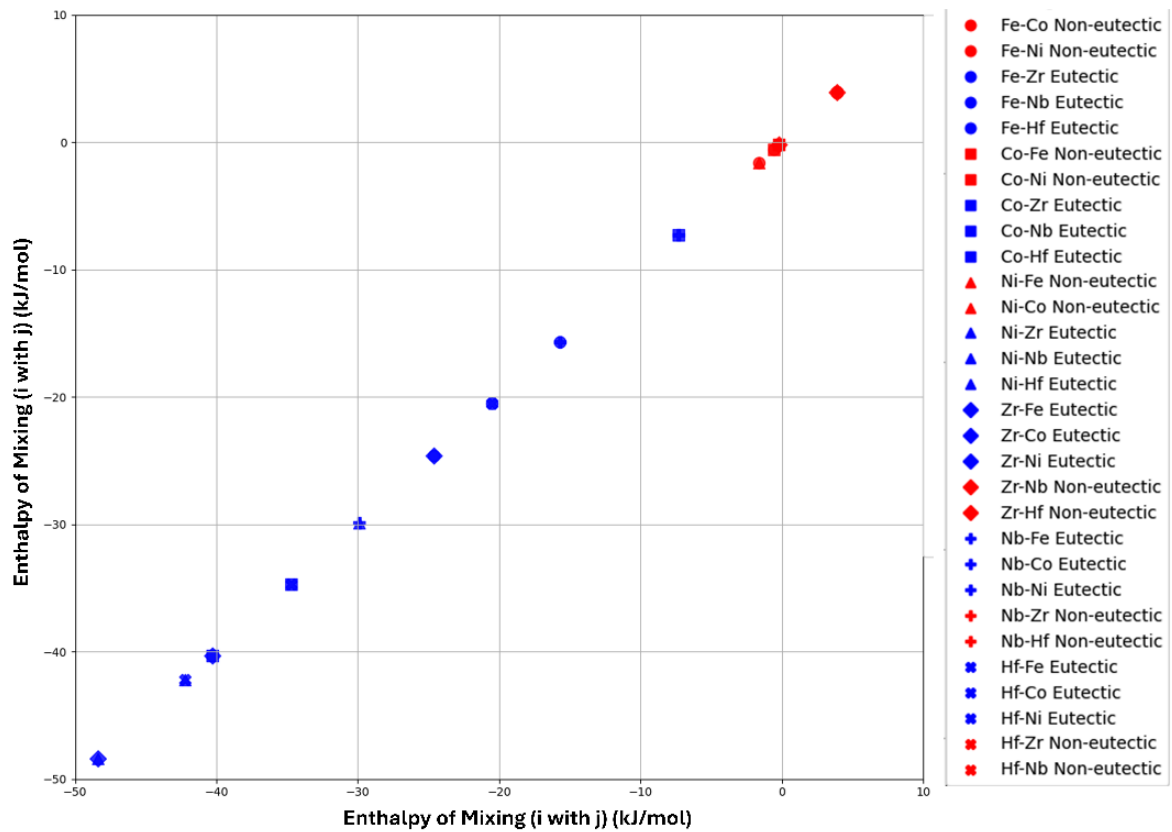


**Figure 4.2:** Comparative analysis of eutectic forming ability against the enthalpy of mixing for Fe, Co, Ni, Zr, Hf and Nb.



This formation reflects the eutectic as thermodynamically a failed compound, with a binary elemental pair eutectic forming ability often resembling its compound forming ability, as shown in **Figure 4.2**. The preference for clustering between the EFE and E1, E2 and E3 suggests a reduced likelihood for the formation of E1-E2, E2-E3 and E1-E3 solid solutions. Therefore, under the assumption that eutectic compositions are influenced by the enthalpy of mixing, the constants  $x$ ,  $y$  and  $z$  can be deduced based on the enthalpy of mixing ratios:  $x(\Delta H_{\text{mix}} \text{ of EFE-E1}) = y(\Delta H_{\text{mix}} \text{ of EFE-E2}) = z(\Delta H_{\text{mix}} \text{ of EFE-E3})$  [87].

#### 4.3.1: Designing a Lightweight EMPEA

The empirical approach detailed above for identifying EMPEA systems and their compositions was applied in an attempt to design a lightweight EMPEA. Therefore, elements with low densities were considered to identify the optimal EMPEA system. According to Criteria 1, presented in Section 4.2, the initial step involved selecting a binary pair forming a single-phase solid solution.

**Table 4.4:** Densities of selected elements.

Element	Al	Ti	V	Cr	Fe	Co	Ni	Zr	Nb	Mo	Hf	Ta
$\rho$ (g/cc)	2.7	4.5	6	7.15	7.87	8.86	8.91	6.52	8.57	10.2	13.3	16.4

Despite aluminium (Al) being the lightest element in **Table 4.4**, it does not form an isomorphous or single-phase disordered solid solution (BCC or FCC) with other elements, as corroborated by data in **Table 4.2** showing Al mixing enthalpy with other elements not approaching zero. Consequently, titanium with a density of approximately 4.5 g/cc, followed by vanadium with a density of about 6.1 g/cc, were selected, leading to the identification of Ti-V as the initial binary pair with a mixing enthalpy of -1.70 kJ/mol. This selection adheres to Criterion 1, with the Ti-V pair mixing enthalpy within the -2.0 to 0.0 kJ/mol range. Following the subsequent criterion, Al, with a 2.7 g/cc density, was chosen as the 'C' type element, acting as a solid solution splitter, with the Al-Ti-V system mixing enthalpy at -32.62 kJ/mol and size difference ( $\delta$ ) exceeding 2.77%, thereby meeting Step 2 requirements. In Step 3, zirconium and chromium, with densities of 6.49 g/cc and 7.2 g/cc, respectively, were to be incorporated for their isomorphous compatibility with Ti and V at elevated temperatures, respectively, leading to the expectation that the Al-Ti-V-Cr-Zr system would form a eutectic and result in a lightweight MPEA system. Notably, Zr was identified as the EFE in this system, having the

most number of binary eutectics with other elements, Al, V and Cr, along with a significantly negative enthalpy, represented in **Table 4.2**.

Thus, by applying the design methodology detailed in Section 4.3, as suggested by Lu *et al.* [87], which focuses on the proportional mixing of binary eutectics, the eutectic composition in Al-Ti-V-Cr-Zr was identified as follows:

- Step 1 entails pinpointing the eutectic compositions in the three binary systems involving Zr (Zr-Al, Zr-V, Zr-Cr). The determined eutectic compositions are  $Zr_{69}Al_{31}$ ,  $Zr_{57}V_{43}$  and  $Zr_{76}Cr_{24}$ .
- Step 2 involves calculating the mixing enthalpies for the Zr-Al, Zr-V and Zr-Cr binary equiatomic alloys, which are -43.7, -3.7 and -12 kJ/mol, respectively, represented in **Table 4.2**.

$$\begin{aligned}
 & \text{Eutectic composition of Zr-(Al-V-Cr):} \\
 & = x(Zr_{69}Al_{31}) + y(Zr_{57}V_{43}) + z(Zr_{76}Cr_{24}) \\
 & x(\Delta H_{\text{mix}} \text{ of Zr - Al}) = y(\Delta H_{\text{mix}} \text{ of Zr - V}) = z(\Delta H_{\text{mix}} \text{ of Zr - Cr}) \\
 & x(43.7) = y(3.7) \text{ and } y(3.7) = z(12), \text{ where } x + y + z = 1 \\
 & y = \frac{x \times 43.7}{3.7} \\
 & x + \frac{x \times 43.7}{3.7} + \frac{\left(\frac{x \times 43.7}{3.7}\right) \times 3.7}{12} = 1 \\
 & x + 11.81x + \frac{43.7x}{12} = 1 \\
 & x + 11.81x + 3.64x = 1 \\
 & x = \frac{1}{16.45} = 0.061 \\
 & y = \frac{x \times 43.7}{3.7} = \frac{0.061 \times 43.7}{3.7} = 0.720 \\
 & z = 1 - x - y = 1 - 0.061 - 0.720 = 0.219 \\
 & = 0.061(Zr_{69}Al_{31}) + 0.720(Zr_{57}V_{43}) + 0.219(Zr_{76}Cr_{24}) \\
 & = Zr_{4.21}Al_{1.89} + Zr_{41.04}V_{30.96} + Zr_{16.64}Cr_{5.26} \\
 & = Zr_{61.89}Al_{1.89}V_{30.96}Cr_{5.26}
 \end{aligned}$$

In this Zr-Al-V-Cr alloy system, it is crucial to note that the EFE represents 61.89 atomic percent, with the specific composition  $Al_{1.86}V_{30.96}Cr_{5.26}$  leading to the formation of a single-phase body-centred cubic (BCC) structure [114]. It is to be noted here that the study conducted by Jiang *et al.* [64] identified a notable eutectic composition,

$\text{Co}_{21.525}\text{Cr}_{22}\text{Fe}_{22.35}\text{Ni}_{21.125}\text{Nb}_{13}$ , with Nb acting as the EFE. This study demonstrated that after identifying the eutectic composition  $\text{Co}_{21.525}\text{Cr}_{22}\text{Fe}_{22.35}\text{Ni}_{21.125}\text{Nb}_{13}$ , treating the equiatomic Co-Cr-Fe-Ni as a single phase while maintaining a 13% atomic percentage of Nb enables the attainment of a binary eutectic composition  $(\text{CoCrFeNi})_{87}\text{Nb}_{13}$ . Pursuing this approach, Jiang *et al.* [64] discovered three other novel eutectic compositions:  $\text{CoCrFeNiTa}_{0.47}$ ,  $\text{CoCrFeNiZr}_{0.5}$  and  $\text{CoCrFeNiHf}_{0.49}$ , each experimentally verified with slight modifications. The precise determination of the EFE composition emerges as a pivotal factor, indicating that adjustments to the single phase without altering its crystal structure are likely to maintain the alloy position within the eutectic range. Consequently, the  $(\text{Zr})_{61.89}(\text{AlVCr})_{38.1}$  composition is also expected to demonstrate the eutectic reaction.

Further to be noted, the study by Qui *et al.* [115] observed that the equiatomic AlTiVCr alloy forms a single-phase body-centred cubic (BCC) structure. Considering that Titanium shares a similar atomic radius (~205 pm) and crystal structure (BCC) with vanadium and Cr is isomorphous with V, particularly at elevated temperatures, the alloy  $(\text{Zr})_{61.9}(\text{AlTiVCr})_{38.1}$  is expected to undergo a eutectic reaction. This expectation is bolstered by the ability to integrate Ti into the alloy system without altering its single-phase BCC structure, simultaneously reducing the alloy density by 0.34 g/cc, thereby offering a cost-effective alternative to vanadium. Consequently, incorporating Ti leads to the formation of a lightweight EMPEA,  $(\text{Zr})_{61.9}(\text{AlTiVCr})_{38.1}$ , with each element (Al, Ti, V, Cr) being equiatomic and contributing 9.53 to the alloy composition. In line with the expectation, the theoretical density of the designed alloy is noted to be 6.05 g/cc only, which is significantly lower than most of the reported alloys in **Table 4.1**.

#### 4.3.2: Experimental Verification of the Designed Composition

To further validate the empirical approach described earlier, the designed alloy  $\text{Zr}_{61.9}(\text{AlTiVCr})_{38.1}$  was synthesized using vacuum arc melting. SEM-EDS analysis conducted at ten different locations, as detailed in **Table 4.5**, confirmed the uniform chemical composition of the cast alloy, which is a characteristic feature of eutectic alloys. Moreover, the micrograph displayed in **Figure 4.3** showcases a two-phase eutectic structure featuring a tiger-skin pattern. This type of eutectic morphology, with its combination of intermetallic phases, bears a resemblance to findings reported by Rios *et al.* [116] in the Nb-Al-Ni system. It is noteworthy that the observed eutectic structure is multi-scale, a likely consequence of varying solidification rates during melting. Chemical composition results from EDS analysis, presented in **Table 4.6**

and performed at eight different locations, highlighted two distinct phases: a "black region" and a "white region."

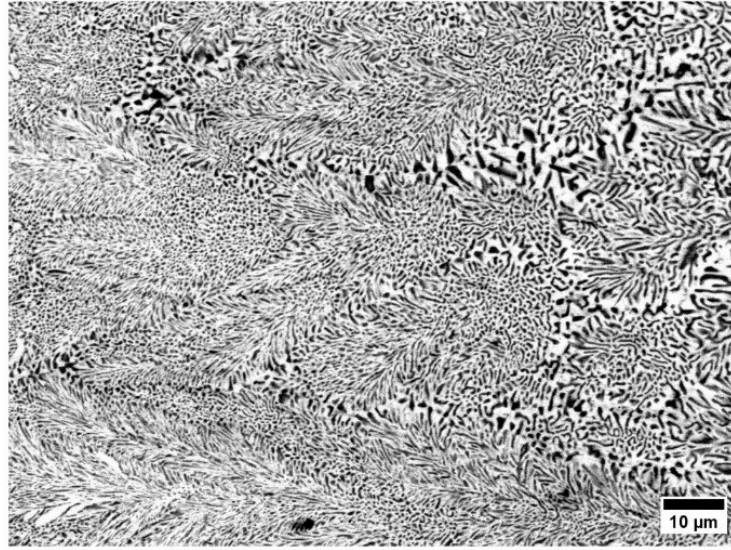


**Figure 4.3:** SEM image (BSE mode) of the as-cast alloy.

In the black region, Zirconium dominates with a concentration of  $53.28 \pm 2.49$  at.%, accompanied by significant levels of Cr, V, Al and Ti, indicating a composition rich in Cr and V. Conversely, the white region features a higher Zirconium concentration of  $66.10 \pm 1.54$  at.%, with a distinct variation in the concentrations of other elements compared to the black region. The predominance of Cr and V in the black phase over the white phase suggests it could be a Zr-(Cr-V) type Laves phase. Elemental mapping, as shown in **Figure 4.4**, corroborates this by clearly illustrating the enrichment of Cr and V in the black phase and their depletion in the white phase.

**Table 4.5:** EDS of the full area at 100x from ten different locations.

Element	Al	Ti	V	Cr	Zr
Nominal	9.58	9.58	9.58	9.58	61.7
Actual	$9.37 \pm 0.42$	$9.75 \pm 0.32$	$9.20 \pm 0.30$	$9.1 \pm 1.27$	$62.6 \pm 0.94$

**Table 4.6:** Point EDS at 8 different locations showing phase compositions.

Element	Al	Ti	V	Cr	Zr
Black Region (#4)	$9.22 \pm 0.10$	$8.52 \pm 0.25$	$11.54 \pm 0.91$	$17.12 \pm 1.46$	$53.28 \pm 2.49$
White Region (#4)	$9.0 \pm 0.17$	$10.50 \pm 0.35$	$06.22 \pm 0.80$	$9.08 \pm 1.27$	$66.10 \pm 1.54$

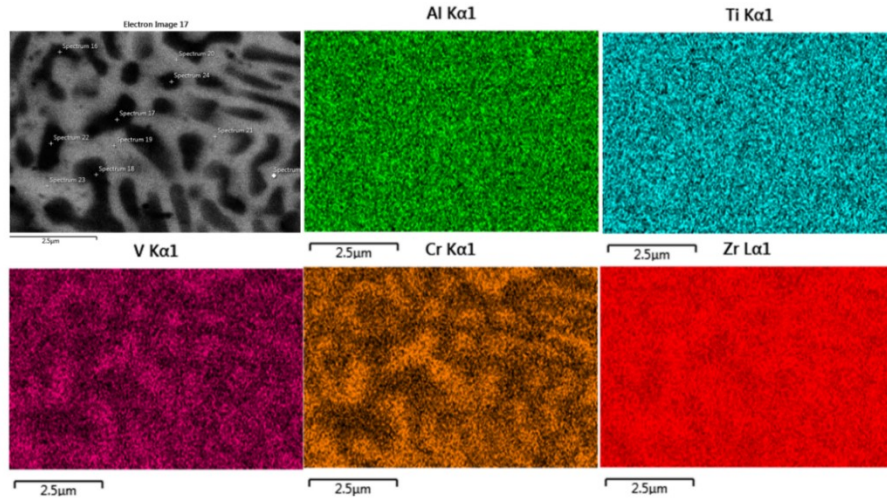


**Figure 4.4:** Elemental mapping of the as-cast alloy depicting the distribution of elements.

The X-ray diffraction in **Figure 4.5** confirms the dual-phase nature, comprising C14 hexagonal Laves and C15 cubic Laves phases. The C14 Laves, with lattice parameters  $a=b=3.15 \text{ \AA}$ ,  $c=5.03 \text{ \AA}$  and angles  $\alpha=\beta=90^\circ$ ,  $\gamma=120^\circ$ , falls under space group  $P63/mmc$  (No. 194), chemically represented as  $Ti_{0.3}Zr_{0.7}$  type. The C15 Laves, cubic with  $a=b=c=7.42 \text{ \AA}$  and angles at  $90^\circ$ , belong to the  $Fd-3m$  space group (No. 227), identified as  $Zr_2V$  type. This dual-phase eutectic nature is further supported by a sharp endothermic peak in the DSC curve in **Figure 4.6**. The compressive stress-strain curve at room temperature shows complete brittle failure with a compressive strength of 780 MPa, indicating the influence of the two Laves phases.

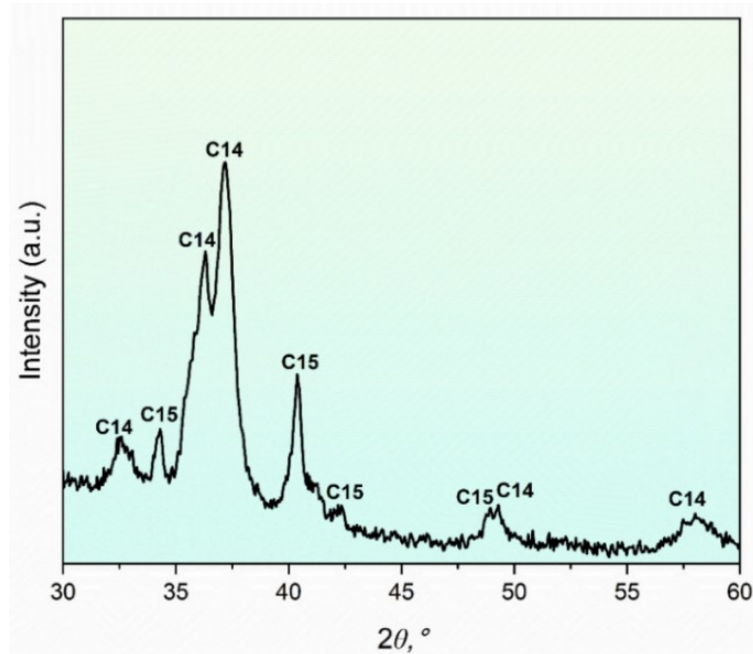


**Figure 4.5:** XRD diffractogram of the as-cast alloy.

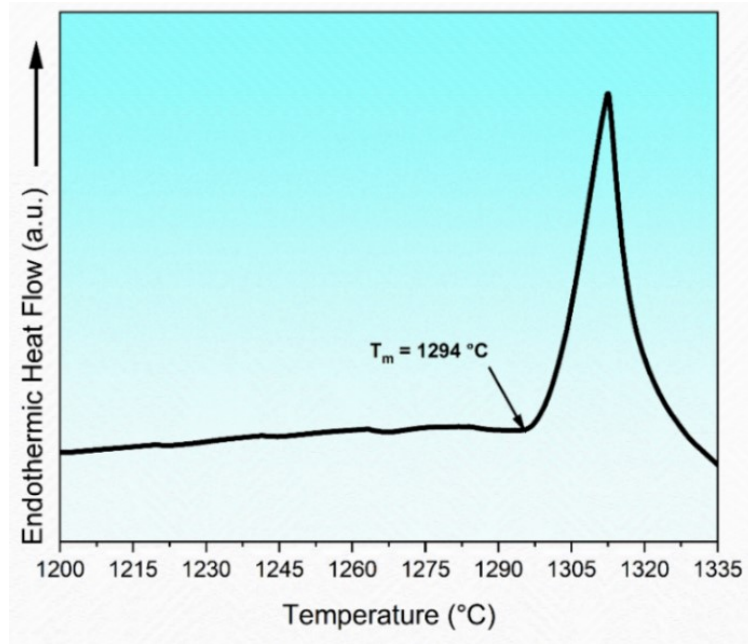


**Figure 4.6:** DSC curve of the as-cast alloy.

#### 4.4: Empirical Approach Extended to Other Systems

The empirical approach presented above can be extended to alloy systems like Co-Fe-Ni-M (where M represents Nb, Zr and Ta), aiding in the identification of novel eutectic compositions. Leveraging the extensive documentation of Co, Fe and Ni in existing databases, this methodology enables cross-validation with CALPHAD predictions (with the *TCHEA* database), as presented below.

##### 4.4.1: Co-Fe-Ni-Ta System

The Co-Fe-Ni-Ta system exemplifies the A-B-C-D methodology presented earlier, with Co-Ni (as A-B) identified as a single-phase solid solution characterized by an FCC structure. Ta, serving as the 'C' element, acts as a solid solution splitter, while Fe is added as an additional component. Within this system, Ta emerges as the EFE, capable of forming binary eutectics with Co, Fe and Ni at atomic percentages of 12, 65.2 and 38, respectively. The mixing enthalpy values for these binary pairs are noted as -23.9, -15 and -29.2 kJ/mol, respectively, as presented in **Table 4.2**. This analysis leads to the identification of the eutectic composition involving Ta and the Co-Fe-Ni combination, as follows:

$$\begin{aligned}
 &\text{Eutectic composition of Ta-(Co-Fe-Ni):} \\
 &= x(\text{Ta}_{12}\text{Co}_{88}) + y(\text{Ta}_{65.2}\text{Fe}_{34.8}) + z(\text{Ta}_{38}\text{Ni}_{62}) \\
 &x(\Delta H_{\text{mix}} \text{ of Ta - Co}) = y(\Delta H_{\text{mix}} \text{ of Ta - Fe}) = z(\Delta H_{\text{mix}} \text{ of Ta - Ni})
 \end{aligned}$$

$x(23.9) = y(15)$  and  $y(15) = z(29.2)$ , where  $x + y + z = 1$

$$y = \frac{x \times 23.9}{15}$$

$$x + \frac{x \times 23.9}{15} + \frac{\left(\frac{x \times 23.9}{15}\right) \times 15}{29.2} = 1$$

$$x + 1.59x + \frac{23.9x}{29.2} = 1$$

$$x + 1.59x + 0.82x = 1$$

$$x = \frac{1}{3.41} = 0.293$$

$$y = \frac{x \times 23.9}{15} = \frac{0.293 \times 23.9}{15} = 0.467$$

$$z = 1 - x - y = 1 - 0.293 - 0.467 = 0.240$$

$$= 0.293(\text{Ta}_{12}\text{Co}_{88}) + 0.467(\text{Ta}_{65.2}\text{Fe}_{34.8}) + 0.240(\text{Ta}_{38}\text{Ni}_{62})$$

$$= \text{Ta}_{3.52}\text{Co}_{25.78} + \text{Ta}_{30.45}\text{Fe}_{16.25} + \text{Ta}_{9.12}\text{Ni}_{14.88}$$

$$= \text{Ta}_{43.09}\text{Co}_{25.78}\text{Fe}_{16.25}\text{Ni}_{14.88}$$

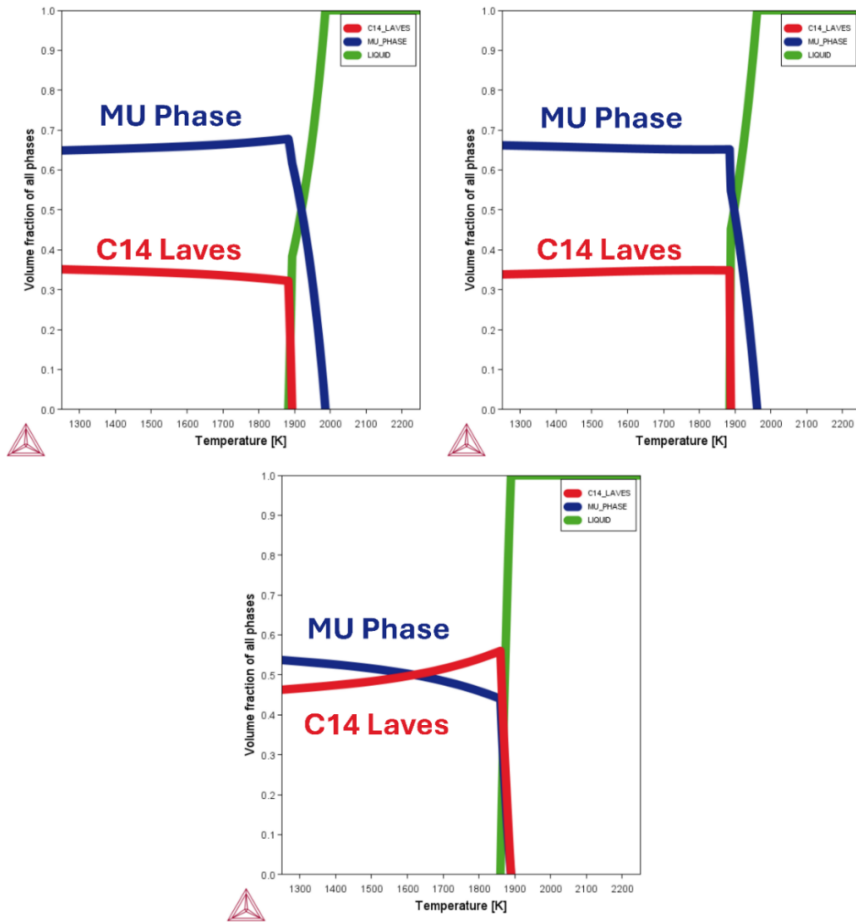


**Figure 4.7:** Phase evolution plots of

(a)  $\text{Ta}_{43.09}\text{Co}_{25.78}\text{Fe}_{16.25}\text{Ni}_{14.88}$ , (b)  $\text{Ta}_{43.09}(\text{CoFeNi})_{56.91}$  and (c)  $\text{Ta}_{43.09}(\text{CoCrFeNi})_{56.91}$ .

Thus, the eutectic composition identified as  $\text{Ta}_{43.09}\text{Co}_{25.78}\text{Fe}_{16.25}\text{Ni}_{14.88}$  exemplifies Tantalum as the eutectic forming element, constituting 43.09 atomic percent of the composition. Co, Fe and Ni complement this by forming a single-phase FCC structure. As a result, the composition  $\text{Ta}_{43.09}(\text{CoFeNi})_{56.91}$  is also expected to demonstrate the eutectic reaction. This prediction is underpinned by phase fraction plots generated through CALPHAD simulations using the *TCHEA* database, confirming the near-eutectic nature of both  $\text{Ta}_{43.09}\text{Co}_{25.78}\text{Fe}_{16.25}\text{Ni}_{14.88}$  and  $\text{Ta}_{43.09}(\text{CoFeNi})_{56.91}$ , as illustrated in **Figures 4.8(a) and 4.8(b)**, respectively. Further exploration reveals that the inclusion of Cr into the FCC of Co-Fe-Ni also leads to a eutectic composition, specifically  $\text{Ta}_{43.09}(\text{CoCrFeNi})_{56.91}$ , as shown in **Figure 4.7(c)**. Similar eutectic reactions can be verified in the following sections in Co-Fe-Ni-M (M = Nb and Zr) systems. Also, it is to be noted that the CALPHAD predicted, calculated below, eutectic composition  $(\text{CoCrFeNi})_{90.5}\text{Zr}_{9.5}$  experimentally verified to be eutectic by Vrtnik *et al.* [102] and the  $(\text{CoCrFeNi})_{88.75}\text{Nb}_{11.25}$  by An *et al.* [117].

#### 4.4.2: Co-Fe-Ni-Zr System

Eutectic composition of Zr-(Co-Fe-Nb):

$$\begin{aligned}
 &= x(\text{Zr}_{9.6}\text{Co}_{90.4}) + y(\text{Zr}_{9.8}\text{Fe}_{90.2}) + z(\text{Zr}_{8.8}\text{Ni}_{91.2}) \\
 x(\Delta H_{\text{mix}} \text{ of Zr - Co}) &= y(\Delta H_{\text{mix}} \text{ of Zr - Fe}) = z(\Delta H_{\text{mix}} \text{ of Zr - Ni}) \\
 x(40.3) &= y(24.6) \text{ and } y(24.6) = z(48.4), \text{ where } x + y + z = 1 \\
 y &= \frac{x \times 40.3}{24.6} \\
 x + \frac{x \times 40.3}{24.6} + \frac{\left(\frac{x \times 40.3}{24.6}\right) \times 24.6}{48.4} &= 1 \\
 x + 1.64x + \frac{40.3x}{48.4} &= 1 \\
 x + 1.64x + 0.83x &= 1 \\
 x &= \frac{1}{3.47} = 0.288 \\
 y &= \frac{x \times 40.3}{24.6} = \frac{0.288 \times 40.3}{24.6} = 0.472 \\
 z &= 1 - x - y = 1 - 0.288 - 0.472 = 0.240 \\
 &= 0.288(\text{Zr}_{9.6}\text{Co}_{90.4}) + 0.472(\text{Zr}_{9.8}\text{Fe}_{90.2}) + 0.240(\text{Zr}_{8.8}\text{Ni}_{91.2}) \\
 &= \text{Zr}_{2.76}\text{Co}_{26.04} + \text{Zr}_{4.63}\text{Fe}_{42.57} + \text{Zr}_{2.11}\text{Ni}_{21.89} \\
 &= \text{Zr}_{9.5}\text{Co}_{26.04}\text{Fe}_{42.57}\text{Ni}_{21.89}
 \end{aligned}$$



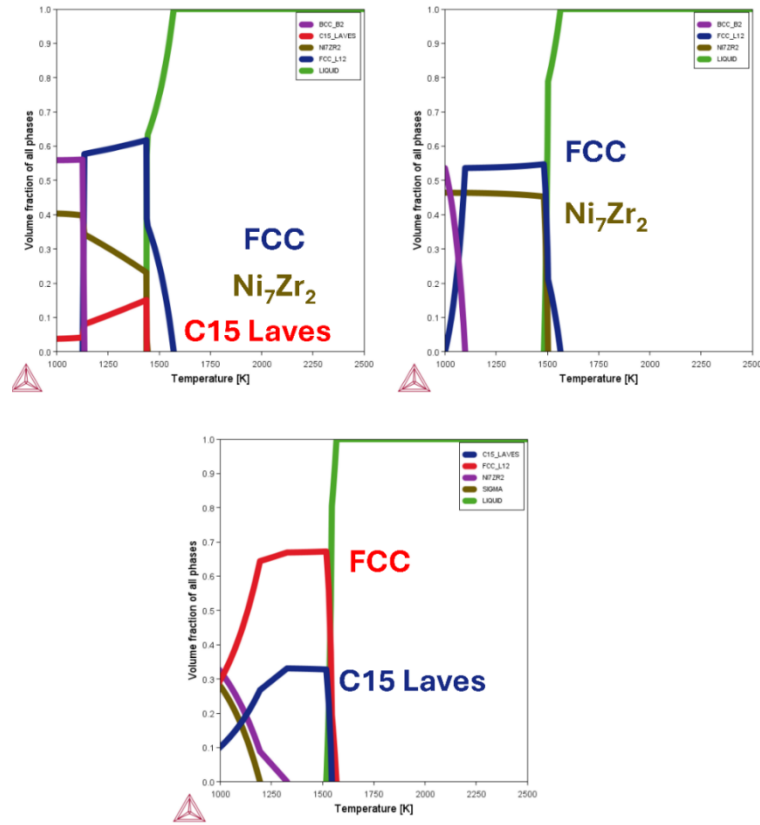


**Figure 4.8:** Phase evolution plots of (a)  $\text{Zr}_{9.5}\text{Co}_{26.04}\text{Fe}_{42.57}\text{Ni}_{21.89}$ , (b)  $\text{Zr}_{9.5}(\text{CoFeNi})_{90.5}$  and (c)  $\text{Zr}_{9.5}(\text{CoCrFeNi})_{90.5}$ .

#### 4.4.3: Co-Fe-Ni-Nb System

Eutectic composition of Nb-(Co-Fe-Ni):

$$= x(\text{Nb}_{13}\text{Co}_{87}) + y(\text{Nb}_{8.2}\text{Fe}_{91.8}) + z(\text{Nb}_{14.9}\text{Ni}_{85.1})$$

$$x(\Delta H_{\text{mix}} \text{ of Nb - Co}) = y(\Delta H_{\text{mix}} \text{ of Nb - Fe}) = z(\Delta H_{\text{mix}} \text{ of Nb - Ni})$$

$$x(24.5) = y(15.7) \text{ and } y(15.7) = z(29.9), \text{ where } x + y + z = 1$$

$$y = \frac{x \times 24.5}{15.7}$$

$$x + \frac{x \times 24.5}{15.7} + \frac{\left(\frac{x \times 24.5}{15.7}\right) \times 15.7}{29.9} = 1$$

$$x + 1.56x + \frac{24.5x}{29.9} = 1$$

$$x + 1.56x + 0.82x = 1$$

$$x = \frac{1}{3.38} = 0.296$$

$$y = \frac{x \times 24.5}{15.7} = \frac{0.296 \times 24.5}{15.7} = 0.462$$

$$\begin{aligned}
z &= 1 - x - y = 1 - 0.296 - 0.462 = 0.242 \\
&= 0.296(\text{Nb}_{13}\text{Co}_{87}) + 0.462(\text{Nb}_{8.2}\text{Fe}_{91.8}) + 0.242(\text{Nb}_{14.9}\text{Ni}_{85.1}) \\
&= \text{Nb}_{3.85}\text{Co}_{25.75} + \text{Nb}_{3.79}\text{Fe}_{42.41} + \text{Nb}_{3.61}\text{Ni}_{20.59} \\
&= \text{Nb}_{11.25}\text{Co}_{25.75}\text{Fe}_{42.41}\text{Ni}_{20.59}
\end{aligned}$$

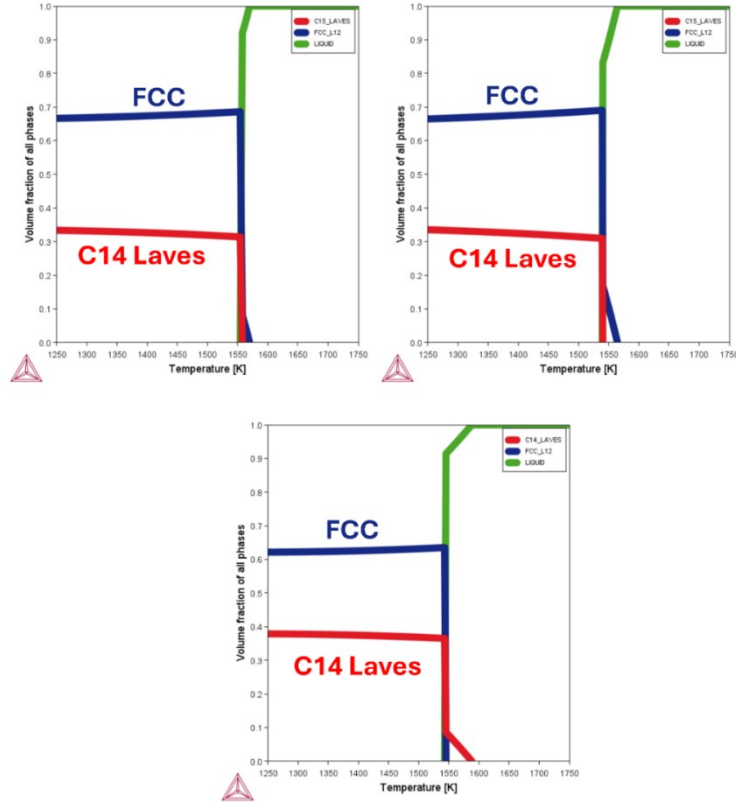


**Figure 4.9:** Phase evolution plots of (a)  $\text{Nb}_{11.25}\text{Co}_{25.75}\text{Fe}_{42.41}\text{Ni}_{20.59}$ , (b)  $\text{Nb}_{11.25}(\text{CoFeNi})_{88.75}$  and (c)  $\text{Nb}_{11.25}(\text{CoCrFeNi})_{88.75}$ .

#### 4.5: Limitations of the Empirical Approach

The proposed empirical approach for identifying novel eutectic compositions in MPEAs has certain limitations, some of which are mentioned below:

- *Lack of specific phase identification:* The method does not indicate which eutectic phases will form. When targeting a specific combination of FCC and BCC phases for structural applications, the approach does not provide a clear direction to achieve this combination.
- *Reliance only on the enthalpy of mixing:* The present method can only predict based on the enthalpy of mixing, which could be improved by considering the other phase formation materials descriptors such as VEC, atomic size difference, etc.
- *Uncertainty around the pro-eutectic phase:* The approach does not offer information about the pro-eutectic phase, raising uncertainty about whether the designed composition will

form an exact eutectic structure or possibly be just hypo-eutectic or hyper-eutectic composition.

- *Focus on single two-phase eutectics*: Primarily, the method identifies compositions leading to two-phase pseudo-eutectics and does not address the identification of higher-order eutectics or the search for an invariant eutectic.
- *Binary eutectic selection*: This empirical approach lacks clarity on the rationale for selecting specific types of binary eutectics, contributing to eutectic formation in MPEAs and does not address the effect of considering other eutectics present in the binary elemental pairs.
- *Constrained EFE*: The strategy focused on the need for the EFE to form binary eutectics, which may exclude potentially valuable compositions, especially in systems like Co-Cr-Fe-Ni. For instance, Fe-based (Fe as an EFE) compositions may be overlooked due to Fe-limited binary eutectic interactions with other elements in these kinds of systems.

## 4.6: Summary

In summary, Chapter 4 presents an advancement in designing new EMPEAs through the introduction and application of an empirical approach based on binary eutectic clusters. The following conclusions can be deduced from Chapter 4:

- *Empirical Approach Validation*: The Chapter validates an empirical approach leveraging binary eutectic clusters for the development of novel EMPEAs, showcasing a viable alternative to *Thermo-Calc* software. This is significant as it circumvents the need for extensive, often inaccessible databases and software.
- *Experimental Validation*: The practical application of this methodology to the Al-Ti-V-Cr-Zr lightweight EMPEA system and subsequent experimental validation of its eutectic composition underscore the effectiveness of the approach proposed.
- *Versatility and Extension to Other Systems*: The methodology extension to additional systems like Co-Fe-Ni-M (M = Nb, Zr and Ta) illustrates its versatility and broad applicability.



## CHAPTER 5

# The Single Phase Plus EFE Design Strategy via CALPHAD

### 5.1: Introduction

Building upon the empirical methodology detailed in Chapter 4, the present chapter introduces a new design strategy that advances existing methods for identifying eutectic compositions in multi-principal element alloys (MPEAs). The proposed methodology, termed "Single Phase Plus EFE," employs pseudo-binary phase diagrams and Scheil solidification simulations via CALPHAD to efficiently identify potential EMPEAs. The accuracy of this approach is validated by comparing its predictions with reported EMPEAs. The practical applicability of this strategy is demonstrated by designing and developing the first eutectic composition in the Al-Fe-Ti-V-Zr system. Furthermore, the efficacy of this methodology is underscored by the successful development of a novel EMPEA in the Al-Co-Fe-Ni system, which exhibited an exceptional strength-ductility synergy, surpassing most as-cast EMPEAs. The chapter concludes with a discussion of the limitations inherent to the proposed design approach.

### 5.2: A Brief Note on the CALPHAD Aid

Identifying optimal compositions that exhibit simple solid solution phases in MPEA systems itself presents a significant challenge. This challenge is primarily due to the extensive compositional design space of these alloy systems, further compounded by the absence of comprehensive phase diagrams. Consequently, the gravity of this challenge intensifies when identifying eutectic compositions, given that eutectic reactions are contingent upon precise elemental combinations and temperatures. Given these complexities, depending exclusively on experimental investigations to identify eutectic compositions proves exceedingly laborious and time-consuming. A prime example of this complexity is identifying a unique sunflower-like eutectic structure in the Al-Cr-Cu-Fe-Ni system in 2013, as mentioned in Chapter 2. This discovery resulted from experimental investigations across 12 alloys in the  $\text{Al}_x\text{CrCuFeNi}_2$  series, with  $x$  ranging from 0.2 to 2.5 [39,93]. This example highlights the extensive experimental efforts required to accurately identify a single eutectic composition in MPEA systems. Further, these experiments become increasingly comprehensive and laborious when adjustments across multiple elements are necessary to pinpoint these eutectic compositions.

In addressing these challenges, the CALPHAD methodology becomes an essential toolbox for the design of new MPEAs. As noted in Chapter 2, the efficacy of the CALPHAD approach in elucidating complex phase diagrams and predicting phase formation tendencies in MPEAs is well-documented in the literature. The CALPHAD methodology involves four key steps to developing material systems databases: (i) collection of experimental data for properties to be modelled, such as phase equilibria and thermochemical data; (ii) critical assessment and selection of an appropriate model based on this data; (iii) optimisation of the model-free parameters; and (iv) incorporation of the optimised parameters into a library of models for various systems. Following the library update, validations against experimental data for higher-order systems are carried out. The primary function of CALPHAD is to determine the phase composition that minimises the total Gibbs energy of the system. This capability enables the precise determination of thermodynamic properties of alloys across a broad compositional spectrum, making CALPHAD an indispensable tool in the accelerated design and development of new EMPEAs.

### 5.3: The "Single Phase Plus EFE" Design Strategy

#### 5.3.1: The Three-Step Design Criteria

The simplistic and accelerated "Single Phase Plus EFE" design methodology for identifying EMPEAs unfolds in three key steps, as follows:

- (Step-1): Identify a multi-component single phase as a starting point, either a solid solution or an ordered/disordered phase.
- (Step-2): Identify a suitable EFE capable of forming an intermetallic compound and a binary eutectic with one of the elements (preferably with an enthalpy of mixing  $< -15 \text{ kJ/mol}$ ) present in the single phase considered in the first step.
- (Step-3): A pseudo-binary phase diagram, obtained through the single phase-EFE in the console mode of *Thermo-Calc* or through Scheil solidification or phase evolution simulations in the graphical interface, will reveal the eutectic in the alloy system.

#### 5.3.2: Reported Alloys Complying with the Single Phase Plus EFE Strategy

**Table 5.1** presents various reported EMPEAs across different alloy systems, demonstrating significant agreement with the proposed design strategy. Notably, most existing design strategies do not specifically identify AlCoCrFeNi<sub>2.1</sub>, the first reported and extensively studied MPEA with a eutectic concept in the Al-Co-Cr-Fe-Ni system, as a potential eutectic

composition [17]. Utilizing the proposed methodology, the  $\text{AlCoCrFeNi}_{2.1}$  ( $\text{Al}_{16.39}\text{Co}_{16.39}\text{Cr}_{16.39}\text{Fe}_{16.39}\text{Ni}_{34.44}$ ) alloy is examined as a case study. Initially, consistent with the first step of the 'Single Phase Plus EFE' methodology, the  $\text{AlCoCrFe}$  alloy is identified as exhibiting a single-phase BCC structure [118]. In the subsequent step, Ni is identified as an EFE based on its capacity to form a binary eutectic and an ordered compound (B2) with aluminium (Al) at a 75 atomic percentage of Ni concentration, with a mixing enthalpy of -22.30 kJ/mol. The eutectic composition is then determined through Scheil solidification simulation, as depicted in **Figure 5.1(a)** and by examining a pseudo-binary phase diagram of  $\text{AlCoCrFe-Ni}$ , as shown in **Figure 5.1(b)**. This analysis promptly reveals the eutectic composition as  $\text{Al}_{16.39}\text{Co}_{16.39}\text{Cr}_{16.39}\text{Fe}_{16.39}\text{Ni}_{34.44}$  at 1605.92 K.

**Table 5.1:** Validation of the reported EMPEAs of different alloy systems of fully eutectic structure with the proposed "single phase plus EFE" design philosophy.

SN	Year Reported	Reported Composition of EMPEA	Single Phase	EFE	Ref
01	2013	$\text{Al}_{23.81}\text{Cr}_{23.81}\text{Fe}_{23.81}\text{Ni}_{23.81}\text{Mo}_{4.76}$	$\text{AlCrFeNi}$	Mo	[92]
02	2014	$\text{Al}_{16.39}\text{Co}_{16.39}\text{Cr}_{16.39}\text{Fe}_{16.39}\text{Ni}_{34.44}$	$\text{AlCoCrFe}$	Ni	[17]
03	2015	$\text{Co}_{21.74}\text{Fe}_{21.74}\text{Ni}_{21.74}\text{V}_{21.74}\text{Mo}_{13.04}$	$\text{CoFeNiV}$	Mo	[95]
04	2016	$\text{Co}_{21.51}\text{Cr}_{21.51}\text{Fe}_{21.51}\text{Nb}_{13.98}\text{Ni}_{21.51}$	$\text{CoCrFeNi}$	Nb	[29]
05	2017	$\text{Co}_{22.22}\text{Cr}_{22.22}\text{Fe}_{22.22}\text{Ni}_{22.22}\text{Zr}_{11.11}$	$\text{CoCrFeNi}$	Zr	[119]
06	2018	$\text{Co}_{22.73}\text{Cr}_{22.73}\text{Fe}_{22.73}\text{Hf}_{9.09}\text{Ni}_{22.73}$	$\text{CoCrFeNi}$	Hf	[64]
07	2018	$\text{Co}_{20.83}\text{Cr}_{20.83}\text{Fe}_{20.83}\text{Mo}_{16.67}\text{Ni}_{20.83}$	$\text{CoCrFeNi}$	Mo	[107]
08	2018	$\text{Co}_{28.57}\text{Fe}_{28.57}\text{Nb}_{14.29}\text{Ni}_{28.57}$	$\text{CoFeNi}$	Nb	[105]
09	2019	$\text{Al}_{14.89}\text{Co}_{21.28}\text{Cr}_{21.28}\text{Fe}_{21.28}\text{Ni}_{21.28}$	$\text{CoCrFeNi}$	Al	[120]
10	2019	$\text{Co}_{22.73}\text{Cr}_{22.73}\text{Fe}_{22.73}\text{Ni}_{22.73}\text{Ta}_{9.09}$	$\text{CoCrFeNi}$	Ta	[121]
11	2020	$\text{Co}_{20.25}\text{Cu}_{20.25}\text{Fe}_{20.25}\text{Ni}_{20.25}\text{Mo}_{19}$	$\text{CoCuFeNi}$	Mo	[122]
12	2020	$\text{Cr}_{21.05}\text{Nb}_{21.05}\text{Ti}_{21.05}\text{Zr}_{21.05}\text{Al}_{15.8}$	$\text{CrNbTiZr}$	Al	[123]
13	2021	$\text{Al}_{12.28}\text{Co}_{17.54}\text{Cr}_{17.54}\text{Fe}_{17.54}\text{Mn}_{17.54}\text{Ni}_{17.54}$	$\text{CoCrFeMnNi}$	Al	[124]
14	2021	$\text{Co}_{30.30}\text{Cr}_{30.30}\text{Hf}_{9.09}\text{Ni}_{30.30}$	$\text{CoCrNi}$	Hf	[125]
15	2021	$\text{Co}_{28.74}\text{Cr}_{28.74}\text{Nb}_{13.79}\text{Ni}_{28.74}$	$\text{CoCrNi}$	Nb	[126]
16	2021	$\text{Co}_{29.41}\text{Cr}_{29.41}\text{Ni}_{29.41}\text{Ta}_{11.76}$	$\text{CoCrNi}$	Ta	[58]
17	2021	$\text{Cr}_{30.21}\text{Fe}_{30.21}\text{Nb}_{9.37}\text{Ni}_{30.21}$	$\text{CrFeNi}$	Nb	[127]
18	2022	$\text{Al}_{20}\text{Cr}_{26.67}\text{Fe}_{26.67}\text{Ni}_{26.67}$	$\text{CrFeNi}$	Al	[128]
19	2023	$\text{Co}_{30}\text{Fe}_{30}\text{Ni}_{30}\text{Zr}_{10}$	$\text{CoFeNi}$	Zr	[129]

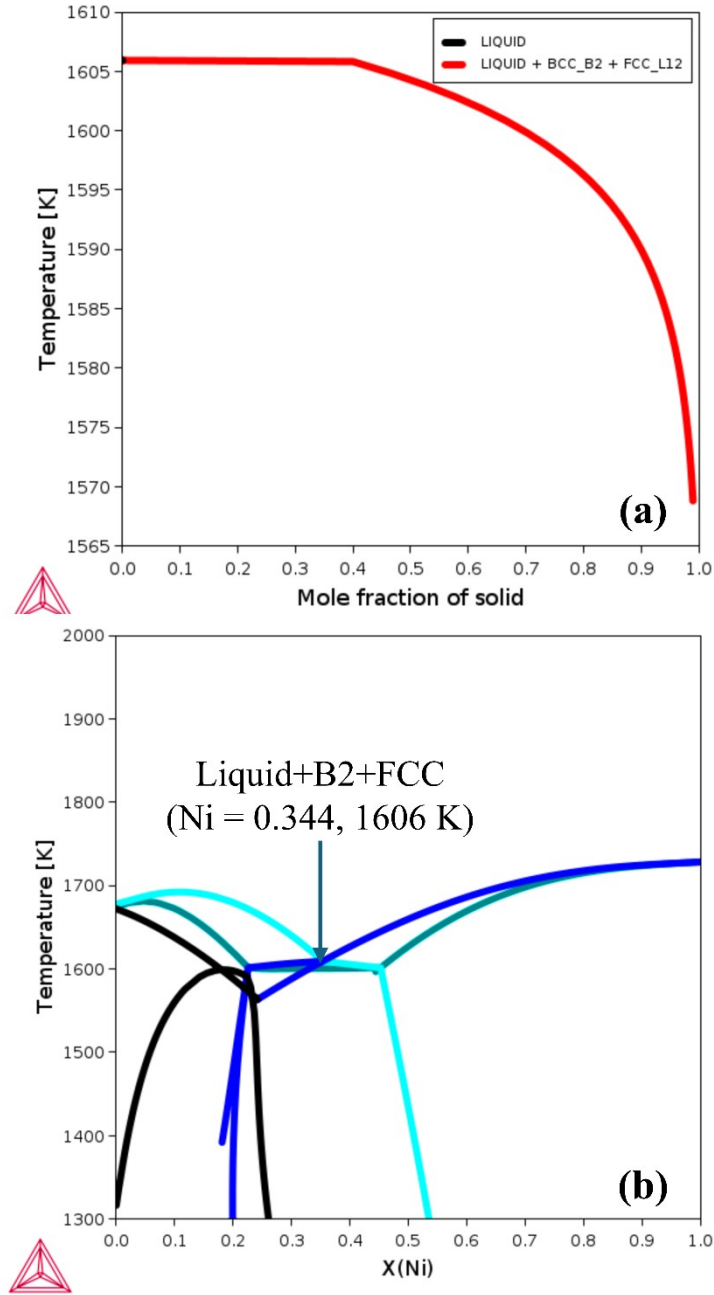


**Figure 5.1:** (a) Classic Scheil solidification simulation for  $\text{Al}_{16.39}\text{Co}_{16.39}\text{Cr}_{16.39}\text{Fe}_{16.39}\text{Ni}_{34.44}$ , (b) Pseudo-binary phase diagram of AlCoCrFe-Ni system.

### 5.3.3: Advantages over Existing Design Strategies

The proposed "Single Phase Plus EFE" design methodology offers several advantages over existing approaches for identifying eutectics in MPEAs. Primarily, it broadens the definition of an EFE. Initially proposed by He *et al.* [29] in 2015, the concept of an EFE was restricted to elements that form binary eutectics with every other element of the alloy system considered. However, the "Single Phase Plus EFE" approach refines this definition by suggesting that an EFE only needs to form a binary eutectic and a compound with one of the



elements in the system. Notably, most eutectic binary pairs exhibit relatively more negative enthalpies of mixing, promoting compound formation. For instance, He *et al.* [29] identified Nb as the EFE in the Co-Cr-Fe-Ni-Nb system because Nb forms binary eutectics with Co, Cr, Fe and Ni at approximately 14 atomic percentages. However, adhering strictly to this definition would hinder the identification of eutectics in the widely studied Al-Co-Cr-Fe-Ni system, as no single element forms binary eutectics with every other element in this system. For reference, the binary eutectic compositions of selected elements are provided in **Table 5.2**.

**Table 5.2:** Binary eutectics among selected elements (✓ = eutectic present)

	Al	Ti	V	Cr	Mn	Fe	Co	Ni	Cu	Zr	Nb	Mo	Hf	Ta	W
Al															
Ti															
V															
Cr															
Mn		✓													
Fe	✓	✓													
Co	✓	✓	✓	✓											
Ni	✓	✓	✓	✓											
Cu	✓	✓	✓												
Zr	✓		✓	✓	✓	✓	✓	✓	✓						
Nb	✓			✓	✓	✓	✓	✓							
Mo	✓						✓	✓		✓					
Hf	✓		✓	✓	✓	✓	✓	✓	✓						
Ta				✓		✓	✓	✓							
W							✓	✓		✓				✓	

In contrast, the "Single Phase Plus EFE" methodology identifies Ni as an EFE in the Al-Co-Cr-Fe-Ni system due to its ability to form both a binary eutectic and a compound with Al. Consequently, the composition AlCoCrFeNi<sub>2.1</sub> is identified as a eutectic composition, as detailed in Section 5.3.2. Another similar case demonstrating the utility of this refined definition is the Al-Cr-Nb-Ti-Zr system. This nuanced definition significantly enhances the methodology flexibility, enabling the identification of numerous new eutectic compositions in MPEA systems.

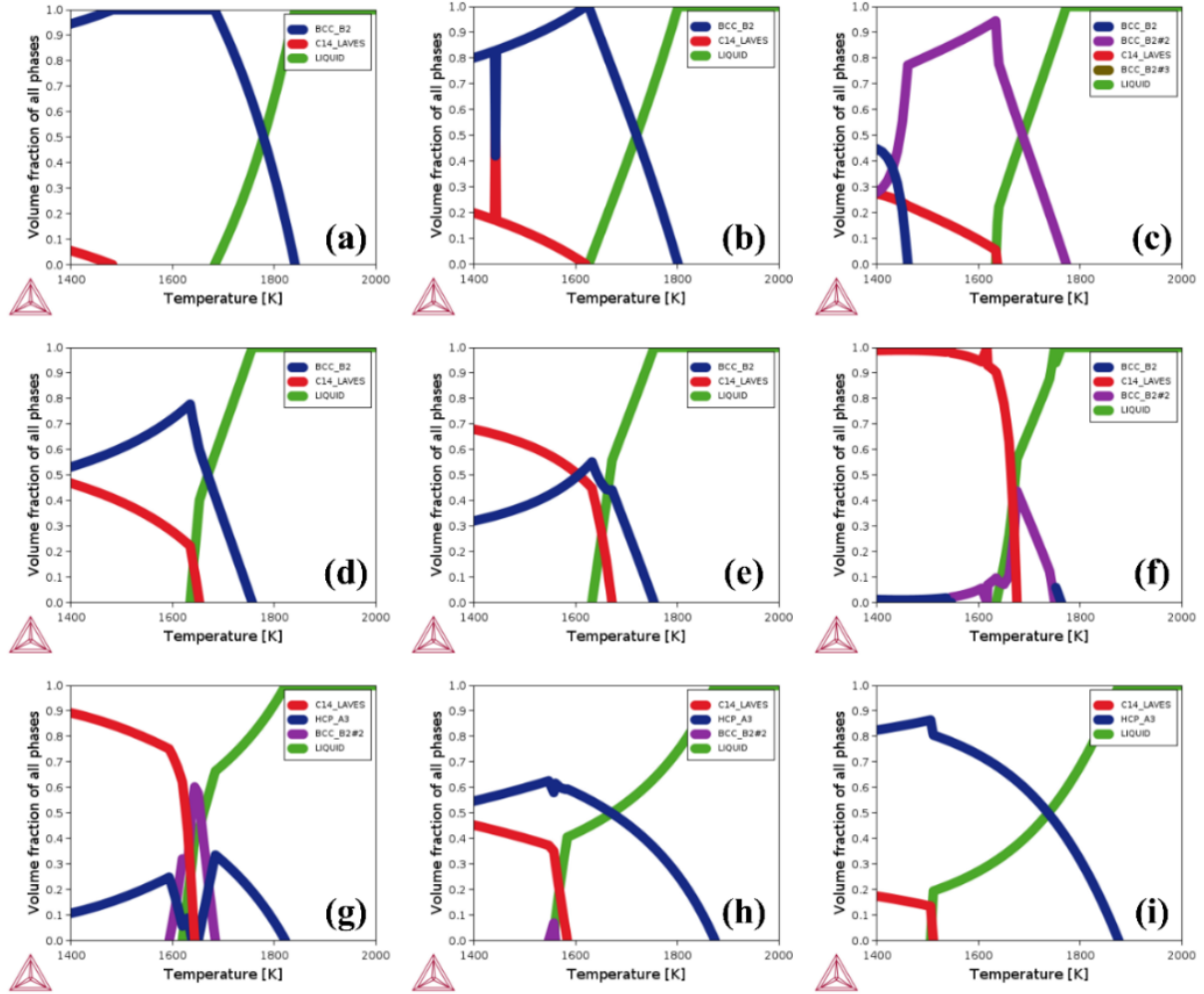


**Figure 5.2:** Phase evolution plots for AlTi-Fe<sub>x</sub>Cr<sub>x</sub> alloys: (a)  $x = 45$ , (b)  $x = 40$ , (c)  $x = 35$ , (d)  $x = 30$ , (e)  $x = 25$ , (f)  $x = 20$ , (g)  $x = 15$ , (h)  $x = 10$ , (i)  $x = 5$ .

Moreover, incorporating an EFE into a single phase simplifies the identification of eutectic formation reactions, offering a more efficient approach than methods that combine intermetallic phases with stable single phases [78]. For example, in the Al-Cr-Fe-Ti system, considering AlTi as a compound (with an enthalpy of mixing of -29.50 kJ/mol) and FeCr as a single-phase BCC structure (with an enthalpy of mixing of -1.50 kJ/mol), the simple combination of an intermetallic phase with a single phase, as depicted in **Figure 5.2**, does not reveal eutectic formation. However, using the proposed "Single Phase Plus EFE" methodology—by treating CrFeTi as a single-phase BCC structure (as shown in **Figure 5.3(a)**) and designating Al as the EFE—a distinct eutectic formation reaction is observed at Al<sub>12.01</sub>(CrFeTi)<sub>87.99</sub>, as illustrated in **Figure 5.3(b)** [130].

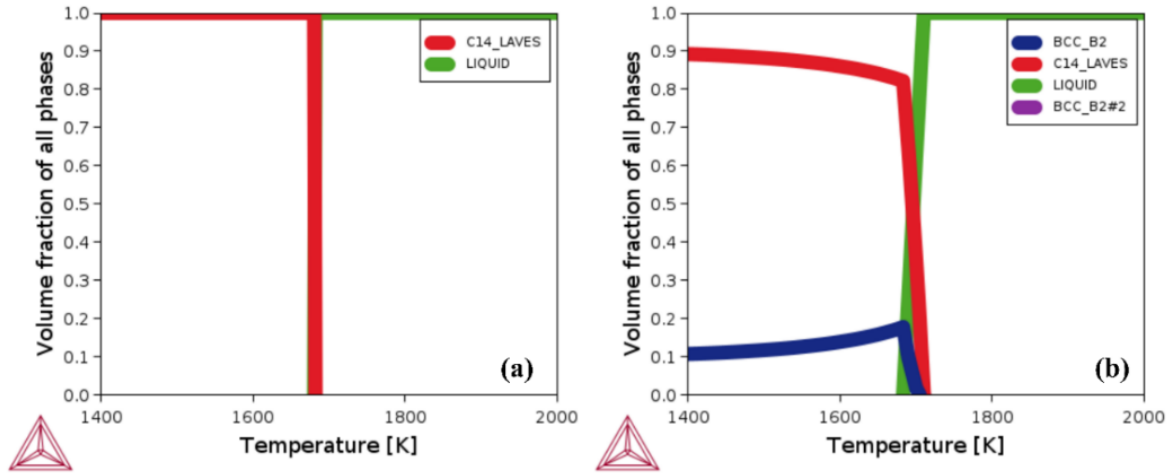


**Figure 5.3:** Phase evolution plots for (a) CrFeTi and (b) Al<sub>12.01</sub>(CrFeTi)<sub>87.99</sub> alloys.

Additionally, the proposed methodology provides valuable insights into thermal stability by analyzing phase evolution plots in conjunction with pseudo-binary phase diagrams. Also, this approach addresses the limitations of existing design criteria, such as the Valence Electron Concentration (VEC) approach [72], the empirical binary eutectic clusters approach detailed in Chapter 4 and mixing enthalpy methods, which often fail to indicate pro-eutectic or third-phase formation [70,74]. Furthermore, the proposed methodology enables the strategic selection of appropriate elements to achieve desired phase combinations, such as BCC + FCC or BCC + Laves or FCC + Laves, marking a significant advancement over existing design strategies [131,132]. Also, by varying only the EFE, the transition from hypo-eutectic to hyper-eutectic compositions can be more readily understood. Finally, the practicality of this approach is enhanced by the use of CALPHAD, which can be implemented in both console mode and the graphical interface of *Thermo-Calc* software, requiring minimal computational time.

#### 5.4: Identifying the First EMPEA in Al-Fe-Ti-V-Zr

A novel EMPEA was designed in the Al-Fe-Ti-V-Zr system to validate the proposed design philosophy further. The selection of elements—Al, Fe, Ti, V and Zr—was strategically made to employ the "Single Phase Plus EFE" methodology for identifying potential eutectic compositions within this quinary system. This system was chosen due to the lack of reported eutectic compositions and the relatively low densities (<8 g/cc) of elements, with the expectation that their combination would result in an alloy density below 8 g/cc.

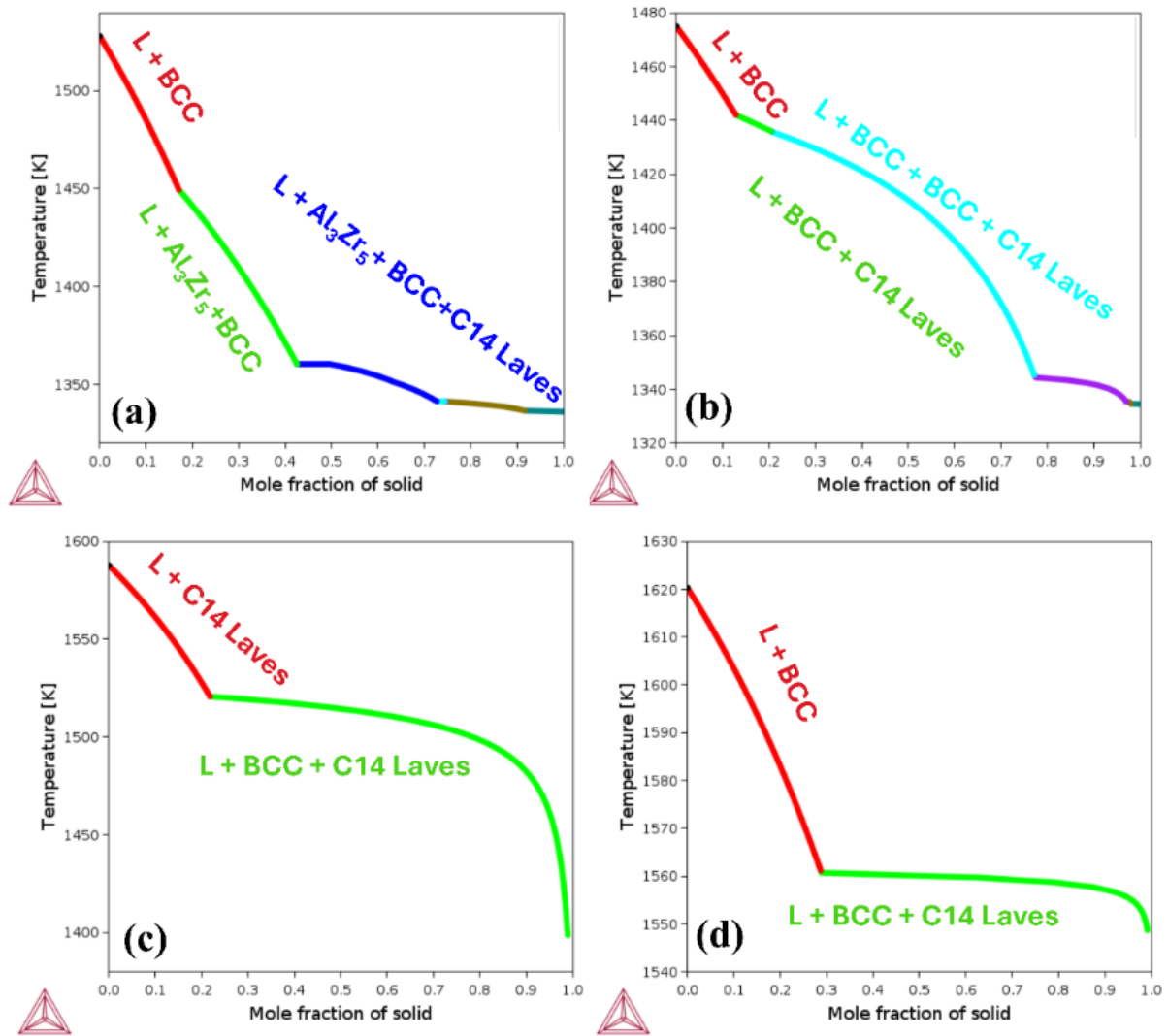


**Figure 5.4:** Scheil solidification simulations of  $\text{Fe}_x(\text{AlTiVZr})_{100-x}$   
(a)  $x = 20$ , (b)  $x = 40$ , (c)  $x = 60$ , (d)  $x = 80$ .

The thermodynamic simulations began with an equiatomic mixture of Al, Ti, V and Zr (AlTiVZr), which has been reported to exhibit a single-phase C14 Laves structure [133]. According to the "Single Phase Plus EFE" design strategy, the next step is to identify a suitable EFE. Fe was selected as the EFE for this alloy system due to its ability to form a Laves phase with Zr ( $\text{Fe}_2\text{Zr}$ ) with an enthalpy of mixing of  $-24.6$  kJ/mol and a binary eutectic at 76 atomic percent. It is important to note that, in the Al-Fe-Ti-V-Zr EMPEA system, not all binary combinations among the constituent elements exhibit similar mixing enthalpies and Fe, designated as the EFE, does not form a binary eutectic with every other element (Al, Ti, V and Zr) (as represented in **Table 5.2**).

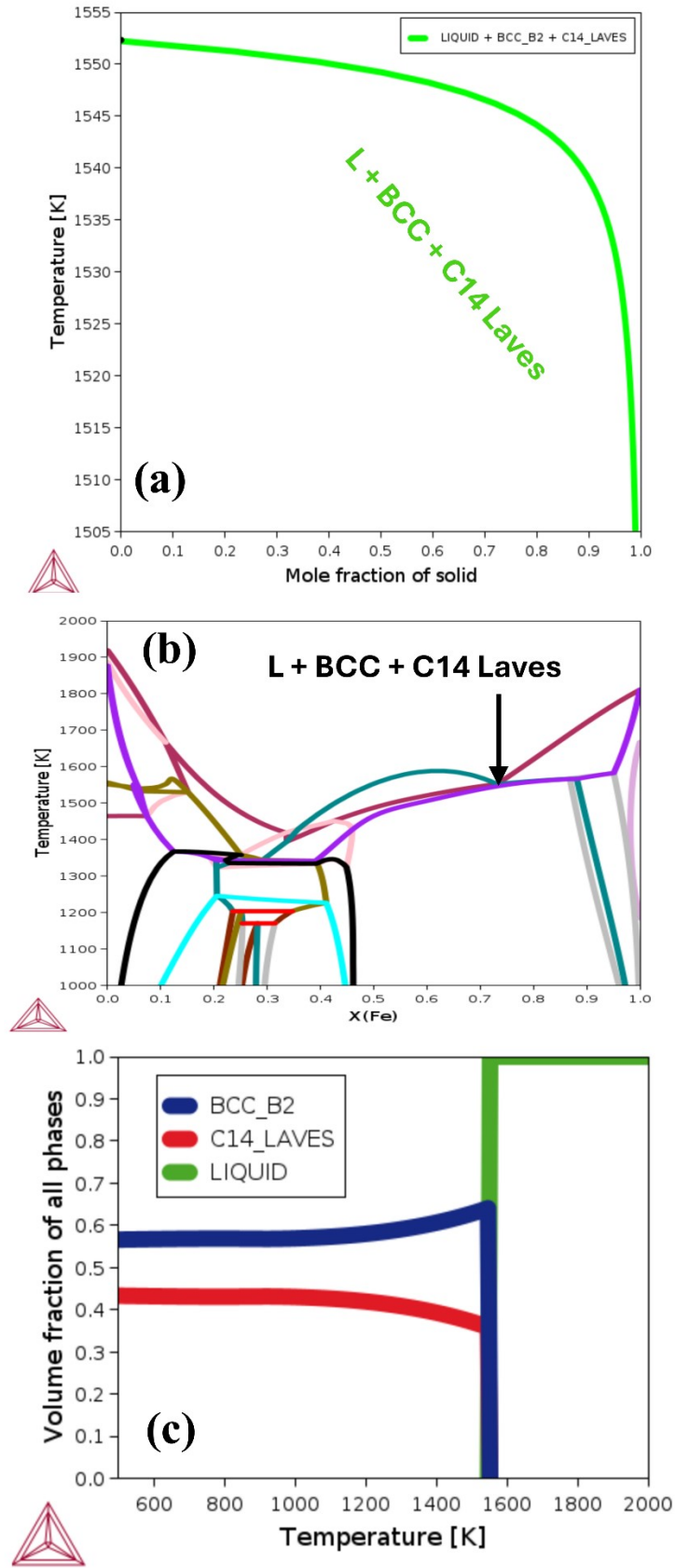


**Figure 5.5:** (a) Scheil solidification simulation for  $\text{Fe}_x(\text{AlTiVZr})_{100-x}$  ( $x = 73$ ), (b) Pseudo-binary phase diagram of AlTiVZr-Fe and (c) Phase evolution plot for  $\text{Fe}_x(\text{AlTiVZr})_{100-x}$  ( $x = 73$ ).

With a basic thermodynamic understanding suggesting that the addition of Fe to AlTiVZr could result in the formation of the Fe<sub>2</sub>Zr Laves phase along with a Fe-rich BCC phase, Scheil solidification simulations were conducted for compositions ranging from Fe<sub>x</sub>(AlTiVZr)<sub>100-x</sub>, where x varied from 20 to 80, as illustrated in **Figure 5.4**. At x= 60, the simulations revealed the formation of the C14 Laves as the primary phase, followed by a two-phase mixture of C14 Laves and BCC, as shown in **Figure 5.4(c)**. At x=80, the BCC phase emerged as the primary phase, accompanied by a mixture of C14 Laves and BCC phases, as depicted in **Figure 5.4(d)**. These results suggest the possibility of a eutectic (or perhaps a two-phase mixture) composition occurring between x=60 and x=80. Subsequent analysis confirmed this hypothesis, identifying the eutectic composition at Fe<sub>73.17</sub>(AlTiVZr)<sub>26.83</sub> at a temperature of 1553 K, as illustrated in **Figure 5.5(a)**. Further confirmation was achieved through a pseudo-binary phase diagram generated in the console mode of *Thermo-Calc*, depicted in **Figure 5.5(b)**. Insights from the phase evolution plot, shown in **Figure 5.5(c)**, revealed a narrow solidification range and no tendency for third-phase formation characteristics for this alloy. As anticipated, the identified Fe<sub>73.17</sub>(AlTiVZr)<sub>26.83</sub> eutectic composition has a maximum theoretical density of 7.09 g/cc.

## 5.5: Experimental Verification of the EMPEAs of AlTiVZr-Fe

To further experimentally validate the proposed design philosophy, three alloy samples, designated as Fe<sub>x</sub>(AlTiVZr)<sub>100-x</sub> (where x=70, 73 and 75), hereafter referred to as Fe70, Fe73 and Fe75, were cast via vacuum arc melting. The elemental compositions of these as-cast buttons, presented in **Table 5.3**, indicate minimal chemical segregation during casting, a desirable characteristic of eutectic alloys.

**Table 5.3:** EDS of the full area at 100x at 5 different locations of the Fe70, Fe73 and Fe75.

Alloy	Composition	Fe	Al	Ti	V	Zr
Fe <sub>70</sub>	Nominal	70	7.5	7.5	7.5	7.5
	Actual	70.7±0.5	6.8±0.5	7.0±0.2	6.4±0.3	9.2±0.3
Fe <sub>73</sub>	Nominal	73	6.75	6.75	6.75	6.75
	Actual	73.4±1.3	4.71±0.8	7.8±0.1	7.9±0.2	6.1±0.8
Fe <sub>75</sub>	Nominal	75	6.25	6.25	6.25	6.25
	Actual	75.7±0.7	7.3±0.4	5.5±0.2	6.3±0.3	5.3±0.5

Further, as anticipated, scanning electron micrographs (**Figure 5.6**) reveal that the Fe70, Fe73 and Fe75 alloys correspond to hypo-eutectic, eutectic and hyper-eutectic compositions,



respectively. The white, flower-like regions observed in the micrographs are identified as the Laves phase containing Zr. In contrast, the black regions represent the Fe-rich BCC phase, which forms a pro-eutectic phase in the Fe70 and Fe75 alloys. The Fe73 alloy exhibits a eutectic composition of these two phases, displaying a distinct cellular eutectic structure without any pro-eutectic phases.

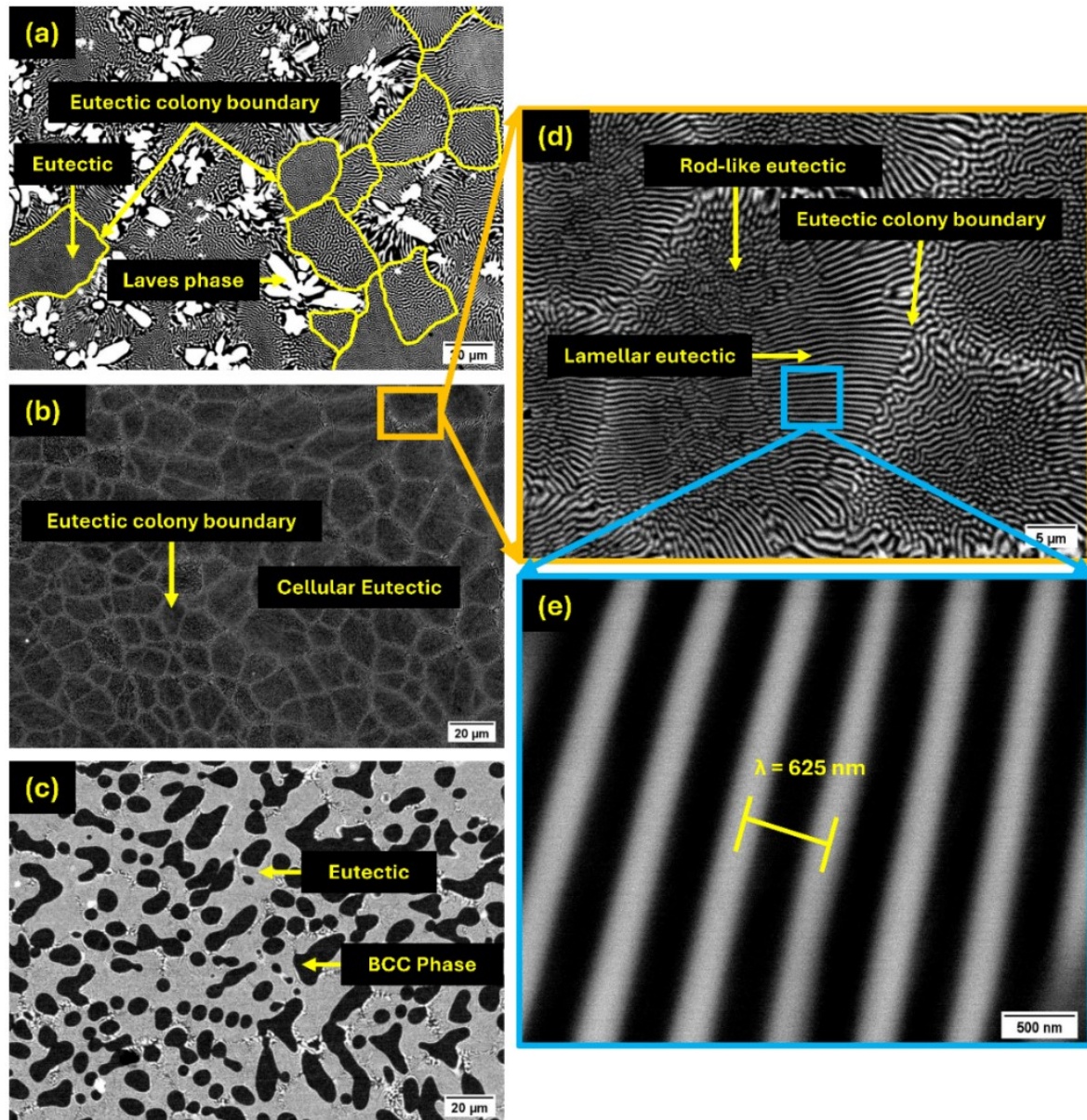


**Figure 5.6:** SEM-BSE micrographs of (a) Fe70, (b) Fe73, (c) Fe75 and (d-e) Fe73 alloy at higher magnifications.

At higher magnifications, as depicted in **Figure 5.6(d)**, the presence of a lamellar and rod-like eutectic morphology within these cellular eutectic colonies becomes evident. This observation suggests alloy sensitivity to the solidification rate, resulting in quasi-regular

lamellae formed due to dynamic metastability caused by varying solidification rates across different parts of the alloy [134]. The lamellar spacing within these colonies is measured to be approximately  $625 \pm 18$  nm. Additionally, a micrograph taken at a very low magnification (180x), shown in **Figure 5.7**, further confirms the eutectic nature throughout the sample, demonstrating uniform microstructural features without compositional segregation or the presence of any third phase.

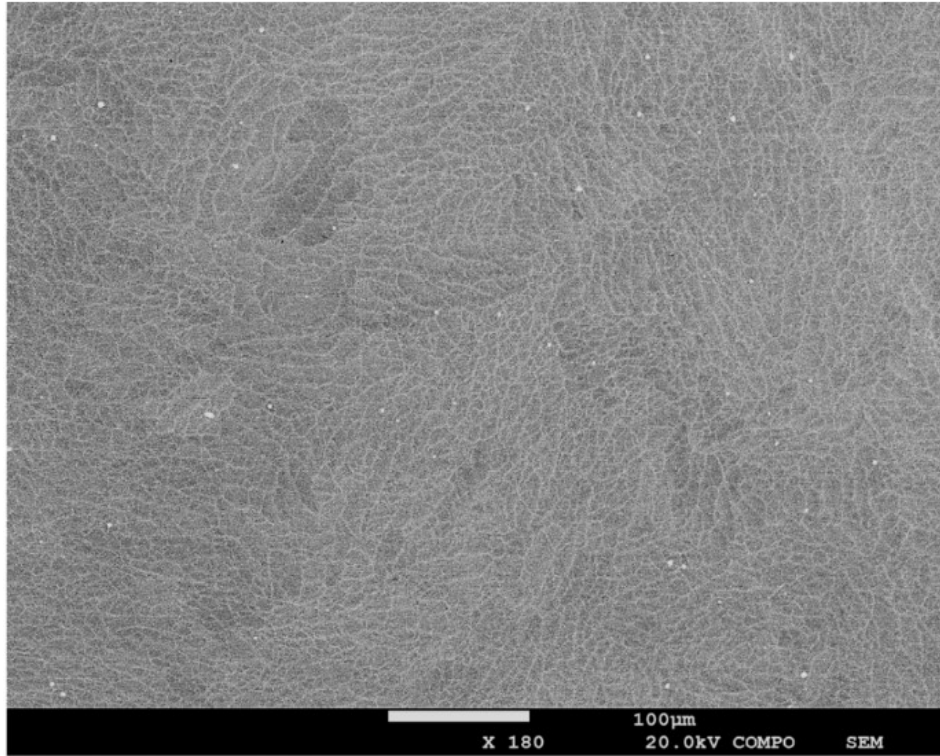


**Figure 5.7:** SEM-BSE micrograph of Fe73 alloy at lower magnification (180x).

The elemental mapping presented in **Figure 5.8** further reveals a clear separation between the Laves and BCC phases. The white phase corresponds to the Zr-rich Laves phase, characterized by a noticeable depletion of V and Fe, while Ti is observed to be dissolved within the Laves phase, as anticipated due to the high miscibility of Zr and Ti at elevated temperatures. The contrasting black phase is predominantly Fe-containing BCC, marked by a significant presence of V and a notable reduction in Zr and Ti. Al is uniformly distributed in both the Laves and BCC phases. The XRD patterns in **Figure 5.9** corroborate the microstructural observations depicted in **Figure 5.8**, confirming the presence of two distinct phases in the developed alloys. The primary phase, BCC, is identified by its characteristic (110) peak attributed to the Im-3m space group (#229), which is more prominent as the Fe content increases, indicating a higher



volume fraction of the BCC phase. Additionally, the Zr-rich C14 Laves phase, associated with the P63/mmc space group (#194), is also identified.

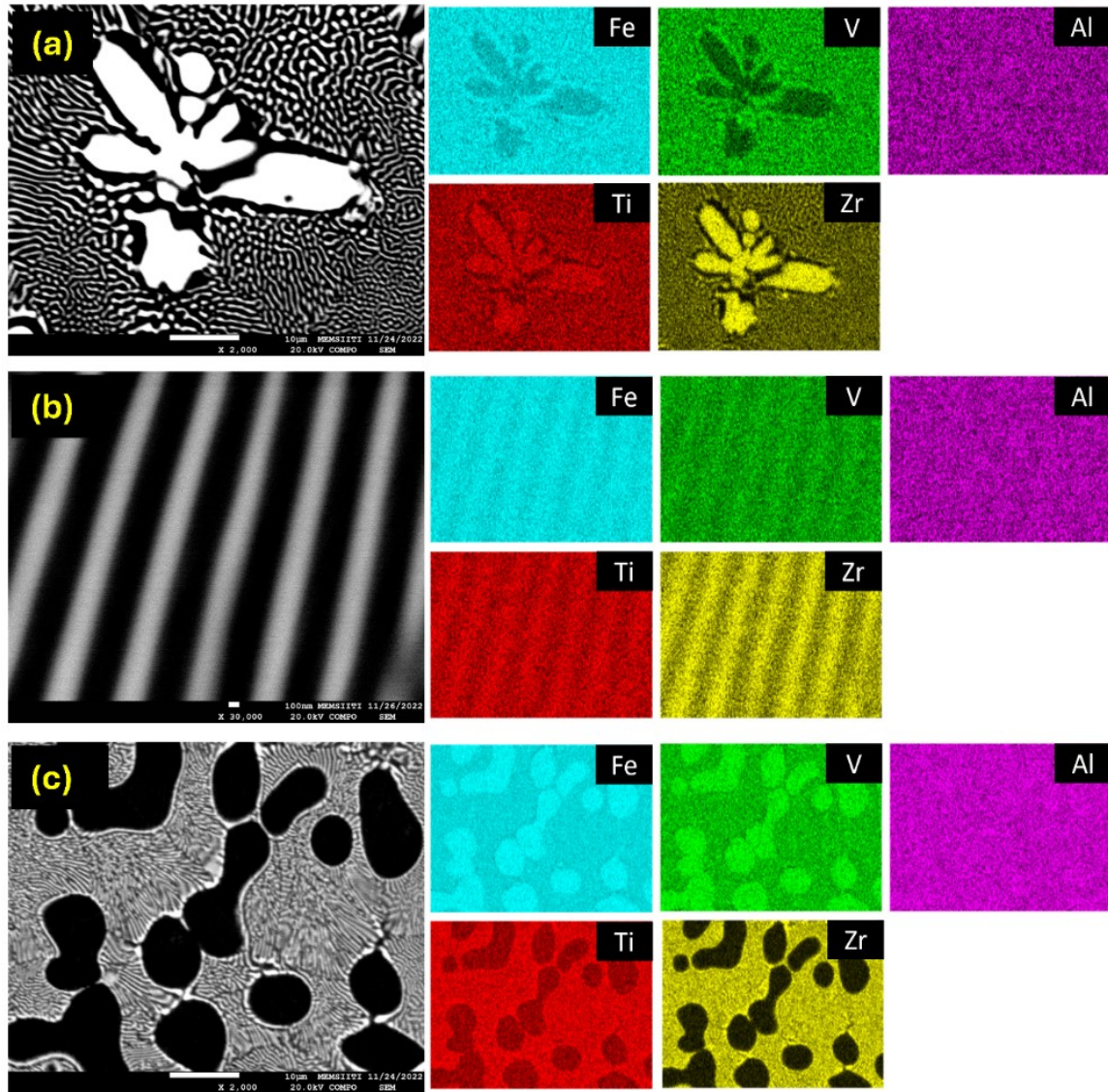


**Figure 5.8:** EDS elemental mapping of (a) Fe70, (b) Fe73 and (c) Fe75 alloys.

The combined analysis from X-ray diffraction and scanning electron microscopy reveals that the alloy, particularly Fe73, exhibits a two-phase mixture of Laves and BCC phases, with cellular eutectic-like colonies containing rod-like and lamellar-like structures within these colonies. To definitively confirm Fe73 as a eutectic composition, it is essential to verify its characteristic eutectic reaction—specifically, the transition from liquid to two solid phases at a single melting point upon cooling or two solid phases melting at the same temperature upon heating. Therefore, to confirm the eutectic nature of Fe73, a 40 mg sample was subjected to heating. The resulting DSC curve in **Figure 5.10** displays a sharp endothermic peak upon heating and a corresponding exothermic peak during cooling. This observation

conclusively confirms Fe73 as a eutectic composition with a narrow solidification range of approximately 20 °C. Additionally, the onset of solidification closely matches the onset of melting, indicating the absence of third-phase formation or chemical segregation, as observed in **Figure 5.7**.

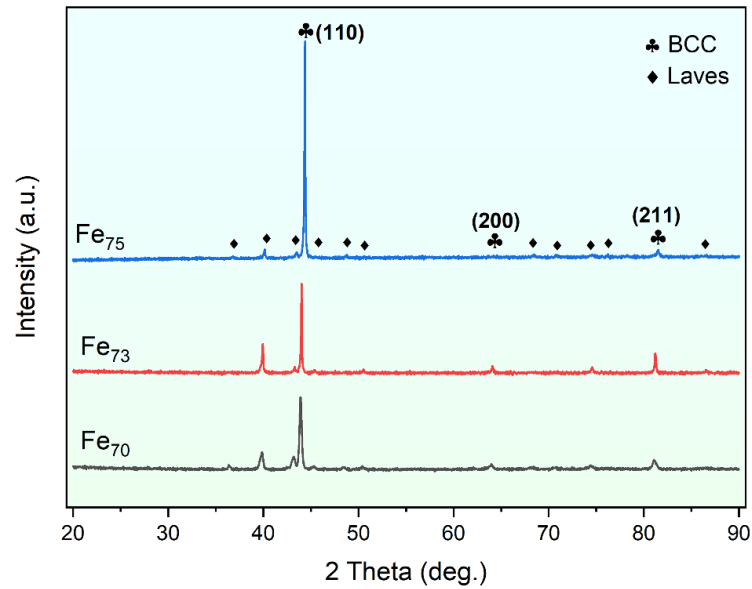


**Figure 5.9:** XRD patterns of Fe70, Fe73 and Fe75 alloys.

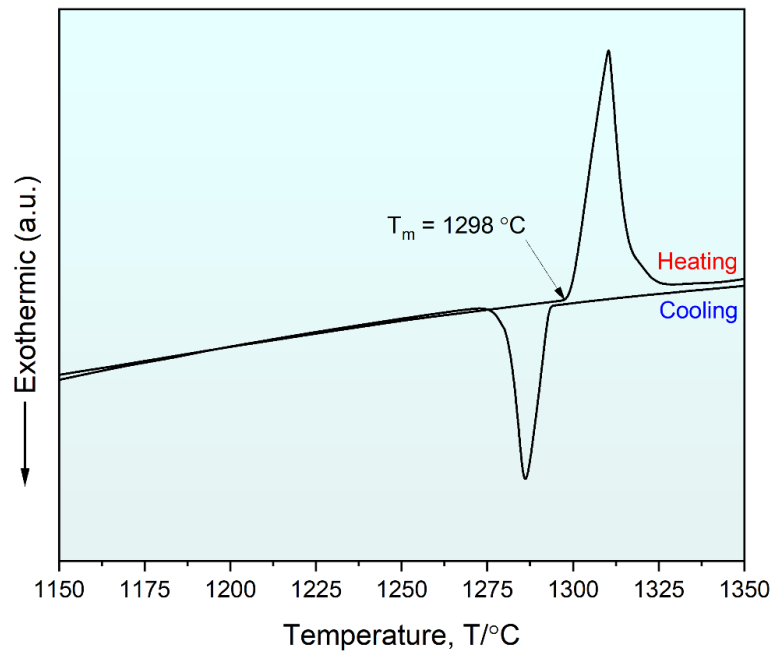


**Figure 5.10:** DSC curve of Fe73 alloy.

The  $\text{Fe}_x(\text{AlTiVZr})_{100-x}$  EMPEAs exhibit a simple solid solution of BCC along with the C14 Laves phase. The formation and stability of phases in MPEAs can be further empirically understood using several thermodynamic parameters, as discussed in Chapter 2. Among these

parameters, atomic size difference ( $\delta$ ), mixing enthalpy ( $\Delta H_{mix}$ ), mixing entropy ( $\Delta S_{mix}$ ) and valence electron concentration (VEC) are particularly noteworthy. These parameters can be calculated using the following equations:

$$\delta = \sqrt{\sum_{i=1}^n c_i \left(1 - r_i / \sum_{i=1}^n c_i r_i\right)^2} \quad (Eq. 5.1)$$

$$\Delta H_{mix} = \sum_{i=1, i \neq j}^n 4\Delta H_{ij}^{mix} x_i x_j \quad (Eq. 5.2)$$

$$\Delta S_{mix} = -R \sum_{i=1}^n x_i \ln x_i \quad (Eq. 5.3)$$

$$VEC = \sum_{i=1}^n x_i VEC_i \quad (Eq. 5.4)$$

$$T_m = \sum_{i=1}^n x_i T_{mi} \quad (Eq. 5.5)$$

$$\Omega = T_m \Delta S_{mix} / |H_{mix}| \quad (Eq. 5.6)$$

Where  $x_i$  = mole fraction of component i,  $x_j$  = mole fraction of component j,  $\Delta H_{ij}^{mix}$  = mixing enthalpy between the ith and jth components, n = number of constituent elements, R = ideal gas constant (8.314 J/K.mol),  $T_{mi}$  = melting temperature of component i,  $r_i$  = the atomic radius of element i,  $r_j$  = the atomic radius of element j and  $VEC_i$  = VEC of component i. The atomic radius (r), melting point ( $T_m$ ), VEC and densities ( $\rho$ ) of the constituent elements are listed in **Tables 5.4 and 5.5**.

**Table 5.4:** The atomic radius (r), melting point ( $T_m$ ), valence electron concentration (VEC) and density ( $\rho$ )

Element	(r) (pm)	$T_m$ (K)	VEC	$\rho$ (g/cc)
Al	143.17	933	3	2.702
Ti	146.15	1941	4	4.540
V	131.60	2183	5	6.110
Zr	160.25	2128	4	6.510
Fe	124.12	1811	8	7.874
Co	125.1	1768.0	9	8.90
Fe	124.1	1811.0	8	7.88
Ni	124.6	1728.0	10	8.91

**Table 5.5:**  $\Delta H_{mix}$  (kJ/mol) values of the constituent elements.

	Al	Co	Cr	Fe	Ni	Ti	V	Zr
Al	0							
Co	-18.8	0						
Cr	-9.9	-4.5	0					
Fe	-11.1	-0.6	-1.5	0				
Ni	-22.3	-0.2	-6.7	-1.6	0			
Ti	-29.5	-28.3	-7.5	-16.8	-34.5	0		
V	-16.3	-14	-2	-7.1	-18	-1.7	0	
Zr	-43.7	-40.3	-12	-24.6	-48.4	-0.2	-3.7	0

The calculated thermodynamic parameters via equations 5.1 to 5.6 are represented in **Table 5.6**, indicating that the configurational mixing entropy is insufficient to compensate for the mixing enthalpy, promoting intermetallic phase formation. Zhang *et al.* [135]. defined a range utilising  $\Delta H_{mix}$  and  $\delta$ :  $20 \leq \Delta H_{mix} \leq 0$  kJ/mol and  $5 \leq \delta\% \leq 6.6$ , to form a mixture of disordered and ordered solid solutions. Also, the eutectic stability in fully eutectic and near EMPEAs was estimated by Chanda *et al.* [121] that the eutectic phases become stable when  $-18 \leq \Delta H_{mix} = -6$ ,  $6 \leq VEC \leq 8.5$  and  $\delta > 3\%$ . The currently developed completely eutectic Fe73 alloy and nearly eutectic Fe73 and Fe75 alloys fulfil this criterion.

**Table 5.6:** Calculated thermodynamic parameters of the developed EMPEAs.

EMPEAs	$\Delta H_{mix}$ (kJ/mol)	$\Delta S_{mix}$ (J/K.mol)	$\Omega$	$\delta$ (%)	VEC
Fe70	-14.66	1.03R	1.05	8.58	6.80
Fe73	-13.48	0.96R	1.07	8.31	6.92
Fe75	-12.66	0.91R	1.08	8.11	7.00

## 5.6: Designing an EMPEA for Strength-Ductility Synergy

After validating the 'Single Phase Plus EFE' design philosophy by developing the first eutectic in the Al-Fe-Ti-V-Zr system with a BCC plus Laves combination, a new lightweight EMPEA featuring a B2 plus FCC combination was designed. The objective was to achieve an appreciable strength-ductility synergy to that of AlCoCrFeNi<sub>2.1</sub>, which demonstrated a density of 7.38 g/cc, remarkable castability, significant elongation (17%) and high fracture strength (1009 MPa) [50]. Despite the development of numerous EMPEAs subsequent to AlCoCrFeNi<sub>2.1</sub>, none have surpassed or replicated its strength-ductility synergy. Additionally, two challenges persist with the AlCoCrFeNi<sub>2.1</sub> alloy: firstly, there is no definitive design rationale for this exact composition and secondly, the coexistence of Cr and Fe in this alloy raises the potential for sigma phase formation [136,137]. Consequently, the new lightweight

EMPEA with a B2 plus FCC combination aimed to address these challenges and further substantiate the 'Single Phase Plus EFE' design philosophy. In this context, four considerations guided the design approach to determine the optimal composition:

1. Considering elements from the *TCHEA5* database of the *Thermo-Calc* program.
2. Metallic elements with densities below 10 g/cc were considered to ensure that the designed alloy density was low.
3. Requiring the FCC phase fraction in the designed alloy to be more than 50% to get a good amount of ductility, as implied from the literature, represented in **Table 5.7**.
4. Avoiding combinations involving both Fe and Cr to prevent the potential formation of the sigma phase.

Here, it is noted that CALPHAD observations by Oliveira *et al.* [138] suggest that the eutectic alloy AlCoCrFeNi<sub>2.1</sub> is predicted to undergo sigma phase formation within the temperature range of 500–800 °C. This prediction aligns with the model proposed by Tsai *et al.* [139,140], which indicates that Cr-containing MPEAs with a VEC between 6.88 and 7.84 are susceptible to sigma phase formation.

**Table 5.7:** Ultimate tensile strength (MPa) and uniform elongation for literature-reported EMPEAs of FCC+B2 at a strain rate of  $1 \times 10^{-3} \text{ s}^{-1}$  done at room temperature in the as-cast condition (DIC = digital image correlation, E = extensometer, MD = machine data).

Composition	FCC %	$\sigma_{max}$ (MPa)	$\epsilon_p$ (%)	$\rho$ (g/cc)	Strain Calculation	Ref
(AlCoFe) <sub>55</sub> (Ni) <sub>45</sub>	61	1014	17.5	7.16	DIC	This work
(AlCoCrFe) <sub>65.36</sub> (Ni) <sub>34.64</sub>	65	1009	17	7.08	DIC	[50]
Ni <sub>30</sub> Co <sub>30</sub> Cr <sub>10</sub> Fe <sub>10</sub> Al <sub>18</sub> W <sub>2</sub>	60	1200	15	7.38	DIC	[141]
Al <sub>17</sub> Cr <sub>8</sub> Fe <sub>32</sub> Ni <sub>43</sub>	60	951	15.2	7.02	E	[142]
Al <sub>16.4</sub> Cr <sub>16</sub> Fe <sub>24</sub> Ni <sub>43.6</sub>	60	1012	12.6	7.01	E	[142]
Al <sub>16.6</sub> Cr <sub>12</sub> Fe <sub>28</sub> Ni <sub>43.4</sub>	60	979	12.1	7.03	E	[113]
Al <sub>16</sub> C <sub>20</sub> Fe <sub>20</sub> Ni <sub>44</sub>	60	1050	10.8	7.02	E	[142]
Al <sub>18</sub> Co <sub>20</sub> Cr <sub>20</sub> Ni <sub>42</sub>	-	1033	6.9	7.03	E	[143]
Al <sub>16.39</sub> Cr <sub>16.39</sub> Fe <sub>24.59</sub> Ni <sub>42.63</sub>	72	1028	18.3	7.00	MD	[72]
Al <sub>19</sub> Co <sub>20</sub> Fe <sub>20</sub> Ni <sub>41</sub>	-	1050	16	7.10	MD	[57]
Al <sub>19.51</sub> Co <sub>24.39</sub> Cr <sub>14.64</sub> Fe <sub>17.07</sub> Ni <sub>24.39</sub>	70	980	14.8	6.86	MD	[144]
Al <sub>17.5</sub> Co <sub>20</sub> Cr <sub>20</sub> Ni <sub>42.5</sub>	82	1273	14.4	7.07	MD	[145]
Al <sub>16.3</sub> Co <sub>25</sub> Cr <sub>25</sub> Ni <sub>33.7</sub>	84.3	1109	13.6	7.08	MD	[145]
Al <sub>18</sub> Co <sub>13</sub> Cr <sub>10</sub> Fe <sub>14</sub> Ni <sub>45</sub>	-	1047	10.83	7.07	MD	[146]
Al <sub>16.67</sub> Cr <sub>16.67</sub> Fe <sub>16.67</sub> Ni <sub>50</sub>	70	1200	10.1	7.05	MD	[113]
(Al <sub>18</sub> Co <sub>13</sub> Cr <sub>10</sub> Fe <sub>14</sub> Ni <sub>45</sub> )( <sub>100-x</sub> )Ti <sub>x</sub> (x=0.5)	-	1065	9.18	7.05	MD	[113]
Al <sub>18</sub> Co <sub>24</sub> Cr <sub>20</sub> Ni <sub>38</sub>	59	1005	8.1	7.03	MD	[147]
(AlCoCrFe) <sub>65.36</sub> (Ni) <sub>34.64</sub>	71	1057	8	7.08	MD	[146]

$(\text{Al}_{18}\text{Co}_{13}\text{Cr}_{10}\text{Fe}_{14}\text{Ni}_{45})(_{100-x})\text{Ti}_x$ ( $x=1$ )	-	1244	7.51	7.03	MD	[148]
$\text{Al}_{18.37}\text{Co}_{20.40}\text{Fe}_{20.40}\text{Ni}_{40.83}$	60	1005	6.2	7.14	MD	[149]
$\text{Al}_{20.45}\text{Co}_{10}\text{Cr}_{10}\text{Ni}_{59.55}$	68	718	1.85	7.01	MD	[145]

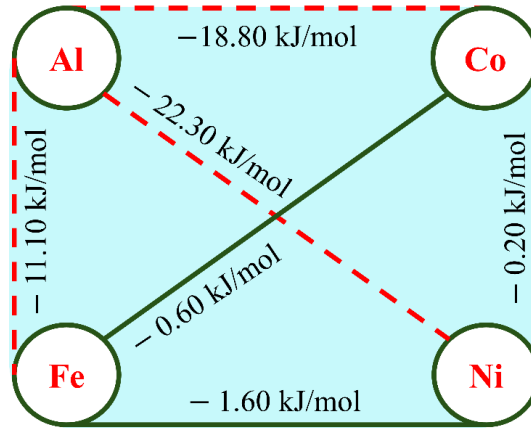


**Figure 5.11:** Chemical mixing enthalpies for atomic pairs among the alloying elements; the dashed line indicates a binary eutectic reaction.

The four criteria presented above were initially addressed by evaluating ten metallic elements: Al, Co, Cr, Cu, Fe, Nb, Ni, Ti, V and Zr. In the subsequent screening process, costly elements such as Ti, V, Nb and Zr were excluded. Additionally, Cu was removed due to its positive enthalpy of mixing with other elements, which could lead to compositional segregation [86,150]. Given the cost-effectiveness of Fe and its potential to form the FCC phase with Ni or Co, the Cr-Fe combination was also excluded to avoid sigma phase formation [137]. Consequently, the elements selected for further consideration include Al, Co, Fe and Ni. The mixing enthalpies and binary eutectic reactions among these elements are illustrated in **Figure 5.11**.

To comply with the first step of the "Single Phase Plus EFE" design approach, the Al-Co-Fe system was selected as a potential B2 phase former, based on the binary phase diagrams of Al-Co and Al-Fe. The CALPHAD analysis, shown in **Figure 5.12(a)**, effectively identified the B2 phase in AlCoFe. This identification was further confirmed by XRD results presented in **Figure 5.13**, which were obtained from the as-cast vacuum arc-melted button. The XRD patterns reveal a distinctive superlattice peak at  $31^\circ$ , corresponding to the (100) plane, validating the presence of the B2 phase in AlCoFe.

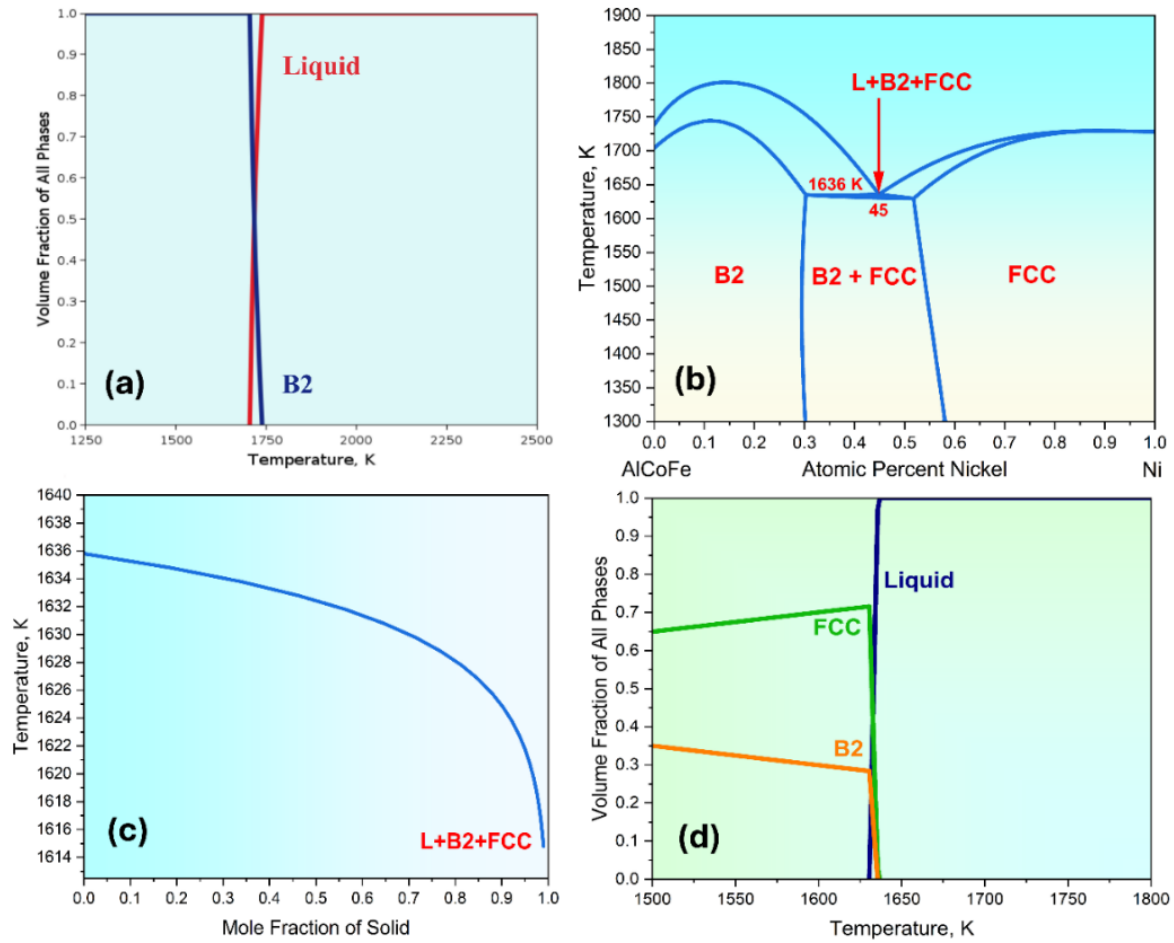


**Figure 5.12:** (a) Phase evolution plot for AlCoFe, (b) Pseudo-binary phase diagram for AlCoFe-Ni, (c) Scheil solidification simulation for (AlCoFe)<sub>55</sub>(Ni)<sub>45</sub> and (d) Phase evolution plot for (AlCoFe)<sub>55</sub>(Ni)<sub>45</sub>.

The second step of the "Single Phase Plus EFE" design approach involves selecting the EFE, with 'Ni' emerging as the sole viable candidate. Nickel is well-suited for this role, as it forms a robust intermetallic compound with Al, characterized by an enthalpy of mixing of -22.30 kJ/mol and a long-range order parameter 'L' of 0.92. Additionally, Ni forms a binary eutectic with Al at 75 at.%. For the third and final step, a pseudo-binary diagram analysis of the AlCoFe-Ni system indicated a eutectic reaction at approximately 45 atomic percent Ni, as illustrated in **Figure 5.12(b)**. To validate the formation of eutectic phases, Scheil solidification simulations and phase evolution plots were conducted for the composition (AlCoFe)<sub>55</sub>(Ni)<sub>45</sub>, as shown in **Figures 5.12(c) and 5.12(d)**. These simulations confirmed the eutectic formation of FCC and B2 phases at 1636 K, with approximately 70% FCC phase fraction. This result is consistent with the goal of achieving an elongation comparable to that of AlCoCrFeNi<sub>2.1</sub>, which has a 65% FCC fraction.



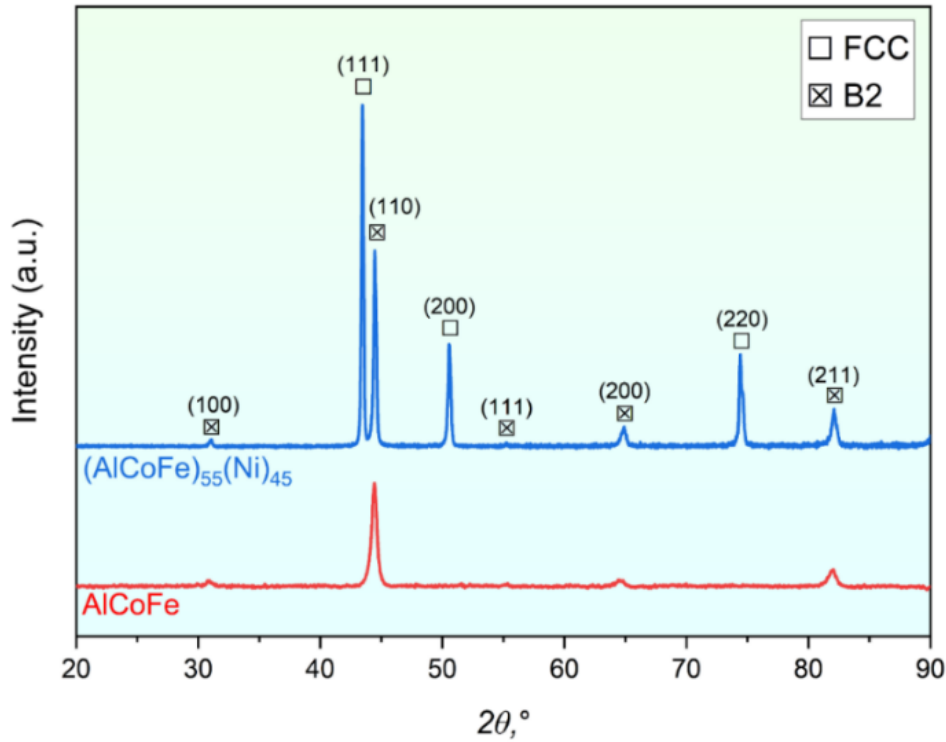


**Figure 5.13:** XRD patterns of the as-cast AlCoFe and (AlCoFe)<sub>55</sub>(Ni)<sub>45</sub> alloys.

The effectiveness of the "Single Phase Plus EFE" design approach is demonstrated through the analysis of potential combinations involving Al, Co, Fe and Ni. Four scenarios were considered for the initial step: (1) CoFeNi, an FCC single phase; (2) AlCoFe; (3) AlFeNi; and (4) AlCoNi, each forming single-phase B2 structures, as illustrated in **Figure 5.14(a-c)**. For the second step, eutectic forming elements are Al, Ni and Co for the first three scenarios, respectively. In the fourth scenario, Fe is proposed as the eutectic forming element. However, Fe does not form compounds with a relatively low enthalpy of mixing with Al, Co, or Ni, failing to meet the requirements of step 2 of the design philosophy. This limitation could impede the eutectic reaction in the AlCoNi-Fe pseudo-binary phase diagram.

**Figure 5.12(b)** showed a eutectic reaction in the AlCoFe-Ni system. To validate this finding, further analyses of the pseudo-binary phase diagrams (CoFeNi-Al, AlFeNi-Co and AlCoNi-Fe) were conducted. The results, shown in **Figures 5.14(d-h)**, confirmed eutectic reactions in the first two cases but not in the latter, supporting the initial hypothesis. Comparing the compositions of EMPEAs—(CoFeNi)<sub>84.8</sub>(Al)<sub>15.2</sub> and (AlFeNi)<sub>47.4</sub>(Co)<sub>52.6</sub>—from the CoFeNi-Al and AlFeNi-Co pseudo-binary phase diagrams revealed that the former compositions contained higher cobalt content (28.27 at.% in (CoFeNi)<sub>84.8</sub>(Al)<sub>15.2</sub> and 52.6 at.% in (AlFeNi)<sub>47.4</sub>(Co)<sub>52.6</sub>). Consequently, the composition (AlCoFe)<sub>55</sub>(Ni)<sub>45</sub>, derived from the



AlCoFe-Ni pseudo-binary phase diagram with 18.33 at.% Co was selected for experimental validation.

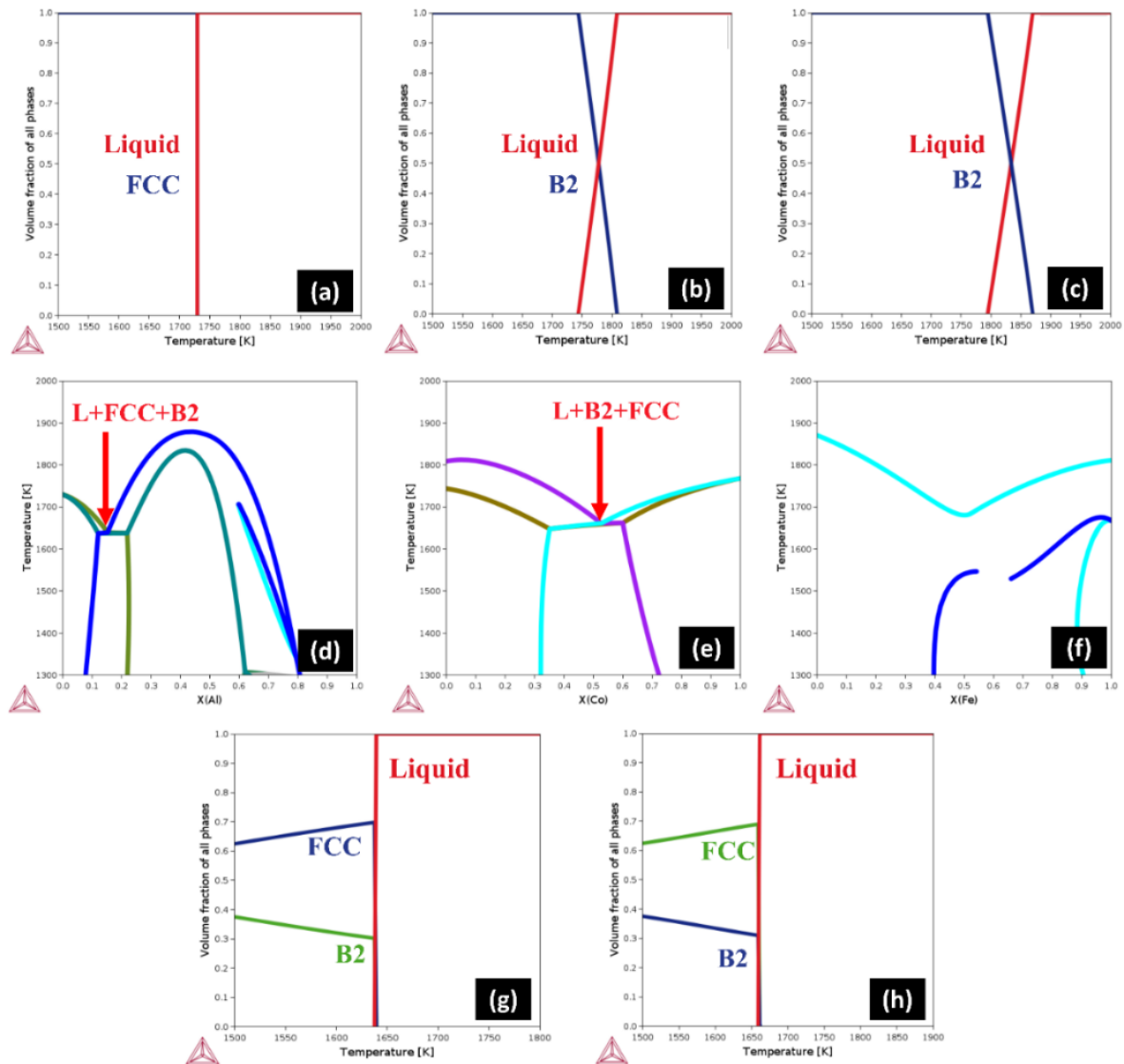


**Figure 5.14:** (a-c) Phase evolution plots of CoFeNi, AlFeNi and AlCoNi, respectively; (d-f) Pseudo-binary phase diagrams of CoFeNi-Al, AlFeNi-Co and AlCoNi-Fe, respectively; and (g-h) Phase evolution plots of (CoFeNi)<sub>84.8</sub>(Al)<sub>15.2</sub> and (AlFeNi)<sub>47.4</sub>(Co)<sub>52.6</sub>, respectively.

## 5.7: Experimental Verification of the (AlCoFe)<sub>55</sub>(Ni)<sub>45</sub> alloy

Guided by CALPHAD predictions, three compositions of (AlCoFe)<sub>100-x</sub>(Ni)<sub>x</sub> (where  $x = 40, 45$  and  $50$ ) were synthesised to substantiate the proposed design philosophy further. Micrographs and EDS elemental composition analyses of (AlCoFe)<sub>60</sub>(Ni)<sub>40</sub> and (AlCoFe)<sub>50</sub>(Ni)<sub>50</sub>, representing hypo- and hyper-eutectic compositions, respectively, along with the eutectic (AlCoFe)<sub>55</sub>(Ni)<sub>45</sub>, were presented in **Figure 5.15** and **Table 5.8**, respectively.

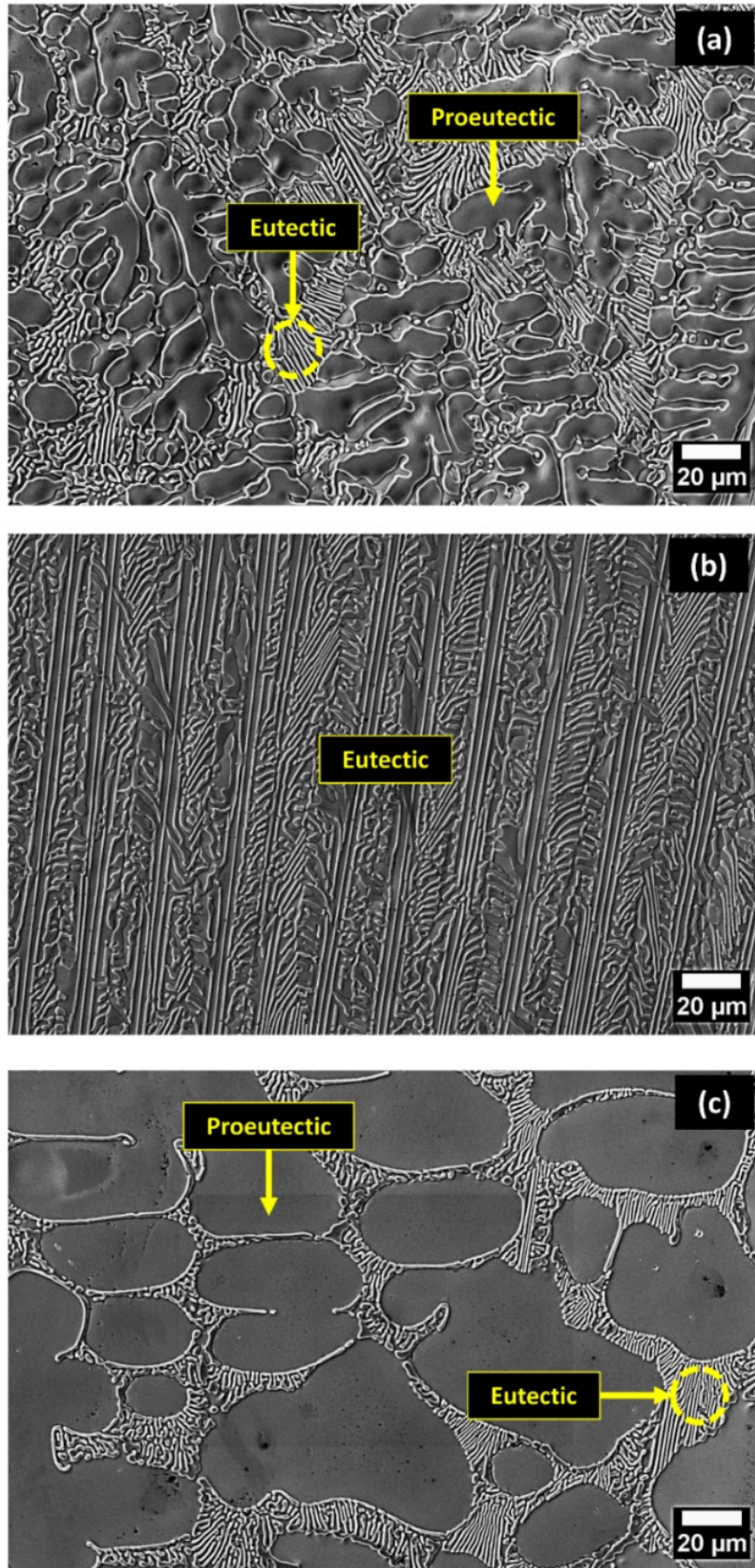


**Figure 5.15:** SEM secondary electron (SE) micrographs of (a)  $(\text{AlCoFe})_{60}(\text{Ni})_{40}$ , (b)  $(\text{AlCoFe})_{55}(\text{Ni})_{45}$  and (c)  $(\text{AlCoFe})_{50}(\text{Ni})_{50}$ .



**Table 5.8:** Elemental composition analysis of  $(\text{AlCoFe})_{100-x}(\text{Ni})_x$  ( $x = 40, 45$  and  $50$ ) at 10 different locations at 100x

Alloy	Composition	Al (at.%)	Co (at.%)	Fe (at.%)	Ni (at.%)
$(\text{AlCoFe})_{60}(\text{Ni})_{40}$	Nominal	20	20	20	40
	Actual	$20.5 \pm 0.6$	$19.9 \pm 0.3$	$19.9 \pm 0.2$	$39.8 \pm 0.3$
$(\text{AlCoFe})_{55}(\text{Ni})_{45}$	Nominal	18.33	18.33	18.33	45
	Actual	$19.2 \pm 0.6$	$17.8 \pm 0.4$	$18.3 \pm 0.3$	$44.7 \pm 0.4$
$(\text{AlCoFe})_{50}(\text{Ni})_{50}$	Nominal	16.66	16.66	16.66	50
	Actual	$16.6 \pm 0.5$	$16.8 \pm 0.4$	$16.6 \pm 0.3$	$50.0 \pm 0.6$

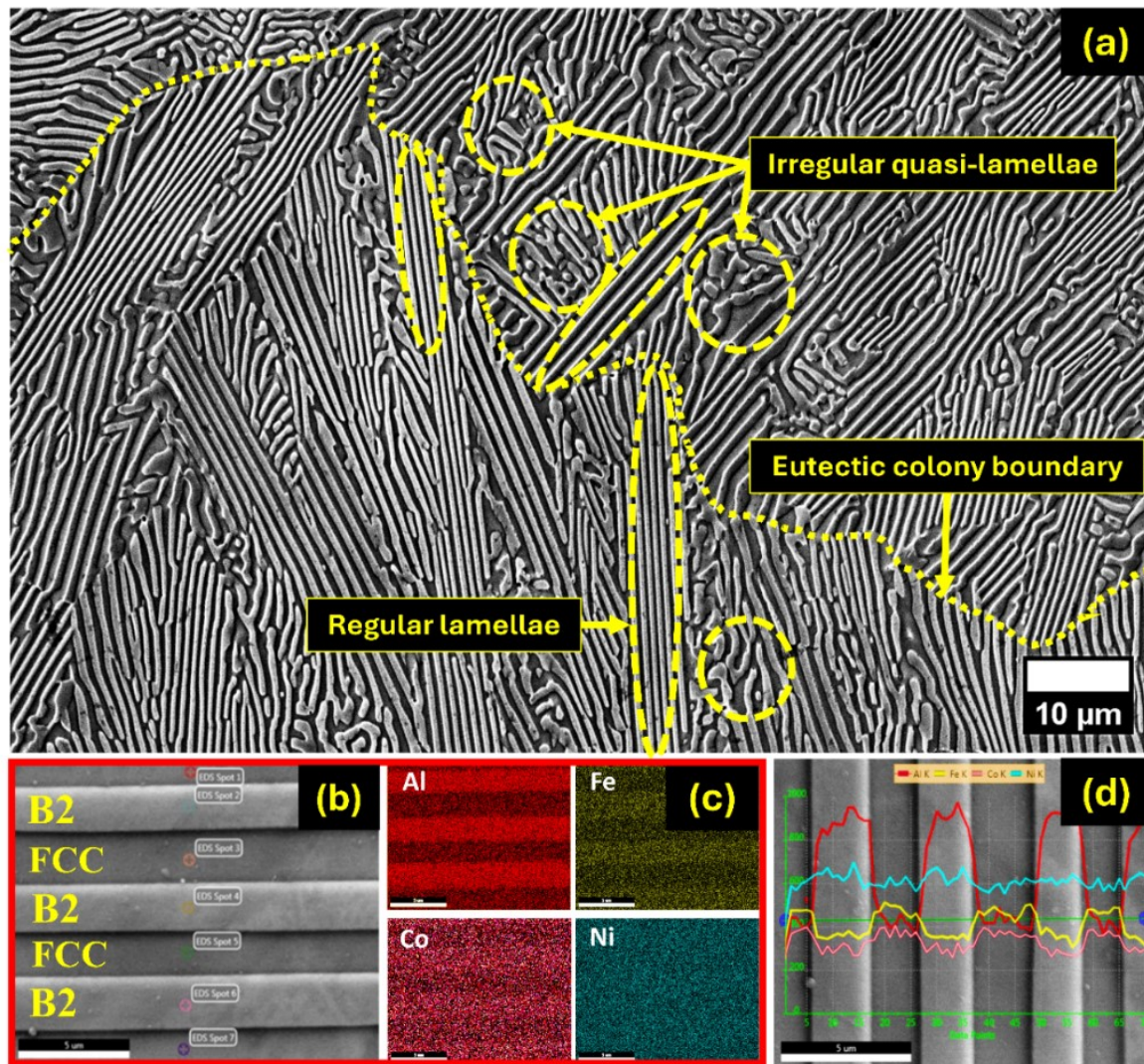


**Figure 5.16:** (a) SEM image of the dual-phase eutectic microstructure of the as-cast  $(\text{AlCoFe})_{55}(\text{Ni})_{45}$ , (b-c) EDS elemental mapping and (d) EDS line analysis showing distributions of Al, Fe, Co and Ni.

Of particular significance is the eutectic composition  $(\text{AlCoFe})_{55}(\text{Ni})_{45}$ , which exhibited an exquisite dual-phase eutectic microstructure, as depicted in **Figure 5.16(a)**, acquired under SEM-BSE (backscattered electron) mode. The phases identified through XRD, as shown in

**Figure 5.13**, agree with the microstructural features presented in **Figure 5.16**, providing further evidence of the dual-phase microstructure in the alloy. The  $\text{Sin}^2\theta_1:\text{Sin}^2\theta_2:\text{Sin}^2\theta_3\dots$  ratio analysis, focusing on the peaks with higher intensities, shows a ratio of 3:4:8:11:12:16, suggesting the presence of FCC as one of the constituent phases. The remaining peaks, which could potentially follow a 2:4:6 ratio indicative of a BCC structure and the identification of superlattice peaks at  $31^\circ$  and  $55^\circ$ , corresponding to the (100) and (111) planes, respectively, confirm the presence of an ordered BCC (B2) phase. Additionally, the DSC trace shown in **Figure 5.17** exhibits a sharp endothermic peak corresponding to the eutectic characteristic, i.e., 'solid phase 1 (FCC) + solid phase 2 (B2)  $\rightarrow$  liquid,' during the melting process. This observation further confirms the eutectic nature of  $(\text{AlCoFe})_{55}(\text{Ni})_{45}$ . The onset of melting was observed at  $1371^\circ\text{C}$  ( $1644\text{ K}$ ), which aligns well with the CALPHAD prediction, further validating the accuracy of the designed eutectic composition  $(\text{AlCoFe})_{55}(\text{Ni})_{45}$ .

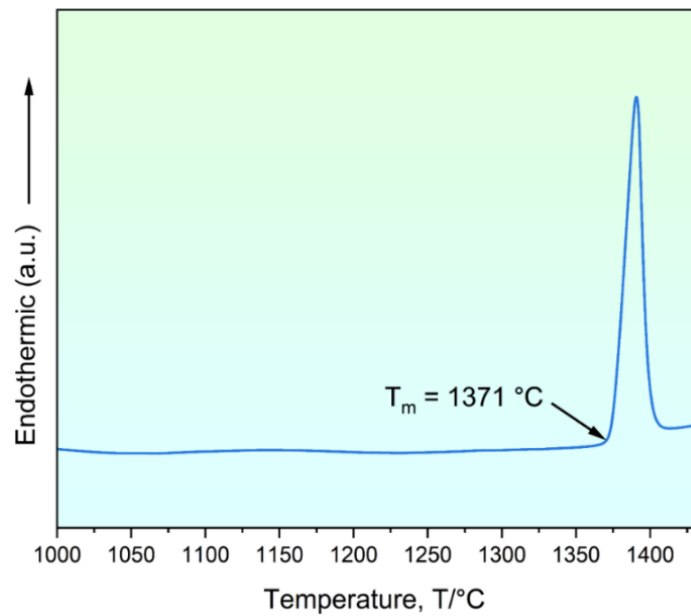


**Figure 5.17:** DSC trace of  $(\text{AlCoFe})_{55}(\text{Ni})_{45}$  alloy.

The calculated thermodynamic parameters for  $(\text{AlCoFe})_{55}(\text{Ni})_{45}$ , as presented in **Table 5.9**, meet the criteria given in equations 5.1 to 5.6, providing further evidence of the eutectic formation of FCC plus B2 phases. The microstructure of the as-cast  $(\text{AlCoFe})_{55}(\text{Ni})_{45}$  alloy, depicted in **Figure 5.16**, displays distinct regions of regular lamellar eutectic (highlighted in ellipses) and irregular eutectic patterns (highlighted in circles). The regular eutectic pattern exhibits a lamellar spacing of  $1098 \pm 265\text{ nm}$ , while the irregular quasi-lamellae demonstrate apparent relative coarsening, indicative of a hierarchical microstructure.

**Table 5.9:** Calculated thermodynamic parameters for (AlCoFe)<sub>55</sub>(Ni)<sub>45</sub>

Composition	$\delta$ (%)	$\Delta H_{mix}$ (kJ/mol)	$\Delta S_{mix}$ (J/K.mol)	VEC
(AlCoFe) <sub>55</sub> (Ni) <sub>45</sub>	5.63	-12.05	10.74	8.17

The solidification of the eutectic mixture commenced with the growth of straight, regular lamellae characterized by slight anisotropic variations. This uniform eutectic pattern arises from the concurrent growth of FCC and B2 phases of the liquid melt, exhibiting a steady-state coupling. As the solidification progresses, deviations from steady-state growth can manifest due to instabilities from the concentration boundary layer ahead of the eutectic front, leading to the transition from uniformity [121]. Furthermore, the partitioning of the eutectic into regular and irregular patterns can also occur due to temperature gradients and variations in cooling rates surpassing a critical threshold [151]. The corresponding EDS maps and line analyses, respectively, for **Figure 5.16(b-c)** and **Figure 5.16(d)**, confirm that the FCC phase contains elevated concentrations of Co and Fe, while the B2 phase is enriched with Al, with Ni being distributed uniformly in both phases. The similar mixing enthalpies ( $\Delta H_{mix}^{Ni-Co} = -0.20$  kJ/mol and  $\Delta H_{mix}^{Ni-Fe} = -1.60$  kJ/mol) and atomic radii (**Table 5.4** and **Table 5.5**) for Co, Fe and Ni explain the dissolution of these elements within the FCC phase and the B2 phase formation of AlNi ( $\Delta H_{mix}^{Al-Ni} = -22.30$  kJ/mol). The corresponding EDS spot analysis of **Figure 5.16(b)** determined the presence of elements in each phase, represented in **Table 5.10**, further informing the enrichment of Al in the B2 phase. Phase fractions were quantified by analyzing multiple micrographs at 500x magnification, revealing volume fractions of 61% for the FCC phase and 39% for the B2 phase. These phase fractions show a minor deviation from the CALPHAD equilibrium phase predictions of 70% for FCC and 30% for B2. This observed slight discrepancy might be ascribed to deviations from equilibrium cooling rates and thermal gradients during the eutectic solidification process, thereby emphasizing the formation of quasi-lamellae.

**Table 5.10:** Phase compositions for (AlCoFe)<sub>55</sub>(Ni)<sub>45</sub>

Phase Fraction	Al (at.%)	Co (at.%)	Fe (at.%)	Ni (at.%)
FCC (61%)	9.9±0.1	21.2±0.2	24.6±0.2	44.3±0.3
B2 (39%)	22.4±0.4	15.5±0.2	16.6±0.1	45.5±0.2

## 5.8: Mechanical Properties of the (AlCoFe)<sub>55</sub>(Ni)<sub>45</sub> alloy

The developed EMPEA (AlCoFe)<sub>55</sub>(Ni)<sub>45</sub> underwent uniaxial tensile and compression tests to reveal its mechanical properties. Under compression, the alloy exhibited a fracture strength of 1994±88.1 MPa and a strain of 42.46±1.47%, as illustrated in **Figure 5.18**. The

observed compressive fracture strain exceeds that of most reported as-cast EMPEAs, as detailed in **Table 5.11**.

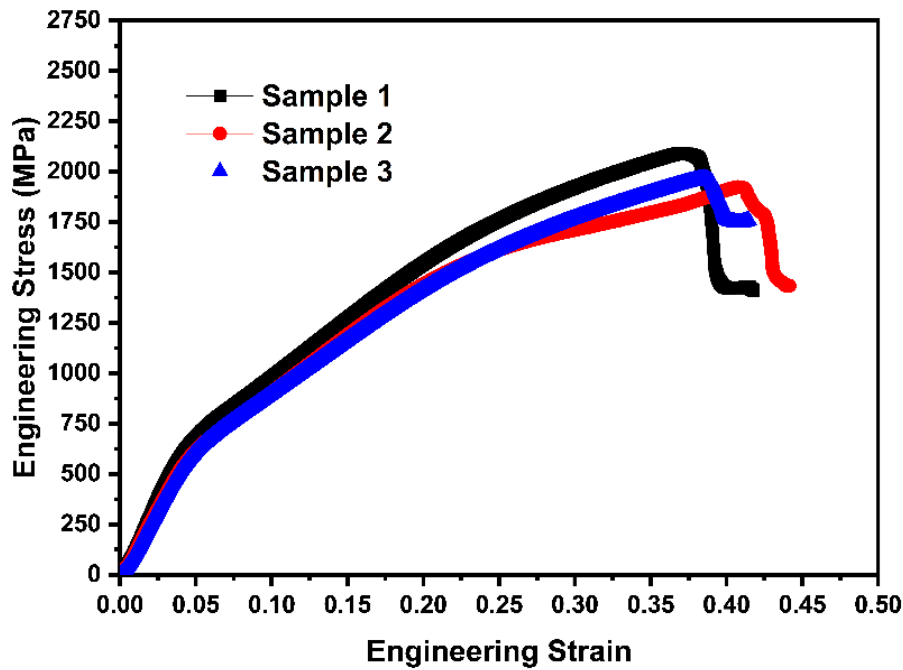


**Figure 5.18:** Compression stress-strain curve of  $(\text{AlCoFe})_{55}(\text{Ni})_{45}$  alloy.

**Table 5.11:** Compression fracture strength vs. elongation for literature-reported EMPEAs containing FCC phase at room temperature and a strain rate of  $1 \times 10^{-3} \text{ s}^{-1}$ .

Alloy	Phases	$\sigma_y$ (MPa)	$\sigma_{max}$ (MPa)	$\epsilon_p$ (%)	Reference
AlCoFeNi <sub>2.4</sub>	FCC+B2	554	1994	42.5	This Work
Fe <sub>2</sub> NiCrNb <sub>0.34</sub>	FCC + Laves	988.7	2267	30.8	[152]
CrFeNiNb <sub>0.35</sub>	FCC + Laves	1204.67	2411.12	30.23	[127]
CoCu <sub>0.5</sub> FeNiTa <sub>0.5</sub>	FCC + Laves	1595	3160	24	[153]
(CoFe <sub>2</sub> NiV <sub>0.5</sub> Mo <sub>0.2</sub> ) <sub>91</sub> (Nb) <sub>9</sub>	FCC + Laves	1118.2	2050.8	19.3	[154]
CoCrFeNiNb <sub>0.5</sub>	FCC + Laves	2060	2200	17	[155]
CrFeNi <sub>2</sub> Nb <sub>0.6</sub>	FCC + Laves	1232.1	2060.6	14.4	[156]
Fe <sub>2</sub> Ni <sub>2</sub> CrMo <sub>1.25</sub>	FCC + $\sigma$	–	1745	9.2	[157]
CoCrFeNiHf <sub>0.4</sub>	FCC + Laves	1200	–	5	[158]
CoCrFeNiHf <sub>0.4</sub>	FCC + Laves	1501	2050	4.5	[32]
Fe <sub>3.5</sub> Ni <sub>2.5</sub> Cr <sub>2.5</sub> Mo <sub>1.5</sub>	FCC + $\sigma$	1065	1875	3.7	[159]
CoFeNi <sub>2</sub> V <sub>0.5</sub> Nb <sub>0.75</sub>	FCC + Laves	2073	2232	3.4	[94]

The tensile stress-strain curve for the as-cast alloy is shown in **Figure 5.19(a)**, obtained at room temperature using DIC to ensure accuracy and minimize potential compliance errors of the testing equipment. The average ultimate tensile strength and elongation were measured at  $1014 \pm 4.95$  MPa and  $17.5 \pm 0.70\%$ , respectively. Notably, the alloy demonstrates a substantial increase in stress, from a yield strength of 498 MPa to an ultimate tensile strength of 1014 MPa, highlighting its excellent strain-hardening ability. Furthermore, the tensile engineering stress-

strain curve shows no significant necking phenomenon, as illustrated in **Figure 5.19(a)**, similar to the behaviour observed in  $\text{AlCoCrFeNi}_{2.1}$ . The absence of significant necking can be attributed to strain distribution resulting from alternating deformation between the softer FCC and harder B2 phases [19]. **Figure 5.19(b)** reveals a typical trench-like morphology on the tensile fracture surface of  $(\text{AlCoFe})_{55}(\text{Ni})_{45}$ , providing insights into its fracture behaviour. During tensile deformation, the harder B2 phase undergoes minimal deformation while the ductile FCC phase extends, contributing to the observed mechanical behaviour. Consequently, the FCC phase experiences gradual thinning, forming dimples (marked in ellipses), while the less deformed B2 phase remains at the trench base, forming quasi-cleavage marks (marked in rectangles), as shown in **Figure 5.19**. This observation was further supported by EDS analysis of the fractured surface, indicating Al enrichment in the quasi-cleavage regions and depletion in the dimples, as presented in **Table 5.12**. This suggests that the dimples are formed due to FCC phase deformation, while the cleavages result from B2 phase deformation.

**Table 5.12:** Chemical composition of phases on the tensile fracture surface of  $(\text{AlCoFe})_{55}(\text{Ni})_{45}$

Region of Interest	Al (at.%)	Co (at.%)	Fe (at.%)	Ni (at.%)
Quasi-cleavages (B2)	12.46±1.95	26.14±1.73	29.04±1.05	32.37±0.96
Dimples (FCC)	05.22±0.84	26.12±1.82	27.97±0.98	40.71±3.63

A comparative assessment presented in **Figure 5.20** highlights the superior tensile performance of the developed alloy, surpassing most reported as-cast EMPEAs, as detailed in **Table 5.7** [160]. The developed alloy,  $(\text{AlCoFe})_{55}(\text{Ni})_{45}$ , demonstrates a density very close to that of alloys containing chromium despite its chromium-free composition. The exceptional strength-ductility synergy can be attributed to the distinct hierarchical eutectic microstructure. The notable elongation was primarily achieved by incorporating Ni, an FCC phase former, into  $\text{AlCoFe}$ , an ordered BCC known for its limited plasticity but high strength. The similar phase fractions of  $\text{AlCoCrFeNi}_{2.1}$  (65% FCC and 35% B2) and  $(\text{AlCoFe})_{55}(\text{Ni})_{45}$  (61% FCC and 39% B2) elucidate the reason for their comparable strength-ductility synergy. It is noteworthy that the only as-cast alloy exhibiting superior elongation compared to  $(\text{AlCoFe})_{55}(\text{Ni})_{45}$  was as-cast  $\text{Al}_{16.39}\text{Cr}_{16.39}\text{Fe}_{24.59}\text{Ni}_{42.63}$ , with an elongation of 18.3% [72]. However, the strain measurement in that report utilized a traditional extensometer, which generally tends to overestimate compared to DIC [72]. However, a very similar composition,  $\text{Al}_{16.4}\text{Cr}_{16}\text{Fe}_{24}\text{Ni}_{43.6}$ , demonstrated a ductility of approximately 12.6% when measured with an extensometer [72,142]. In contrast,



the strain measurements in the present study were conducted using the DIC technique, which provides more accurate strain measurements.

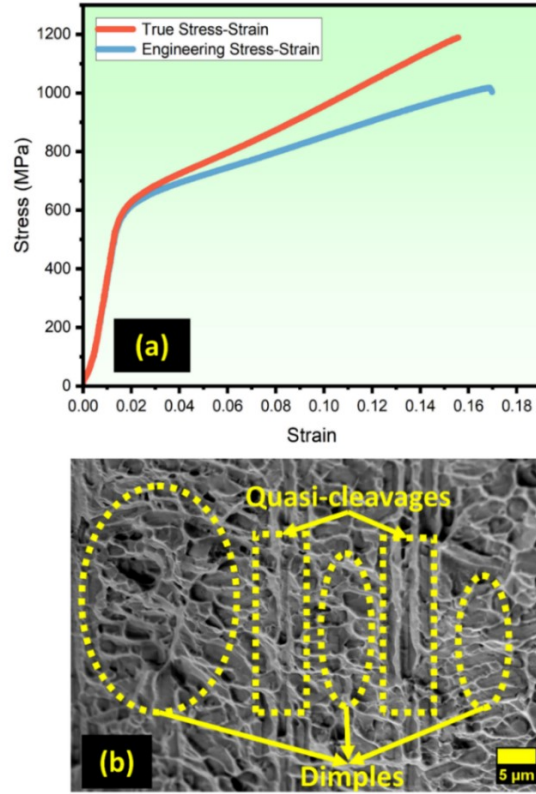


**Figure 5.19:** (a) Tensile stress-strain curve and (b) tensile fracture surface morphology of (AlCoFe)<sub>55</sub>(Ni)<sub>45</sub> alloy.

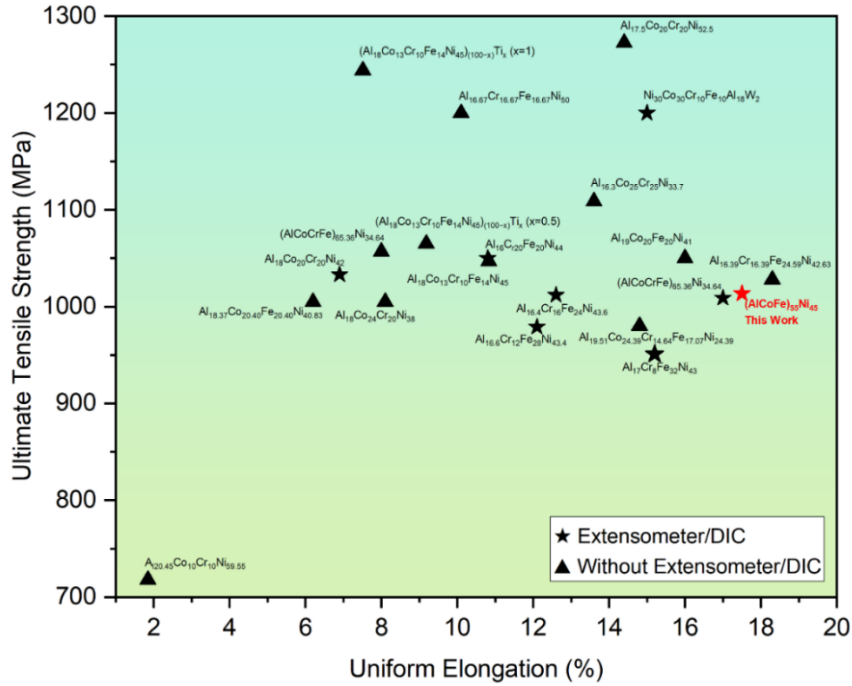


**Figure 5.20:** Comparison of ultimate tensile strength versus uniform elongation for (AlCoFe)<sub>55</sub>(Ni)<sub>45</sub> and literature-reported FCC+B2 EMPEAs at a strain rate of  $1 \times 10^{-3} \text{ s}^{-1}$  and room temperature in the as-cast condition.



## 5.9: Inherent Limitations of the Single Phase Plus EFE Design Strategy

Despite the significant advancements offered by the "Single Phase Plus EFE" design strategy in expediting the identification of new eutectic compositions in MPEA systems, this methodology has inherent limitations. These limitations include:

- *Limited to Identifying Single Two-Phase Eutectics:* The methodology primarily identifies a single two-phase pseudo-eutectic, lacking the ability to detect higher-order eutectics or an invariant eutectic.
- *Restriction Due to EFE Binary Eutectic Requirement:* The strategy reliance on the EFE having a binary eutectic may inadvertently exclude some desirable compositions. For instance, in systems like Co-Cr-Fe-Ni, the pursuit of Fe-based compositions might be limited due to the absence of binary eutectics involving Fe or its low enthalpy of mixing with other elements (Co, Cr and Ni).
- *Constraint on Non-Equiatomic EMPEA Identification:* The current strategy, based on a pseudo-binary approach, does not naturally identify non-equiatomic EMPEAs unless started with a non-equiatomic single phase in the first step.

## 5.10: Summary

- *Introduction of the "Single Phase Plus EFE" Strategy:* This chapter introduces a novel alloy design approach that leverages CALPHAD to redefine the concept of the 'EFE' (Eutectic Forming Element).
- *Experimental Verification:* The efficacy of the proposed strategy is demonstrated through practical experiments, leading to the design and development of the first eutectic composition in the Al-Fe-Ti-V-Zr system and an EMPEA in the Al-Co-Fe-Ni system. The (AlCoFe)<sub>55</sub>(Ni)<sub>45</sub> alloy exhibited a remarkable strength-ductility synergy, surpassing most reported as-cast EMPEAs at room temperature.
- *Advantages and Limitations:* The strategy provides a streamlined and insightful approach compared to traditional alloy design methods, facilitating the rapid identification of new eutectic compositions. However, the chapter also acknowledges the inherent limitations of the methodology, outlining areas for future research.



## CHAPTER 6

# The High-Throughput CALPHAD Approach

### 6.1: Introduction

Eutectic reactions in binary alloy systems are characterized by the simultaneous melting of two solid phases at a specific temperature and composition, known as the invariant eutectic point. This thermal equilibrium state, with zero degrees of freedom, is typically represented as an invariant point in binary phase diagrams, as illustrated in **Figure 6.1(a)**. In ternary alloy systems, the Gibbs phase rule indicates that the invariant eutectic reaction involves the melting of three solid phases at a specific temperature, depicted as a point in the ternary phase diagram. This transition from binary to ternary systems shifts the binary eutectic representation from a point to a line, as shown in **Figure 6.1(b)**. In quaternary and quinary systems, the binary eutectic points further evolve into areas and volumes, respectively, as demonstrated in **Figures 6.1(c) and 6.1(d)**.

This progression from a point to a line and then to an area and volume underscores a crucial distinction: in systems beyond binary alloys, eutectics with only two solid phases are not true invariant eutectics. Invariant eutectics in multi-element alloy systems involve the simultaneous melting of multiple solid phases at a single temperature—specifically, four phases in quaternary systems and five in quinary systems. Consequently, the two-phase combinations commonly referred to as eutectics in HEAs literature, such as BCC plus FCC or FCC plus Laves phases, are more accurately described as pseudo-eutectics rather than true (invariant) eutectics. As the number of elements in higher-order alloy systems increases, the compositional range of these pseudo-eutectics expands. This insight highlights the potential existence of thousands, or even hundreds of thousands, of these pseudo-eutectics in higher-order multi-principal element alloy (MPEA) systems.

Identifying a singular pseudo-eutectic composition presents a significant challenge, as discussed in Chapter 2. Thus, expanding the search to encompass a broader compositional space exacerbates this difficulty. Further, existing design strategies, including the empirical and single phase plus EFE approaches presented in Chapters 4 and 5, respectively, have not yet addressed the search for higher-order eutectics or an invariant eutectic. This gap highlights the urgent need for a new design strategy capable of navigating the complex compositional landscape of pseudo-eutectics and exploring the quest for invariant eutectics in MPEAs.

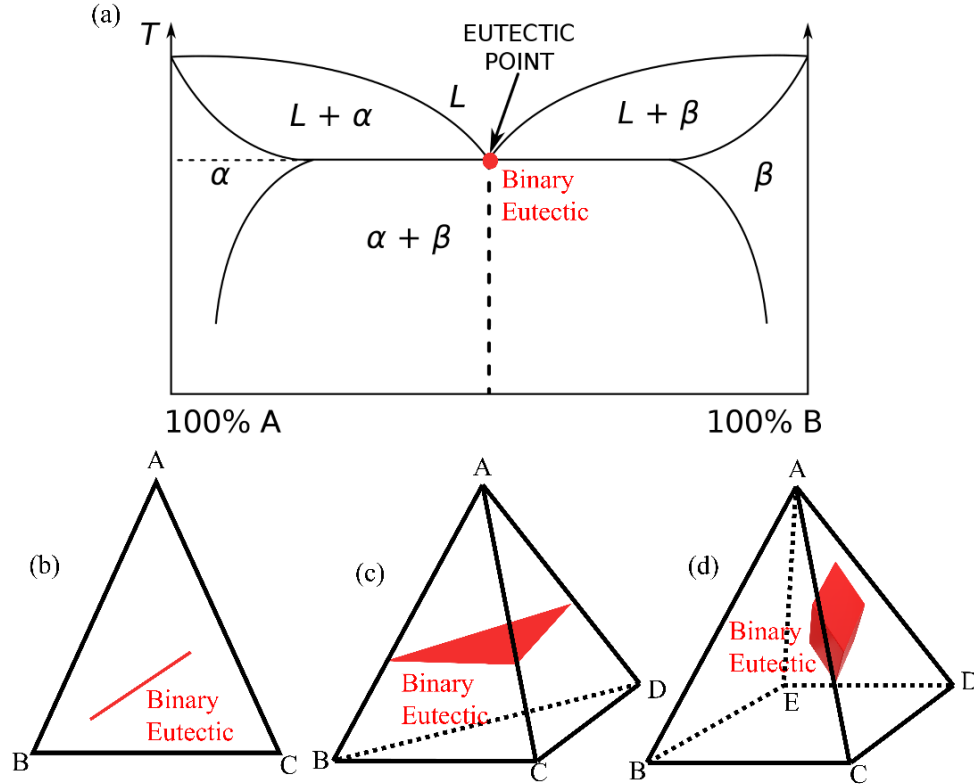


**Figure 6.1:** Representation of two-phase eutectics in different alloy systems: (a) binary, (b) ternary, (c) quaternary and (d) quinary.

To this end, Chapter 6 investigates the complex eutectic compositional landscape in the Al-Cr-Fe-Ni alloy system, selected as a case study due to its cost-effectiveness and potential for lightweight alloy development. Further, the cobalt-free Al-Cr-Fe-Ni system is particularly suited for this systematic exploration, as previous studies have identified two types of dual-phase eutectics in this system: BCC plus B2 and FCC plus B2 [42,142]. This suggests the potential for higher-order eutectics, which Chapter 6 aims to explore in depth. The investigation employs high-throughput (HT) CALPHAD methodology integrated with the *TC-Python* API (Application Programming Interface). The HT CALPHAD approach, known for its computational efficiency and comprehensive databases, enables precise predictions of high-entropy alloy (HEA) compositions and facilitates the down-selection of design space prior to experimental characterization. It has been reported that HT CALPHAD calculations can reliably predict phase stabilities in the Al-Co-Cr-Fe-Ni system [161,162].

## 6.2: Latin Hypercube Sampling in the Al-Cr-Fe-Ni System

The exploration of eutectic compositional space in the Al-Cr-Fe-Ni system commenced with the implementation of Latin Hypercube Sampling (LHS). LHS is a statistical method used to generate samples from multi-dimensional distributions, ensuring efficient mapping of an

alloy composition space. By dividing each element concentration range into equally probable intervals and randomly sampling within these intervals, LHS provides broad coverage with a limited number of samples. This approach is particularly advantageous in high-throughput computational methods like the CALPHAD technique, as it significantly reduces computational costs while maintaining high exploratory dataset representativeness.

In the Al-Cr-Fe-Ni quaternary system, as mentioned above, the compositional landscape is rich and complex. Invariant eutectic points are characterized by the simultaneous presence of four solid phases as a point, while triple-phase eutectics are depicted as lines and dual-phase eutectics as areas. The potential for more complex, higher-order eutectics—whether triple-phase or quadruple-phase—is expected to fall within the bounds established by dual-phase eutectics. A comprehensive literature review of fully eutectic microstructures in the Al-Cr-Fe-Ni system identified the following elemental ranges for complete dual-phase eutectic structures (expressed in atomic percent): Al between 16% and 37%, Cr from 8% to 30%, Fe from 16% to 33% and Ni from 21% to 50%. The LHS script workflow executed on the Google Colab platform, generating 100,000 datasets within these defined confidence intervals for Al, Cr, Fe and Ni, is detailed below.

### 6.2.1: Importing Essential Libraries

```
import pandas as pd  
import numpy as np
```

The script starts by importing pandas and Numpy. 'Pandas is crucial for data manipulation, offering robust tools for organizing generated alloy compositions into structured data formats. Numpy is key for numerical operations, such as generating random numbers, which are essential for the random sampling process in the alloy composition.

### 6.2.2: Ensuring Reproducible Results

```
np.random.seed(0)
```

To ensure that our computational experiments can be replicated, the random number generator is seeded with a value of 0.

### 6.2.3: Setting Parameters for Dataset Generation

```
num_datasets = 100000  
min_values = {'Al': 0.160, 'Cr': 0.080, 'Fe': 0.160, 'Ni': 0.210}  
max_values = {'Al': 0.370, 'Cr': 0.300, 'Fe': 0.330, 'Ni': 0.500}
```

```
target_sum = 1.0000
```

A target of generating 100,000 unique alloy compositions is set to ensure a thorough exploration of the Al-Cr-Fe-Ni system compositional space. The `min_values` and `max_values` dictionaries outline the minimum and maximum atomic percentages for each element, setting the boundaries. The `target_sum` variable ensures that the total proportion of all elements in each composition equals 100%, maintaining a stoichiometric balance.

#### 6.2.4: Preparing Data Structures for Composition Generation

```
datasets = []
```

```
unique_combinations = set()
```

An empty list, `datasets` and `unique_combinations` are prepared to store generated alloy compositions and to ensure each composition is unique, preventing duplicate entries.

#### 6.2.5: Generating Unique Alloy Compositions

```
while len(datasets) < num_datasets:
```

```
    Al = np.random.uniform(min_values['Al'], max_values['Al'])
```

```
    Cr = np.random.uniform(min_values['Cr'], max_values['Cr'])
```

```
    Fe = np.random.uniform(min_values['Fe'], max_values['Fe'])
```

```
    Ni = target_sum - (Al + Cr + Fe)
```

```
    if min_values['Ni'] <= Ni <= max_values['Ni']:
```

```
        Al, Cr, Fe, Ni = round(Al, 4), round(Cr, 4), round(Fe, 4), round(Ni, 4)
```

```
        if dataset_str not in unique_combinations:
```

```
            unique_combinations.add(dataset_str)
```

```
            datasets.append({'Al': Al, 'Cr': Cr, 'Fe': Fe, 'Ni': Ni})
```

The script iterates until 100,000 unique compositions are generated. Random values for Al, Cr and Fe are generated within specified ranges, with the Ni proportion adjusted to ensure the sum of all elements equals 100%. Compositions are rounded for precision and uniqueness is ensured before addition to the datasets.

#### 6.2.6: Saving the Generated Dataset

```
df = pd.DataFrame(datasets)
```

```
csv_filename = 'LHS_Al-Cr-Fe-Ni.csv'
```

```
df.to_csv(csv_filename, index=False)
```

```
print(f'DataFrame saved to {csv_filename}')
```

Generated alloy compositions are saved into a pandas DataFrame and exported to a CSV file named 'LHS\_Al-Cr-Fe-Ni.csv', with index=False to omit row indices. A message confirms the successful saving of the data, enhancing transparency and accessibility for further analysis.

### 6.2.7: Confirmation of Effective LHS Execution

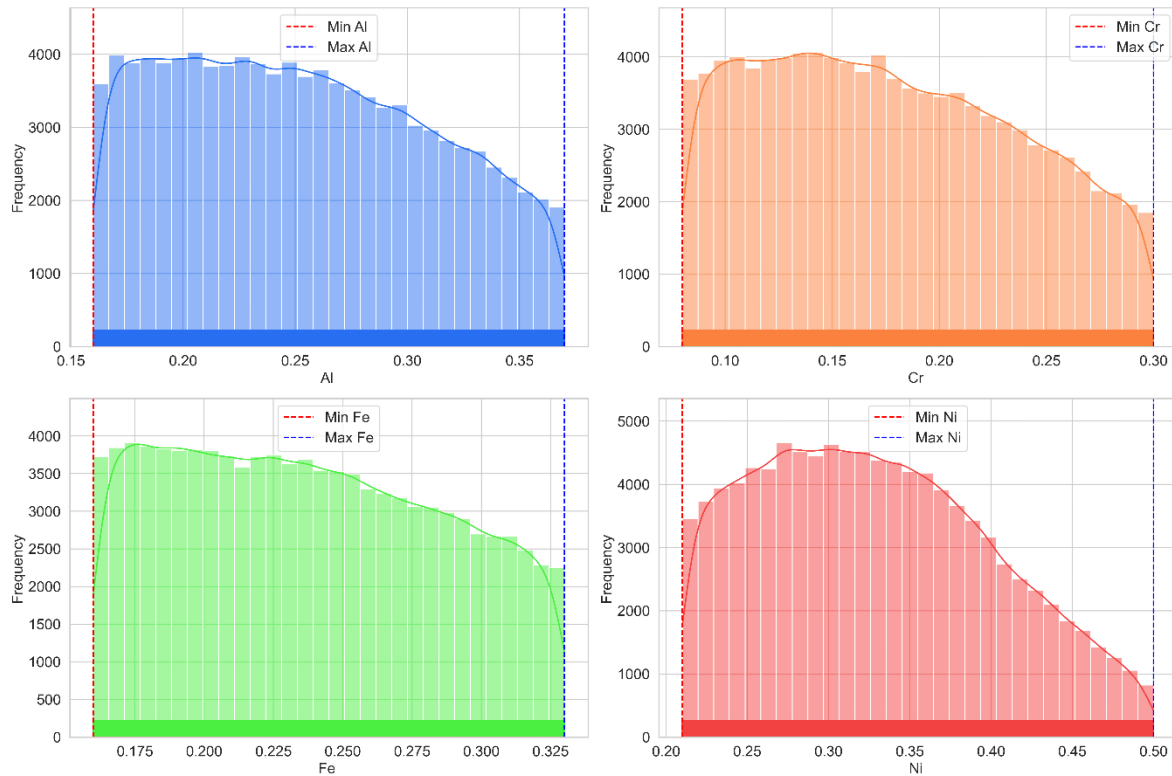


**Figure 6.2:** Histograms showing the LHS distributions of Al, Cr, Fe and Ni.

To validate the LHS results, the output file "LHS\_Al-Cr-Fe-Ni.csv" was analyzed with a focus on two critical aspects: the uniformity across the value ranges for each element (Al, Cr, Fe, Ni) and the orthogonality among these parameters. Uniformity ensures comprehensive coverage of the parameter space, while orthogonality guarantees that sampling of one parameter is independent of others—both are essential for unbiased sampling in multi-dimensional space. The initial analysis involved generating histograms and kernel density estimates (KDE) for each element. As depicted in **Figure 6.2**, the distributions for Al, Cr, Fe and Ni were relatively uniform, confirming that a diverse set of compositions was evenly sampled. This uniformity indicates that the LHS method effectively covered the range of possible values for each element, demonstrating its capability to uniformly sample the parameter space. Following this, a correlation matrix was computed to evaluate orthogonality. The correlation coefficients were close to zero, indicating a minimal linear relationship among

the parameters, as shown in **Figure 6.3**. This low correlation confirms the orthogonality of the LHS process, affirming that the value selection for any given element is statistically independent of the others.

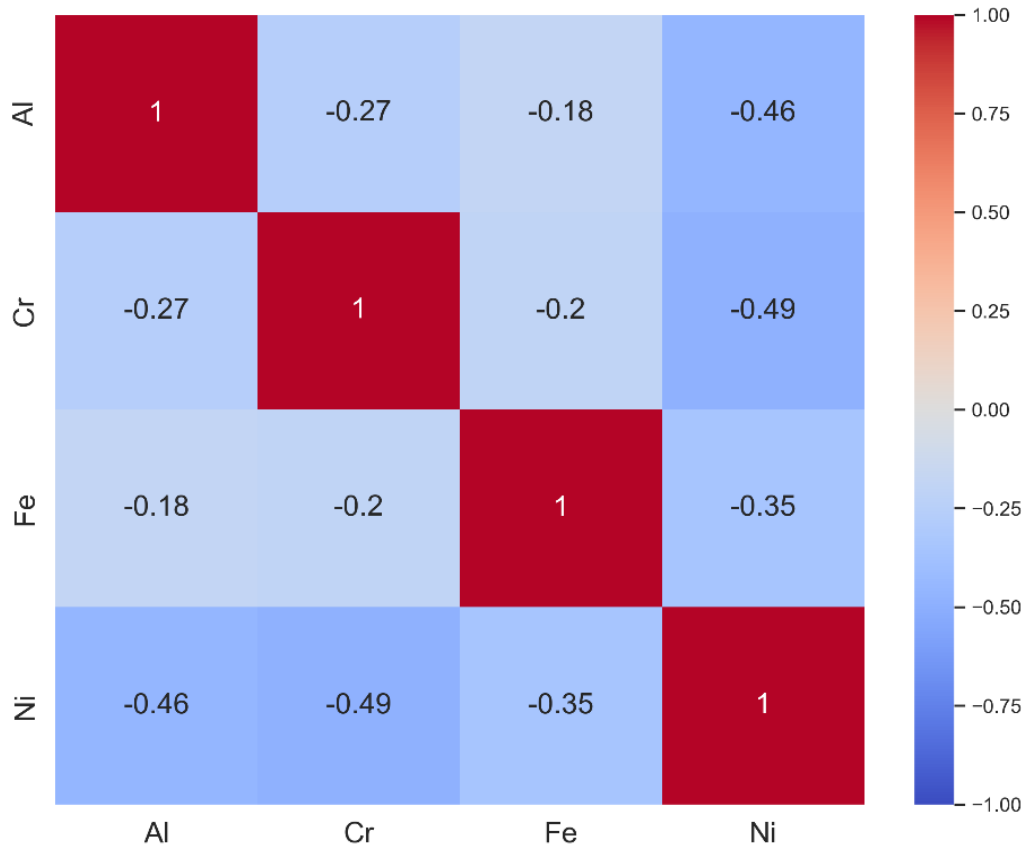


**Figure 6.3:** Heatmap of correlation coefficients among the elements Al, Cr, Fe and Ni.

### 6.3: In-House *Python* Script for Eutectic Identification

The solidification behaviour at the eutectic point, illustrated in **Figure 6.1(a)**, is further clarified by the schematic phase evolution plot in **Figure 6.4(a)**. At the eutectic temperature,  $T_E$ , the liquid phase, L, transitions directly to the solid phases  $\alpha$  and  $\beta$ , similar to the melting behaviour of pure metals. This transition is marked by a vertical liquidus line, indicating a single, distinct melting temperature without a solidification range. In quaternary alloy systems, the invariant eutectic involves the simultaneous melting of four solid phases  $\alpha$ ,  $\beta$ ,  $\gamma$  and  $\delta$  at  $T_E$ . This scenario is depicted in **Figure 6.4(b)**, where  $T_\alpha$ ,  $T_\beta$ ,  $T_\gamma$ ,  $T_\delta$  and  $T_L$  are all aligned at the same temperature point.

However, as discussed in Chapter 2, most reported eutectic compositions in multi-principal element systems, whether quaternary or higher, typically exhibit only two-phase eutectics. These systems are more accurately represented by the schematic in **Figure 6.4(c)**,



where the  $\alpha$  and  $\beta$  phases solidify over a temperature range. Such systems are more appropriately termed pseudo-eutectics. Even if temperatures  $T_L$ ,  $T_\alpha$  and  $T_\beta$ , many compositions may display similar behaviour. They still do not satisfy the Gibbs phase rule, which requires that the number of phases melting simultaneously must be achieved at a single temperature, thereby maintaining their classification as pseudo-eutectics.

This observation highlights a clear distinction between pseudo-eutectics and true (invariant) eutectics. A system with 'n' elements exhibits true eutectic behaviour only if all 'n' solid phases melt simultaneously at a single temperature without any temperature range. In contrast, formations that do not meet this stringent criterion should be classified as pseudo-eutectics. An in-house *Python* script has been developed based on this understanding to identify invariant eutectic compositions and map the pseudo-eutectic compositional space in these complex alloy systems utilizing *Thermo-Calc*. The following sections provide a brief, logical workflow of this script.

### 6.3.1: Imports and Initialization:

- The script begins by importing necessary *Python* modules: '**TC-Python**' for accessing *Thermo-Calc Python* API, '**os**' for operating system interfaces (such as file paths), '**numpy**' (aliased as '**np**') for numerical operations and '**pandas**' (aliased as '**pd**') for handling tabular data.

### 6.3.2: Function Definitions:

- **get\_liquidus(calc\_obj)**: Determines the liquidus temperature of an alloy. This function modifies the thermodynamic calculation object to fix the phase of the alloy to 'LIQUID' and calculates the corresponding temperature at which the alloy is fully liquid.
- **get\_solidus(calc\_obj)**: Similar to '**get\_liquidus**', but calculates the solidus temperature, the temperatures below which the alloy is completely solid, by setting the 'LIQUID' phase fraction to be zero.
- **get\_phases(calc\_obj)**: Returns the names of stable phases present under the current conditions set in the calculation object.
- **get\_phases\_fractions(calc\_obj, phase\_names)**: calculates and returns the fractions of specified phases within the alloy.
- **Set\_multiple\_conditions(solutes, conc, comp\_choice)**: Constructs a string command for setting the composition of the alloy in *Thermo-Calc* based on the solutes and their concentrations.

### 6.3.3: Configuration and Input Data:

- The script specifies the thermodynamic database and the elements involved in the calculations. For this case, the database is "TCHEA5" with 'Ni' as the solvent and "Al", "Cr" and "Fe" as solutes.
- It reads an input CSV file ("chunk 1.csv") containing alloy compositions into a pandas DataFrame and prepares additional columns for the calculated properties.

### 6.3.4: Thermo-Calc Setup and Calculations:

- The script initializes a *Thermo-Calc* session and configures it for single-point equilibrium calculations with specific conditions.
- For each alloy composition in the DataFrame, the script:
  - Constructs a condition string for the composition.
  - Performs equilibrium calculations at 1000 degrees to establish a baseline.
  - Calculates each phase formation temperature.
  - Determines the difference between liquidus and solidus temperatures to infer the range of temperatures over which the alloy transitions from liquid to solid.
  - Identifies if a composition is eutectic based on the narrow liquidus-solidus range and the presence of more than one phase just below the solidus temperature.
  - Extracts and records the stable phases and their fractions at a temperature slightly below the solidus.

### 6.3.5: Error Handling and Logging:

- The script includes try-except blocks to gracefully handle errors during calculations, allowing the script to skip problematic compositions without halting execution.

### 6.3.6: Output:

- After processing all alloy compositions, the script writes the updated DataFrame to a new CSV file, including the calculated thermodynamic properties and phase information.

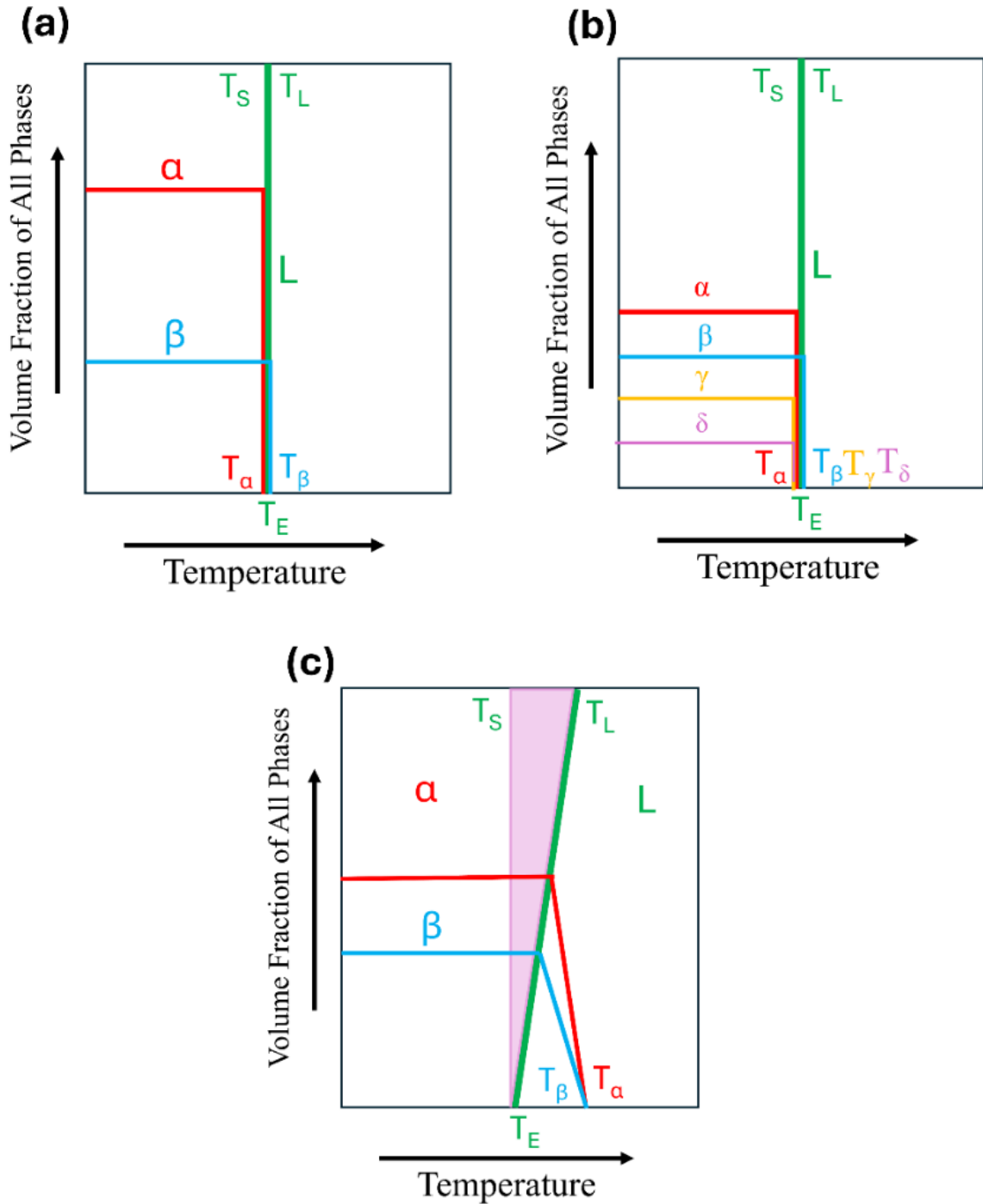


**Figure 6.4:** Schematic illustrations of (a) binary and (b) quaternary systems with the invariant eutectic at a single melting temperature and (c) quaternary system displaying the pseudo-eutectic behaviour over a temperature range.

Utilizing the *TCHEA5.1* database for equilibrium calculations, the in-house *Python* script interfaces with *Thermo-Calc* software to process all 100,000 LHS compositions. This script calculates key thermodynamic parameters, including liquidus and solidus temperatures, identifies stable phases along with their formation temperatures and determines eutectic

compositions. The results are organized into a pandas DataFrame and exported to Excel, with a classification column indicating '1' for eutectic compositions and '0' for non-eutectic ones.

To identify eutectic compositions within the Al-Cr-Fe-Ni system, the script employs a criterion based on minimal temperature differences ( $\Delta T$ ) among the solid phase formation temperatures. This approach ensures the identification of compositions with multiple solid phases just below the solidus temperature, thereby excluding results related to spinodal decomposition or congruent melting. Although the Gibbs phase rule implies that a true invariant four-phase eutectic point would exhibit no temperature difference between the liquidus and solidus, practical observations often show a dual-phase structure with a measurable solidification range rather than a strict zero temperature difference ( $\Delta T(L-S)$ ). This highlights that a zero or near-zero  $\Delta T(L-S)$  may not fully capture all eutectics, particularly those with broad solidification ranges, such as pseudo-eutectics.

Accordingly, the script uses a criterion based on the temperature difference ( $\Delta T$ ) among all solid phases formed within the liquidus-solidus interval. This method encompasses both narrow and broad solidification eutectics. Supported by literature, including DSC analyses of fully eutectic dual-phase structures in the Al-Cr-Fe-Ni system, a threshold of  $\Delta T \leq 25$  K is established. This threshold effectively identifies eutectics, whether comprising dual, triple, or quadruple phases. Thus, the in-house *Python* script is designed to search for all possible eutectics, including both invariant and pseudo-eutectics.

#### 6.4: No Invariant Eutectic in Al-Cr-Fe-Ni

Using the *Spyder* platform, the in-house *TC-Python* script evaluated 100,000 compositions. The results, shown in **Figures 6.5 and 6.6**, revealed 15,660 dual-phase eutectics with BCC plus B2, 5,699 eutectics with FCC plus B2 and 1,260 triple-phase eutectics involving FCC, B2 and BCC phases. However, no compositions resulting in four-phase eutectics were identified. This finding aligns with the observed trend in MPEAs, where invariant (four-phase) eutectics have not been reported, even in high-throughput calculations.

High configurational entropy in high-entropy alloys (HEAs) typically promotes the formation of at least one disordered solid solution phase, such as FCC or BCC, rather than a complete array of compounds. This trend is evident even in binary systems, where metals A and B form eutectic phases only when lacking solid-state affinity, solidifying separately as  $A_xB_y$  below their respective temperatures  $T_A$  and  $T_B$  (thermodynamically, the eutectic is a failed chemical compound) [163]. Conversely, elements with solid-phase affinity and close mixing

enthalpy in the liquid phase, such as Co-Ni ( $\Delta H_{\text{mix}} = -0.20 \text{ kJ/mol}$ ) or Fe-Cr ( $\Delta H_{\text{mix}} = -1.50 \text{ kJ/mol}$ ), are less likely to form eutectic phases and instead favour the formation of FCC and BCC disordered solid solutions, respectively, even with sub-regular solutions [86]. In eutectic high-entropy alloys (EHEAs) like Al-Co-Cr-Fe-Ni, disordered solid solution phases, typically FCC or BCC, usually consist of Ni-Co-Fe-Cr or Al-Co-Cr-Fe, with only one intermetallic phase, NiAl, regardless of Al content [164]. The frequent formation of either a BCC-disordered solid solution of Fe-Cr or an FCC of Ni-Fe-Cr further underscores the improbability of forming an invariant eutectic in the Al-Cr-Fe-Ni system. This preference for a disordered solid solution as one of the phases in eutectic HEAs deviates from conventional pathways, making invariant eutectic formation less favourable. This preference, driven by the negative Gibbs free energy change associated with high configurational entropy, disrupts the specific compositional and thermal conditions necessary for a eutectic reaction, which requires the simultaneous solidification of four phases from a liquid at a specific temperature and composition. Thus, achieving an invariant eutectic in HEAs would necessitate suppressing configurational entropy, possibly through high negative enthalpy of mixing among all elements, resulting in distinct compounds or ordered solid solutions rather than a single disordered solid solution. Additional CALPHAD calculations across a broad compositional range (~100,000 compositions with 5 to 85 atomic percent for each element) in the Al-Cr-Fe-Ni system also did not reveal any invariant eutectic formations, reinforcing this hypothesis.

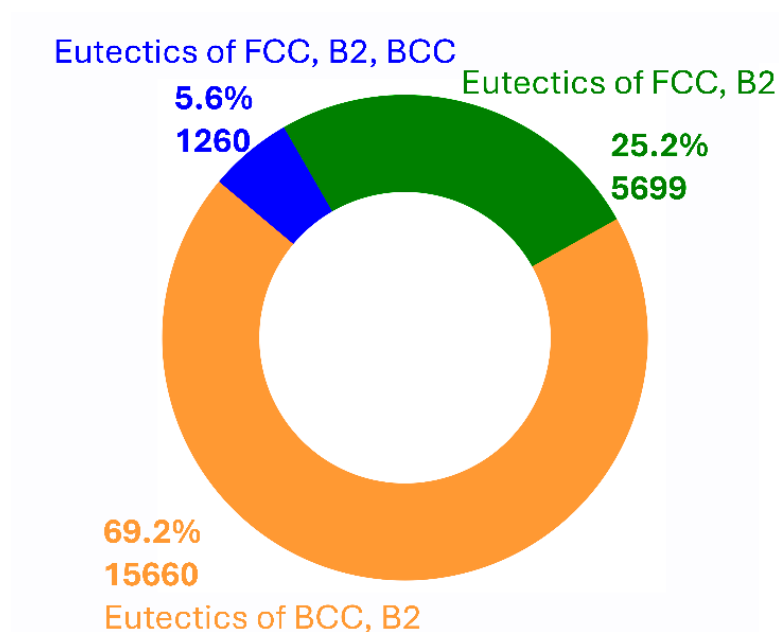


**Figure 6.5:** Proportion of eutectic types in the Al-Cr-Fe-Ni alloy system.

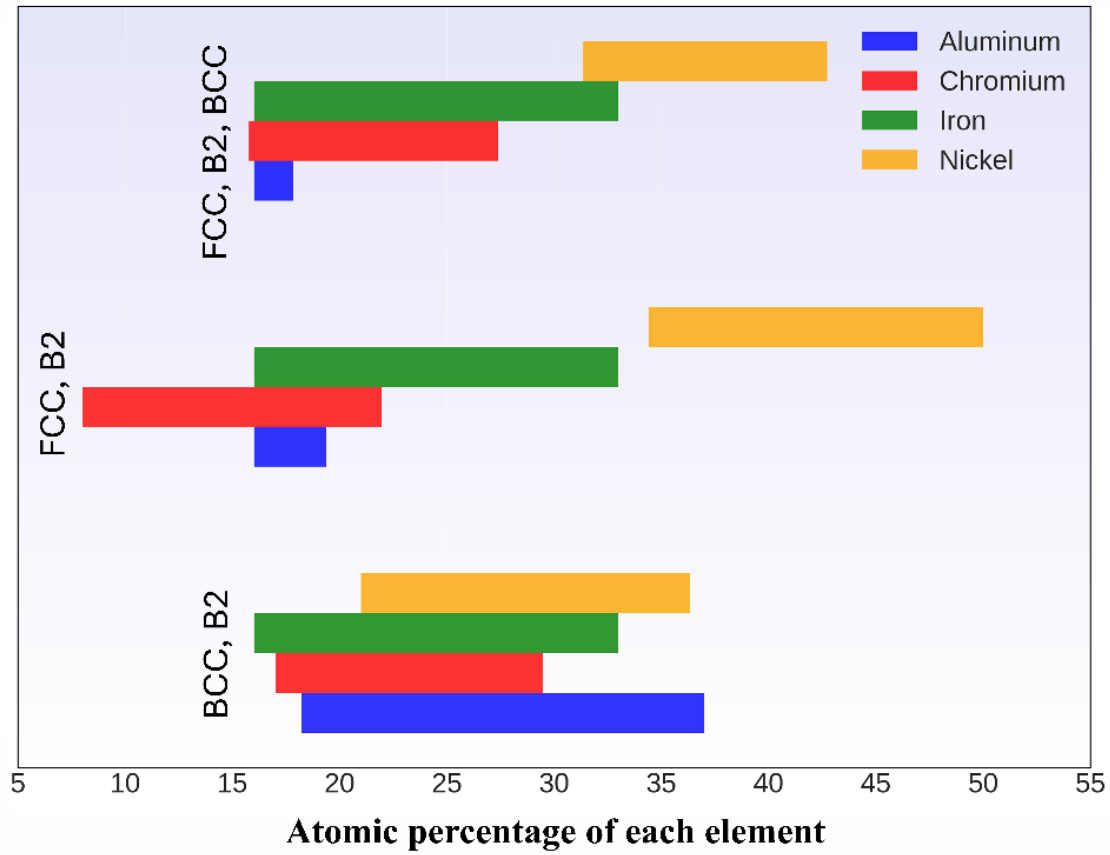


**Figure 6.6:** Elemental composition ranges for eutectics in the Al-Cr-Fe-Ni alloy system.

### 6.5: Comparison of *TC-Python* Predictions with Reported Alloys

The scatter plot in **Figure 6.7** illustrates the relationship between the liquidus-solidus temperature difference ( $\Delta T(L-S)$ , on the X-axis) and the temperature difference among solid phase formation temperatures ( $\Delta T$ , on the Y-axis) or compositions in the Al-Cr-Fe-Ni system. Data points falling within a  $\Delta T \leq 25$  K threshold are indicative of potential eutectic compositions. Points exhibiting minimal  $\Delta T$  but greater  $\Delta T(L-S)$  values correspond to pseudo-eutectics, which likely represent dual or triple-phase structures with broader solidification ranges. This distribution confirms the capability of the script in identifying a range of eutectic behaviours, from true invariant eutectic to prevalent pseudo-eutectics, adhering to the Gibbs phase rule.

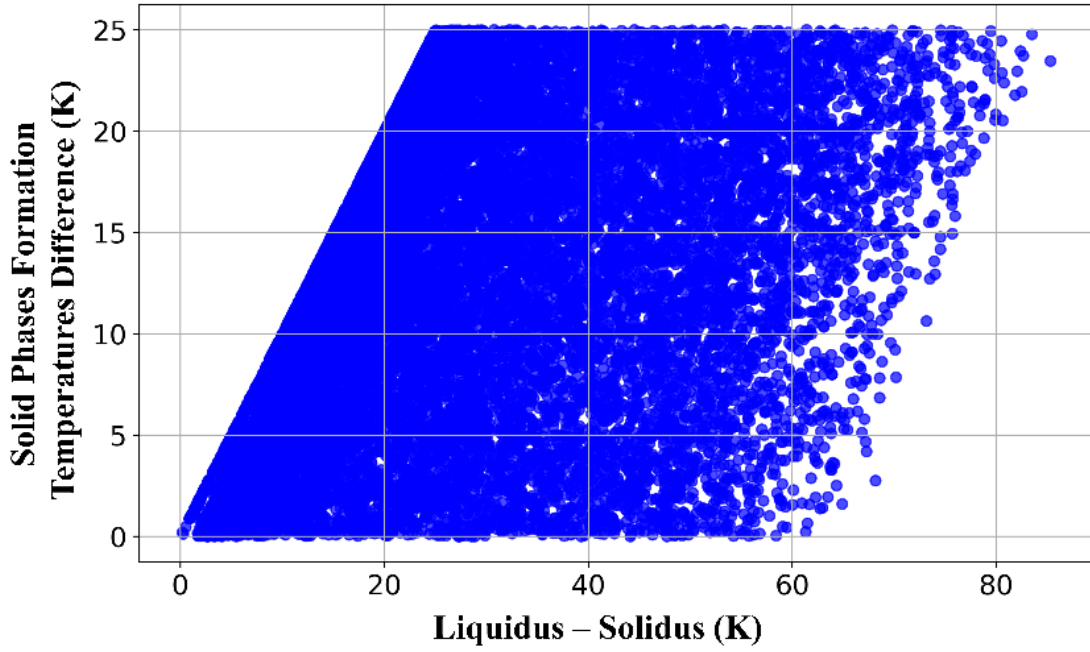


**Figure 6.7:** Scatter plot of temperature differences between solid phase formation and liquidus-solidus temperatures for eutectics in the Al-Cr-Fe-Ni alloy system.

To validate the *TC-Python* approach, **Table 6.1** compares its predictions with experimentally reported eutectic alloys in the Al-Cr-Fe-Ni system. The comparison criteria include composition accuracy, Euclidean distance as a measure of compositional similarity, eutectic phases and temperature differences ( $\Delta T$ ). Euclidean distance, calculated in multi-dimensional compositional space, reflects the proximity between predicted and experimental compositions; smaller distances indicate higher compositional similarity. The results in **Table 6.1** reveal a strong correlation between *TC-Python* predictions and experimental data, with Euclidean distances ranging from 0.00024 to 0.00432. This close agreement underscores the method precision attributed to the large dataset of 100,000 data points and the narrow confidence composition intervals considered. The predictions encompass various eutectic phases, including BCC-ordered (B2) and disordered (A2) structures, demonstrating the *TC-Python* capability to forecast complex microstructural characteristics accurately. The sublattice symmetry approach effectively differentiates between ordered and disordered structures. Additionally, the  $\Delta T$  values provide insights into thermal stability and phase formation temperatures, further validating the reliability of the method. However, the elemental range for these predictions is based on a limited number of reported alloys with fully eutectic dual-phase microstructures, implying the need for further exploration of the broader compositional space.

**Table 6.1:** Comparison of *TC-Python* calculated and experimentally reported EHEA compositions of Al-Cr-Fe-Ni (E = Experimental, C = Calculated).

SN	E/C	Composition	Euclidean distance	Eutectic phases	$\Delta T$ (L-S) (K)	Ref.
01	E	Al <sub>16.4</sub> Cr <sub>16</sub> Fe <sub>24</sub> Ni <sub>43.6</sub>	0.00187	FCC, B2	5.80	[142]
	C	Al <sub>16.46</sub> Cr <sub>16.03</sub> Fe <sub>24.07</sub> Ni <sub>43.44</sub>		BCC_B2 ORD (AL,FE:NI:VA); FCC_L12 DISORD (NI,FE:NI,FE:VA)		
02	E	Al <sub>16.67</sub> Cr <sub>16.67</sub> Fe <sub>16.67</sub> Ni <sub>50</sub>	0.00214	FCC, B2	11.45	[113]
	C	Al <sub>16.79</sub> Cr <sub>16.72</sub> Fe <sub>16.5</sub> Ni <sub>49.99</sub>		BCC_B2 ORD (AL:NI:VA); FCC_L12 DISORD (NI,CR:NI,CR:VA)		
03	E	Al <sub>16.6</sub> Cr <sub>12</sub> Fe <sub>28</sub> Ni <sub>43.4</sub>	0.00068	FCC, B2	7.24	[142]
	C	Al <sub>16.61</sub> Cr <sub>11.96</sub> Fe <sub>27.98</sub> Ni <sub>43.45</sub>		BCC_B2 ORD (AL,FE:NI:VA); FCC_L12 DISORD (NI,FE:NI,FE:VA)		
04	E	Al <sub>16.7</sub> Cr <sub>19.8</sub> Fe <sub>16.7</sub> Ni <sub>46.8</sub>	0.00273	FCC, B2	5.71	[71]
	C	Al <sub>16.7</sub> Cr <sub>20.01</sub> Fe <sub>16.53</sub> Ni <sub>46.76</sub>		BCC_B2 ORD (AL:NI:VA); FCC_L12#2 DISORD (NI,CR:NI,CR:VA)		
05	E	Al <sub>16.95</sub> Cr <sub>16.95</sub> Fe <sub>19.1</sub> Ni <sub>47</sub>	0.00190	L12/B2	5.29	[165]
	C	Al <sub>16.92</sub> Cr <sub>17.01</sub> Fe <sub>18.96</sub> Ni <sub>47.11</sub>		BCC_B2 ORD (AL:NI:VA); FCC_L12#2 DISORD (NI,FE:NI,FE:VA)		
06	E	Al <sub>17</sub> Cr <sub>17</sub> Fe <sub>24.5</sub> Ni <sub>41.5</sub>	0.00227	FCC, B2	3.15	[71]
	C	Al <sub>16.86</sub> Cr <sub>17.02</sub> Fe <sub>24.67</sub> Ni <sub>41.45</sub>		BCC_B2 ORD (AL,FE:NI:VA); FCC_L12 DISORD (NI,FE:NI,FE:VA)		
07	E	Al <sub>16</sub> Cr <sub>20</sub> Fe <sub>20</sub> Ni <sub>44</sub>	0.00352	FCC, B2	7.56	[46,142,166,167]
	C	Al <sub>16.11</sub> Cr <sub>20.23</sub> Fe <sub>19.85</sub> Ni <sub>43.81</sub>		BCC_B2 ORD (AL:NI:VA); FCC_L12 DISORD (NI,CR:NI,CR:VA)		
08	E	Al <sub>17</sub> Cr <sub>8</sub> Fe <sub>32</sub> Ni <sub>43</sub>	0.00253	FCC, B2	8.20	[142]
	C	Al <sub>16.8</sub> Cr <sub>8.15</sub> Fe <sub>32.02</sub> Ni <sub>43.03</sub>		BCC_B2 ORD (AL,FE:NI:VA); FCC_L12#2 DISORD (NI,FE:NI,FE:VA)		
09	E	Al <sub>25</sub> Cr <sub>25</sub> Fe <sub>25</sub> Ni <sub>25</sub>	0.00095	BCC, B2	< 30	[168,169]



	C	Al <sub>25.01</sub> Cr <sub>24.98</sub> Fe <sub>25.07</sub> Ni <sub>24.94</sub>		BCC_B2 DISORD (CR,FE:CR,FE:VA); BCC_B2#2 ORD (NI:AL:VA)	7.75	
	E	Al <sub>26.83</sub> Cr <sub>24.39</sub> Fe <sub>24.39</sub> Ni <sub>24.39</sub>		BCC, B2	< 30	[42]
10	C	Al <sub>26.82</sub> Cr <sub>24.38</sub> Fe <sub>24.39</sub> Ni <sub>24.41</sub>	0.00024	BCC_B2 DISORD (CR,FE:CR,FE:VA); BCC_B2#2 ORD (AL:NI:VA)	1.80	
	E	Al <sub>16.39</sub> Cr <sub>16.39</sub> Fe <sub>24.59</sub> Ni <sub>42.62</sub>		FCC, B2		[72]
11	C	Al <sub>16.42</sub> Cr <sub>16.29</sub> Fe <sub>24.46</sub> Ni <sub>42.83</sub>	0.00268	BCC_B2 ORD (AL,FE:NI:VA); FCC_L12#2 DISORD (NI,FE:NI,FE:VA)	5.35	
	E	Al <sub>28.57</sub> Cr <sub>23.81</sub> Fe <sub>23.81</sub> Ni <sub>23.81</sub>		BCC, B2	< 30	[42]
12	C	Al <sub>28.65</sub> Cr <sub>23.92</sub> Fe <sub>23.72</sub> Ni <sub>23.71</sub>	0.00191	BCC_B2 DISORD (CR,FE:CR,FE:VA); BCC_B2#2 ORD (NI:AL:VA)	6.78	
	E	Al <sub>29.41</sub> Cr <sub>23.53</sub> Fe <sub>23.53</sub> Ni <sub>23.53</sub>		BCC, B2		[168,170]
13	C	Al <sub>29.7</sub> Cr <sub>23.37</sub> Fe <sub>23.65</sub> Ni <sub>23.28</sub>	0.00432	BCC_B2 DISORD (CR,FE:CR,FE:VA); BCC_B2#2 ORD (AL:NI:VA)	10.58	
	E	Al <sub>30.23</sub> Cr <sub>23.25</sub> Fe <sub>23.25</sub> Ni <sub>23.25</sub>		BCC, B2	< 30	[42,171]
14	C	Al <sub>30.33</sub> Cr <sub>23.54</sub> Fe <sub>23.14</sub> Ni <sub>22.99</sub>	0.00417	BCC_B2 DISORD (CR,FE:CR,FE:VA); BCC_B2#2 ORD (AL:NI:VA)	10.45	
	E	Al <sub>33.33</sub> Cr <sub>22.22</sub> Fe <sub>22.22</sub> Ni <sub>22.22</sub>		BCC, B2		[168,170]
15	C	Al <sub>33.5</sub> Cr <sub>22.15</sub> Fe <sub>22.19</sub> Ni <sub>22.16</sub>	0.00196	BCC_B2 DISORD (CR,FE:CR,FE:VA); BCC_B2#2 ORD (AL:NI:VA)	21.15	

## 6.6: The Compositional Space of B2 Plus FCC Eutectics in Al-Cr-Fe-Ni

Among the various phases frequently reported in the literature on EMPEAs—namely, FCC, BCC, B2, L1<sub>2</sub>, Laves, Sigma and  $\mu$  phases—the combination of a dual-phase eutectic comprising FCC and B2 phases has been shown to offer superior strength-ductility synergy. This is illustrated in Chapter 5, where the (AlCoFe)<sub>55</sub>(Ni)<sub>45</sub> alloy exhibits a strength-ductility synergy comparable to AlCoCrFeNi<sub>2.1</sub>. However, the cobalt content, constituting 18.3 atomic percent in this alloy, may not be cost-effective or lightweight enough for applications limited to room temperature. As discussed in Chapter 1, the Al-Cr-Fe-Ni system, featuring the FCC plus B2 phase combination, is identified as suitable for use in centrifugal pump impellers. This

positions the compositional space of this two-phase combination as a promising area for further exploration. To facilitate the development of new alloys beyond the existing dataset, it is essential to understand the elemental ranges and phase formation rules. Thus, eight alloy design descriptors—enthalpy of mixing, entropy of mixing, melting point, omega, density, electronegativity, valence electron concentration and atomic size difference—are calculated for all compositions. Given the extensive number of compositions, efficient calculation of these descriptors is crucial. An in-house *Python* script, executed on the Google Colab platform, has been developed to address this need. A generalized workflow for this script is outlined below.

#### **6.6.1: Initialization and Data Preparation**

- The class is initialized with an Excel file containing alloy compositions. This file is read into a pandas DataFrame.
- Missing values in the DataFrame are filled with 0.0 to ensure numerical calculations can proceed without interruption.

#### **6.6.2: Element Data and Enthalpy of Mixing Definitions**

- A dictionary, `element_data_dict`, contains detailed properties for each element, such as atomic number, atomic weight, density, melting point, electronegativity, atomic radius and VEC.
- Another dictionary, `enthalpy_mix_dict`, defines the enthalpy of mixing between element pairs, which is essential for calculating the enthalpy of mixing for the alloys.

#### **6.6.3: Composition Adjustments**

- The method `divide_100` adjusts the alloy compositions from percentages to fractions if the values exceed 1, assuming they're meant to be represented as fractions of 1 for the calculation.

#### **6.6.4: Sum of Elements Check**

- Methods `sum_elements` and `sum_acceptable` are used to calculate the total sum of elements in a composition and check if this sum is within an acceptable range (0.990 to 1.010), ensuring that the alloy compositions are correctly normalized.

#### **6.6.5: Property Calculations**

- The class includes methods to calculate each of the desired properties:

- `calculate_vec`: Calculates the VEC for an alloy.
- `Find_entropy`: Calculates the entropy of mixing ( $\Delta S_{mix}$ ) using the ideal solution model.
- `electronegativity`: Calculates the standard deviation of electronegativity ( $\Delta\chi$ ) for the alloy, indicating the uniformity of electronegativity among constituents.
- `find_asd`: Calculates the atomic size difference ( $\delta$ ) to measure size mismatch among constituent elements.
- `find_enthalpy`: Calculates the enthalpy of mixing ( $\Delta H_{mix}$ ) for the alloy.
- `density`: Calculates the theoretical density ( $\rho$ ) of the alloy using the rule of mixtures.
- `find_Tm`: Calculates the theoretical melting point ( $T_m$ ) of the alloy.
- `find_omega`: Calculates the omega parameter ( $\Omega$ ), which is a function of  $T_m$ ,  $\Delta S_{mix}$  and  $\Delta H_{mix}$ .

#### 6.6.6: Processing the DataFrame

- The method `process_dataframe` applies all the previously defined calculation methods to the DataFrame containing the alloy compositions. It adjusts composition values, calculates all the defined properties for each alloy and appends these properties as new columns in the DataFrame.

#### 6.6.7: Output

- Finally, the updated DataFrame with all calculated properties is exported to an Excel file, named using the input file name prefixed with 'Output'.

Executed in the Google Colab environment, the in-house *Python* script has elucidated the correlation between thermodynamic descriptors and eutectic formation. As illustrated in **Figure 6.8**, the heatmap generated reveals significant correlations between VEC, density and atomic size difference. These descriptors are particularly crucial for predicting the formation of eutectics featuring B2 plus FCC phases. Notably, VEC exhibits a strong positive correlation with density (0.92) and with the indicator for B2 plus FCC eutectic formation (0.45). This suggests that an increase in the average number of valence electrons not only increases density but also enhances the likelihood of forming a B2 plus FCC eutectic structure. In contrast, VEC shows a pronounced negative correlation with atomic size difference (-0.80), indicating that alloys with a higher count of valence electrons tend to have smaller atomic size differences. The entropy of mixing displays a weaker negative correlation with the B2 plus FCC eutectic criterion (-0.38), suggesting limited capability to predict this eutectic type. Conversely, the

enthalpy of mixing is moderately positively correlated with density (0.77) and shows a slight positive relationship with the B2 plus FCC eutectic (0.30). This implies that higher enthalpy values may be associated with denser materials and slightly increase the probability of forming a B2 plus FCC eutectic. The most substantial negative correlation is observed between atomic size difference and density (-0.96), highlighting a strong inverse relationship: as atomic size differences increase, alloy density significantly decreases. This attribute also shows a negative correlation with the B2 plus FCC eutectic characteristic (-0.40), indicating that larger atomic size differences may reduce the likelihood of forming a B2 plus FCC eutectic. These findings highlight the significant differences in VEC and atomic size between Al and the elements Cr, Fe and Ni, which are crucial for eutectic formation and contribute to a narrower compositional range for Al compared to the other elements.

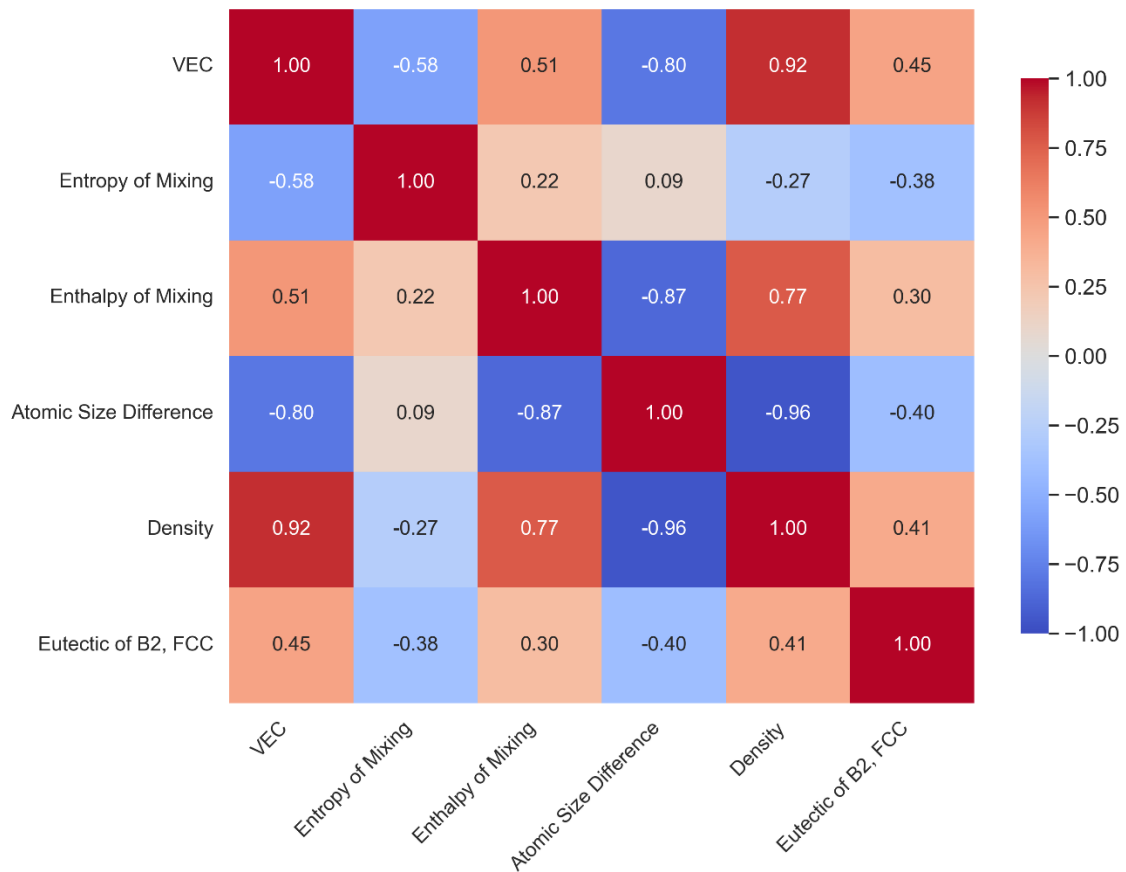


**Figure 6.8:** Heatmap displaying the correlations between thermodynamic descriptors for B2 and FCC eutectics.

As depicted in **Figure 6.6**, the compositional range for Al is indeed confined to 15 to 20 atomic percent. The 2D scatter plots in **Figure 6.9** illustrate the intricate interplay between the enthalpy of mixing, VEC and atomic size difference within the B2 plus FCC phases eutectic

space of the Al-Cr-Fe-Ni system. Alloys within this defined space are highly likely to exhibit eutectic behaviour with the B2 and FCC phases. Specifically, the compositional ranges where this eutectic formation is prevalent are  $16 \leq \text{Al} \leq 19.38$ ,  $8 \leq \text{Cr} \leq 21.95$ ,  $16 \leq \text{Fe} \leq 33$  and  $34.40 \leq \text{Ni} \leq 50$  atomic percent.

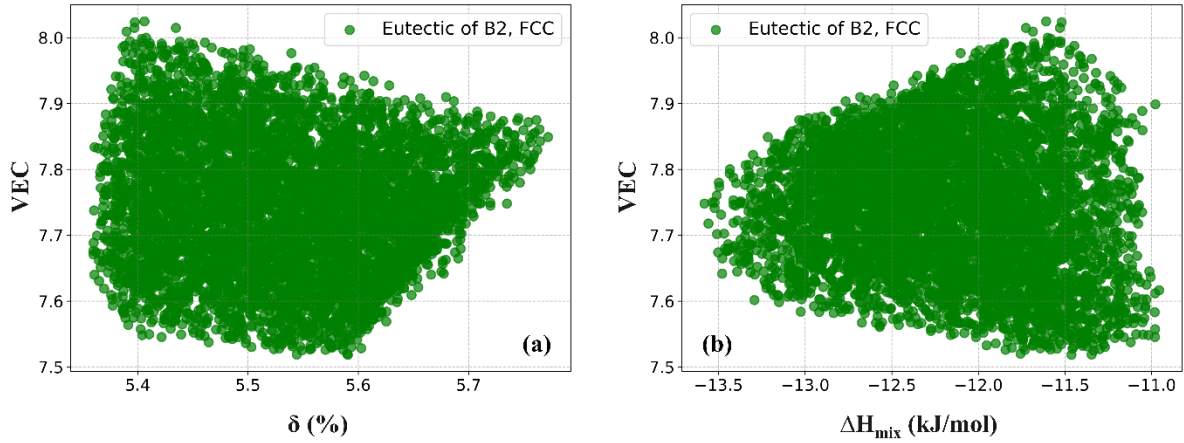


**Figure 6.9:** Scatter plots of (a) Valence Electron Concentration (VEC) vs atomic size difference ( $\delta\%$ ) and (b) VEC vs enthalpy of mixing ( $\Delta H_{\text{mix}}$ ).

To further validate the identified compositional space, the next step involves synthesizing an alloy with a B2 plus FCC eutectic structure and conducting experimental validation. Designing an alloy that balances lightweight and cost-effective characteristics with optimal mechanical properties requires empirical insights into how each element influences the overall properties within the Al-Cr-Fe-Ni system. In this context, Mao *et al.* [142] have demonstrated that Cr enhances yield strength in Al-Cr-Fe-Ni eutectic alloys. Conversely, Diao *et al.* [172] have observed that increasing Fe content adversely affects yield strength. Given that the Al content is specified to range between 16 and 19.38 atomic percent, as indicated in **Figure 6.6**, an optimized alloy composition would favor higher allocations of Al and Cr while minimizing Fe. This strategic composition is anticipated to result in an alloy that is both lightweight and yet has higher yield strength. Advancing this notion, the "single phase plus EFE" methodology introduced in the previous Chapter (5) was applied to develop an alloy with a nominal composition of  $(\text{AlCrFe})_{52.8}(\text{Ni})_{47.2}$ , where Al, Cr and Fe each constitute 17.6 atomic percent and Ni makes up the remaining 47.2 percent. Theoretical calculations suggest that this alloy has a density of 6.95 g/cc. A comparison of the VEC, enthalpy of mixing and other thermodynamic descriptors of the designed alloy with those in the B2 plus FCC eutectic compositional space in the Al-Cr-Fe-Ni system is presented in **Table 6.2**. This comparison

confirms that  $(\text{AlCrFe})_{52.8}(\text{Ni})_{47.2}$  is within the compositional space associated with the identified B2 plus FCC.

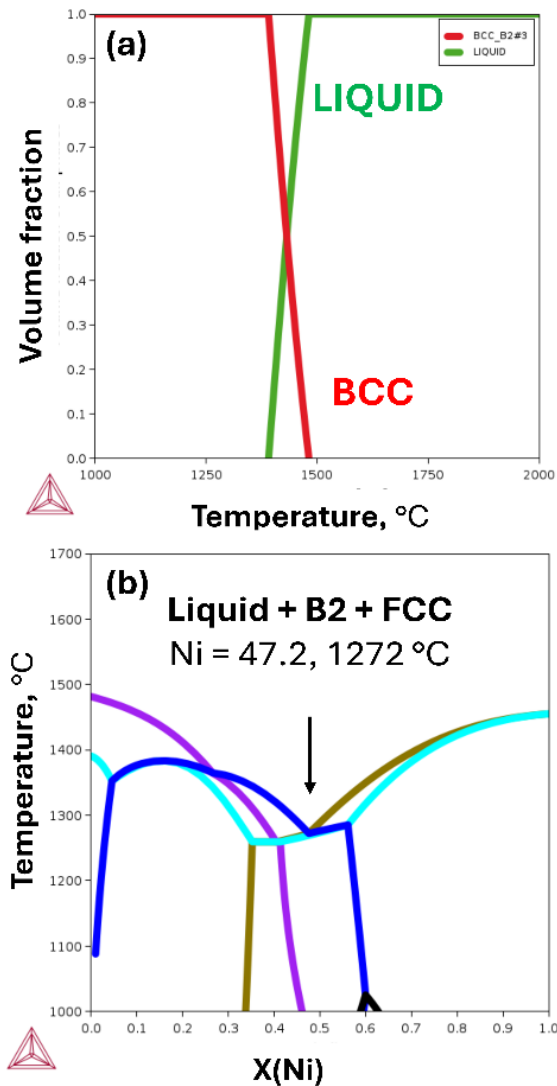


**Figure 6.10:** (a) Phase evolution plot for AlCrFe and (b) pseudo-binary phase diagram of AlCrFe-Ni.

Following the initial step of the single-phase plus EFE approach, AlCrFe is identified as a single-phase BCC, as depicted in **Figure 6.10(a)**. This observation was in line with the known tendency of Fe-Cr to form a disordered BCC structure and the similar BCC formation tendencies of both Al-Cr and Al-Fe combinations. Nickel is identified as the EFE, forming an ordered BCC (B2) phase with Al, characterized by an enthalpy of mixing of -22.30 kJ/mol and a long-range order parameter ('L') of 0.92. Notably, Ni forms a binary eutectic with Al at 75 atomic percent. In the final step, the pseudo-binary diagram analysis of AlCrFe-Ni indicates that the eutectic reaction occurs at approximately 47.2 atomic percent Ni, as shown in **Figure 6.10(b)**. The EDS analysis of the as-cast  $(\text{AlCrFe})_{52.8}(\text{Ni})_{47.2}$  alloy, detailed in **Table 6.3**, confirms the chemical homogeneity of the cast alloy. The microstructure, illustrated in **Figure**

**6.11**, reveals a lamellar eutectic pattern. Elemental mapping of this microstructure further confirms that the white phase is enriched with Al-Ni, while the dark phase is predominantly composed of Fe-Cr-Ni. This observation suggests a potential eutectic combination of B2 plus FCC.

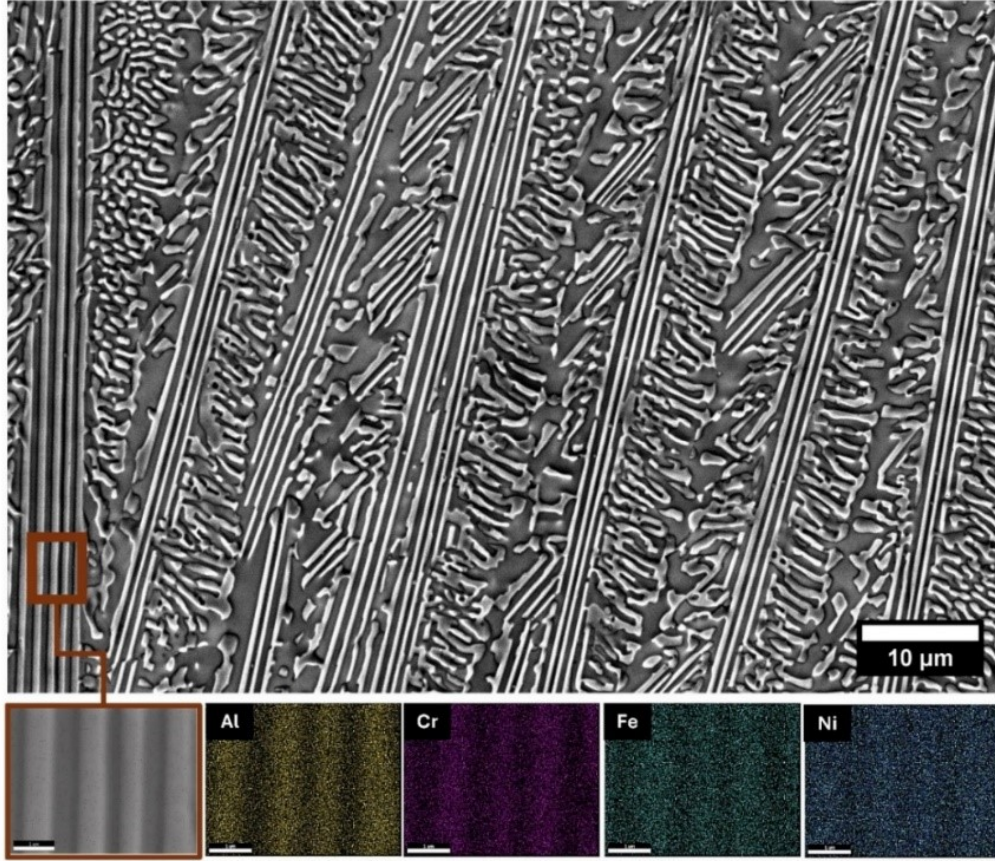


**Figure 6.11:** SEM-BSE micrograph and elemental distribution map of the as-cast  $(\text{AlCrFe})_{52.8}(\text{Ni})_{47.2}$  alloy.

**Table 6.2:** Comparison between overall B2 plus FCC compositional space and the designed alloy  $(\text{AlCrFe})_{52.8}(\text{Ni})_{47.2}$

Parameter	B2 plus FCC eutectic compositional space	$(\text{AlCrFe})_{52.8}(\text{Ni})_{47.2}$
VEC	7.52 to 8.02	7.71
$\Delta S_{\text{mix}} \text{ (J/K.mol)}$	9.95 to 11.07	10.57
$\Delta H_{\text{mix}} \text{ (kJ/mol)}$	-13.58 to -10.96	-12.96
$\Delta\chi$	0.11 to 0.13	0.13
$\delta \text{ (%)}$	5.36 to 5.77	5.56
$T_m \text{ (K)}$	1630 to 1713.71	1682.32
$\Omega$	1.25 to 1.71	1.37
$\rho \text{ (g/cc)}$	6.87 to 7.14	6.95

**Table 6.3:** EDS of the full area at 100x from three locations.

Composition	Al	Cr	Fe	Ni
Nominal	17.6	17.6	17.6	47.2
Actual	18.1±0.10	17.9±0.6	17.7±0.2	46.3±0.6



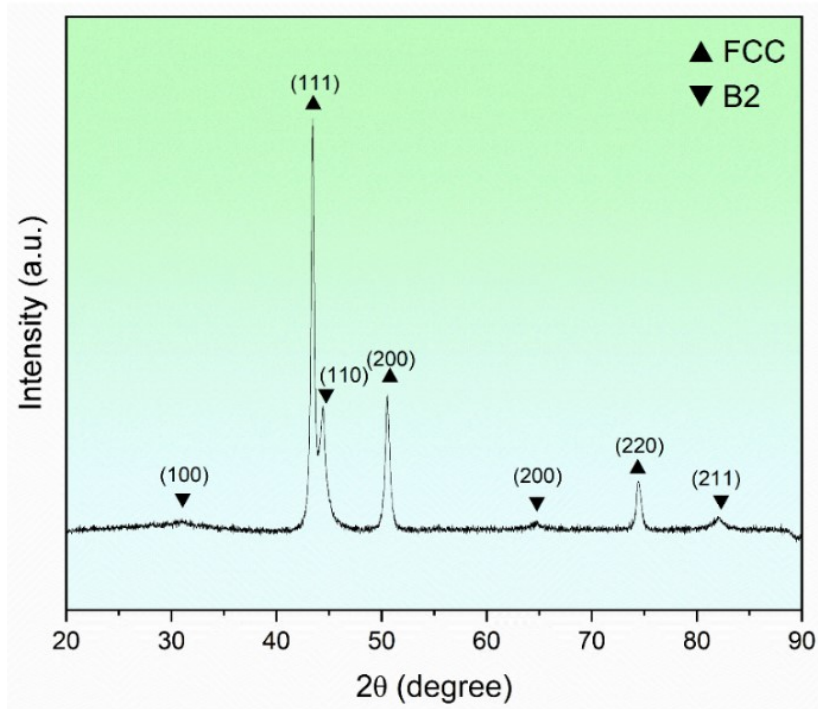


**Figure 6.12:** XRD pattern of the as-cast (AlCrFe)<sub>52.8</sub>(Ni)<sub>47.2</sub> alloy.

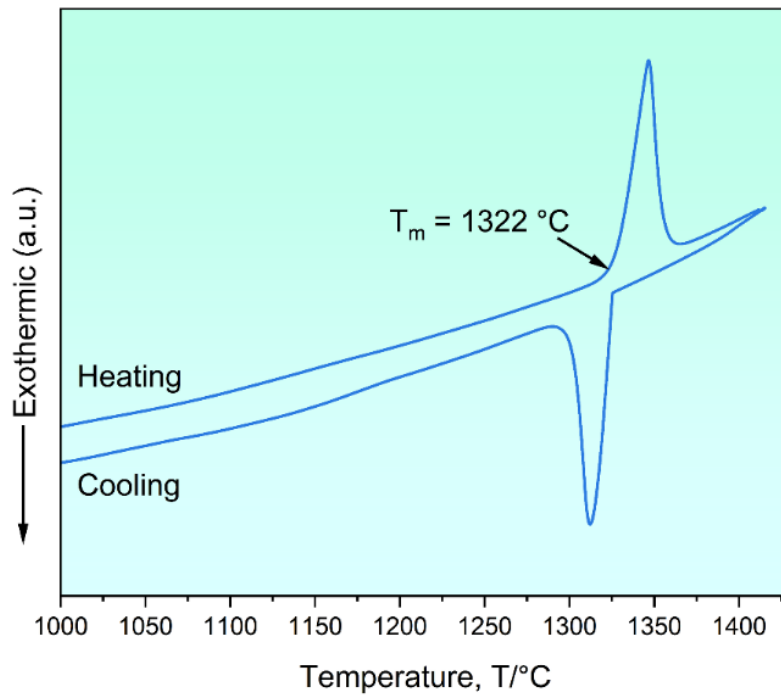


**Figure 6.13:** XRD pattern of the as-cast (AlCrFe)<sub>52.8</sub>(Ni)<sub>47.2</sub> alloy.

From the X-ray diffraction pattern depicted in **Figure 6.12**, a distinct two-phase structure is evident. A minor peak at 31 degrees suggests the possible presence of a B2 phase. The peak ratio analysis, specifically the  $\sin \frac{\theta_2}{\theta_1}$  for peaks at 44.4 and 43.4 degrees, resulting in a



value of 1.018. Additionally, the  $\sin \frac{\theta_3}{\theta_1}$  ratio for peaks at 50.5 and 43.4 degrees is calculated to be 1.1, indicative of FCC structure corresponding to the (111) and (200) lattice planes. Consequently, the peak at 43.3 degrees is identified as the FCC (111) plane, while the peak at 50.5 degrees corresponds to the (200) plane. The peak at 44.4 degrees is associated with the (110) plane. Further analysis utilising X'pert HighScore Plus software confirms the presence of an FCC phase (Fm-3m) with a lattice parameter of 3.61 Å and a B2 phase (Im-3m) with a lattice parameter of 2.89 Å. The DSC trace in **Figure 6.13** displays a single sharp endothermic peak, further validating the eutectic nature of the developed alloy.

The room temperature (RT) tensile engineering stress-strain curve of the as-cast (AlCrFe)<sub>52.8</sub>(Ni)<sub>47.2</sub> alloy, shown in **Figure 6.14**, reveals a tensile yield strength of 622 MPa and an ultimate tensile strength of 1106 MPa. The alloy exhibits significant strain hardening in the plastic regime, resulting in an elongation of 10.35% without necking, as measured using DIC. **Figure 6.15** compares the tensile properties of the (AlCrFe)<sub>52.8</sub>(Ni)<sub>47.2</sub> alloy with other advanced as-cast EMPEAs in the Al-Co-Cr-Fe-Ni system, highlighting its superior tensile performance, particularly in terms of specific yield strength and adhering with the anticipated design expectations.

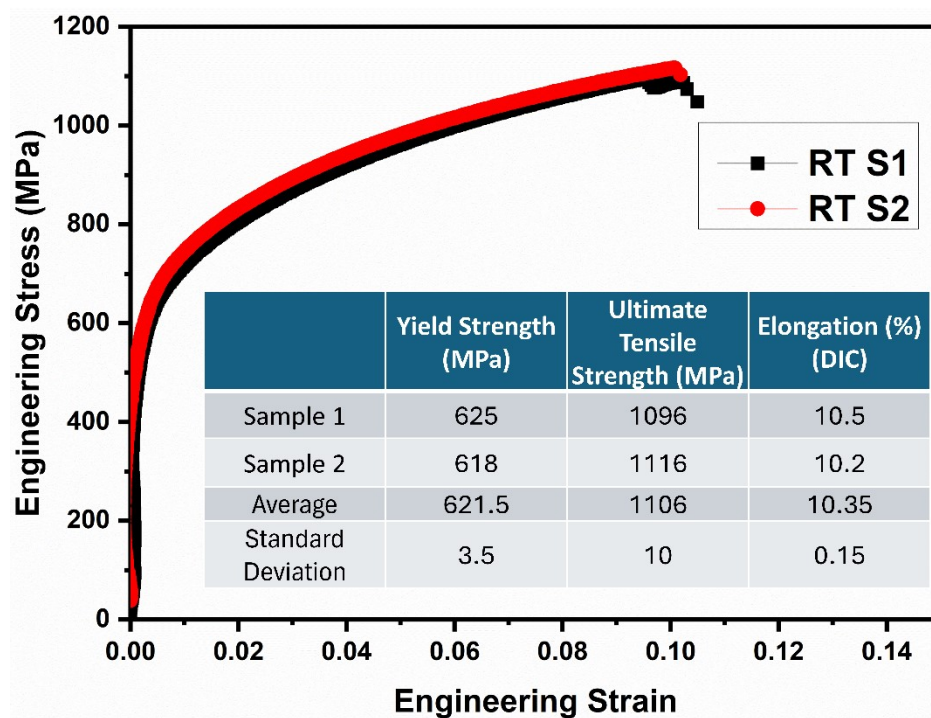


**Figure 6.14:** Tensile engineering stress-strain curve of (AlCrFe)<sub>52.8</sub>(Ni)<sub>47.2</sub> alloy.

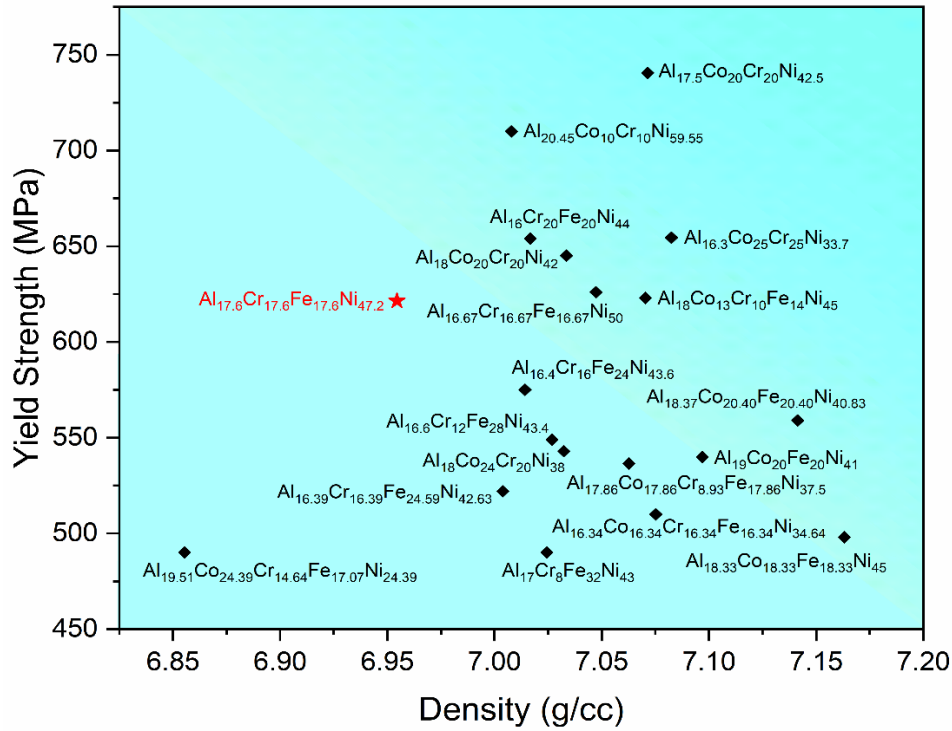


**Figure 6.15:** Mapping of yield strength versus density for EMPEAs in the Al-Co-Cr-Fe-Ni alloy system [50,57,72,113,141–149,173].

## 6.7: Designing a Triple-Phase EMPEA from a Two-Phase EMPEA

Further observations reveal that the formation of dual-phase and triple-phase eutectics in the Al-Cr-Fe-Ni system shows a significant correlation with key thermodynamic design parameters, notably with VEC and percentage atomic size difference ( $\delta\%$ ). As illustrated in **Figure 6.16(a)**, dual-phase eutectics with a BCC structure typically have an atomic size difference ranging from 5.65 to 6.85. In contrast, dual-phase eutectics with FCC exhibit an atomic size difference between 5.36 and 5.77, while triple-phase eutectics fall within the range of 5.35 to 5.58.

Additionally, analysis of the VEC parameter reveals that triple-phase eutectics have a VEC range of 7.37 to 7.55. In contrast, dual-phase eutectics with FCC have VEC values ranging from 7.52 to 8.02, while those with BCC vary between 6.07 and 7.25. This observation suggests that minor adjustments to elements with similar atomic radii and VEC values in dual-phase eutectics with FCC plus B2 can lead to the formation of a triple-phase eutectic. The absence of a noticeable difference in enthalpy of mixing between dual-phase eutectics with FCC and triple-phase eutectics, as shown in **Figures 6.16(b) and 6.17(a)**, implies that the additional phase in an FCC plus B2 dual-phase eutectic is likely a disordered BCC (A2) or an ordered FCC (L1<sub>2</sub>) phase, rather than a Laves phase or other compounds. This is supported by the fact that a higher enthalpy of mixing typically favours phase separation and the formation

of intermetallic compounds like the Laves phase, which is notably absent in the Al-Cr-Fe-Ni binaries. Furthermore, the VEC versus enthalpy of mixing plot in **Figure 6.17(a)** indicates that while triple-phase eutectics are similar to dual-phase eutectics with FCC in terms of enthalpy of mixing, their VEC values are slightly lower, suggesting that the third phase is likely BCC. Literature supports this observation, noting that BCC HEAs generally have lower VEC values compared to FCC HEAs and similarly, dual-phase eutectics with BCC exhibit lower VEC values than those with FCC [121,161].

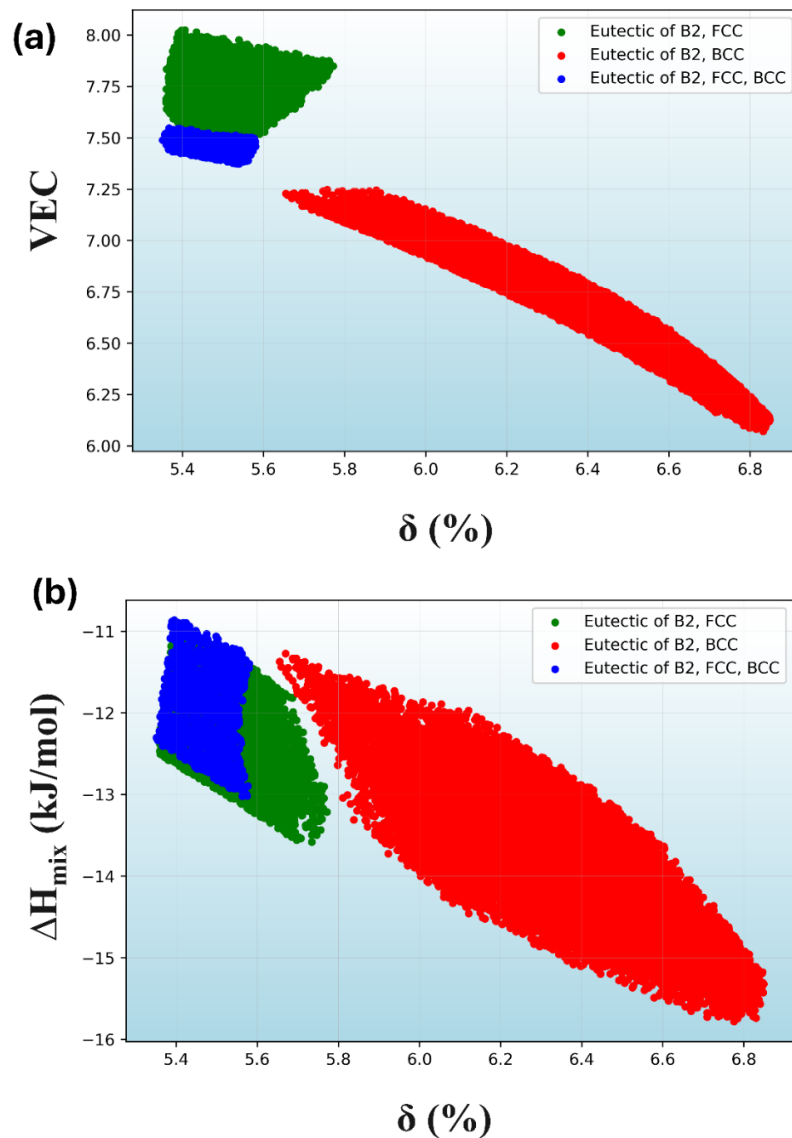


**Figure 6.16:** Scatter plots of (a) Valence Electron Concentration (VEC) vs atomic size difference ( $\delta\%$ ) and (b) enthalpy of mixing ( $\Delta H_{\text{mix}}$ ) vs  $\delta\%$ .

The density versus VEC plot shown in **Figure 6.17(b)** indicates no significant density difference between triple-phase eutectics and dual-phase eutectics with FCC, although a

distinct difference is observed with dual-phase eutectics containing BCC. This suggests that the formation of triple-phase eutectics originates from dual-phase eutectics with FCC plus B2. The additional phase is identified as BCC, derived from elements present in the FCC phase, specifically Ni, Fe and Cr, which have VEC values of 10, 8 and 6, atomic radii of 1.246 Å, 1.241 Å and 1.249 Å and densities of 8.9 g/cc, 7.88 g/cc and 7.2 g/cc, respectively. This observation implies that a higher concentration of Cr or Fe relative to Ni in dual-phase eutectics with B2 plus FCC could promote the segregation of a BCC phase, leading to the formation of triple-phase eutectics comprising B2, FCC and BCC.

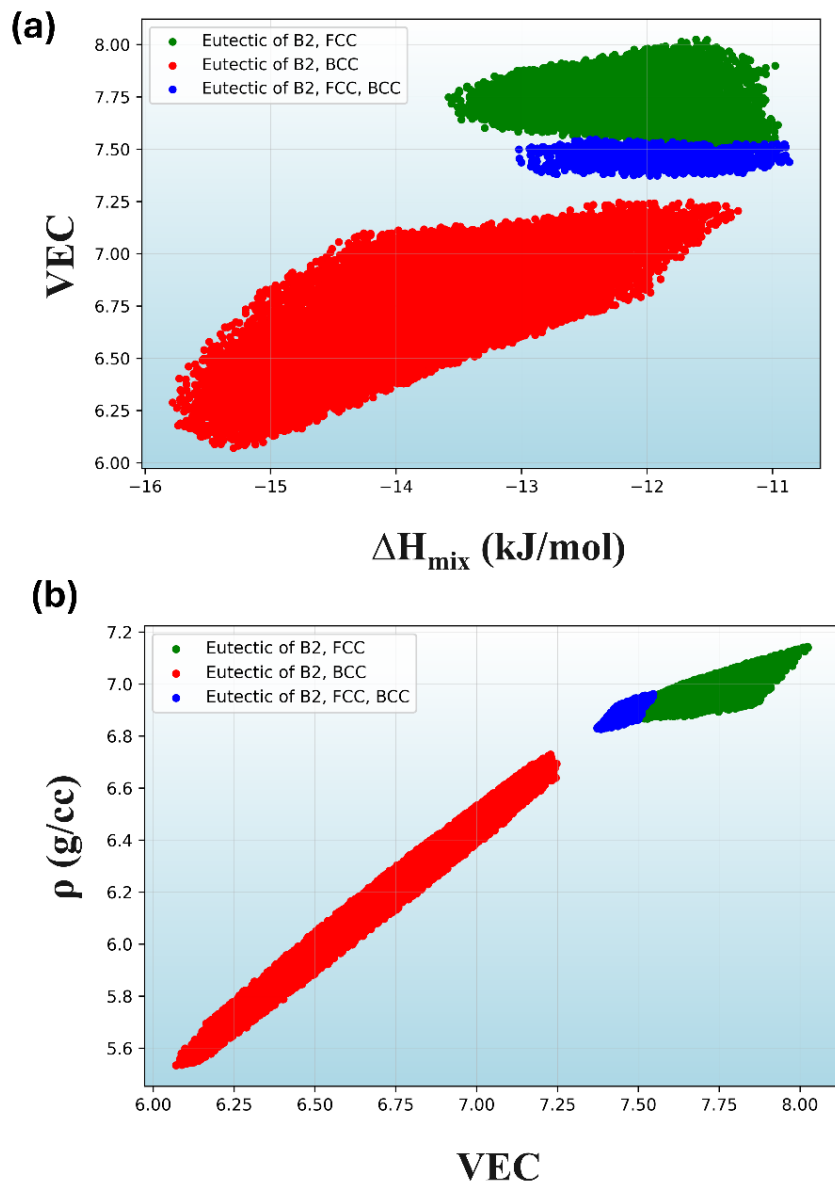


**Figure 6.17:** Scatter plots of (a) Valence Electron Concentration (VEC) vs enthalpy of mixing ( $\Delta H_{\text{mix}}$ ) and (b) density ( $\rho$ ) vs VEC.

The parallel coordinate plot in **Figure 6.18** offers additional insights into the elemental correlations among Al, Cr, Fe and Ni in dual- and triple-phase eutectic compositions featuring FCC as one of the phases. The plot reveals an inverse linear relationship between Cr and Ni, suggesting that an increase in chromium content coupled with a decrease in nickel content can transform a two-phase eutectic into a triple-phase eutectic. This indicates that a dual-phase eutectic consisting of FCC (Ni-Fe-Cr) and B2 (Ni-Al) could potentially develop an additional phase if the chromium content is sufficiently high to interact with iron, resulting in the formation of a separate Cr-Fe BCC phase.

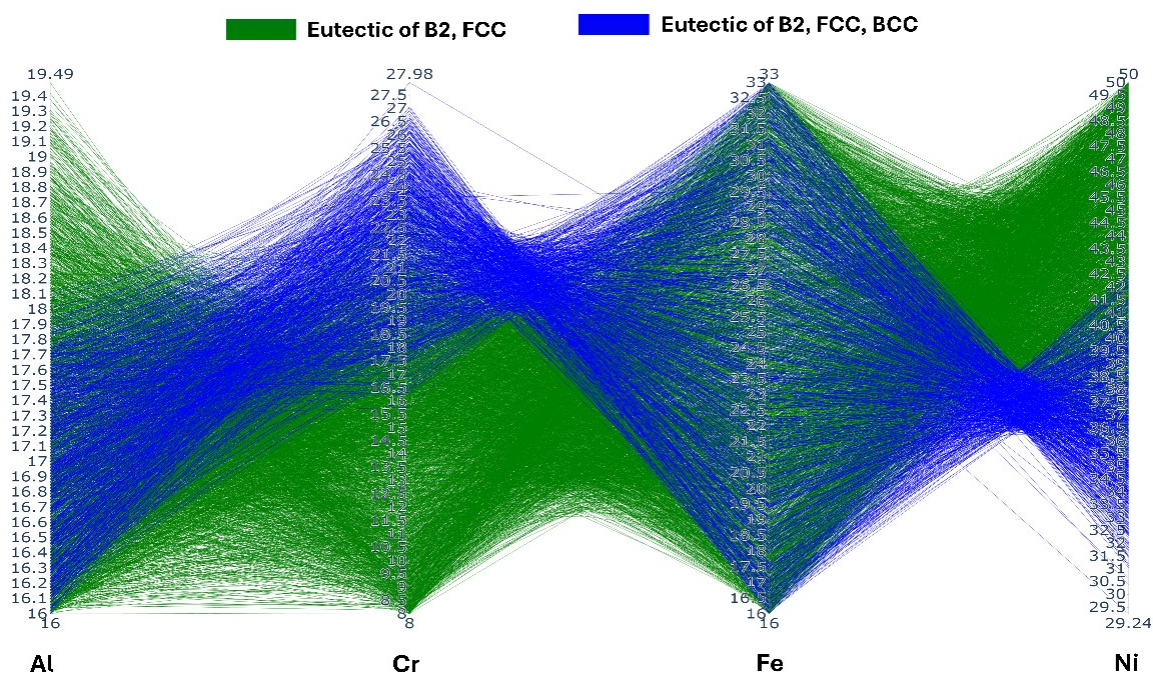


**Figure 6.18:** Parallel coordinate plot of Al, Cr, Fe and Ni relative to eutectic types with FCC as a phase.

However, it is important to note that these kinds of triple-phase eutectics will generally have lower nickel content and, consequently, a reduced FCC phase fraction compared to their dual-phase counterparts. This reduction in nickel, which typically contributes to the ductility of the FCC phase, may result in less elongation for triple-phase alloys compared to two-phase alloys, where the FCC phase is rich in nickel. An alternative approach to achieve a triple-phase eutectic with substantial nickel content involves reducing Fe while increasing Cr. However, this strategy is not cost-effective and offers only a minor density difference. Additionally, the inverse linear trend observed between Cr and Ni may not be as pronounced as Fe and Ni. Fe is present throughout a similar range in both triple-phase and dual-phase eutectics ( $16 \leq \text{Fe} \leq 33$  at.%). Also, Fe can form either a BCC structure with Cr or an FCC structure with Ni at high



temperatures. The report by Diao *et al.* [172] indicates that increasing Fe content in  $\text{AlCrFe}_x\text{Ni}$  alloys enhances the fracture strain. Therefore, increasing Fe while keeping Cr constant can lead to the formation of Fe-Cr BCC in dual-phase eutectics with FCC plus B2, resulting in triple-phase eutectics with relatively higher elongation and cost-effectiveness. The role of Al is primarily to form a B2 phase with Ni without significantly influencing the formation of triple-phase eutectics [42,170]. Thus, it is hypothesized that by maintaining constant Al and Cr levels and varying Fe in relation to Ni in a dual-phase eutectic alloy of B2 and FCC, a transformation into a triple-phase eutectic alloy with B2, FCC and BCC can be achieved. This hypothesis is visualized in **Figure 6.19**, where varying Fe and Ni in the phase composition of a dual-phase eutectic alloy,  $\text{Al}_{17.6}\text{Cr}_{17.6}\text{Fe}_{(17.6+x)}\text{Ni}_{(47.2-x)}$ , results in the formation of a triple-phase eutectic alloy,  $\text{Al}_{17.6}\text{Cr}_{17.6}\text{Fe}_{33.6}\text{Ni}_{31.2}$ , when  $x=16$ , with phase fractions of 41% B2, 32% FCC and 27% BCC.

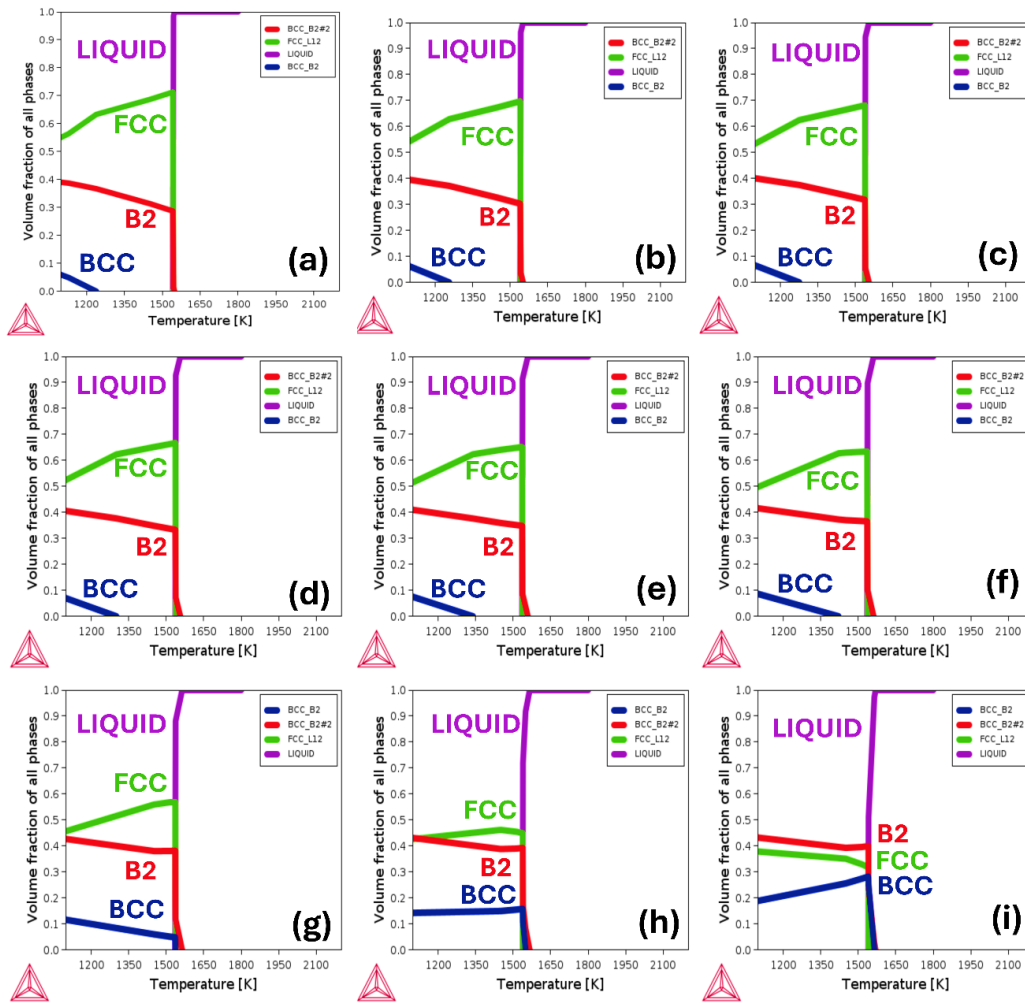


**Figure 6.19:** Phase evolution plots for  $\text{Al}_{17.6}\text{Cr}_{17.6}\text{Fe}_{(17.6+x)}\text{Ni}_{(47.2-x)}$ :  
(a)  $x = 0$ , (b)  $x = 2$ , (c)  $x = 4$ , (d)  $x = 6$ , (e)  $x = 8$ , (f)  $x = 10$ , (g)  $x = 12$ , (h)  $x = 14$ , (i)  $x = 16$ .

## 6.8: Limitations

The high-throughput CALPHAD approach utilized to explore the Al-Cr-Fe-Ni system has effectively identified all possible eutectics and addressed several design strategy limitations. Nonetheless, the study encounters certain limitations:

- *Computational Methodology Constraints:* The reliance on CALPHAD via the *TC-Python* API is limited to elemental combinations included in the *TCHEA5* or *TCHEA6* database, which encompasses only 26 elements from the full 105-element periodic table.
- *Kinetic Factors Consideration:* The study emphasizes phase formation and stability from a thermodynamic perspective but lacks consideration of kinetic factors, which significantly affect microstructural features, such as lamellar thickness and, thus, mechanical properties.
- *Scope of High-Throughput Methodology:* While the high-throughput CALPHAD methodology allows for investigation across a broad compositional space, it may involve computational costs and otherwise potentially overlook narrow compositional windows where unique eutectic compositions might exist. To enhance exploration capabilities and discover novel compositions with greater computational efficiency, integrating advanced techniques such as machine learning and artificial intelligence could be beneficial.

## 6.9: Summary

Chapter 6 provides a comprehensive examination of the eutectic compositional landscape within the Al-Cr-Fe-Ni system, utilizing the high-throughput CALPHAD approach through an in-house *Python* script. Key insights from this chapter include:

- *Classification of Pseudo and Invariant Eutectics:* In a multi-principal element alloy (MPEA) system with 'n' elements, a true invariant eutectic reaction occurs only if all 'n' solid phases melt at a single temperature without any range. Eutectic formations that do not meet this strict criterion are classified as pseudo-eutectics.
- *Identification of Pseudo-Eutectics Compositional Space:* The in-house *Python* script, which emphasizes solid phase formation temperatures rather than merely the difference between liquidus and solidus temperatures, has successfully identified the pseudo-eutectics compositional space in the Al-Cr-Fe-Ni system.
- *Unlikelihood of Invariant Eutectics:* The study suggests that invariant eutectic reactions are improbable in high-entropy alloys (HEAs) unless the eutectic phases are compounds or ordered solid solution phases, without any disordered solid solution phases.

- *Significance of Thermodynamic Parameters:* The chapter highlights the significance of thermodynamic parameters, particularly VEC and enthalpy of mixing, correlating with eutectic formations.
- *Validation of Predictive Accuracy:* Comparison of high-throughput CALPHAD predictions with experimentally reported compositions shows excellent agreement, as indicated by minimal Euclidean distances between predicted and observed values.
- *Experimental Confirmation of Compositional Space:* Experimental casting of the alloy  $\text{Al}_{17.6}\text{Cr}_{17.6}\text{Fe}_{17.6}\text{Ni}_{47.2}$ , using the single-phase plus EFE approach from Chapter 5, demonstrated both B2 and FCC phases. The observed lamellar eutectic morphology and narrow solidification range substantiate the computationally identified eutectic compositional space, confirming the effectiveness of the predictive framework.



## CHAPTER 7

# Conclusions and Future Research Directions

### 7.1: Conclusions

The thesis introduces three progressively distinct design approaches for developing eutectic multi-principal element alloys (EMPEAs), addressing the research questions posed in Section 2.6 as follows:

- *Empirical Design Approach Using Binary Eutectic Clusters (Chapter 4):*

Objective: To design binary eutectics in MPEA systems without reliance on computational tools.

Method: This approach involves using empirical methods to identify stable compounds and mix them to achieve a eutectic composition. It is a practical alternative to computational tools like *Thermo-Calc*, focusing on the enthalpy of mixing values and eutectic points of binary pairs. Although it is limited to alloy systems with binary eutectic interactions and may lead to the inclusion of Laves phases—which may not be ideal for structural applications—this method can effectively identify near-eutectic compositions using simple calculations.

- *Single-Phase Plus EFE Approach via CALPHAD (Chapter 5):*

Objective: To quickly locate eutectic points in MPEAs with minimal calculations.

Method: This approach refines the definition of the "Eutectic Forming Element" (EFE) to include binary eutectics with only one of the elements in the alloy system. It enables rapid identification of eutectic compositions for different eutectic types, using pseudo-binary phase diagrams both graphically and via console mode. The method can identify eutectic points within 2 minutes but is limited to a maximum of four eutectic compositions in a quaternary system and five in a quinary system. However, this method does not reveal all possible dual-phase eutectic compositions or higher-order eutectics governed by the Gibbs phase rule.

- *High-Throughput CALPHAD Approach (Chapter 6):*

Objective: To identify all potential binary and higher-order eutectics in MPEA systems, including invariant reactions.

Method: This approach involves calculating the phase formation temperatures of all solid phases and analyzing their differences to discover both binary and higher-order eutectics. Despite its computational time and the need for *Python* programming expertise, this method

offers a comprehensive solution for exploring complex alloy systems. As illustrated in Chapter 6 with the Al-Cr-Fe-Ni case study, invariant eutectic reactions are less likely in MPEAs with transition elements unless the eutectic phases are compounds or ordered solid solutions devoid of disordered solid solution phases. **Table 7.1** provides examples of compositions with fully eutectic microstructures that comply with this approach.

**Table 7.1:** Reported compositions across alloy systems complying with the high-throughput CALPHAD approach proposed in Chapter 6 ( $\Delta T$  = solidification range).

SN	Published on	Composition	Eutectic Phases	$\Delta T$	Ref.
001	2013.04.10	Al <sub>23.81</sub> Cr <sub>23.81</sub> Fe <sub>23.81</sub> Mo <sub>4.76</sub> Ni <sub>23.81</sub>	BCC_B2#1, BCC_B2#2	44	[92]
002	2013.04.10	Al <sub>24.75</sub> Cr <sub>24.75</sub> Fe <sub>24.75</sub> Ni <sub>24.75</sub> Ti <sub>0.99</sub>	BCC_B2#1, BCC_B2#2	42	[92]
003	2014.08.27	Al <sub>16.39</sub> Co <sub>16.39</sub> Cr <sub>16.39</sub> Fe <sub>16.39</sub> Ni <sub>34.43</sub>	BCC_B2#2, FCC_L12#2	15	[17]
004	2015.01.18	Co <sub>19.05</sub> Fe <sub>19.05</sub> Nb <sub>14.29</sub> Ni <sub>38.1</sub> V <sub>9.52</sub>	C15_LAVES#1, FCC_L12#1	24	[94]
005	2015.09.24	Co <sub>21.51</sub> Cr <sub>21.51</sub> Fe <sub>21.51</sub> Nb <sub>13.98</sub> Ni <sub>21.51</sub>	C14_LAVES#1, FCC_L12#1	119	[29]
006	2016.07.25	Co <sub>30.3</sub> Mo <sub>12.12</sub> Ni <sub>30.3</sub> V <sub>15.15</sub> W <sub>12.12</sub>	BCC_B2#1, FCC_L12#1	105	[47]
007	2016.09.26	Co <sub>22.47</sub> Cr <sub>22.47</sub> Fe <sub>22.47</sub> Nb <sub>10.11</sub> Ni <sub>22.47</sub>	C14_LAVES#1, FCC_L12#1	20	[100]
008	2016.11.11	Al <sub>23.08</sub> Cr <sub>25.64</sub> Fe <sub>25.64</sub> Ni <sub>25.64</sub>	BCC_B2#1, BCC_B2#2	42	[42]
009	2016.11.11	Al <sub>25</sub> Cr <sub>25</sub> Fe <sub>25</sub> Ni <sub>25</sub>	BCC_B2#1, BCC_B2#2	23	[42]
010	2016.11.11	Al <sub>30.24</sub> Cr <sub>23.25</sub> Fe <sub>23.25</sub> Ni <sub>23.25</sub>	BCC_B2#1, BCC_B2#2	15	[42]
011	2016.11.11	Al <sub>28.57</sub> Cr <sub>23.81</sub> Fe <sub>23.81</sub> Ni <sub>23.81</sub>	BCC_B2#1, BCC_B2#2	13	[42]
012	2016.11.11	Al <sub>26.83</sub> Cr <sub>24.39</sub> Fe <sub>24.39</sub> Ni <sub>24.39</sub>	BCC_B2#1, BCC_B2#2	12	[42]
013	2017.05.30	Co <sub>22.73</sub> Cr <sub>22.73</sub> Fe <sub>22.73</sub> Ni <sub>22.73</sub> Ta <sub>9.09</sub>	C14_LAVES#1, FCC_L12#1	27	[44]
014	2017.06.01	Al <sub>30.23</sub> Cr <sub>23.26</sub> Fe <sub>23.26</sub> Ni <sub>23.26</sub>	BCC_B2#1, BCC_B2#2	15	[171]
015	2017.08.12	Co <sub>22.22</sub> Cr <sub>22.22</sub> Fe <sub>22.22</sub> Ni <sub>22.22</sub> Zr <sub>11.11</sub>	C15_LAVES#1, FCC_L12#1	28	[119]
016	2017.09.10	Co <sub>18.02</sub> Cr <sub>18.02</sub> Fe <sub>18.02</sub> Hf <sub>9.91</sub> Ni <sub>36.04</sub>	FCC_L12#1, Ni7ZR2#1	73	[63]
017	2017.09.10	Co <sub>17.42</sub> Cr <sub>17.42</sub> Fe <sub>17.42</sub> Nb <sub>12.89</sub> Ni <sub>34.84</sub>	C14_LAVES#1, FCC_L12#1	43	[63]
018	2017.12.05	Co <sub>22.57</sub> Cr <sub>22.57</sub> Fe <sub>22.57</sub> Ni <sub>22.57</sub> Ta <sub>9.71</sub>	C14_LAVES#1, FCC_L12#1	14	[60]
019	2017.12.13	Co <sub>22.22</sub> Cr <sub>22.22</sub> Fe <sub>22.22</sub> Nb <sub>11.11</sub> Ni <sub>22.22</sub>	C14_LAVES#1, FCC_L12#1	48	[155]

020	2018.01.04	Al <sub>19</sub> Co <sub>20</sub> Fe <sub>20</sub> Ni <sub>41</sub>	BCC_B2#2, FCC_L12#1	30	[101]
021	2018.01.13	Co <sub>21.98</sub> Cr <sub>21.98</sub> Fe <sub>21.98</sub> Ni <sub>21.98</sub> Zr <sub>12.09</sub>	C15_LAVES#1, FCC_L12#1	43	[64]
022	2018.01.31	Al <sub>17</sub> Co <sub>14.3</sub> Cr <sub>14.3</sub> Fe <sub>28.6</sub> Ni <sub>25.8</sub>	BCC_B2#2, FCC_L12#1	41	[74]
023	2018.01.31	Al <sub>17</sub> Co <sub>28.6</sub> Cr <sub>14.3</sub> Fe <sub>14.3</sub> Ni <sub>25.8</sub>	BCC_B2#2, FCC_L12#1	28	[74]
024	2018.01.31	Al <sub>17</sub> Co <sub>14.3</sub> Cr <sub>14.3</sub> Fe <sub>14.3</sub> Ni <sub>40.1</sub>	BCC_B2#2, FCC_L12#1	10	[74]
025	2018.03.07	Co <sub>28.57</sub> Fe <sub>28.57</sub> Nb <sub>14.29</sub> Ni <sub>28.57</sub>	C15_LAVES#1, FCC_L12#1	36	[105]
026	2018.03.21	Al <sub>19.3</sub> Co <sub>15</sub> Cr <sub>15</sub> Ni <sub>50.7</sub>	BCC_B2#2, FCC_L12#2	18	[174]
027	2018.08.20	Al <sub>16</sub> Cr <sub>20</sub> Fe <sub>20</sub> Ni <sub>44</sub>	BCC_B2#2, FCC_L12#2	11	[46]
028	2019.02.23	Al <sub>18</sub> Co <sub>30</sub> Cr <sub>10</sub> Fe <sub>10</sub> Ni <sub>32</sub>	BCC_B2#2, FCC_L12#2	20	[110]
029	2019.04.09	Co <sub>10</sub> Cr <sub>15</sub> Fe <sub>25.3</sub> Mn <sub>5</sub> Nb <sub>9.7</sub> Ni <sub>25</sub> V <sub>10</sub>	C14_LAVES#1, FCC_L12#1	55	[175]
030	2019.04.23	Al <sub>14.89</sub> Co <sub>21.28</sub> Cr <sub>21.28</sub> Fe <sub>21.28</sub> Ni <sub>21.28</sub>	BCC_B2#2, FCC_L12#1	18	[120]
031	2019.06.20	Al <sub>18</sub> Co <sub>30</sub> Cr <sub>10</sub> Fe <sub>10</sub> Ni <sub>30</sub> W <sub>2</sub>	BCC_B2#2, FCC_L12#1	36	[109]
032	2019.10.26	Al <sub>16</sub> Co <sub>41</sub> Cr <sub>15</sub> Fe <sub>10</sub> Ni <sub>18</sub>	BCC_B2#2, FCC_L12#2	14	[111]
033	2019.11.05	Al <sub>18</sub> Co <sub>27.33</sub> Fe <sub>27.33</sub> Ni <sub>27.33</sub>	BCC_B2#2, FCC_L12#1	47	[68]
034	2019.11.05	Al <sub>18</sub> Co <sub>30</sub> Fe <sub>20</sub> Ni <sub>32</sub>	BCC_B2#2, FCC_L12#1	30	[68]
035	2019.11.05	Al <sub>18</sub> Co <sub>24</sub> Cr <sub>10</sub> Fe <sub>10</sub> Ni <sub>36</sub> W <sub>2</sub>	BCC_B2#2, FCC_L12#1	26	[68]
036	2019.11.05	Al <sub>18</sub> Co <sub>20</sub> Cr <sub>10</sub> Fe <sub>10</sub> Ni <sub>40</sub> W <sub>2</sub>	BCC_B2#2, FCC_L12#1	19	[68]
037	2019.11.08	Al <sub>17.8</sub> Co <sub>32.88</sub> Cr <sub>8.22</sub> Fe <sub>4.11</sub> Mo <sub>4.11</sub> Ni <sub>32.88</sub>	BCC_B2#2, FCC_L12#1	26	[176]
038	2019.11.18	Co <sub>25</sub> Cu <sub>12.5</sub> Fe <sub>25</sub> Ni <sub>25</sub> Ta <sub>12.5</sub>	C14_LAVES#1, FCC_L12#1	156	[153]
039	2019.12.13	Al <sub>17.4</sub> Co <sub>21.7</sub> Cr <sub>21.7</sub> Ni <sub>39.2</sub>	BCC_B2#2, FCC_L12#1	15	[177]
040	2020.01.17	Al <sub>16.67</sub> Cr <sub>16.67</sub> Fe <sub>16.67</sub> Ni <sub>50</sub>	BCC_B2#2, FCC_L12#1	15	[113]
041	2020.02.05	Co <sub>28.99</sub> Fe <sub>28.99</sub> Nb <sub>13.04</sub> Ni <sub>28.99</sub>	C15_LAVES#1, FCC_L12#1	11	[117]
042	2020.02.27	Al <sub>18</sub> Co <sub>20</sub> Cr <sub>20</sub> Ni <sub>42</sub>	BCC_B2#1, FCC_L12#2	15	[143]
043	2020.03.05	Al <sub>19.5</sub> Co <sub>47.5</sub> Cr <sub>7.5</sub> Ni <sub>25.5</sub>	BCC_B2#2, FCC_L12#1	10	[82]
044	2020.04.24	Al <sub>15.79</sub> Cr <sub>21.05</sub> Nb <sub>21.05</sub> Ti <sub>21.05</sub> Zr <sub>21.05</sub>	BCC_B2#1, C14_LAVES#1	63	[123]

045	2020.06.01	Al <sub>1.7</sub> Co <sub>25.1</sub> Cr <sub>18.8</sub> Fe <sub>23.3</sub> Ni <sub>22.6</sub> Ta <sub>8.5</sub>	C14_LAVES#1, FCC_L12#1	36	[178]
046	2020.07.01	Al <sub>1</sub> Co <sub>25</sub> Cr <sub>18</sub> Fe <sub>23</sub> Ni <sub>23</sub> Ta <sub>10</sub>	C14_LAVES#1, FCC_L12#1	14	[179]
047	2020.07.06	Co <sub>17.15</sub> Cr <sub>17.15</sub> Fe <sub>17.15</sub> Nb <sub>12.52</sub> Ni <sub>36.02</sub>	C14_LAVES#1, FCC_L12#1	28	[21]
048	2020.07.09	Al <sub>18.37</sub> Co <sub>20.41</sub> Fe <sub>20.41</sub> Ni <sub>40.82</sub>	BCC_B2#2, FCC_L12#1	20	[149]
049	2020.12.05	Co <sub>23.5</sub> Cr <sub>16.38</sub> Fe <sub>19.75</sub> Nb <sub>15</sub> Ni <sub>25.37</sub>	C14_LAVES#1, FCC_L12#1	107	[132]
050	2020.12.05	Co <sub>20.92</sub> Cr <sub>20.92</sub> Fe <sub>10.46</sub> Mo <sub>2.09</sub> Nb <sub>14.23</sub> Ni <sub>31.38</sub>	C14_LAVES#1, FCC_L12#1	95	[66]
051	2020.12.05	Co <sub>24.17</sub> Cr <sub>20.21</sub> Fe <sub>22.08</sub> Ni <sub>25.21</sub> Ta <sub>8.33</sub>	C14_LAVES#1, FCC_L12#1	57	[132]
052	2020.12.16	Cr <sub>16</sub> Fe <sub>32</sub> Mo <sub>20</sub> Ni <sub>32</sub>	FCC_L12#1, P_PHASE#1	90	[157]
053	2020.12.19	Co <sub>21.05</sub> Cr <sub>21.05</sub> Fe <sub>21.05</sub> Ni <sub>21.05</sub> Ta <sub>15.79</sub>	C14_LAVES#1, FCC_L12#1	167	[59]
054	2020.12.26	Cr <sub>21.74</sub> Fe <sub>21.74</sub> Nb <sub>13.04</sub> Ni <sub>43.48</sub>	C14_LAVES#1, FCC_L12#1	82	[156]
055	2021.01.11	Al <sub>19</sub> Co <sub>20.7</sub> Fe <sub>20.7</sub> Ni <sub>39.6</sub>	BCC_B2#2, FCC_L12#2	34	[75]
056	2021.03.03	Al <sub>28</sub> Cr <sub>20</sub> Nb <sub>15</sub> Ti <sub>27</sub> Zr <sub>10</sub>	BCC_B2#2, C14_LAVES#1	46	[180]
057	2021.03.30	Al <sub>32.5</sub> Cr <sub>10</sub> Mo <sub>5</sub> Ni <sub>32.5</sub> V <sub>20</sub>	BCC_B2#1, BCC_B2#2	19	[76]
058	2021.04.13	Al <sub>19.25</sub> Co <sub>18.86</sub> Fe <sub>18.36</sub> Ni <sub>43.53</sub>	BCC_B2#2, FCC_L12#1	25	[181]
059	2021.05.24	Al <sub>16.95</sub> Co <sub>32.2</sub> Cr <sub>16.95</sub> Fe <sub>16.95</sub> Ni <sub>16.95</sub>	BCC_B2#2, FCC_L12#1	39	[73]
060	2021.05.30	Al <sub>17.39</sub> Co <sub>21.74</sub> Cr <sub>13.04</sub> Fe <sub>15.22</sub> Ni <sub>32.61</sub>	BCC_B2#2, FCC_L12#1	27	[144]
061	2021.06.10	Cr <sub>23.04</sub> Fe <sub>46.08</sub> Nb <sub>7.83</sub> Ni <sub>23.04</sub>	C14_LAVES#1, FCC_L12#1	52	[152]
062	2021.06.30	Co <sub>29.41</sub> Cr <sub>29.41</sub> Ni <sub>29.41</sub> Ta <sub>11.76</sub>	C14_LAVES#1, FCC_L12#1	23	[58]
063	2021.07.12	Co <sub>10</sub> Cr <sub>15</sub> Fe <sub>25</sub> Mn <sub>5</sub> Nb <sub>10</sub> Ni <sub>25</sub> V <sub>10</sub>	C14_LAVES#1, FCC_L12#1	64	[182]
064	2021.07.13	Al <sub>18.87</sub> Cr <sub>24.53</sub> Ni <sub>37.74</sub> Ti <sub>18.87</sub>	BCC_B2#1, HEUSLER_L21#1	140	[24]
065	2021.08.27	Co <sub>25.42</sub> Fe <sub>43.96</sub> Hf <sub>9.79</sub> Ni <sub>20.83</sub>	C15_LAVES#1, FCC_L12#1	137	[131]
066	2021.08.27	Co <sub>27.36</sub> Fe <sub>44.34</sub> Nb <sub>12.58</sub> Ni <sub>15.72</sub>	C15_LAVES#1, FCC_L12#1	26	[131]
067	2021.08.27	Co <sub>25.31</sub> Fe <sub>41.08</sub> Nb <sub>12.86</sub> Ni <sub>20.75</sub>	C15_LAVES#1, FCC_L12#1	24	[131]
068	2021.09.03	Al <sub>17.86</sub> Co <sub>17.86</sub> Cr <sub>8.93</sub> Fe <sub>17.86</sub> Ni <sub>37.5</sub>	BCC_B2#2, FCC_L12#1	27	[173]
069	2021.09.20	Al <sub>20</sub> Co <sub>30</sub> Cr <sub>10</sub> Ni <sub>40</sub>	BCC_B2#2, FCC_L12#2	7	[183]

070	2021.10.02	Al <sub>18</sub> Co <sub>30</sub> Cr <sub>10</sub> Fe <sub>10</sub> Mo <sub>1</sub> Ni <sub>30</sub> W <sub>1</sub>	BCC_B2#2, FCC_L12#2	38	[184]
071	2021.11.12	Al <sub>28.25</sub> Cr <sub>14.5</sub> Fe <sub>14.5</sub> Mo <sub>14.5</sub> Ni <sub>28.25</sub>	BCC_B2#1, BCC_B2#2	149	[78]
072	2021.11.12	Al <sub>36.95</sub> Cr <sub>8.7</sub> Mo <sub>8.7</sub> Ni <sub>36.95</sub> V <sub>8.7</sub>	BCC_B2#1, BCC_B2#2	67	[78]
073	2021.11.12	Al <sub>30</sub> Cr <sub>10</sub> Fe <sub>10</sub> Mo <sub>10</sub> Ni <sub>30</sub> V <sub>10</sub>	BCC_B2#1, BCC_B2#2	61	[78]
074	2021.11.23	Al <sub>16.31</sub> Co <sub>9.79</sub> Cr <sub>16.31</sub> Fe <sub>23.33</sub> Ni <sub>34.26</sub>	BCC_B2#2, FCC_L12#2	19	[70]
075	2021.11.23	Al <sub>16.39</sub> Co <sub>19.67</sub> Cr <sub>16.39</sub> Fe <sub>16.39</sub> Ni <sub>31.15</sub>	BCC_B2#2, FCC_L12#1	19	[70]
076	2021.11.23	Al <sub>16.39</sub> Co <sub>16.39</sub> Cr <sub>13.11</sub> Fe <sub>19.67</sub> Ni <sub>34.43</sub>	BCC_B2#2, FCC_L12#1	15	[70]
077	2021.11.23	Al <sub>16.39</sub> Co <sub>16.39</sub> Cr <sub>19.67</sub> Fe <sub>13.11</sub> Ni <sub>34.43</sub>	BCC_B2#2, FCC_L12#2	14	[70]
078	2021.11.23	Al <sub>16.37</sub> Co <sub>19.64</sub> Cr <sub>13.26</sub> Fe <sub>16.37</sub> Ni <sub>34.37</sub>	BCC_B2#2, FCC_L12#2	10	[70]
079	2021.11.23	Al <sub>16.39</sub> Co <sub>13.11</sub> Cr <sub>16.39</sub> Fe <sub>16.39</sub> Ni <sub>37.7</sub>	BCC_B2#2, FCC_L12#1	9	[70]
080	2021.11.23	Al <sub>16.37</sub> Co <sub>19.64</sub> Cr <sub>16.37</sub> Fe <sub>13.26</sub> Ni <sub>34.37</sub>	BCC_B2#2, FCC_L12#1	9	[70]
081	2022.01.15	Al <sub>20</sub> Cr <sub>26.67</sub> Fe <sub>26.67</sub> Ni <sub>26.67</sub>	BCC_B2#1, BCC_B2#2	74	[128]
082	2022.01.20	Al <sub>20.45</sub> Co <sub>10</sub> Cr <sub>10</sub> Ni <sub>59.55</sub>	BCC_B2#2, FCC_L12#2	21	[145]
083	2022.01.20	Al <sub>17.5</sub> Co <sub>20</sub> Cr <sub>20</sub> Ni <sub>42.5</sub>	BCC_B2#2, FCC_L12#2	19	[145]
084	2022.01.20	Al <sub>18.3</sub> Co <sub>15</sub> Cr <sub>20</sub> Ni <sub>46.7</sub>	BCC_B2#1, FCC_L12#2	17	[69]
085	2022.01.20	Al <sub>16.3</sub> Co <sub>25</sub> Cr <sub>25</sub> Ni <sub>33.7</sub>	BCC_B2#2, FCC_L12#1	15	[145]
086	2022.03.14	Al <sub>30</sub> Cr <sub>20</sub> Fe <sub>20</sub> Ni <sub>30</sub>	BCC_B2#1, BCC_B2#2	59	[101]
087	2022.03.31	Al <sub>23.81</sub> Cr <sub>23.81</sub> Fe <sub>23.81</sub> Ni <sub>23.81</sub> Ti <sub>4.76</sub>	BCC_B2#1, BCC_B2#2	91	[169]
088	2022.05.11	Al <sub>17</sub> Co <sub>28.57</sub> Cr <sub>14.29</sub> Fe <sub>14.29</sub> Ni <sub>25.86</sub>	BCC_B2#2, FCC_L12#2	28	[185]
089	2022.05.16	Al <sub>36.84</sub> Cr <sub>21.05</sub> Fe <sub>21.05</sub> Ni <sub>21.05</sub>	BCC_B2#1, BCC_B2#2	34	[168]
090	2022.05.16	Al <sub>33.33</sub> Cr <sub>22.22</sub> Fe <sub>22.22</sub> Ni <sub>22.22</sub>	BCC_B2#1, BCC_B2#2	22	[168]
091	2022.05.16	Al <sub>29.41</sub> Cr <sub>23.53</sub> Fe <sub>23.53</sub> Ni <sub>23.53</sub>	BCC_B2#1, BCC_B2#2	14	[168]
092	2022.05.18	Al <sub>16.78</sub> Co <sub>12.59</sub> Cr <sub>13.79</sub> Fe <sub>11.79</sub> Ni <sub>45.05</sub>	BCC_B2#2, FCC_L12#2	20	[85]
093	2022.05.30	Co <sub>11.32</sub> Cr <sub>21.83</sub> Fe <sub>34.77</sub> Hf <sub>9.97</sub> Ni <sub>22.1</sub>	C15_LAVES#1, FCC_L12#1	103	[186]
094	2022.05.30	Co <sub>22.99</sub> Cr <sub>40.23</sub> Fe <sub>23.56</sub> Hf <sub>8.62</sub> Ni <sub>4.6</sub>	BCC_B2#1, C15_LAVES#1	75	[186]

095	2022.05.30	Co <sub>39.58</sub> Cr <sub>22.02</sub> Fe <sub>5.95</sub> Hf <sub>10.12</sub> Ni <sub>22.32</sub>	FCC_L12#1, NI7ZR2#1	23	[186]
096	2022.05.31	Al <sub>16.39</sub> Cr <sub>16.39</sub> Fe <sub>24.59</sub> Ni <sub>42.62</sub>	BCC_B2#2, FCC_L12#1	7	[72]
097	2022.06.08	Al <sub>17.74</sub> Co <sub>16.13</sub> Cr <sub>16.13</sub> Fe <sub>16.13</sub> Ni <sub>33.87</sub>	BCC_B2#2, FCC_L12#1	36	[149]
098	2022.07.14	Al <sub>6.25</sub> Co <sub>20.83</sub> Cr <sub>20.83</sub> Fe <sub>20.83</sub> Nb <sub>10.42</sub> Ni <sub>20.83</sub>	C14_LAVES#1, FCC_L12#1	96	[187]
099	2022.09.27	Al <sub>18</sub> Co <sub>30</sub> Cr <sub>10</sub> Fe <sub>10</sub> Ni <sub>31</sub> Ti <sub>1</sub>	BCC_B2#2, FCC_L12#2	58	[188]
100	2022.10.04	Al <sub>18</sub> Co <sub>24</sub> Cr <sub>7</sub> Fe <sub>17</sub> Ni <sub>34</sub>	BCC_B2#2, FCC_L12#2	30	[83]
101	2022.10.04	Al <sub>18</sub> Co <sub>34</sub> Cr <sub>11</sub> Fe <sub>8</sub> Ni <sub>29</sub>	BCC_B2#2, FCC_L12#1	20	[83]
102	2022.10.04	Al <sub>19</sub> Co <sub>47</sub> Cr <sub>8</sub> Ni <sub>26</sub>	BCC_B2#2, FCC_L12#1	4	[83]
103	2022.10.27	Al <sub>16.67</sub> Co <sub>16.67</sub> Cr <sub>16.67</sub> Fe <sub>16.67</sub> Ni <sub>33.33</sub>	BCC_B2#2, FCC_L12#1	21	[137]
104	2022.11.12	Al <sub>16.95</sub> Cr <sub>16.95</sub> Fe <sub>19.1</sub> Ni <sub>47</sub>	BCC_B2#2, FCC_L12#2	7	[165]
105	2022.11.12	Al <sub>33.5</sub> Co <sub>4</sub> Cr <sub>33</sub> Ni <sub>29.5</sub>	BCC_B2#1, BCC_B2#2	6	[165]
106	2022.11.24	Al <sub>17.5</sub> Co <sub>24</sub> Cr <sub>20</sub> Ni <sub>38.5</sub>	BCC_B2#2, FCC_L12#2	15	[147]
107	2022.12.05	Al <sub>18</sub> Co <sub>30</sub> Cr <sub>11</sub> Fe <sub>11</sub> Ni <sub>30</sub>	BCC_B2#2, FCC_L12#2	27	[189]
108	2022.12.21	Al <sub>16.72</sub> Cr <sub>19.73</sub> Fe <sub>16.72</sub> Ni <sub>46.82</sub>	BCC_B2#2, FCC_L12#1	8	[71]
109	2022.12.21	Al <sub>16.78</sub> Cr <sub>16.78</sub> Fe <sub>24.5</sub> Ni <sub>41.95</sub>	BCC_B2#2, FCC_L12#2	2	[71]
110	2023.01.20	Co <sub>22.47</sub> Cr <sub>22.47</sub> Fe <sub>22.47</sub> Nb <sub>5.62</sub> Ni <sub>22.47</sub> Ta <sub>4.49</sub>	C14_LAVES#1, FCC_L12#1	18	[67]
111	2023.02.01	Al <sub>16.6</sub> Cr <sub>12</sub> Fe <sub>28</sub> Ni <sub>43.4</sub>	BCC_B2#2, FCC_L12#1	9	[142]
112	2023.02.01	Al <sub>16.4</sub> Cr <sub>16</sub> Fe <sub>24</sub> Ni <sub>43.6</sub>	BCC_B2#2, FCC_L12#1	9	[142]
113	2023.02.01	Al <sub>17</sub> Cr <sub>8</sub> Fe <sub>32</sub> Ni <sub>43</sub>	BCC_B2#2, FCC_L12#2	8	[142]
114	2023.02.10	Al <sub>19.05</sub> Co <sub>19.05</sub> Cr <sub>19.05</sub> Fe <sub>19.05</sub> Mn <sub>9.52</sub> Mo <sub>1.9</sub> Nb <sub>12.38</sub>	BCC_B2#2, C14_LAVES#1	258	[190]
115	2023.02.24	Al <sub>17</sub> Ni <sub>34</sub> Ti <sub>17</sub> V <sub>32</sub>	BCC_B2#1, HEUSLER_L21#1	163	[191]
116	2023.02.25	Al <sub>16.67</sub> Cr <sub>16.67</sub> Fe <sub>16.67</sub> Mn <sub>16.67</sub> Ni <sub>33.33</sub>	BCC_B2#1, BCC_B2#2	62	[192]
117	2023.03.15	Cr <sub>15</sub> Fe <sub>32.5</sub> Mn <sub>10</sub> Nb <sub>10</sub> Ni <sub>32.5</sub>	C14_LAVES#1, FCC_L12#1	100	[193]
118	2023.04.23	Al <sub>15.38</sub> Co <sub>15.38</sub> Cr <sub>15.38</sub> Fe <sub>15.38</sub> Ni <sub>38.46</sub>	BCC_B2#2, FCC_L12#1	21	[194]
119	2023.05.20	Co <sub>8</sub> Cr <sub>39</sub> Fe <sub>8</sub> Ni <sub>37</sub> V <sub>8</sub>	BCC_B2#2, FCC_L12#1	13	[195]

120	2023.05.20	Co <sub>10</sub> Cr <sub>41</sub> Ni <sub>39</sub> V <sub>10</sub>	BCC_B2#1, FCC_L12#1	12	[195]
121	2023.05.20	Cr <sub>37</sub> Fe <sub>10</sub> Ni <sub>43</sub> V <sub>10</sub>	BCC_B2#2, FCC_L12#1	9	[195]
122	2023.05.20	Co <sub>10</sub> Cr <sub>47</sub> Fe <sub>10</sub> Ni <sub>33</sub>	BCC_B2#1, FCC_L12#1	9	[195]
123	2023.05.24	Al <sub>17.91</sub> Co <sub>12.94</sub> Cr <sub>9.95</sub> Fe <sub>13.93</sub> Ni <sub>44.77</sub> Ti <sub>0.5</sub>	BCC_B2#2, FCC_L12#1	23	[196]
124	2023.05.24	Al <sub>18</sub> Co <sub>13</sub> Cr <sub>10</sub> Fe <sub>14</sub> Ni <sub>45</sub>	BCC_B2#2, FCC_L12#1	10	[196]
125	2023.05.26	Al <sub>14.29</sub> Co <sub>28.57</sub> Cr <sub>28.57</sub> Ni <sub>28.57</sub>	BCC_B2#2, FCC_L12#1	20	[175]
126	2023.06.09	Cr <sub>23.53</sub> Fe <sub>23.53</sub> Nb <sub>14.71</sub> Ni <sub>38.24</sub>	C14_LAVES#1, FCC_L12#1	168	[197]
127	2023.06.09	Cr <sub>29.55</sub> Fe <sub>29.55</sub> Nb <sub>11.35</sub> Ni <sub>29.55</sub>	C14_LAVES#1, FCC_L12#1	149	[197]
128	2023.06.09	Cr <sub>22.22</sub> Fe <sub>33.33</sub> Nb <sub>11.11</sub> Ni <sub>33.33</sub>	C14_LAVES#1, FCC_L12#1	102	[197]
129	2023.06.15	Co <sub>21.05</sub> Cr <sub>21.05</sub> Fe <sub>21.05</sub> Ni <sub>21.05</sub> W <sub>15.79</sub>	FCC_L12#1, SIGMA#1	148	[198]
130	2023.07.16	Al <sub>20</sub> Co <sub>36</sub> Cr <sub>4</sub> Fe <sub>4</sub> Ni <sub>36</sub>	BCC_B2#2, FCC_L12#2	14	[174]
131	2023.07.25	Al <sub>6.32</sub> Co <sub>21.05</sub> Cr <sub>21.05</sub> Fe <sub>21.05</sub> Nb <sub>9.47</sub> Ni <sub>21.05</sub>	C14_LAVES#1, FCC_L12#	65	[199]
132	2023.09.26	Al <sub>18</sub> Co <sub>30</sub> Cr <sub>10</sub> Fe <sub>10</sub> Mo <sub>2</sub> Ni <sub>30</sub>	BCC_B2#2, FCC_L12#1	41	[200]
133	2023.10.18	Al <sub>17</sub> Co <sub>10</sub> Cr <sub>12</sub> Fe <sub>15</sub> Ni <sub>44</sub> W <sub>2</sub>	BCC_B2#2, FCC_L12#2	12	[201]
134	2023.10.30	Co <sub>14.29</sub> Cr <sub>14.29</sub> Fe <sub>14.29</sub> Nb <sub>42.85</sub> Ni <sub>14.29</sub>	C14_LAVES#1, MU_PHASE	176	[202]
135	2023.11.29	Al <sub>17</sub> Fe <sub>28</sub> Ni <sub>49</sub> V <sub>6</sub>	BCC_B2#2, FCC_L12#1	29	[203]
136	2024.01.23	Co <sub>28.57</sub> Fe <sub>28.57</sub> Ni <sub>28.57</sub> Ta <sub>14.29</sub>	C14_LAVES#1, FCC_L12#1	52	[61]
137	2024.02.05	Al <sub>17</sub> Co <sub>33</sub> Cr <sub>17</sub> Ni <sub>33</sub>	BCC_B2#2, FCC_L12#1	15	[204]
138	2024.03.08	Al <sub>21</sub> Co <sub>19.5</sub> Fe <sub>9.5</sub> Ni <sub>50</sub>	BCC_B2#2, FCC_L12#2	16	[205]
139	2024.03.16	Al <sub>20.33</sub> Co <sub>21.6</sub> Fe <sub>30.46</sub> Ni <sub>27.61</sub>	BCC_B2#2, FCC_L12#1	82	[206]
140	2024.04.09	Al <sub>21</sub> Co <sub>14</sub> Cr <sub>10</sub> Fe <sub>5</sub> Ni <sub>50</sub>	BCC_B2#2, FCC_L12#1	28	[184]

## 7.2: Future Research Directions

While this thesis presents new design strategies for EMPEAs, certain limitations remain for future research. A few limitations and suggested directions are outlined below:

1. Exploration of All Eutectic Points:

Current Limitation: Chapter 4 focuses on deep eutectic pairs in binary systems but does not investigate all other eutectic points.

Future Direction: It is possible that aggregating not only deep eutectic points but also other eutectic points in binary elemental pairs could lead to the identification of eutectic compositions in MPEAs.

2. Accuracy of the Single-Phase Plus EFE Strategy:

Current Limitation: The success of this method depends on *Thermo-Calc* and low FAB (fraction of assessed binaries) values, which can lead to inaccuracies, especially for elements outside the standard set.

Future Direction: Validate more eutectics experimentally to improve the database and enhance the accuracy of the single-phase plus EFE strategy.

3. High Computational Time of the High-Throughput CALPHAD Method:

Current Limitation: The method has high computational time due to the separation execution of single-point equilibrium calculations and property models.

Future Direction: Explore more efficient approaches through *TC-Python* or other tools to reduce computational time. Perhaps doing all calculations in the single-point equilibrium model or the property model can solve this problem to a great extent via *TC-Python*.

4. Integration of Machine Learning:

Current Limitation: The thesis does not incorporate machine learning to reduce computational costs, which should have been done, keeping the logical progression it had from mathematical formulas to CALPHAD to high-throughput CALPHAD.

Future Direction: Employ machine learning techniques to further reduce computational costs, completing high-throughput CALPHAD and enabling predictions beyond the existing CALPHAD dataset.

5. Development of Phase Formation Rules:

Current Limitation: Lack of phase formation rules specific to eutectic multi-principal element alloys.

Future Direction: Use machine learning to develop universal phase formation rules, advancing the design strategy for EMPEAs.



6. *Incorporation of Mechanical Properties:*

*Current Limitation:* Current design strategies do not account for mechanical properties at the design stage.

*Future Direction:* Considering FCC percentage in the design stage can be helpful in this regard.



## References:

- [1] J.W. Yeh, S.K. Chen, S.J. Lin, J.Y. Gan, T.S. Chin, T.T. Shun, C.H. Tsau, S.Y. Chang, Nanostructured high-entropy alloys with multiple principal elements: Novel alloy design concepts and outcomes, *Adv Eng Mater* 6 (2004) 299–303. <https://doi.org/10.1002/adem.200300567>.
- [2] B.S. Murty, J.W. Yeh, S. Ranganathan, P.P. Bhattacharjee, *High-Entropy Alloys*, Elsevier Science, 2019. <https://books.google.co.in/books?id=VU2NDwAAQBAJ>.
- [3] B. Cantor, I.T.H. Chang, P. Knight, A.J.B. Vincent, Microstructural development in equiatomic multicomponent alloys, *Materials Science and Engineering: A* 375–377 (2004) 213–218. <https://doi.org/10.1016/j.msea.2003.10.257>.
- [4] S. Ranganathan, *Alloyed pleasures: Multimetalllic cocktails*, 2003.
- [5] D.B. Miracle, O.N. Senkov, A critical review of high entropy alloys and related concepts, *Acta Mater* 122 (2017) 448–511. <https://doi.org/10.1016/j.actamat.2016.08.081>.
- [6] W. Li, D. Xie, D. Li, Y. Zhang, Y. Gao, P.K. Liaw, Mechanical behavior of high-entropy alloys, *Prog Mater Sci* 118 (2021). <https://doi.org/10.1016/j.pmatsci.2021.100777>.
- [7] X. Yan, Y. Zhang, Functional properties and promising applications of high entropy alloys, *Scr Mater* 187 (2020) 188–193. <https://doi.org/10.1016/j.scriptamat.2020.06.017>.
- [8] W. Zhang, P.K. Liaw, Y. Zhang, Science and technology in high-entropy alloys, *Sci China Mater* 61 (2018) 2–22. <https://doi.org/10.1007/s40843-017-9195-8>.
- [9] Q. Fan, C. Chen, C. Fan, Z. Liu, X. Cai, S. Lin, C. Yang, AlCoCrFeNi high-entropy alloy coatings prepared by gas tungsten arc cladding: Microstructure, mechanical and corrosion properties, *Intermetallics (Barking)* 138 (2021). <https://doi.org/10.1016/j.intermet.2021.107337>.
- [10] S. Ma, W. Liu, Q. Li, J. Zhang, S. Huang, Y. Xiong, B. Xu, T. Yang, S. Zhao, Mechanism of elemental segregation around extended defects in high-entropy alloys and its effect on mechanical properties, *Acta Mater* 264 (2024). <https://doi.org/10.1016/j.actamat.2023.119537>.
- [11] O.N. Senkov, G.B. Wilks, J.M. Scott, D.B. Miracle, Mechanical properties of Nb<sub>25</sub>Mo<sub>25</sub>Ta<sub>25</sub>W<sub>25</sub> and V<sub>20</sub>Nb<sub>20</sub>Mo<sub>20</sub>Ta<sub>20</sub>W<sub>20</sub> refractory high entropy alloys, *Intermetallics (Barking)* 19 (2011) 698–706. <https://doi.org/10.1016/j.intermet.2011.01.004>.
- [12] B. Gludovatz, A. Hohenwarter, D. Catoor, E.H. Chang, E.P. George, R.O. Ritchie, A fracture-resistant high-entropy alloy for cryogenic applications, *Science* (1979) 345 (2014) 1153–1158. <https://doi.org/10.1126/science.1254581>.
- [13] Y. Deng, C.C. Tasan, K.G. Pradeep, H. Springer, A. Kostka, D. Raabe, Design of a twinning-induced plasticity high entropy alloy, *Acta Mater* 94 (2015) 124–133. <https://doi.org/10.1016/j.actamat.2015.04.014>.
- [14] M.J. Yao, K.G. Pradeep, C.C. Tasan, D. Raabe, A novel, single phase, non-equiatomic FeMnNiCoCr high-entropy alloy with exceptional phase stability and tensile ductility, *Scr Mater* 72–73 (2014) 5–8. <https://doi.org/10.1016/j.scriptamat.2013.09.030>.
- [15] D. Karlsson, A. Marshal, F. Johansson, M. Schuisky, M. Sahlberg, J.M. Schneider, U. Jansson, Elemental segregation in an AlCoCrFeNi high-entropy alloy – A comparison between selective laser melting and induction melting, *J Alloys Compd* 784 (2019) 195–203. <https://doi.org/10.1016/j.jallcom.2018.12.267>.
- [16] Y.F. Ye, Q. Wang, Y.L. Zhao, Q.F. He, J. Lu, Y. Yang, Elemental segregation in solid-solution high-entropy alloys: Experiments and modeling, *J Alloys Compd* 681 (2016) 167–174. <https://doi.org/10.1016/j.jallcom.2016.04.239>.

- [17] Y. Lu, Y. Dong, S. Guo, L. Jiang, H. Kang, T. Wang, B. Wen, Z. Wang, J. Jie, Z. Cao, H. Ruan, T. Li, A promising new class of high-temperature alloys: Eutectic high-entropy alloys, *Sci Rep* 4 (2014). <https://doi.org/10.1038/srep06200>.
- [18] Y. Lu, Y. Dong, H. Jiang, Z. Wang, Z. Cao, S. Guo, T. Wang, T. Li, P.K. Liaw, Promising properties and future trend of eutectic high entropy alloys, *Scr Mater* 187 (2020) 202–209. <https://doi.org/10.1016/j.scriptamat.2020.06.022>.
- [19] Y. Lu, X. Gao, L. Jiang, Z. Chen, T. Wang, J. Jie, H. Kang, Y. Zhang, S. Guo, H. Ruan, Y. Zhao, Z. Cao, T. Li, Directly cast bulk eutectic and near-eutectic high entropy alloys with balanced strength and ductility in a wide temperature range, *Acta Mater* 124 (2017) 143–150. <https://doi.org/10.1016/j.actamat.2016.11.016>.
- [20] L.F. Lin, C.W. Tsai, Study on the damping behaviour of eutectic high-entropy alloys with lamellar structures, *Philos Mag Lett* 99 (2019) 226–234. <https://doi.org/10.1080/09500839.2019.1660819>.
- [21] W. Tillmann, & L. Wojarski, & D. Stangier, & M. Manka, & C. Timmer, Application of the eutectic high entropy alloy Nb<sub>0.73</sub>CoCrFeNi<sub>2.1</sub> for high temperature joints, (n.d.). <https://doi.org/10.1007/s40194-020-00944-w/Published>.
- [22] Oerlikon Introduces New High Entropy Alloy to Replace Super Duplex Stainless Steels, n.d. <https://www.oerlikon.com/am>.
- [23] B. Chanda, G. Potnis, P.P. Jana, J. Das, A review on nano-/ultrafine advanced eutectic alloys, *J Alloys Compd* 827 (2020). <https://doi.org/10.1016/j.jallcom.2020.154226>.
- [24] M. Wang, Y. Lu, T. Wang, C. Zhang, Z. Cao, T. Li, P.K. Liaw, A novel bulk eutectic high-entropy alloy with outstanding as-cast specific yield strengths at elevated temperatures, *Scr Mater* 204 (2021). <https://doi.org/10.1016/j.scriptamat.2021.114132>.
- [25] J. Lu, H. Zhang, Y. Chen, L. Li, X. Liu, W. Xiao, N. Ni, X. Zhao, F. Guo, P. Xiao, Y-doped AlCoCrFeNi<sub>2.1</sub> eutectic high-entropy alloy with excellent oxidation resistance and structure stability at 1000 °C and 1100 °C, *Corros Sci* 180 (2021). <https://doi.org/10.1016/j.corsci.2020.109191>.
- [26] J. Lu, H. Zhang, L. Li, Y. Chen, X. Liu, X. Zhao, F. Guo, Y-Hf co-doped AlCoCrFeNi<sub>2.1</sub> eutectic high-entropy alloy with excellent oxidation and spallation resistance under thermal cycling conditions at 1100 °C and 1200 °C, *Corros Sci* 187 (2021). <https://doi.org/10.1016/j.corsci.2021.109515>.
- [27] V. Hasannaemi, A. V. Ayyagari, S. Muskeri, R. Salloom, S. Mukherjee, Surface degradation mechanisms in a eutectic high entropy alloy at microstructural length-scales and correlation with phase-specific work function, *Npj Mater Degrad* 3 (2019). <https://doi.org/10.1038/s41529-019-0079-0>.
- [28] S. Shuang, Q. Yu, X. Gao, Q.F. He, J.Y. Zhang, S.Q. Shi, Y. Yang, Tuning the microstructure for superb corrosion resistance in eutectic high entropy alloy, *J Mater Sci Technol* 109 (2022) 197–208. <https://doi.org/10.1016/j.jmst.2021.08.069>.
- [29] F. He, Z. Wang, P. Cheng, Q. Wang, J. Li, Y. Dang, J. Wang, C.T. Liu, Designing eutectic high entropy alloys of CoCrFeNiNb<sub>x</sub>, *J Alloys Compd* 656 (2016) 284–289. <https://doi.org/10.1016/j.jallcom.2015.09.153>.
- [30] W.D. Callister, D.G. Rethwisch, Callister's Materials Science and Engineering, Wiley, 2020. <https://books.google.co.in/books?id=IUjODwAAQBAJ>.
- [31] T. Bhattacharjee, R. Zheng, Y. Chong, S. Sheikh, S. Guo, I.T. Clark, T. Okawa, I.S. Wani, P.P. Bhattacharjee, A. Shibata, N. Tsuji, Effect of low temperature on tensile properties of AlCoCrFeNi<sub>2.1</sub> eutectic high entropy alloy, *Mater Chem Phys* 210 (2018) 207–212. <https://doi.org/10.1016/j.matchemphys.2017.06.023>.
- [32] H. Ma, C.H. Shek, Effects of Hf on the microstructure and mechanical properties of CoCrFeNi high entropy alloy, *J Alloys Compd* 827 (2020). <https://doi.org/10.1016/j.jallcom.2020.154159>.

- [33] X. Gong, H. Chen, F. Zhang, W. Zhu, H. Ma, B. Pang, Y. Yin, Degradation of tensile mechanical properties of two  $\text{Al}_x\text{CoCrFeNi}$  ( $x=0.3$  and  $0.4$ ) high-entropy alloys exposed to liquid lead-bismuth eutectic at 350 and 500 °C, *Journal of Nuclear Materials* 558 (2022) 153364. <https://doi.org/https://doi.org/10.1016/j.jnucmat.2021.153364>.
- [34] P.P. Bhattacharjee, S.R. Reddy, A Brief Perspective on the Status and Future Prospects of Eutectic High-Entropy Alloys, *Transactions of the Indian National Academy of Engineering* (2023). <https://doi.org/10.1007/s41403-023-00442-7>.
- [35] I. Baker, M. Wu, Z. Wang, Eutectic/eutectoid multi-principle component alloys: A review, *Mater Charact* 147 (2019) 545–557. <https://doi.org/10.1016/j.matchar.2018.07.030>.
- [36] Y. Liao, I. Baker, Microstructure and room-temperature mechanical properties of  $\text{Fe}_{30}\text{Ni}_{20}\text{Mn}_{35}\text{Al}_{15}$ , *Mater Charact* 59 (2008) 1546–1549. <https://doi.org/10.1016/j.matchar.2008.01.017>.
- [37] S. Peng, S. Feng, Z. Jiang, J. Ren, S. Zhang, Y. Liu, L. Zhang, W. He, Z. Liu, S. Guan, Z. Xiao, W. Chen, High strength and ductility in a dual-phase hetero-structured  $\text{AlCoCrFeNi}_{2.1}$  eutectic high-entropy alloy by powder metallurgy, *Mater Res Lett* 12 (2024) 363–372. <https://doi.org/10.1080/21663831.2024.2332608>.
- [38] W. Pan, P. Fu, Z. Li, H. Chen, Q. Tang, P. Dai, C. Liu, L. Lin, Microstructure and mechanical properties of  $\text{AlCoCrFeNi}_{2.1}$  eutectic high-entropy alloy synthesized by spark plasma sintering of gas-atomized powder, *Intermetallics (Barking)* 144 (2022). <https://doi.org/10.1016/j.intermet.2022.107523>.
- [39] S. Guo, C. Ng, C.T. Liu, Sunflower-like solidification microstructure in a near-eutectic high-entropy alloy, *Mater Res Lett* 1 (2013) 228–232. <https://doi.org/10.1080/21663831.2013.844737>.
- [40] Y. Tan, J. Li, J. Wang, H. Kou, Seaweed eutectic-dendritic solidification pattern in a  $\text{CoCrFeNiMnPd}$  eutectic high-entropy alloy, *Intermetallics (Barking)* 85 (2017) 74–79. <https://doi.org/10.1016/j.intermet.2017.02.004>.
- [41] X. Cao, C. Wu, Y. Liu, H. Peng, X. Su, Eutectic Reaction and Microstructure Stability in  $\text{CoCrFeNiNb}_x$  High-Entropy Alloys, *Metals (Basel)* 12 (2022). <https://doi.org/10.3390/met12050756>.
- [42] X. Chen, J.Q. Qi, Y.W. Sui, Y.Z. He, F.X. Wei, Q.K. Meng, Z. Sun, Effects of aluminum on microstructure and compressive properties of  $\text{Al-Cr-Fe-Ni}$  eutectic multi-component alloys, *Materials Science and Engineering: A* 681 (2017) 25–31. <https://doi.org/10.1016/j.msea.2016.11.019>.
- [43] L. Jiang, Y. Lu, W. Wu, Z. Cao, T. Li, Microstructure and Mechanical Properties of a  $\text{CoFeNi}_2\text{V}_{0.5}\text{Nb}_{0.75}$  Eutectic High Entropy Alloy in As-cast and Heat-treated Conditions, *J Mater Sci Technol* 32 (2016) 245–250. <https://doi.org/10.1016/j.jmst.2015.08.006>.
- [44] H. Jiang, K. Han, D. Qiao, Y. Lu, Z. Cao, T. Li, Effects of Ta addition on the microstructures and mechanical properties of  $\text{CoCrFeNi}$  high entropy alloy, *Mater Chem Phys* 210 (2018) 43–48. <https://doi.org/10.1016/j.matchemphys.2017.05.056>.
- [45] H. Jiang, D. Qiao, Y. Lu, Z. Ren, Z. Cao, T. Wang, T. Li, Direct solidification of bulk ultrafine-microstructure eutectic high-entropy alloys with outstanding thermal stability, *Scr Mater* 165 (2019) 145–149. <https://doi.org/10.1016/j.scriptamat.2019.02.035>.
- [46] X. Jin, J. Bi, L. Zhang, Y. Zhou, X. Du, Y. Liang, B. Li, A new  $\text{CrFeNi}_2\text{Al}$  eutectic high entropy alloy system with excellent mechanical properties, *J Alloys Compd* 770 (2019) 655–661. <https://doi.org/10.1016/j.jallcom.2018.08.176>.
- [47] H. Jiang, H. Zhang, T. Huang, Y. Lu, T. Wang, T. Li, Microstructures and mechanical properties of  $\text{Co}_2\text{Mo}_x\text{Ni}_2\text{VW}_x$  eutectic high entropy alloys, *Mater Des* 109 (2016) 539–546. <https://doi.org/10.1016/j.matdes.2016.07.113>.

- [48] L. Rogal, J. Morgiel, Z. Świątek, F. Czerwiński, Microstructure and mechanical properties of the new Nb<sub>25</sub>Sc<sub>25</sub>Ti<sub>25</sub>Zr<sub>25</sub> eutectic high entropy alloy, *Materials Science and Engineering: A* 651 (2016) 590–597. <https://doi.org/10.1016/j.msea.2015.10.071>.
- [49] I. Chang, Q. Cai, From simple binary to complex multicomponent eutectic alloys, *Prog Mater Sci* 123 (2022). <https://doi.org/10.1016/j.pmatsci.2021.100779>.
- [50] S.R. Reddy, S. Yoshida, U. Sunkari, A. Lozinko, J. Joseph, R. Saha, D. Fabijanic, S. Guo, P.P. Bhattacharjee, N. Tsuji, Engineering heterogeneous microstructure by severe warm-rolling for enhancing strength-ductility synergy in eutectic high entropy alloys, *Materials Science and Engineering: A* 764 (2019). <https://doi.org/10.1016/j.msea.2019.138226>.
- [51] E.P. George, D. Raabe, R.O. Ritchie, High-Entropy alloys, *Nat Rev Mater* 4 (2019) 515–534. <https://doi.org/10.1038/s41578-019-0121-4>.
- [52] J.P. Liu, J.X. Chen, T.W. Liu, C. Li, Y. Chen, L.H. Dai, Superior strength-ductility CoCrNi medium-entropy alloy wire, *Scr Mater* 181 (2020) 19–24. <https://doi.org/10.1016/j.scriptamat.2020.02.002>.
- [53] S. Zhao, G.M. Stocks, Y. Zhang, Stacking fault energies of face-centered cubic concentrated solid solution alloys, *Acta Mater* 134 (2017) 334–345. <https://doi.org/10.1016/j.actamat.2017.05.001>.
- [54] Z. Li, K.G. Pradeep, Y. Deng, D. Raabe, C.C. Tasan, Metastable high-entropy dual-phase alloys overcome the strength–ductility trade-off, *Nature* 534 (2016) 227–230. <https://doi.org/10.1038/nature17981>.
- [55] Z. Zhang, M.M. Mao, J. Wang, B. Gludovatz, Z. Zhang, S.X. Mao, E.P. George, Q. Yu, R.O. Ritchie, Nanoscale origins of the damage tolerance of the high-entropy alloy CrMnFeCoNi, *Nat Commun* 6 (2015) 10143. <https://doi.org/10.1038/ncomms10143>.
- [56] Z. Zhang, H. Sheng, Z. Wang, B. Gludovatz, Z. Zhang, E.P. George, Q. Yu, S.X. Mao, R.O. Ritchie, Dislocation mechanisms and 3D twin architectures generate exceptional strength-ductility-toughness combination in CrCoNi medium-entropy alloy, *Nat Commun* 8 (2017) 14390. <https://doi.org/10.1038/ncomms14390>.
- [57] Y. Li, P. Shi, M. Wang, Y. Yang, Y. Wang, Y. Li, Y. Wen, W. Ren, N. Min, Y. Chen, Y. Guo, Z. Shen, T. Zheng, N. Liang, W. Lu, P.K. Liaw, Y. Zhong, Y. Zhu, Unveiling microstructural origins of the balanced strength–ductility combination in eutectic high-entropy alloys at cryogenic temperatures, *Mater Res Lett* 10 (2022) 602–610. <https://doi.org/10.1080/21663831.2022.2078169>.
- [58] T. Huang, J. Zhang, J. Zhang, L. Liu, Effective design of Cr-Co-Ni-Ta eutectic medium entropy alloys with high compressive properties using combined CALPHAD and experimental approaches, *Applied Sciences (Switzerland)* 11 (2021). <https://doi.org/10.3390/app11136102>.
- [59] M. Mukarram, M. Mujahid, K. Yaqoob, Design and development of CoCrFeNiTa eutectic high entropy alloys, *Journal of Materials Research and Technology* 10 (2021) 1243–1249. <https://doi.org/10.1016/j.jmrt.2020.12.042>.
- [60] C. Ai, F. He, M. Guo, J. Zhou, Z. Wang, Z. Yuan, Y. Guo, Y. Liu, L. Liu, Alloy design, micromechanical and macromechanical properties of CoCrFeNiTa<sub>x</sub> eutectic high entropy alloys, *J Alloys Compd* 735 (2018) 2653–2662. <https://doi.org/10.1016/j.jallcom.2017.12.015>.
- [61] Y. Xue, N. Feng, C. Kang, K. Tian, Y. Shao, H. Liu, Y. Wu, L. Yuan, Designing eutectic medium-entropy alloys CoFeNiTa<sub>x</sub> with outstanding mechanical properties, *Journal of Materials Research and Technology* 29 (2024) 1244–1252. <https://doi.org/10.1016/j.jmrt.2024.01.191>.
- [62] M. Wu, S. Wang, F. Xiao, G. Shen, Y. Tian, C. Yang, G. Zhu, D. Wang, D. Shu, B. Sun, Designing lightweight dual-phase refractory VNbTiSi-based eutectic high-entropy

- alloys for use at elevated temperatures, *Materials Science and Engineering: A* 842 (2022). <https://doi.org/10.1016/j.msea.2022.143112>.
- [63] Y. Lu, H. Jiang, S. Guo, T. Wang, Z. Cao, T. Li, A new strategy to design eutectic high-entropy alloys using mixing enthalpy, *Intermetallics* (Barking) 91 (2017) 124–128. <https://doi.org/10.1016/j.intermet.2017.09.001>.
- [64] H. Jiang, K. Han, X. Gao, Y. Lu, Z. Cao, M.C. Gao, J.A. Hawk, T. Li, A new strategy to design eutectic high-entropy alloys using simple mixture method, *Mater Des* 142 (2018) 101–105. <https://doi.org/10.1016/j.matdes.2018.01.025>.
- [65] H. Jiang, Z. Ni, J. Wang, L. Li, T. Huang, K. Han, Q. Zhang, H. Sui, Design Multicomponent Eutectic Alloys in the Co–Cr–Fe–Ni–Nb System Using Simple Mixing Method, *Adv Eng Mater* 24 (2022). <https://doi.org/10.1002/adem.202101339>.
- [66] X. Wen, X. Cui, G. Jin, Y. Liu, Y. Zhang, Y. Fang, In-situ synthesis of nano-lamellar  $\text{Ni}_{1.5}\text{CrCoFe}_{0.5}\text{Mo}_{0.1}\text{Nb}_x$  eutectic high-entropy alloy coatings by laser cladding: Alloy design and microstructure evolution, *Surf Coat Technol* 405 (2021). <https://doi.org/10.1016/j.surfcoat.2020.126728>.
- [67] W. Jiao, J. Miao, Y. Lu, X. Chen, Z. Ren, G. Yin, T. Li, Designing CoCrFeNi-M (M = Nb, Ta, Zr and Hf) eutectic high-entropy alloys via a modified simple mixture method, *J Alloys Compd* 941 (2023). <https://doi.org/10.1016/j.jallcom.2023.168975>.
- [68] Q. Wu, Z. Wang, X. Hu, T. Zheng, Z. Yang, F. He, J. Li, J. Wang, Uncovering the eutectics design by machine learning in the Al–Co–Cr–Fe–Ni high entropy system, *Acta Mater* 182 (2020) 278–286. <https://doi.org/10.1016/j.actamat.2019.10.043>.
- [69] F. Liu, X. Xiao, L. Huang, L. Tan, Y. Liu, Design of NiCoCrAl eutectic high entropy alloys by combining machine learning with CALPHAD method, *Mater Today Commun* 30 (2022). <https://doi.org/10.1016/j.mtcomm.2022.103172>.
- [70] Y. Dong, J. Yuan, Z. Zhong, S. Liu, J. Zhang, C. Li, Z. Zhang, Accelerated design eutectic-high-entropy-alloys using simple empirical rules, *Mater Lett* 309 (2022). <https://doi.org/10.1016/j.matlet.2021.131340>.
- [71] J. Yuan, Y. Yang, S. Duan, Y. Dong, C. Li, Z. Zhang, Rapid Design, Microstructures and Properties of Low-Cost Co-Free Al–Cr–Fe–Ni Eutectic Medium Entropy Alloys, *Materials* 16 (2023). <https://doi.org/10.3390/ma16010056>.
- [72] H. Wu, J. Xie, H. Yang, D. Shu, G. Hou, J. Li, Y. Zhou, X. Sun, A cost-effective eutectic high entropy alloy with an excellent strength-ductility combination designed by VEC criterion, *Journal of Materials Research and Technology* 19 (2022) 1759–1765. <https://doi.org/10.1016/j.jmrt.2022.05.165>.
- [73] R.J. Vikram, K. Gupta, S. Suwas, Design of a new cobalt base nano-lamellar eutectic high entropy alloy, *Scr Mater* 202 (2021). <https://doi.org/10.1016/j.scriptamat.2021.113993>.
- [74] X. Jin, Y. Zhou, L. Zhang, X. Du, B. Li, A new pseudo binary strategy to design eutectic high entropy alloys using mixing enthalpy and valence electron concentration, *Mater Des* 143 (2018) 49–55. <https://doi.org/10.1016/j.matdes.2018.01.057>.
- [75] X.K. Zhang, T.H. Chou, W.P. Li, Y.N. Wang, J.C. Huang, L. Cheng, Microstructure and mechanical properties of  $(\text{FeCoNi})_{100-x}(\text{NiAl})_x$  eutectic multi-principal element alloys, *J Alloys Compd* 862 (2021). <https://doi.org/10.1016/j.jallcom.2020.158349>.
- [76] X. Ye, J. Xiong, X. Wu, C. Liu, D. Xu, W. Zhang, D. Fang, B. Li, A new infinite solid solution strategy to design eutectic high entropy alloys with B2 and BCC structure, *Scr Mater* 199 (2021). <https://doi.org/10.1016/j.scriptamat.2021.113886>.
- [77] X. Ye, H. Lei, xinwang Liu, G. Zhao, J. Feng, J. Chen, B. Li, D. Fang, N. Gao, Design of synergistic alloying CoCrFeNi eutectic high entropy alloy based on infinite solid solution, *Mater Lett* 343 (2023). <https://doi.org/10.1016/j.matlet.2023.134395>.

- [78] L. Wang, C. Yao, J. Shen, Y. Zhang, G. Liu, X. Wu, G. Zhang, A new method to design eutectic high-entropy alloys by determining the formation of single-phase solid solution and calculating solidification paths, *Materials Science and Engineering: A* 830 (2022). <https://doi.org/10.1016/j.msea.2021.142325>.
- [79] H. Li, Y. Zhou, L. Yu, Q. Chen, W. Liu, S. Zeng, H. Zhang, Y. Zhu, H. Zhang, H. Zhang, Z. Zhu, Designing hierarchical eutectic high-entropy alloys via partial similar substitution in the Ni-Fe-Ti-Hf-Nb alloys, *Materials Science and Engineering: A* 880 (2023). <https://doi.org/10.1016/j.msea.2023.145263>.
- [80] S. Hao, L. Cui, D. Jiang, X. Han, Y. Ren, J. Jiang, Y. Liu, Z. Liu, S. Mao, Y. Wang, Y. Li, X. Ren, X. Ding, S. Wang, C. Yu, X. Shi, M. Du, F. Yang, Y. Zheng, Z. Zhang, X. Li, D.E. Brown, J. Li, A Transforming Metal Nanocomposite with Large Elastic Strain, Low Modulus and High Strength, *Science* (1979) 339 (2013) 1191–1194. <https://doi.org/10.1126/science.1228602>.
- [81] T. Li, Y. Lu, T. Wang, T. Li, Grouping strategy via d-orbit energy level to design eutectic high-entropy alloys, *Appl Phys Lett* 119 (2021). <https://doi.org/10.1063/5.0061641>.
- [82] A. Shafiei, Design of Eutectic High Entropy Alloys in Al–Co–Cr–Fe–Ni System, *Metals and Materials International* 27 (2021) 127–138. <https://doi.org/10.1007/s12540-020-00655-3>.
- [83] A. Shafiei, Design of Eutectic High Entropy Alloys, *Metall Mater Trans A Phys Metall Mater Sci* 53 (2022) 4349–4361. <https://doi.org/10.1007/s11661-022-06831-x>.
- [84] J.F. Löffler, S. Bossuyt, A. Peker, W.L. Johnson, High-temperature centrifugation: A tool for finding eutectic compositions in multicomponent alloys, *Appl Phys Lett* 81 (2002) 4159–4161. <https://doi.org/10.1063/1.1522820>.
- [85] Y. He, M. Lei, W. Ma, R. Zhang, Y. Lei, A new approach to determine/design the eutectic composition of binary, ternary and high-entropy alloys using electromagnetic directional crystallization, *J Alloys Compd* 916 (2022). <https://doi.org/10.1016/j.jallcom.2022.165410>.
- [86] A. Takeuchi, A. Inoue, Mixing enthalpy of liquid phase calculated by miedema's scheme and approximated with sub-regular solution model for assessing forming ability of amorphous and glassy alloys, *Intermetallics (Barking)* 18 (2010) 1779–1789. <https://doi.org/10.1016/j.intermet.2010.06.003>.
- [87] Z.P. Lu, J. Shen, D.W. Xing, J.F. Sun, C.T. Liu, Binary eutectic clusters and glass formation in ideal glass-forming liquids, *Appl Phys Lett* 89 (2006). <https://doi.org/10.1063/1.2336597>.
- [88] D. Turnbull, A. Structure information amorphous solid formation and interstitial solution behaviour in metallic alloy systems, *Le Journal de Physique Colloques* 35 (1974) C4-1-C4-10. <https://doi.org/10.1051/jphyscol:1974401>.
- [89] Y.J. Sun, D.D. Qu, Y.J. Huang, K.D. Liss, X.S. Wei, D.W. Xing, J. Shen, Zr-Cu-Ni-Al bulk metallic glasses with superhigh glass-forming ability, *Acta Mater* 57 (2009) 1290–1299. <https://doi.org/10.1016/j.actamat.2008.11.007>.
- [90] Y.J. Yang, D.W. Xing, C.P. Li, S.D. Wei, J.K. Sun, Q.K. Shen, A new way of designing bulk metallic glasses in Cu-Ti-Zr-Ni system, *Materials Science and Engineering A* 448 (2007) 15–19. <https://doi.org/10.1016/j.msea.2006.11.075>.
- [91] Y. Zhang, W.G. Zhang, J.P. Lin, G.J. Hao, G.L. Chen, P.K. Liaw, Glass-forming ability and competitive crystalline phases for lightweight Ti-Be-based alloys, *Metall Mater Trans A Phys Metall Mater Sci* 41 (2010) 1670–1676. <https://doi.org/10.1007/s11661-009-0122-9>.
- [92] Y. Dong, Y. Lu, J. Kong, J. Zhang, T. Li, Microstructure and mechanical properties of multi-component AlCrFeNiMo<sub>x</sub> high-entropy alloys, *J Alloys Compd* 573 (2013) 96–101. <https://doi.org/10.1016/j.jallcom.2013.03.253>.



- [93] S. Guo, C. Ng, C.T. Liu, Anomalous solidification microstructures in Co-free  $\text{Al}_x\text{CrCuFeNi}_2$  high-entropy alloys, *J Alloys Compd* 557 (2013) 77–81. <https://doi.org/10.1016/j.jallcom.2013.01.007>.
- [94] L. Jiang, Y. Lu, Y. Dong, T. Wang, Z. Cao, T. Li, Effects of Nb addition on structural evolution and properties of the  $\text{CoFeNi}_2\text{V}_{0.5}$  high-entropy alloy, *Appl Phys A Mater Sci Process* 119 (2015) 291–297. <https://doi.org/10.1007/s00339-014-8964-4>.
- [95] L. Jiang, Z.Q. Cao, J.C. Jie, J.J. Zhang, Y.P. Lu, T.M. Wang, T.J. Li, Effect of Mo and Ni elements on microstructure evolution and mechanical properties of the  $\text{CoFeNi}_x\text{VMo}_y$  high entropy alloys, *J Alloys Compd* 649 (2015) 585–590. <https://doi.org/10.1016/j.jallcom.2015.07.185>.
- [96] F. Meng, I. Baker, Nitriding of a high entropy  $\text{FeNiMnAlCr}$  alloy, *J Alloys Compd* 645 (2015) 376–381. <https://doi.org/10.1016/j.jallcom.2015.05.021>.
- [97] S. Liu, M.C. Gao, P.K. Liaw, Y. Zhang, Microstructures and mechanical properties of  $\text{Al}_x\text{CrFeNiTi}_{0.25}$  alloys, *J Alloys Compd* 619 (2015) 610–615. <https://doi.org/10.1016/j.jallcom.2014.09.073>.
- [98] I. Baker, F. Meng, M. Wu, A. Brandenburg, Recrystallization of a novel two-phase  $\text{FeNiMnAlCr}$  high entropy alloy, *J Alloys Compd* 656 (2016) 458–464. <https://doi.org/10.1016/j.jallcom.2015.09.264>.
- [99] Z. Wang, M. Wu, Z. Cai, S. Chen, I. Baker, Effect of Ti content on the microstructure and mechanical behavior of  $(\text{Fe}_{36}\text{Ni}_{18}\text{Mn}_{33}\text{Al}_{13})_{100-x}\text{Ti}_x$  high entropy alloys, *Intermetallics* (Barking) 75 (2016) 79–87. <https://doi.org/10.1016/j.intermet.2016.06.001>.
- [100] H. Jiang, L. Jiang, D. Qiao, Y. Lu, T. Wang, Z. Cao, T. Li, Effect of Niobium on Microstructure and Properties of the  $\text{CoCrFeNb}_x\text{Ni}$  High Entropy Alloys, *J Mater Sci Technol* 33 (2017) 712–717. <https://doi.org/10.1016/j.jmst.2016.09.016>.
- [101] X. Jin, Y. Zhou, L. Zhang, X. Du, B. Li, A novel  $\text{Fe}_{20}\text{Co}_{20}\text{Ni}_{41}\text{Al}_{19}$  eutectic high entropy alloy with excellent tensile properties, *Mater Lett* 216 (2018) 144–146. <https://doi.org/10.1016/j.matlet.2018.01.017>.
- [102] S. Vrtnik, S. Guo, S. Sheikh, A. Jelen, P. Koželj, J. Luzar, A. Kocjan, Z. Jagličić, A. Meden, H. Guim, H.J. Kim, J. Dolinšek, Magnetism of  $\text{CoCrFeNiZr}_x$  eutectic high-entropy alloys, *Intermetallics* (Barking) 93 (2018) 122–133. <https://doi.org/10.1016/j.intermet.2017.11.017>.
- [103] W. Huo, H. Zhou, F. Fang, X. Zhou, Z. Xie, J. Jiang, Microstructure and properties of novel  $\text{CoCrFeNiTa}_x$  eutectic high-entropy alloys, *J Alloys Compd* 735 (2018) 897–904. <https://doi.org/10.1016/j.jallcom.2017.11.075>.
- [104] R. Jain, M.R. Rahul, S. Jain, S. Samal, V. Kumar, Phase Evolution and Mechanical Behaviour of Co–Fe–Mn–Ni–Ti Eutectic High Entropy Alloys, *Transactions of the Indian Institute of Metals* 71 (2018) 2795–2799. <https://doi.org/10.1007/s12666-018-1437-2>.
- [105] Z.Y. Ding, Q.F. He, Q. Wang, Y. Yang, Superb strength and high plasticity in laves phase rich eutectic medium-entropy-alloy nanocomposites, *Int J Plast* 106 (2018) 57–72. <https://doi.org/10.1016/j.ijplas.2018.03.001>.
- [106] D. Liu, P. Yu, G. Li, P.K. Liaw, R. Liu, High-temperature high-entropy alloys  $\text{Al}_x\text{Co}_{15}\text{Cr}_{15}\text{Ni}_{70-x}$  based on the Al–Ni binary system, *Materials Science and Engineering: A* 724 (2018) 283–288. <https://doi.org/10.1016/j.msea.2018.03.058>.
- [107] Y. Guo, L. Liu, Y. Zhang, J. Qi, B. Wang, Z. Zhao, J. Shang, J. Xiang, A superfine eutectic microstructure and the mechanical properties of  $\text{CoCrFeNiMo}_x$  high-entropy alloys, *J Mater Res* 33 (2018) 3258–3265. <https://doi.org/10.1557/jmr.2018.177>.

- [108] Y. Tan, J. Li, J. Wang, M. Kolbe, H. Kou, Microstructure characterization of CoCrFeNiMnPd<sub>x</sub> eutectic high-entropy alloys, *J Alloys Compd* 731 (2018) 600–611. <https://doi.org/10.1016/j.jallcom.2017.09.057>.
- [109] Q. Wu, Z. Wang, T. Zheng, D. Chen, Z. Yang, J. Li, J. jung Kai, J. Wang, A casting eutectic high entropy alloy with superior strength-ductility combination, *Mater Lett* 253 (2019) 268–271. <https://doi.org/10.1016/j.matlet.2019.06.067>.
- [110] Z. Yang, Z. Wang, Q. Wu, T. Zheng, P. Zhao, J. Zhao, J. Chen, Enhancing the mechanical properties of casting eutectic high entropy alloys with Mo addition, *Appl Phys A Mater Sci Process* 125 (2019). <https://doi.org/10.1007/s00339-019-2506-z>.
- [111] A. Shafiei, S. Rajabi, A cobalt-rich eutectic high-entropy alloy in the system Al–Co–Cr–Fe–Ni, *Appl Phys A Mater Sci Process* 125 (2019). <https://doi.org/10.1007/s00339-019-3084-9>.
- [112] M.R. Rahul, G. Phanikumar, Design of a Seven-Component Eutectic High-Entropy Alloy, *Metall Mater Trans A Phys Metall Mater Sci* 50 (2019) 2594–2598. <https://doi.org/10.1007/s11661-019-05210-3>.
- [113] Y. Dong, Z. Yao, X. Huang, F. Du, C. Li, A. Chen, F. Wu, Y. Cheng, Z. Zhang, Microstructure and mechanical properties of AlCo<sub>x</sub>CrFeNi<sub>3-x</sub> eutectic high-entropy-alloy system, *J Alloys Compd* 823 (2020). <https://doi.org/10.1016/j.jallcom.2020.153886>.
- [114] D.F. Barros, J.C.P. Santos, D.A. Abreu, A.A.A.P. Silva, K.E. Borowski, N. Chaia, C.A. Nunes, G.C. Coelho, Liquidus projection of the Al–Cr–V system, *J Alloys Compd* 899 (2022). <https://doi.org/10.1016/j.jallcom.2021.163258>.
- [115] Y. Qiu, Y.J. Hu, A. Taylor, M.J. Styles, R.K.W. Marceau, A. V. Ceguerra, M.A. Gibson, Z.K. Liu, H.L. Fraser, N. Birbilis, A lightweight single-phase AlTiVCr compositionally complex alloy, *Acta Mater* 123 (2017) 115–124. <https://doi.org/10.1016/j.actamat.2016.10.037>.
- [116] C.T. Rios, S. Milenkovic, R. Caram, A novel ternary eutectic in the Nb–Al–Ni system, *Scr Mater* 48 (2003) 1495–1500. [https://doi.org/10.1016/S1359-6462\(03\)00073-3](https://doi.org/10.1016/S1359-6462(03)00073-3).
- [117] X. An, C. Chu, H. Zhao, B. Shen, L. Zhou, P.K. Chu, CoNiFeNb<sub>0.45</sub> eutectic multi-principal element alloy with excellent mechanical properties and corrosion resistance, *Materials Science and Engineering: A* 777 (2020). <https://doi.org/10.1016/j.msea.2020.139026>.
- [118] G. Hillel, L. Natovitz, S. Salhov, S. Haroush, M. Pinkas, L. Meshi, Understanding the role of the constituting elements of the AlCoCrFeNi high entropy alloy through the investigation of quaternary alloys, *Metals (Basel)* 10 (2020) 1–11. <https://doi.org/10.3390/met10101275>.
- [119] W. Huo, H. Zhou, F. Fang, Z. Xie, J. Jiang, Microstructure and mechanical properties of CoCrFeNiZr<sub>x</sub> eutectic high-entropy alloys, *Mater Des* 134 (2017) 226–233. <https://doi.org/10.1016/j.matdes.2017.08.030>.
- [120] B. Gwalani, S. Gangireddy, Y. Zheng, V. Soni, R.S. Mishra, R. Banerjee, Influence of ordered L1<sub>2</sub> precipitation on strain-rate dependent mechanical behavior in a eutectic high entropy alloy, *Sci Rep* 9 (2019). <https://doi.org/10.1038/s41598-019-42870-y>.
- [121] B. Chanda, J. Das, An assessment on the stability of the eutectic phases in high entropy alloys, *J Alloys Compd* 798 (2019) 167–173. <https://doi.org/10.1016/j.jallcom.2019.05.241>.
- [122] Y. Shao, H. Ma, Y. Wang, Effect of mo addition on the microstructure and mechanical properties of CoCuFeNi high entropy alloy, *Metals (Basel)* 10 (2020) 1–10. <https://doi.org/10.3390/met10081017>.

- [123] M. Zhu, L. Yao, Y. Liu, M. Zhang, K. Li, Z. Jian, Microstructure evolution and mechanical properties of a novel CrNbTiZrAl<sub>x</sub> ( $0.25 \leq x \leq 1.25$ ) eutectic refractory high-entropy alloy, *Mater Lett* 272 (2020). <https://doi.org/10.1016/j.matlet.2020.127869>.
- [124] H.T. Jeong, H.K. Park, W.J. Kim, Dynamic recrystallization and hot deformation mechanisms of a eutectic Al<sub>0.7</sub>CoCrFeMnNi high-entropy alloy, *J Alloys Compd* 871 (2021). <https://doi.org/10.1016/j.jallcom.2021.159488>.
- [125] Y. Du, X. Pei, Z. Tang, F. Zhang, Q. Zhou, H. Wang, W. Liu, Mechanical and tribological performance of CoCrNiHf<sub>x</sub> eutectic medium-entropy alloys, *J Mater Sci Technol* 90 (2021) 194–204. <https://doi.org/10.1016/j.jmst.2021.03.023>.
- [126] J. Zhang, T. Huang, Z. Shen, H.J. Su, J. Zhang, L. Liu, Enhanced structural refinement on eutectic medium-entropy alloy CrCoNiNb<sub>0.48</sub> by laser remelting, *Mater Lett* 304 (2021). <https://doi.org/10.1016/j.matlet.2021.130710>.
- [127] Y. Lu, M. Zhang, L. Zhang, P. Yu, R. Li, X. Liu, Y. Zhang, G. Li, Cobalt-element-free eutectic medium-entropy alloys with superior mechanical performance and processability, *Materials Science and Engineering: A* 801 (2021). <https://doi.org/10.1016/j.msea.2020.140421>.
- [128] W. Jiao, T. Li, X. Chang, Y. Lu, G. Yin, Z. Cao, T. Li, A novel Co-free Al<sub>0.75</sub>CrFeNi eutectic high entropy alloy with superior mechanical properties, *J Alloys Compd* 902 (2022). <https://doi.org/10.1016/j.jallcom.2022.163814>.
- [129] X. An, W. Zhang, Y. Li, L. Zhang, Y. Zhang, W. Wei, C. Chu, Microstructure and Solidification Behavior of Co<sub>30</sub>Ni<sub>30</sub>Fe<sub>30</sub>Zr<sub>10</sub> Eutectic Multi-Principal Element Alloy, *Adv Eng Mater* 25 (2023). <https://doi.org/10.1002/adem.202201601>.
- [130] B. Sundman, I. Ohnuma, N. Dupin, U.R. Kattner, S.G. Fries, An assessment of the entire Al-Fe system including D03 ordering, *Acta Mater* 57 (2009) 2896–2908. <https://doi.org/10.1016/j.actamat.2009.02.046>.
- [131] D. Duan, Y. Wu, H. Chen, X. Wang, X. Liu, H. Wang, S. Jiang, Z. Lu, A strategy to design eutectic high-entropy alloys based on binary eutectics, *J Mater Sci Technol* 103 (2022) 152–156. <https://doi.org/10.1016/j.jmst.2021.06.038>.
- [132] T. Xie, Z. Xiong, Z. Xu, Z. Liu, X. Cheng, Another eutectic point of Co–Cr–Fe–Ni–M (Hf, Ta, Nb) high-entropy system determined using a simple mixture method correlated with mixing enthalpy, *Materials Science and Engineering: A* 802 (2021). <https://doi.org/10.1016/j.msea.2020.140634>.
- [133] X. Ma, X. Ding, R. Chen, X. Gao, Y. Su, H. Cui, Enhanced hydrogen storage properties of ZrTiVAl<sub>1-x</sub>Fe<sub>x</sub> high-entropy alloys by modifying the Fe content, *RSC Adv* 12 (2022) 11272–11281. <https://doi.org/10.1039/d2ra01064j>.
- [134] S. Bottin-Rousseau, V.T. Witusiewicz, U. Hecht, J. Fernandez, A. Laveron-Simavilla, S. Akamatsu, Coexistence of rod-like and lamellar eutectic growth patterns, *Scr Mater* 207 (2022). <https://doi.org/10.1016/j.scriptamat.2021.114314>.
- [135] Y. Zhang, T.T. Zuo, Z. Tang, M.C. Gao, K.A. Dahmen, P.K. Liaw, Z.P. Lu, Microstructures and properties of high-entropy alloys, *Prog Mater Sci* 61 (2014) 1–93. <https://doi.org/10.1016/j.pmatsci.2013.10.001>.
- [136] W. Al Khoury, N. Tamura, G. Geandier, P. Goudeau, New structural insight into interface-controlled  $\alpha$ – $\sigma$  phase transformation in Fe–Cr alloys, *Quantum Beam Science* 2 (2018). <https://doi.org/10.3390/qubs2040027>.
- [137] T.S. Kumar, L. Chauhan, K. Chakravarthy, A. Chelvane, T. Shanmugasundaram, The improved galvanic corrosion resistance of a eutectic high entropy alloy through heat treatment, *J Mater Res* 37 (2022) 4211–4221. <https://doi.org/10.1557/s43578-022-00787-9>.
- [138] P.H.F. Oliveira, P.H.S. Mancilha, R.A.V. Reyes, G.L. de Gouveia, C. Bolfarini, J.E. Spinelli, F.G. Coury, Influence of the cooling rate on the solidification path and

- microstructure of a AlCoCrFeNi<sub>2.1</sub> alloy, *Mater Charact* 203 (2023). <https://doi.org/10.1016/j.matchar.2023.113121>.
- [139] M.H. Tsai, K.C. Chang, J.H. Li, R.C. Tsai, A.H. Cheng, A second criterion for sigma phase formation in high-entropy alloys, *Mater Res Lett* 4 (2016) 90–95. <https://doi.org/10.1080/21663831.2015.1121168>.
- [140] M.H. Tsai, K.Y. Tsai, C.W. Tsai, C. Lee, C.C. Juan, J.W. Yeh, Criterion for sigma phase formation in Cr- and V-Containing high-entropy alloys, *Mater Res Lett* 1 (2013) 207–212. <https://doi.org/10.1080/21663831.2013.831382>.
- [141] Q. Wu, F. He, J. Li, H.S. Kim, Z. Wang, J. Wang, Phase-selective recrystallization makes eutectic high-entropy alloys ultra-ductile, *Nat Commun* 13 (2022). <https://doi.org/10.1038/s41467-022-32444-4>.
- [142] Z. Mao, X. Jin, Z. Xue, M. Zhang, J. Qiao, Understanding the yield strength difference in dual-phase eutectic high-entropy alloys, *Materials Science and Engineering: A* 867 (2023). <https://doi.org/10.1016/j.msea.2023.144725>.
- [143] X. Jin, Y. Liang, J. Bi, B. Li, Enhanced strength and ductility of Al<sub>0.9</sub>CoCrNi<sub>2.1</sub> eutectic high entropy alloy by thermomechanical processing, *Materialia (Oxf)* 10 (2020). <https://doi.org/10.1016/j.mtla.2020.100639>.
- [144] L. Ma, J. Wang, P. Jin, Microstructure and mechanical properties variation with Ni content in Al<sub>0.8</sub>CoCr<sub>0.6</sub>Fe<sub>0.7</sub>Ni<sub>x</sub> (x = 1.1, 1.5, 1.8, 2.0) eutectic high-entropy alloy system, *Mater Res Express* 7 (2020). <https://doi.org/10.1088/2053-1591/ab6580>.
- [145] Q. Liu, X. Liu, X. Fan, R. Li, X. Tong, P. Yu, G. Li, Designing novel AlCoCrNi eutectic high entropy alloys, *J Alloys Compd* 904 (2022). <https://doi.org/10.1016/j.jallcom.2022.163775>.
- [146] J. Miao, M. Wang, A. Zhang, Y. Lu, T. Wang, T. Li, Tribological Properties and Wear Mechanism of AlCr<sub>1.3</sub>TiNi<sub>2</sub> Eutectic High-Entropy Alloy at Elevated Temperature, *Jinshu Xuebao/Acta Metallurgica Sinica* 59 (2023) 267–276. <https://doi.org/10.11900/0412.1961.2021.00589>.
- [147] L. Ma, J. Wang, Z. Lai, Z. Wu, B. Yang, P. Zhao, Microstructure and mechanical property of Al<sub>56-x</sub>Co<sub>24</sub>Cr<sub>20</sub>Ni<sub>x</sub> eutectic high-entropy alloys with an ordered FCC/BCT phase structure, *J Alloys Compd* 936 (2023). <https://doi.org/10.1016/j.jallcom.2022.168194>.
- [148] S. Shukla, T. Wang, S. Cotton, R.S. Mishra, Hierarchical microstructure for improved fatigue properties in a eutectic high entropy alloy, *Scr Mater* 156 (2018) 105–109. <https://doi.org/10.1016/j.scriptamat.2018.07.022>.
- [149] H. Jiang, D. Qiao, W. Jiao, K. Han, L. Yiping, P.K. Liaw, Tensile deformation behavior and mechanical properties of a bulk cast Al<sub>0.9</sub>CoFeNi<sub>2</sub> eutectic high-entropy alloy, *J Mater Sci Technol* 61 (2021) 119–124. <https://doi.org/10.1016/j.jmst.2020.05.053>.
- [150] S. Mukanov, P. Loginov, A. Fedotov, M. Bychkova, M. Antonyuk, E. Levashov, The Effect of Copper on the Microstructure, Wear and Corrosion Resistance of CoCrCuFeNi High-Entropy Alloys Manufactured by Powder Metallurgy, *Materials* 16 (2023). <https://doi.org/10.3390/ma16031178>.
- [151] Q. Wang, Y. Lu, Q. Yu, Z. Zhang, The Exceptional Strong Face-centered Cubic Phase and Semi-coherent Phase Boundary in a Eutectic Dual-phase High Entropy Alloy AlCoCrFeNi, *Sci Rep* 8 (2018). <https://doi.org/10.1038/s41598-018-33330-0>.
- [152] J. Song, Z. Chai, J. Zheng, Q. Wu, F. He, Z. Yang, J. Li, J. Wang, H. Yang, Z. Wang, Design Fe-based Eutectic Medium-Entropy Alloys Fe<sub>2</sub>NiCrNb<sub>x</sub>, *Acta Metallurgica Sinica (English Letters)* 34 (2021) 1103–1108. <https://doi.org/10.1007/s40195-021-01234-0>.
- [153] T. Xu, Y. Lu, Z. Cao, T. Wang, T. Li, Effects of Ta Addition on the Microstructure and Mechanical Properties of CoCu<sub>0.5</sub>FeNi High-Entropy Alloy, *J Mater Eng Perform* 28 (2019) 7642–7648. <https://doi.org/10.1007/s11665-019-04463-8>.

- [154] R. Li, J. Ren, G.J. Zhang, J.Y. He, Y.P. Lu, T.M. Wang, T.J. Li, Novel (CoFe<sub>2</sub>NiV<sub>0.5</sub>Mo<sub>0.2</sub>)<sub>100-x</sub>Nb<sub>x</sub> Eutectic High-Entropy Alloys with Excellent Combination of Mechanical and Corrosion Properties, *Acta Metallurgica Sinica (English Letters)* 33 (2020) 1046–1056. <https://doi.org/10.1007/s40195-020-01072-6>.
- [155] B. Chanda, J. Das, Composition Dependence on the Evolution of Nanoeutectic in CoCrFeNiNb<sub>x</sub> (0.45 ≤ x ≤ 0.65) High Entropy Alloys, *Adv Eng Mater* 20 (2018). <https://doi.org/10.1002/adem.201700908>.
- [156] W. hyuk Lee, Y. Oh, M.G. Jo, H.N. Han, Y. Kim, Microstructures and mechanical properties of CrFeNi<sub>2</sub>Nb<sub>x</sub> eutectic multicomponent alloys, *J Alloys Compd* 860 (2021). <https://doi.org/10.1016/j.jallcom.2020.158502>.
- [157] W. Jiao, H. Jiang, D. Qiao, J. He, H. Zhao, Y. Lu, T. Li, Effects of Mo on microstructure and mechanical properties of Fe<sub>2</sub>Ni<sub>2</sub>CrMo<sub>x</sub> eutectic high entropy alloys, *Mater Chem Phys* 260 (2021). <https://doi.org/10.1016/j.matchemphys.2020.124175>.
- [158] Z.Q. Xu, Z.L. Ma, G.H. Xia, M. Wang, T.B. Xie, X.W. Cheng, Microstructures and mechanical properties of CoCrFeNiHf<sub>x</sub> high-entropy alloys, *Materials Science and Engineering: A* 792 (2020). <https://doi.org/10.1016/j.msea.2020.139820>.
- [159] Y. Yin, Q. Tan, T. Wang, D. Kent, N. Mo, M. Bermingham, H. Li, M.X. Zhang, Eutectic modification of Fe-enriched high-entropy alloys through minor addition of boron, *J Mater Sci* 55 (2020) 14571–14587. <https://doi.org/10.1007/s10853-020-05025-3>.
- [160] T. Bhattacharjee, I.S. Wani, S. Sheikh, I.T. Clark, T. Okawa, S. Guo, P.P. Bhattacharjee, N. Tsuji, Simultaneous strength-ductility enhancement of a nano-lamellar AlCoCrFeNi<sub>2.1</sub> eutectic high entropy alloy by cryo-rolling and annealing, *Sci Rep* 8 (2018). <https://doi.org/10.1038/s41598-018-21385-y>.
- [161] S. Yang, J. Lu, F. Xing, L. Zhang, Y. Zhong, Revisit the VEC rule in high entropy alloys (HEAs) with high-throughput CALPHAD approach and its applications for material design-A case study with Al–Co–Cr–Fe–Ni system, *Acta Mater* 192 (2020) 11–19. <https://doi.org/10.1016/j.actamat.2020.03.039>.
- [162] Y. chen Liu, S. yu Yen, S. hsiang Chu, S. kang Lin, M.H. Tsai, Mechanical and thermodynamic data-driven design of Al-Co-Cr-Fe-Ni multi-principal element alloys, *Mater Today Commun* 26 (2021). <https://doi.org/10.1016/j.mtcomm.2021.102096>.
- [163] M.J.Q. Hernandez, J.A. Pero-Sanz, L.F. Verdeja, *Solidification and Solid-State Transformations of Metals and Alloys*, Elsevier Science, 2017. <https://books.google.co.in/books?id=zxZ2DQAAQBAJ>.
- [164] W.R. Wang, W.L. Wang, S.C. Wang, Y.C. Tsai, C.H. Lai, J.W. Yeh, Effects of Al addition on the microstructure and mechanical property of Al<sub>x</sub>CoCrFeNi high-entropy alloys, *Intermetallics* (Barking) 26 (2012) 44–51. <https://doi.org/10.1016/j.intermet.2012.03.005>.
- [165] K. Bai, C.K. Ng, M. Lin, F. Wei, S. Li, S.L. Teo, D.C.C. Tan, P. Wang, D. Wu, J.J. Lee, Y.W. Zhang, Short-range ordering heredity in eutectic high entropy alloys: A new model based on pseudo-ternary eutectics, *Acta Mater* 243 (2023). <https://doi.org/10.1016/j.actamat.2022.118512>.
- [166] Q. Zhao, Z. Pan, X. Wang, H. Luo, Y. Liu, X. Li, Corrosion and passive behavior of Al<sub>x</sub>CrFeNi<sub>3-x</sub> (x = 0.6, 0.8, 1.0) eutectic high entropy alloys in chloride environment, *Corros Sci* 208 (2022). <https://doi.org/10.1016/j.corsci.2022.110666>.
- [167] X. Wan, A. Lan, M. Zhang, X. Jin, H. Yang, J. Qiao, Corrosion and passive behavior of Al<sub>0.8</sub>CrFeNi<sub>2.2</sub> eutectic high entropy alloy in different media, *J Alloys Compd* 944 (2023). <https://doi.org/10.1016/j.jallcom.2023.169217>.
- [168] M. Wang, Z. Wen, J. Liu, B. Ma, M. Wang, Z. Zou, Y. Zhao, Labyrinthine structure Al<sub>x</sub>CrFeNi (x ≥ 1) eutectic high entropy alloys with duplex reinforced phases, *J Alloys Compd* 918 (2022). <https://doi.org/10.1016/j.jallcom.2022.165441>.

- [169] S. Li, F. Chen, X. Tang, G. Ge, Z. Sun, Z. Geng, M. Fan, P. Huang, Effect of Ti on the Microstructure and Mechanical Properties of AlCrFeNiTi<sub>x</sub> Eutectic High-Entropy Alloys, *J Mater Eng Perform* 31 (2022) 8294–8303. <https://doi.org/10.1007/s11665-022-06825-1>.
- [170] M. Wang, G. Lu, J. Li, Z. Wen, G. Wei, Y. Zhao, Effects of Al on Structure Evolution and Mechanical Performance of Al<sub>x</sub>CrFeNi ( $x > 1$ ) Eutectic High-Entropy Alloys, *Transactions of the Indian Institute of Metals* 76 (2023) 1045–1051. <https://doi.org/10.1007/s12666-022-02765-5>.
- [171] X. Chen, Y. Sui, J. Qi, Y. He, F. Wei, Q. Meng, Z. Sun, Microstructure of Al<sub>1.3</sub>CrFeNi eutectic high entropy alloy and oxidation behavior at 1000 °C, *J Mater Res* 32 (2017) 2109–2116. <https://doi.org/10.1557/jmr.2017.10>.
- [172] G. Diao, M. Wu, A. He, Z. Xu, S.E. Mousavi, D. Li, Manipulate A2/B2 Structures in AlCrFe<sub>x</sub>Ni Alloys for Improved Mechanical Properties and Wear Resistance, *Lubricants* 11 (2023). <https://doi.org/10.3390/lubricants11090392>.
- [173] H. Jiang, L. Li, R. Wang, K. Han, Q. Wang, Effects of Chromium on the Microstructures and Mechanical Properties of AlCoCr<sub>x</sub>FeNi<sub>2.1</sub> Eutectic High Entropy Alloys, *Acta Metallurgica Sinica (English Letters)* 34 (2021) 1565–1573. <https://doi.org/10.1007/s40195-021-01303-4>.
- [174] W. Jiao, T. Li, G. Yin, T. He, T. Li, Y. Lu, Hot deformation characteristics and microstructure evolution of Al<sub>20</sub>Co<sub>36</sub>Cr<sub>4</sub>Fe<sub>4</sub>Ni<sub>36</sub> eutectic high entropy alloy, *Mater Charact* 204 (2023). <https://doi.org/10.1016/j.matchar.2023.113180>.
- [175] M. Zheng, C. Li, X. Zhang, Z. Ye, Y. Liao, J. Gu, Design of a novel (CoCrNi)<sub>84.5</sub>(Al)<sub>15.5</sub> eutectic medium-entropy alloy with hierarchically nano-lamellar microstructure through additively manufactured compositionally graded materials, *Materials Science and Engineering: A* 878 (2023). <https://doi.org/10.1016/j.msea.2023.145209>.
- [176] H. Gasan, A. Ozcan, New Eutectic High-Entropy Alloys Based on Co–Cr–Fe–Mo–Ni–Al: Design, characterization and mechanical properties, *Metals and materials international* 26 (2020) 1152–1167. <https://doi.org/10.1007/s12540-019-00515-9>.
- [177] M. Wu, S. Wang, H. Huang, D. Shu, B. Sun, CALPHAD aided eutectic high-entropy alloy design, *Mater Lett* 262 (2020). <https://doi.org/10.1016/j.matlet.2019.127175>.
- [178] L. Han, X. Xu, Z. Li, B. Liu, C.T. Liu, Y. Liu, A novel equiaxed eutectic high-entropy alloy with excellent mechanical properties at elevated temperatures, *Mater Res Lett* 8 (2020) 373–382. <https://doi.org/10.1080/21663831.2020.1772395>.
- [179] L. Han, T. Quan, B. Liu, X. Xu, Y. Liu, Revealing the excellent high-temperature oxidation resistance of a non-equimolar Al<sub>1</sub>Co<sub>25</sub>Cr<sub>18</sub>Fe<sub>23</sub>Ni<sub>23</sub>Ta<sub>10</sub> compositional complex eutectic alloy, *J Alloys Compd* 846 (2020). <https://doi.org/10.1016/j.jallcom.2020.156265>.
- [180] N. Yurchenko, E. Panina, S. Zhrebtssov, N. Stepanov, Design and characterization of eutectic refractory high entropy alloys, *Materialia (Oxf)* 16 (2021). <https://doi.org/10.1016/j.mtla.2021.101057>.
- [181] P. Shi, Y. Li, Y. Wen, Y. Li, Y. Wang, W. Ren, T. Zheng, Y. Guo, L. Hou, Z. Shen, Y. Jiang, J. Peng, P. Hu, N. Liang, Q. Liu, P.K. Liaw, Y. Zhong, A precipitate-free AlCoFeNi eutectic high-entropy alloy with strong strain hardening, *J Mater Sci Technol* 89 (2021) 88–96. <https://doi.org/10.1016/j.jmst.2021.03.005>.
- [182] R. Jain, S.K. Dewangan, P. Umre, V. Kumar, S. Samal, Microstructure Evolution and an ANN Approach for Microhardness Prediction of Suction Cast FeCoNiCrMnVNb Eutectic High-Entropy Alloys, *Transactions of the Indian Institute of Metals* 74 (2021) 2671–2679. <https://doi.org/10.1007/s12666-021-02335-1>.

- [183] J.W. Choi, J.T. Kim, J.H. Park, S.H. Hong, H.J. Park, T.J. Choi, K.B. Kim, Stress-induced transformation behavior in near-eutectic  $(\text{AlNi}_2)_{70-x}\text{Co}_{30}\text{Cr}_x$  medium entropy alloys, *J Alloys Compd* 891 (2022). <https://doi.org/10.1016/j.jallcom.2021.161995>.
- [184] Y. Zeng, M. Man, C. Koon Ng, Z. Aitken, K. Bai, D. Wu, J. Jun Lee, S. Rong Ng, F. Wei, P. Wang, D. Cheng Cheh Tan, Y.W. Zhang, Search for eutectic high entropy alloys by integrating high-throughput CALPHAD, machine learning and experiments, *Mater Des* 241 (2024). <https://doi.org/10.1016/j.matdes.2024.112929>.
- [185] X. Zhong, Q. Zhang, M. Ma, J. Xie, M. Wu, S. Ren, Y. Yan, Dynamic compressive properties and microstructural evolution of  $\text{Al}_{1.19}\text{Co}_2\text{CrFeNi}_{1.81}$  eutectic high entropy alloy at room and cryogenic temperatures, *Mater Des* 219 (2022). <https://doi.org/10.1016/j.matdes.2022.110724>.
- [186] K. Chen, Z. Xiong, M. An, T. Xie, W. Zou, Y. Xue, X. Cheng, Machine learning correlated with phenomenological mode unlocks the vast compositional space of eutectics of multi-principal element alloys, *Mater Des* 219 (2022). <https://doi.org/10.1016/j.matdes.2022.110795>.
- [187] B. Preuß, T. Lindner, T. Uhlig, G. Wagner, T. Lampke, Niobium and Molybdenum as Alloying Constituents in  $\text{Al}_{0.3}\text{CoCrFeNi}$  to Develop Eutectic High-Entropy Alloys for HVOF Spraying, *Journal of Thermal Spray Technology* 32 (2023) 415–424. <https://doi.org/10.1007/s11666-022-01417-w>.
- [188] M. Qi, Q. Wu, Z. Yang, Y. Wang, Y. Li, L. Wang, J. Li, Z. Wang, J. Wang, Surface strengthening of  $\text{Ni}_{32-x}\text{Co}_{30}\text{Cr}_{10}\text{Fe}_{10}\text{Al}_{18}\text{Ti}_x$  eutectic high-entropy alloys by laser remelting and heat treatment, *Appl Phys A Mater Sci Process* 128 (2022). <https://doi.org/10.1007/s00339-022-06073-z>.
- [189] D.H. Chung, J. Lee, Q.F. He, Y.K. Kim, K.R. Lim, H.S. Kim, Y. Yang, Y.S. Na, Hetero-deformation promoted strengthening and toughening in BCC rich eutectic and near eutectic high entropy alloys, *J Mater Sci Technol* 146 (2023) 1–9. <https://doi.org/10.1016/j.jmst.2022.10.036>.
- [190] X. Wen, X. Cui, G. Jin, Y. Liu, Y. Zhang, H. Tian, X. Zhang, Novel nano-lamellar  $\text{AlCoCrFeMn}_{0.5}\text{Mo}_{0.1}\text{Nb}_x$  eutectic high-entropy alloy coatings by ultrasonic assisted laser cladding: Microstructure and tribological behaviors, *Intermetallics (Barking)* 156 (2023). <https://doi.org/10.1016/j.intermet.2023.107851>.
- [191] M. Wang, Y. Lu, J. Lan, T. Wang, C. Zhang, Z. Cao, T. Li, P.K. Liaw, Lightweight, ultrastrong and high thermal-stable eutectic high-entropy alloys for elevated-temperature applications, *Acta Mater* 248 (2023). <https://doi.org/10.1016/j.actamat.2023.118806>.
- [192] X. Wei, L. Zhang, C. Zhang, G. Li, A sunflower-like eutectic microstructure in the  $\text{AlCrFeMnNi}_2$  high-entropy alloy with excellent compressive mechanical properties, *Mater Lett* 339 (2023). <https://doi.org/10.1016/j.matlet.2023.134107>.
- [193] D. Fang, X. Wu, W. Xu, L. Yu, M. Liu, A. Zhang, B. Li, X. Ye, Microstructure and properties of a novel cost-effective FeNi-based eutectic high entropy alloys, *Materials Science and Engineering: A* 870 (2023). <https://doi.org/10.1016/j.msea.2023.144919>.
- [194] J. Zhang, J. Fan, Y. Peng, D. Yang, K. Wang, Microstructures and properties of  $\text{AlCoCrFeNi}_{2.5}$  eutectic high entropy alloy fabricated by selective laser melting, *Materials Science and Engineering: A* 875 (2023). <https://doi.org/10.1016/j.msea.2023.145081>.
- [195] X. Jin, Z. Xue, Z. Mao, R. Guo, X. Wang, X. Shi, S. Yin, M. Zhang, A. Lan, P.K. Liaw, J. Qiao, Exploring multicomponent eutectic alloys along an univariant eutectic line, *Materials Science and Engineering: A* 877 (2023). <https://doi.org/10.1016/j.msea.2023.145136>.

- [196] J.Q. Zheng, M.L. Wang, W.N. Jiao, L.J. Zou, Y. Di, Effect of Ti Addition on Microstructure Evolution and Mechanical Properties of  $\text{Al}_{18}\text{Co}_{13}\text{Cr}_{10}\text{Fe}_{14}\text{Ni}_{45}$  Eutectic High-Entropy Alloys, *Acta Metallurgica Sinica (English Letters)* 36 (2023) 1493–1501. <https://doi.org/10.1007/s40195-023-01564-1>.
- [197] X. Shi, G. Li, M. Zhang, H. Xu, Z. Li, Laves phase assisted the passive behaviours of Co-free non-equiatomic Cr-Fe-Ni-Nb eutectic high-entropy alloys, *J Alloys Compd* 960 (2023). <https://doi.org/10.1016/j.jallcom.2023.170905>.
- [198] M. Abdullah, M. Mukarram, T. Bin Yaqub, F. Fernandes, K. Yaqoob, Development of eutectic high entropy alloy by addition of W to CoCrFeNi HEA, *Int J Refract Metals Hard Mater* 115 (2023). <https://doi.org/10.1016/j.ijrmhm.2023.106300>.
- [199] Z. Liao, N. Li, W. Yang, S. Pang, N. Hua, Y. Meng, P.K. Liaw, T. Zhang, Effects of niobium on the microstructure, corrosion and mechanical behavior of ultra-fine lamellar  $\text{Al}_{0.3}\text{CrFeCoNiNb}_x$  eutectic high-entropy alloys, *J Alloys Compd* 966 (2023). <https://doi.org/10.1016/j.jallcom.2023.171521>.
- [200] Q. Zhao, H. Luo, Z. Yang, Z. Pan, Z. Wang, R.K. Islamgaliev, X. Li, Hydrogen induced cracking behavior of the dual-phase  $\text{Co}_{30}\text{Cr}_{10}\text{Fe}_{10}\text{Al}_{18}\text{Ni}_{30}\text{Mo}_2$  eutectic high entropy alloy, *Int J Hydrogen Energy* 50 (2024) 134–147. <https://doi.org/10.1016/j.ijhydene.2023.09.053>.
- [201] X. Liu, Z. Yang, D. Cui, Q. Wu, Z. Wang, J. Li, J. Wang, F. He, Enhancing the Yield Strength of Casting Eutectic High-Entropy Alloys via Coherent Precipitates, *Metall Mater Trans A Phys Metall Mater Sci* 54 (2023) 4620–4624. <https://doi.org/10.1007/s11661-023-07225-3>.
- [202] C. Liu, Y. Gao, K. Chong, Y. Zhang, Y. Zou, F. Guo, Corrosion and passivation behavior of  $\text{FeCoCrNiNb}_x$  eutectic high-entropy alloys in  $\text{H}_2\text{SO}_4$  solution, *Journal of Materials Research and Technology* 27 (2023) 4962–4977. <https://doi.org/10.1016/j.jmrt.2023.10.313>.
- [203] S. Feng, S. Guan, X. Liu, S. Peng, K. Dong, Y. Yang, X. Chen, Y. Liang, Q. Wang, Y. Liu, Y. Peng, K. Wang, W. Chen, J. Kong, Lightweight Co-free eutectic high-entropy alloy with high strength and ductility by casting, *Mater Res Lett* 12 (2024) 26–33. <https://doi.org/10.1080/21663831.2023.2284328>.
- [204] C. Su, S. Konovalov, X. Chen, Y. Wang, Y. Jin, Microstructure and mechanical property of the novel  $\text{Al}_{17}\text{Cr}_{17}\text{Co}_{33}\text{Ni}_{33}$  eutectic medium entropy alloy fabricated by powder plasma arc additive manufacturing, *Mater Lett* 361 (2024). <https://doi.org/10.1016/j.matlet.2024.136074>.
- [205] X. Liu, H. Liu, Y. Wu, M. Li, C. Xing, Y. He, Tailoring phase transformation and precipitation features in a  $\text{Al}_{21}\text{Co}_{19.5}\text{Fe}_{9.5}\text{Ni}_{50}$  eutectic high-entropy alloy to achieve different strength-ductility combinations, *J Mater Sci Technol* 195 (2024) 111–125. <https://doi.org/10.1016/j.jmst.2024.01.044>.
- [206] Y. Huang, X. Chen, S. Ma, M. Wen, Y. Wang, Y. Wang, Double-wire arc additive manufacturing of AlCoFeNi eutectic high entropy alloy with balanced strength and plasticity, *Mater Lett* 363 (2024) 136312. <https://doi.org/10.1016/j.matlet.2024.136312>.